COMPUTATIONAL DIFFRACTIVE OPTICS FOR IMAGING AND NONIMAGING APPLICATIONS

by

Peng Wang

A dissertation submitted to the faculty of
The University of Utah
in partial fulfillment of the requirements for the degree of

Doctor of Philosophy

Department of Electrical and Computing Engineering

The University of Utah

December 2016

The University of Utah Graduate School

STATEMENT OF DISSERTATION APPROVAL

The dissertation of **Peng Wang**

has been approved by the following supervisory committee members:

Rajesh Menon	, Chair	**03/17/2016** Date Approved
Steven Blair	, Member	**03/04/2016** Date Approved
Michael Scarpulla	, Member	**03/04/2016** Date Approved
Ling Zang	, Member	**03/04/2016** Date Approved
Prashant Tathireddy	, Member	**03/04/2016** Date Approved

and by **Gianluca Lazzi** , Chair/Dean of

the Department/College/School of **Electrical and Computer Engineering**

and by David B. Kieda, Dean of The Graduate School.

ABSTRACT

Optics is an old topic in physical science and engineering. Historically, bulky materials and components were dominantly used to manipulate light. A new hope arrived when Maxwell unveiled the essence of electromagnetic waves in a micro perspective. On the other side, our world recently embraced a revolutionary technology, metasurface, which modifies the properties of matter-interfaces in subwavelength scale. To complete this story, diffractive optic fills right in the gap. It enables ultrathin flat devices without invoking the concept of nanostructured metasurfaces when only scalar diffraction comes into play.

This dissertation contributes to developing a new type of digital diffractive optic, called a polychromat. It consists of uniform pixels and multilevel profile in micrometer scale. Essentially, it modulates the phase of a wavefront to generate certain spatial and spectral responses. Firstly, a complete numerical model based on scalar diffraction theory was developed. In order to functionalize the optic, a nonlinear algorithm was then successfully implemented to optimize its topography. The optic can be patterned in transparent dielectric thin film by single-step grayscale lithography and it is replicable for mass production. The microstructures are 3μm wide and no more than 3μm thick, thus do not require slow and expensive nanopatterning techniques, as opposed to metasurfaces. Polychromat is also less demanding in terms of fabrication and scalability.

The next theme is focused on demonstrating unprecedented performances of the

diffractive optic when applied to address critical issues in modern society. Photovoltaic efficiency can be significantly enhanced using this optic to split and concentrate the solar spectrum. Focusing through a lens is no news, but we transformed our optic into a flat lens that corrects broadband chromatic aberrations. It can also serve as a phase mask for microlithography on oblique and multiplane surfaces. By introducing the powerful tool of computation, we devised two imaging prototypes, replacing the conventional Bayer filter with the diffractive optic. One system increases light sensitivity by 3 times compared to commercial color sensors. The other one renders the monochrome sensor a new function of high-resolution multispectral video-imaging.

To my wife, Wen

TABLE OF CONTENTS

ABSTRACT iii

ACKNOWLEDGEMENTS ix

Chapters

1. INTRODUCTION 1

    1.1 Diffractive Optics 1
    1.2 Computational Optics 6
    1.3 Optical Systems 8
    1.4 Outlines 14
    1.5 References 16

2. NUMERICAL AND EXPERIMENTAL TECHNIQUES 18

    2.1 Device Modeling 18
    2.2 Device Fabrication 24
    2.3 Device Replication 33
    2.4 Direct-binary-search Algorithm 37
    2.5 Regularization Algorithm 41
    2.6 Optical Characterization Setup 46
    2.7 References 51

3. HIGH-EFFICIENCY MULTIBANDGAP PHOTOVOLTAICS 52

    3.1 Abstract 53
    3.2 Introduction 53
    3.3 Methods 55
    3.4 Experimental Results 59
    3.5 Numerical Analysis 62
    3.6 Conclusion 65
    3.7 Supplementary Information 66
    3.8 References 69

4. BROADBAND CHROMATIC-ABERRATION-CORRECTED LENS 72

    4.1 Abstract 73

4.2 Introduction 73
4.3 Working Principles 76
4.4 Experiments and Results 79
4.5 Discussions 83
4.6 Supplementary Information 87
4.7 References 93

5. MICROLITHOGRAPHY ON OBLIQUE AND MULTIPLANE SURFACES 96

5.1 Abstract 97
5.2 Introduction 97
5.3 Lithography Principles 98
5.4 Exposure Results 100
5.5 Analysis 106
5.6 Conclusion 109
5.7 Supplementary Information 110
5.8 References 112

6. ULTRA-HIGH-SENSITIVITY COLOR IMAGING 115

6.1 Abstract 116
6.2 Introduction 116
6.3 Principle of Operation 118
6.4 Experiments 122
6.5 Discussion 126
6.6 Small Sensor Pixel 131
6.7 Conclusion 134
6.8 Supplementary Information 135
6.9 References 142

7. COMPUTATIONAL SINGLE-SHOT MULTISPECTRAL IMAGING 145

7.1 Abstract 145
7.2 Introduction 145
7.3 Methods 148
7.4 Experimental Results 152
7.5 Analysis 156
7.6 Larger Field-of-view 161
7.7 Conclusion 163
7.8 References 163

8. OTHER WORKS ON NANOPHOTONICS PART 1: LIGHT TRAPPING 167

8.1 Abstract 168
8.2 Introduction 168
8.3 Methodology 169

8.4 Results 172
8.5 Beyond the Ergodic Limit 175
8.6 References 177

9. OTHER WORKS ON NANOPHOTONICS PART 2: INTEGRATED PHOTONICS 180

9.1 Abstract 181
9.2 Background Introduction 181
9.3 Methodology 182
9.4 Results 185
9.5 More Functionalities 188
9.6 References 189

10. SUMMARY AND FUTURE WORK 192

10.1 Summary 192
10.2 Future Work 194
10.3 References 199

ACKNOWLEDGEMENTS

This dissertation work could not have been done without the help of many people. First of all, I would like to thank my Ph.D. advisor Prof. Rajesh Menon for guiding me into this fantastic arena of research in optics and photonics. It has been an inspiring and extremely helpful five years. What I learned and experienced in his lab taught me to enjoy the beauty of exploration, the value of endurance and the excitement of innovation. It will definitely be a good start for my future career.

Many thanks go to the lab members. Bing Shen worked on the nanophotonics project with me. Ganghun Kim started the polychromat project in our lab and after he returned for his Ph.D. we had lots of discussions on imaging optics. Nabil Mohammad took over the multibandgap photovoltaics and also worked on the polychromat replication process. Dr. Eyal Shafran joined our group to help on the computational side of the imaging project. Carl Ebeling built and maintained the complex multicolor confocal microscopy system. Apratim Majumder helped me on the microlithography setup.

I have also received a lot of useful help from the Utah NanoFab Staff regarding device fabrication and characterization, including Brian Baker, Steve Pritchett, Brian van Devener, Randy Polson, Charles Fisher and Paulo Perez. I also felt thrilled to collaborate with Daniel J. Friedman from the National Renewable Energy Lab and Tolga Aytug from the Oak Ridge National Lab on solar cell projects. I would also offer my gratitude to Dr. Jose A. Dominguez-Cabellero from Intel, who started the DBS algorithm, and Prof. Chris

Johnson from the Scientific Computing Institute for teaching me the regularization technique. I thank Prof. Jordan Gerton for inspiring me on the concept of computational spectroscopy. Mark Ogden and Stewart Brock from the CADE Lab offered part of the computational tools in this work. During my Ph.D., my research was generously supported by the USTAR Initiative, Department of Energy, NASA, US Navy, and NIH.

I would like to thank my friends in Salt Lake City for all those wonderful times: Jinqi Wang, Xiaojin Jiao, Jingchi Yan, Shuchang Liu, Hongyu Ma, Zhe Yang, Zhuo Su, Qingbo Guo, Juan Gu, Yaqiong Zhang, Huizhong Li, Yipin Chen, Long Luo, Pradeep Kasinadhuni, Jingxiang Zhou, Keith Phinney, Shuai Xu, Vincent Holt, Raheel Samuel, and Chi Yen. I also thank my committee members: Prof. Steve Blair, Prof. Mike Scarpulla, Prof. Ling Zang and Prof. Prashant Tathireddy. Lori Sather and Megan McAllister at the ECE department office are also acknowledged. Finally, special thanks go to my parents and my beloved wife, Wen, for their unending love, care and support.

CHAPTER 1

INTRODUCTION

1.1 Diffractive Optics

Optics, in general, studies the propagation of electromagnetic wave and its interactions with matter [1]. Electromagnetic radiation covers a wide range of frequencies, from microwave, radio-frequency (RF), terahertz (THz), infrared (IR), visible (Vis), ultraviolet (UV), to X-ray and Gamma-ray. This dissertation focuses on studies in the visible band, which is historically called, light. In quantum physics, the electromagnetic radiation has wave-particle-duality [1], but in this work only its wave characteristics are considered. The electromagnetic wave is essentially a coupling of electric and magnetic fields that oscillate. Its wave behavior, including propagation and interactions with matter, can be fully described by Maxwell's equations [1]:

$$\begin{aligned} \nabla \cdot \vec{\mathbf{D}} &= \rho \\ \nabla \cdot \vec{\mathbf{B}} &= 0 \\ \nabla \times \vec{\mathbf{E}} &= -\frac{\partial \vec{\mathbf{B}}}{\partial t} \\ \nabla \times \vec{\mathbf{H}} &= \vec{\mathbf{J}} + \frac{\partial \vec{\mathbf{D}}}{\partial t} \end{aligned} \tag{1.1}$$

and the constitutive equations of material properties:

$$\begin{aligned}\vec{\mathbf{D}} &= \varepsilon_0 \varepsilon_r \vec{\mathbf{E}} \\ \vec{\mathbf{B}} &= \mu_0 \mu_r \vec{\mathbf{H}} \\ \vec{\mathbf{J}} &= \sigma \vec{\mathbf{E}}\end{aligned} \quad . \tag{1.2}$$

Here, **E** and **H** represent the vectors of electric and magnetic fields, respectively. **J** is current density. ε, μ, and σ are permittivity, permeability, and conductivity of the material, respectively. According to the properties of mathematical operators, we can derive the vector wave equation of propagation in a linear, isotropic, homogeneous and nondispersive medium [2]:

$$\nabla^2 \vec{\mathbf{E}} - \frac{n^2}{c^2} \frac{\partial^2 \vec{\mathbf{E}}}{\partial t^2} = 0 \quad . \tag{1.3}$$

n is the refractive index of propagation material and c is the speed of light in a vacuum. In such an ideal medium, all the components of the vectors of both electric and magnetic fields behave in the same way. Thus, the vector form of the wave equation can be simplified to the scalar form [2]:

$$\nabla^2 u - \frac{n^2}{c^2} \frac{\partial^2 u}{\partial t^2} = 0 \quad . \tag{1.4}$$

In Equation (1.4), u can stand for any component of the electric and magnetic fields.

It is not much use to only consider light propagation in an ideal medium. It is more interesting to study the behaviors of light when the medium is perturbed, as by introducing some degrees of inhomogeneity. This is where the theory of scalar diffraction comes into play. Note that scalar diffraction does not hold when the spatial extension of

inhomogeneity is on par or smaller than the wavelength of light [1,2].

To start with, it is helpful to borrow some commonly used concepts from the field of electrical signal processing [3]. In a classic model, there is input, output, and system. The system takes the data from input, processes the data, and then outputs results, similar to a mathematical operation. For a linear time-invariant system, it follows a number of useful properties in both time and frequency domains [3]. Diffraction and any optical systems can also be considered to be analogous with this model. The optical component, either bulk lens, mirror, aperture, diffraction structure, or nanophotonic device, just like a signal processing system, manipulates the incoming light as the input to the system. The light comes out of systems, either refracted, reflected, or diffracted, are the output of the system. This is schematically depicted in Figure 1.1.

Calculating output with input and system known is a forward problem. An example is to plot the point-spread-function (PSF) and all kinds of aberrations for an imaging device. Nonetheless, usually it is the input or the systems that is unknown. To search for a system that accurately relates both input and output and satisfies the laws of physics is a design process. Lens system optimization is a typical example. Actually, this general concept also summarizes our work in Chapters 3, 4, 5, 8, and 9 in this dissertation. In other scenarios, we attempt to solve for the input after carefully calibrating the system and measuring the output signals. Spectrometer is an application that follows this rule. This last concept is basically a summary of our work in Chapters 6 and 7.

Now, let us come back to the topic of diffraction itself. Diffraction studies the interactions of light with inhomogeneous matters. Without loss of generality, a typical physical model consisting of incident light impinging an aperture is often utilized. Light

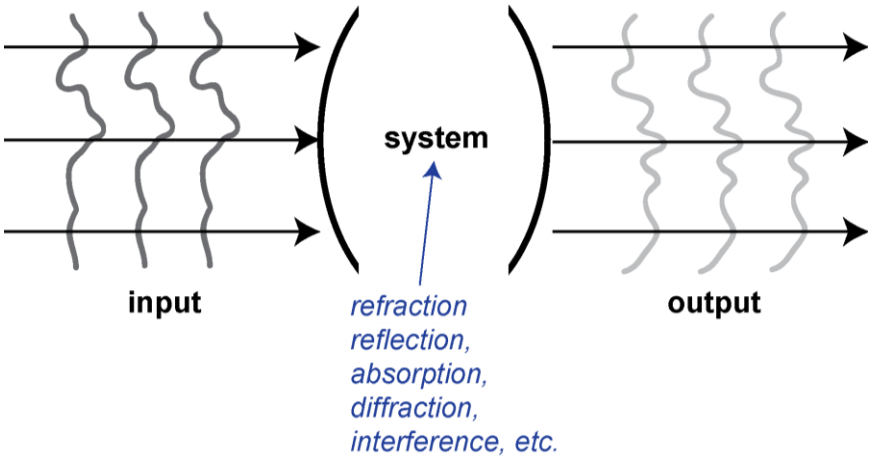

Figure 1.1. A typical signal processing model, including input, output, and system. Optical systems, including diffraction, can be analogous with this traditional model.

propagates from left to right (see Figure 1.2). Based on the Huygens principle, the wavefront on the aperture can be decomposed into a group of secondary point sources [2]. Each of them emits a spherical wave. The wavefront at the next time spot can be equivalently represented by a coherent sum of the spherical waves from these secondary light sources [2]. Light propagates by repeating this process. By applying Green's theorem and assuming that the observation screen is much farther than the wavelength of light, we can derive the following Huygens-Fresnel principle [2]:

$$U(x',y') = \frac{d}{i\lambda}\iint_{\Sigma} U(x,y)\frac{e^{ikr_{01}}}{r_{01}^2}dxdy \quad . \tag{1.5}$$

In Equation (1.5), $U(x',y')$ is the electrical field received by an observation screen at distance d from the aperture (along Z axis), as illustrated in Figure 1.2(b). $U(x,y)$ is the function describing the aperture. And r_{01} is the distance between any point in the aperture (x,y) and any point in the observation screen (x',y'). λ is the wavelength of light and $k=2\pi/\lambda$ is wave-number. The integral is over the aperture, Σ.

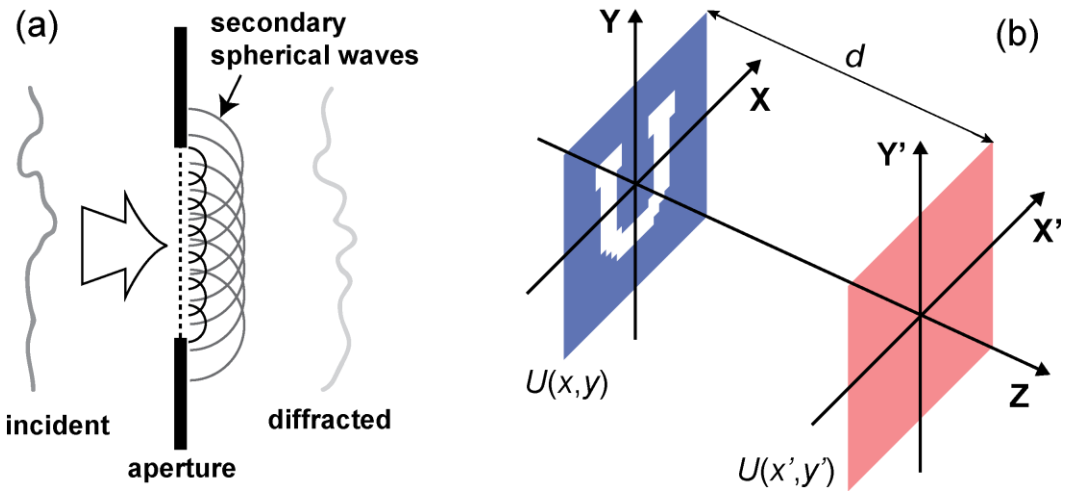

Figure 1.2. Explanation of diffraction theory. (a) Schematic illustration of the Huygens-Fresnel principle for diffraction calculation. (b) Schematic of a diffraction system. The red block represents the observation screen and the blue block represents the aperture. They are separated by *d*. $U(x,y)$ is the aperture function and $U(x',y')$ describes the electric field of the diffraction pattern.

Next, it is useful to derive an analytical formulation that is convenient and fast to compute. This is realized by making further approximations to the system. By removing all high-order terms in binominal expansion, the distance r_{01} may be expressed by

$$\begin{aligned} r_{01} &= \sqrt{d^2 + (x-x')^2 + (y-y')^2} \\ &\approx d\left[1 + \frac{1}{2}\left(\frac{x-x'}{d}\right)^2 + \frac{1}{2}\left(\frac{y-y'}{d}\right)^2\right]. \end{aligned} \tag{1.6}$$

Taking Equation (1.6) into Equation (1.5), we end up with the Fresnel transform of calculating diffraction pattern [2]:

$$U(x',y') = \frac{e^{ikd}}{i\lambda d}\iint U(x,y)e^{i\frac{k}{2d}\left[(x-x')^2+(y-y')^2\right]}dxdy \tag{1.7}$$

Note that the Fresnel approximation offers accurate results as long as the following

geometric condition is satisfied:

$$d^3 >> \frac{\pi}{4\lambda}\left[(x-x')^2+(y-y')^2\right]^2_{\max}. \tag{1.8}$$

This implies that the distance between the observation plane (or an image plane) is much larger than the dimension of the aperture. Equation (1.7) is the formula used for modeling the polychromat in this dissertation since Equation (1.8) is always satisfied for all the applications.

It eventually comes to the geometric optics regime when the system has feature sizes much larger than the wavelength. Diffraction effects may be negligible and ray-tracing is usually applied to describe the behaviors of light.

1.2 Computational Optics

In recent years, computational optics has become one of the hot topics in research and innovation. The word ‘computational’ can be assigned two different meanings. On one hand, it represents a whole family of computer models that simulate the behaviors of light at different length scales. On the other hand, it is also a token of the marriage between traditional optical systems and advanced numerical algorithms. This gives birth to new technologies that either enhance performances of optical systems or change the ways optical systems work. Both aspects are explored in this dissertation.

1.2.1 The first meaning

Besides the scalar diffraction model of polychromat, we also exploited full-wave solutions of the Maxwell’s equation in studying nanophotonics. To be specific, the finite-difference time-domain (FDTD) [4,5] and the rigorous-couple-wave-analysis (RCWA)

[6] are used. These numerical techniques are useful when the physical size of the photonic structures reaches subwavelength regime, and thus the condition of scalar diffraction breaks. Figure 1.3 gives an example of FDTD simulation of light propagation in silicon-on-insulator (SOI) waveguide. The poly-Si waveguide has a 400nm×360nm cross-section. Both fundamental TE and TM modes are shown.

1.2.2 The second meaning

Although we emphasize that computational optics is an emerging field of study, in reality the applications of numerical algorithms in optical systems have already become ubiquitous. Two examples are given in Figure 1.4. One is demosaicing [7], computationally reconstructing the RGB image from the raw Bayer image. The other technique is deblurring [8], which is able to sharpen an originally blurred image.

Recently, the most important application of algorithms is in computational imaging (or microscopy) such as high-dynamic-range (imaging HDR) [9] and light-field imaging [10]. One successful example is Fourier ptychographic microscopy (FPM) [11]. In FPM, the sample is illuminated by wavefronts of different spatial frequencies, created by an array of LED's incidence at different angles. A set of micrographs, representing different

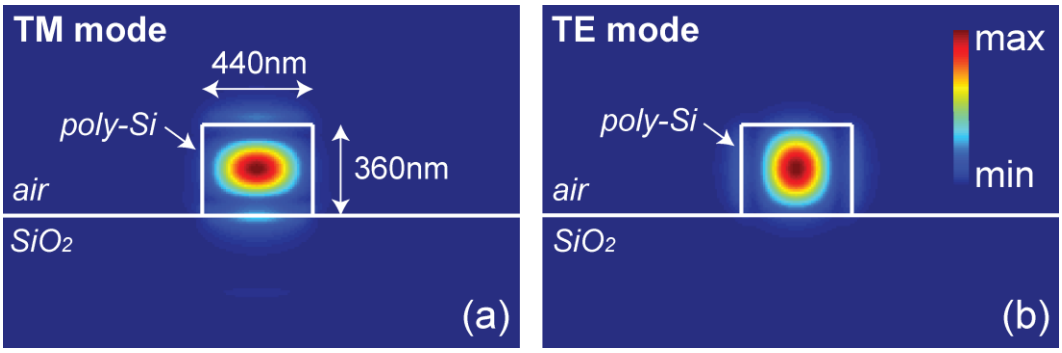

Figure 1.3. FDTD simulation of an SOI waveguide (cross-section view). Both TM (a) and TE (b) fundamental modes are simulated. White lines sketch its shape.

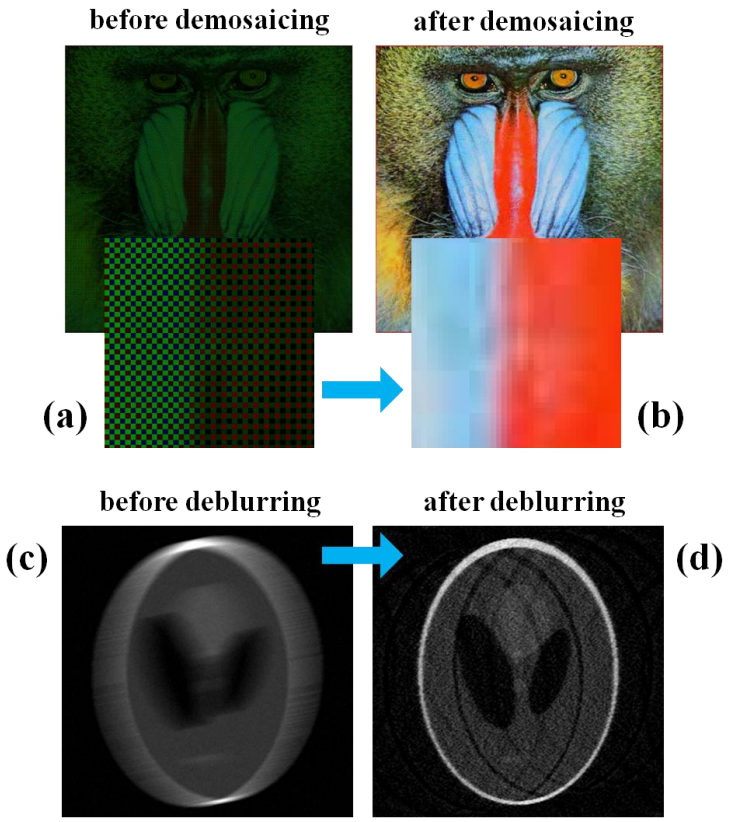

Figure 1.4. Examples of using numerical algorithms in imaging systems. Before (a) and after (b) applying demosaicing algorithm. Before (c) and after (d) applying deblurring algorithm.

regions in the spatial frequency domain, are captured and stored. Then these images are numerically stitched. The final image is computationally recovered from the frequency domain. Since it significantly augments the NA-limited frequency extent of the single raw image, it allows for high-resolution giga-pixel microscopy [11].

1.3 Optical Systems

1.3.1 Reflection and refraction

In traditional optical engineering, light is often treated as bundles of rays. These bulk optical components are composed of planar or curved interfaces [1] (see Figure 1.5). Depending on the properties of the matter interface, light ray is refracted or reflected.

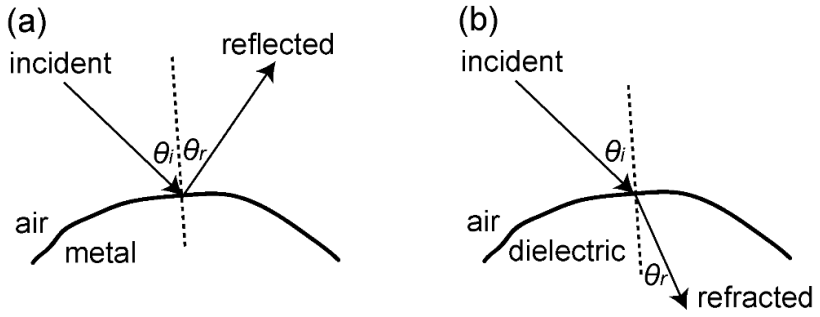

Figure 1.5. Illustration of reflection (a) and refraction (b) at the air-metal and air-dielectric interface. The dashed lines represent the surface normal.

Its behavior is fundamentally dictated by Snell's law of refraction and reflection [1]. Figure 1.5 illustrates the phenomena of reflection and refraction. The relationship between the angles of incidence and reflection is [1]

$$\theta_r = \theta_i \tag{1.9}$$

and the relationship between the angles of incidence and refraction is [1]

$$\sin(\theta_r) = \frac{n_i}{n_r}\sin(\theta_i) \quad . \tag{1.10}$$

Traditional optical designs are made and analyzed based on the laws of reflection and refraction, described by Equations (1.9) and (1.10).

1.3.2 Imaging optical system

To facilitate understanding of how polychromat is applied in a variety of optical systems, this and the following subsections offer a brief introduction to conventional imaging and nonimaging optical systems.

Optics was used in imaging for centuries. The basic principle remained the same. An object, whether emitting light by itself or reflecting illumination, can be treated as a

cluster of points. Each point is equivalent to a light source, emitting light in a divergence cone of angle. In order to image such a cluster of points, optical components are required to collect and reshape the light from each point source. Usually, curved interfaces, such as a lens or nonplanar mirror, are used to bend light rays. There is always a one-to-one mapping, meaning that one object point is projected to one unique image point [1]. This image may be recorded by light-sensitive pigments in human retinal cells, photographic films or semiconductor sensors.

Figure 1.6(a) is an example of using a refractive lens for imaging. A photograph of a commercial compact camera is shown as an inset. Note that in an aberration-free system, an infinitely small object point is imaged to a point mathematically described as an Airy disk (Figure 1.6(b)), which is calculated by diffraction formulation.

The scheme of imaging optics does not convey any color or spectrum information. This is because in an ideal system light rays of different colors follow the same path. In order to distinguish colors, a Bayer filter array is widely used together with a CCD or CMOS sensor [12]. It is periodic in 2D, and each single period corresponds to one single image point. Within one period, there are four color filters, two transmit green, one transmits blue, and one transmits red. A schematic and a micrograph of this famous filter are given in Figures 1.7(a) and (b). Since they are absorptive, two thirds of light are wasted, thus the light sensitivity of the sensor is dramatically reduced. In addition, these square-shape filters need to exactly cover the sensor pixels, thus high-precision alignment is necessary.

However, for some applications, seeing three colors is not enough. This is where multi- and hyper-spectral cameras come to the stage [13]. The market of these cameras

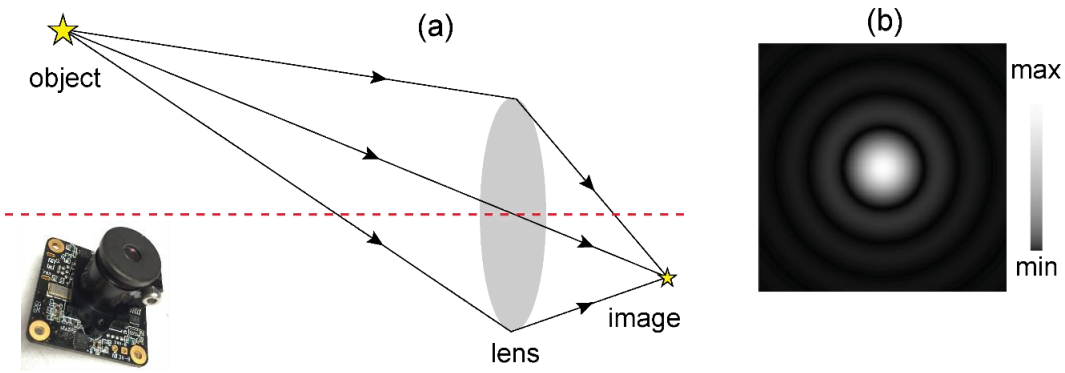

Figure 1.6. Optical imaging system. (a) Illustration of a conventional imaging system using a lens. One object point is projected to one image point. Red dashed line is the optical axis. Inset: photograph of a compact camera. (b) An ideal image point of Airy pattern in a diffraction-limited system.

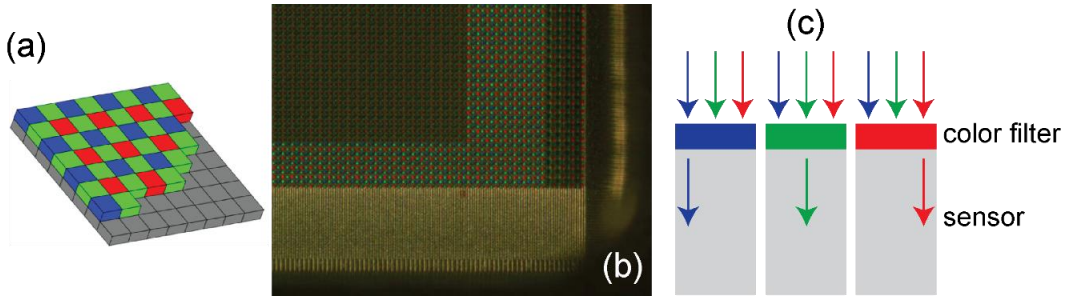

Figure 1.7. Color sensor. (a) Schematic of a Bayer filter array. Each unit consists of four absorption filters to transmit blue, green, and red. (b) A micrograph of the Bayer filter on top of a semiconductor sensor array. (c) Illustration explaining the working principle of the Bayer color filter. Only one third of incident photons are allowed to pass through.

has been dominated by complicated, expensive, and slow produces. In our imaging projects, we attempt to tackle these issues by introducing the polychromat into the semiconductor sensor, as a replacement of the Bayer filter. It not only improves photon throughput, but also enables compact, fast, and inexpensive hyperspectral imaging.

1.3.3 Nonimaging optical system

Besides imaging, optics also enables a huge number of nonimaging applications. In nonimaging systems, the one-to-one relationship underlying the imaging system is

broken [1]. Again, it can be generalized as a signal processing system, drawn in Figure 1.2. Any arbitrary input wavefront of any arbitrary spectral component may be reshaped or reconfigured to any arbitrary spatial-spectral output.

Figure 1.8 summarizes some of the important nonimaging optical systems. One application is focusing light, such as that from the sun or a lamp. A parabolic mirror is able to reflect and divert collimated rays of large area to a tiny spot (see Figure 1.8(a)) [1]. It can be a key component in a solar thermal system to collect solar energy to heat up anything at the focus, such as a cooker [14].

A collimator lens works in the reverse manner. It expands and collimates the light from a point source located at its focus (Figure 1.8(b)). It provides uniform illumination and finds applications in microscopy. Usually, a combination of two convex lenses with their curved surfaces facing each other replaces a single lens for aberration correction. In conjunction with a spherical mirror on the back side of the source, a condenser is constructed [15]. It is critical in a microscope to uniformly illuminate the sample.

Often, lights of different wavelengths are mixed together, like in an imaging system. However, they can be evidently separated by passing through either a prism or a grating (see Figure 1.8(c)) [1]. A prism disperses light by accumulating differential optical paths between wavelengths, while grating diffracts light since the diffraction angle is proportional to wavelength. Most of the commercial spectrum analyzers utilize either of these two schemes.

Besides diffraction, interference is another phenomenon that can only be explained by the wave nature of light. Interference occurs only when two or more coherent beams of the same frequency and the same polarization state coincide at the same spatial location.

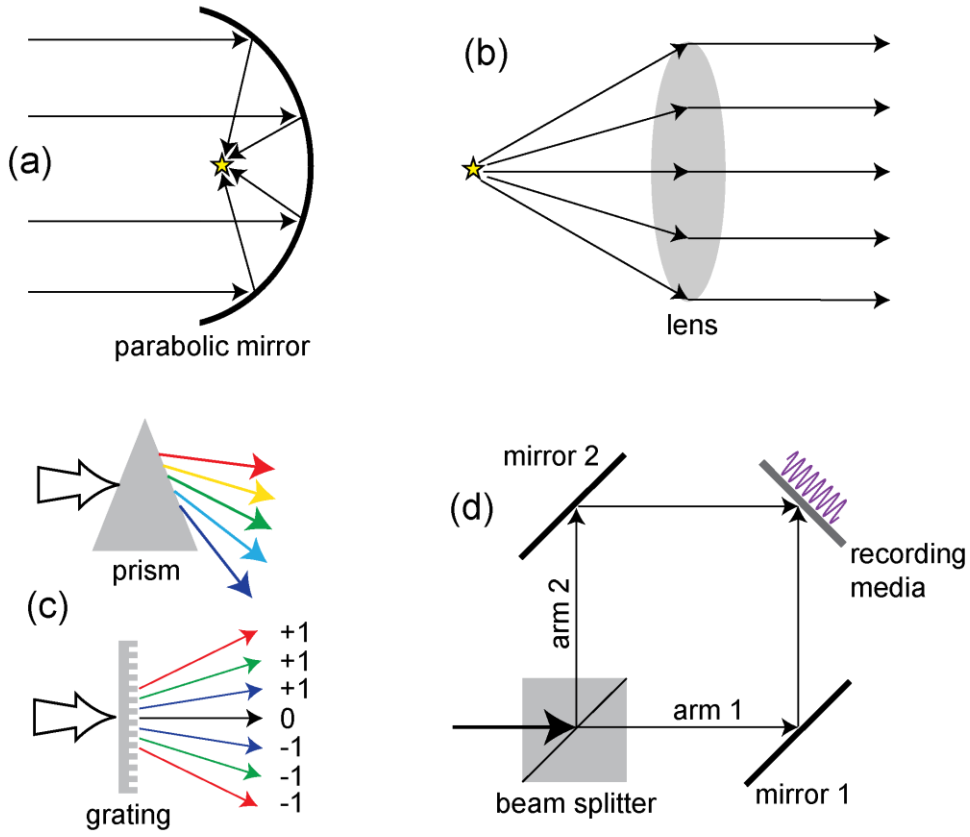

Figure 1.8. Illustrations of some nonimaging optical systems. (a) A parabolic mirror concentrates the collimated beam to a focus. (b) Lens collimates divergence beam from a point source located at its focus. (c) Prism and grating separate white incoming light to beams of different colors (or wavelengths) using material dispersion and diffraction. (d) Mach-Zehnder interferometer. A coherent laser beam is split by a beam splitter and the two arms interfere on a recording media.

Figure 1.8(d) is an example of a Mach-Zehnder interferometer, where a laser beam is split into two arms by a beam splitter, and the two arms then interfere. It has applications in integrated optical communication [16] and interference nanolithography [17].

The polychromat may be designed to outperform the conventional optic in these nonimaging systems. On one hand, the polychromat is much more compact since it is micropatterned in ultrathin film on a flat surface. On the other hand, the polychromat can integrate multiple functionalities thanks to its enormous degree of design freedom. For a polychromat with N pixels and P height levels, it occupies P^N design freedom.

1.4 Outlines

The first chapter briefly introduces the principles of diffractive optics and the concept of computational optics. The basic theory of diffraction laid foundations for the numerical model, which describes the studied digital diffractive optic element. In addition, a background introduction to some simple optical systems is given in this chapter. This is very helpful in understanding the applications of the optic discussed in the following chapters.

Chapter 2 contains explicit descriptions on the device model based upon the formula of far-field scalar diffraction, or Fresnel transform. This chapter also talks in detail about how the diffractive optic is fabricated by the commercially available grayscale lithography approach. We emphasize that grayscale calibration and scanscale calibration are keys to successful patterning. A standard procedure is given as well. Next, a preliminary device replication method based on hot embossing is also included. The polychromat topography is optimized by a direct-binary-search (DBS) algorithm to equip it with multiple functionalities. A detailed description of regularization algorithm forms another section. Regularization is extensively explored to solve inverse problems in our imaging applications. For experimental characterization, we built several optical setups. They are described in the final section of Chapter 3.

With all this knowledge in mind, we showcase the potentials of the diffractive optic in changing numerous optics-enabled applications. In Chapter 3, the polychromat works as a spectrum splitter/concentrator in planar multibandgap photovoltaics. Sorting out different bands of solar spectrum can theoretically push photovoltaic efficiency towards the thermodynamic limit. Our experiments demonstrate a 20% efficiency enhancement.

Excitingly, numerical studies predict that an overall efficiency of 50% is possible, given more bandgaps and larger concentration factors.

In Chapter 4, the polychromat is designed to perform far-field focusing. Due to its enormous degree of design freedom, it can be optimized to correct chromatic aberration over the entire visible spectrum. The measured optical efficiency of the apochromat is about 25%, and that of the super-achromat is ~10%. Such a flat lens is polarization-independent and has much lower aspect ratios and better scalability in comparison with metalenses. Ultrahigh efficiency and correction for other aberrations are also possible.

Next, we turn to maneuver the 3D spatial response of polychromat under single-line coherent illumination. It is used as a phase mask for 3D rapid patterning, described in the fifth chapter. For proof of concept, we simply demonstrated optical microlithography on oblique and multiplane surfaces. Spatial resolution, depth-of-focus, and fabrication error tolerance are discussed in detail.

Chapters 6 and 7 talk about applications of polychromat in imaging systems. In Chapter 6, the diffractive filter array made in optically transparent material replaces the Bayer filter. This allows for improved photon throughput. Computational algorithms are exploited to extract color with high accuracy. A maximum sensitivity enhancement of 3.12 is achieved. It also enables multispectral imaging.

Chapter 7 explores the application of polychromat in computational single-shot hyperspectral imaging. Placing the diffractive optic in proximity to a monochrome sensor creates both spatially-variant and spectrally-variant point-spread functions. Hyper-spectral data cubes can be efficiently and accurately reconstructed from the highly multiplexed and scrambled image by numerical algorithm. Interestingly, due to the

structured PSFs by diffraction, this allows for remarkably enhanced spatial resolution. Imaging the 3D space is a side benefit as well.

Chapters 8 and 9 include some other important works on nanophotonics that went along with this polychromat project. We modeled and optimized the generalized periodic multilayer nanostructures to boost light absorption in ultra-thin-film solar cells. Enhancement beyond the ergodic limit of light trapping may be obtained via increasing mode occupancy and local density of optical states. The same DBS algorithm was adapted to design all-dielectric digital metamaterials for ultracompact integrated photonics devices, such as wavelength splitter, polarization splitter, polarization rotator, and free-space-to-waveguide coupler. These nanophotonic devices control the vector properties of light.

This dissertation concludes in Chapter 10. Prospective directions for ongoing research are pointed out and discussed. We want to extend the photovoltaic project to a larger number of bandgaps and greater concentrations. 3D patterning may take a longer path to achieve. We are devoted to promoting the development of a hyperspectral imager prototype that can compute full-frame images in real time. Light-field imaging could be another bonus out of the polychromat project.

1.5 References

[1] M. Born, and E. Wolf, *Principles of Optics: Electromagnetic Theory of Propagation, Interference and Diffraction of Light* (Cambridge University Press, 1999).

[2] J. W. Goodman, *Introduction to Fourier Optics* (Roberts and Company Publishers, 2005).

[3] A. V. Oppenheim, A. S. Willsky, and S. H. Naweb, *Signals and Systems* (Prentice Hall, 2nd edition, 1996).

[4] K. S. Yee, “Numerical solution of initial boundary value problems involving Maxwell's equations in isotropic media,” IEEE Trans. Antenn. Propag. **14**, 302-307 (1966).

[5] G. Mur, “Absorbing boundary conditions for the finite-difference approximation of the time-domain electromagnetic-field equations,” IEEE Trans. Electromagn. Compatibility **23**, 377 (1981).

[6] M. G. Moharam, and T. K. Gaylord, “Rigorous coupled-wave analysis of planar-grating diffraction,” J. Opt. Soc. Am. **71**, 811-818 (1981).

[7] Color image demosaicing project from the Tokyo Institute of Technology: http://www.ok.ctrl.titech.ac.jp/res/DM/RI.html.

[8] Webpage on “Enhancement methods in image processing” from MathWorks: http://www.mathworks.com/discovery/image-enhancement.html.

[9] P. E. Debevec, and J. Malik, “Recovering High Dynamic Range Radiance Maps from Photographs,” SIGGRAPH '97 Proceedings of the 24th Annual Conference on Computer Graphics and Interactive Techniques, 369-378 (1997).

[10] M. Levoy, Z. Zhang, and I. McDowall, “Recording and controlling the 4D light field in a microscope using microlens arrays,” J. Microscopy **235**, 144-162 (2009).

[11] G. Zheng, R. Horstmeyer, and C. Yang, “Wide-field, high-resolution Fourier ptychographic microscopy,” Nat. Photonics **7**, 739–745 (2013).

[12] B. E. Bayer, “Color imaging array,” US Patent 3,971,065 (1976).

[13] N. Hagen, and M. W. Kudenov, “Review of snapshot spectral imaging technologies,” Opt. Eng. **52**, 090901 (2013).

[14] D. Mills, “Advances in solar thermal electricity technology,” Sol. Energ. **76**, 19-31 (2004).

[15] Online tutorial on optical microscopy from Nikon MicroscopyU: http://microscopyu.com/articles/optics/components.html

[16] D. A. B. Miller, “Perfect optics with imperfect components,” Optica **2**, 747-750 (2015).

[17] T. L. Andrew, H-Y. Tsai, and R. Menon, “Confining light to deep subwavelength dimensions to enable optical nanopatterning,” Science **324**, 917-921 (2009).

CHAPTER 2

NUMERICAL AND EXPERIMENTAL TECHNIQUES

2.1 Device Modeling

2.1.1 Model and formulation

The generalized model of the diffractive optic element (or polychromat) is described in Figure 2.1. There are two major parts in the model: the device plane and the image plane [1]. Since our polychromat is a planar optic, it is abstracted as a flat surface. The diffraction pattern is also imaged and analyzed on a flat surface parallel to the polychromat plane. The diffractive optic can be categorized into a 1D form and a 2D form. In its 2D form, the diffractive optic (blue grid in Figure 2.1(b)) is discretized into square pixels with uniform sizes (Δ) in two orthogonal directions (X and Y). The 1D form only has height variation along the X direction, while remaining uniform along the Y direction, as shown in Figure 2.1(a). The discretization in the X direction is also defined with a grid width of Δ. For clarity of definition, the single square grid in 2D form is called a "pixel", while a single linear grid in 1D form can be called either "pixel" or "groove". Generally, the image space (red grids in Figures 2.1(a) and (b)) is defined in the same grid size. Different from a traditional diffractive optic element with a continuously varying height profile [2], the polychromat is a type of digital diffractive optic, composed of an array of discrete pixels [3]. Such a digital diffractive optic allows for direct-writing in fabrication, as opposed to interference patterning.

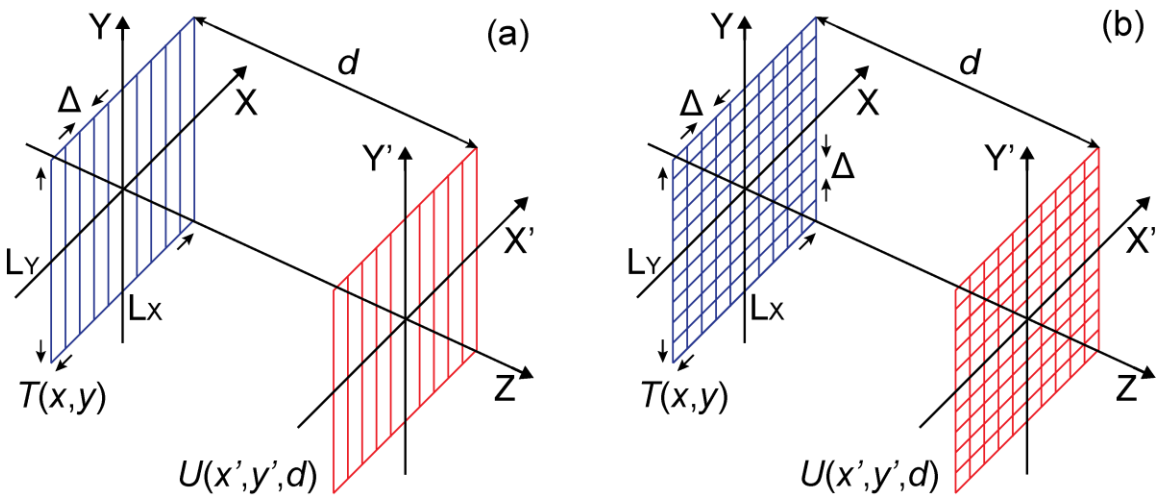

Figure 2.1. Schematic illustration of the generalized simulation model of the studied diffractive optic element in (a) 1D form and (b) 2D form. The blue grids represent the coordinate plane of the polychromat, and the red grids represent the coordinate plane (or image plane) of far-field diffraction.

The topographies of the polychromat in 1D and 2D forms are expressed by [1,3]:

$$h(x) = \sum_{m} \Delta h \cdot p_{(m)} \cdot rect\left(\frac{x - m\Delta}{\Delta}\right) \tag{2.1}$$

$$h(x,y) = \sum_{m}\sum_{n} \Delta h \cdot p_{(m,n)} \cdot rect\left(\frac{x - m\Delta}{\Delta}\right) \cdot rect\left(\frac{y - n\Delta}{\Delta}\right) \tag{2.2}$$

in which $\Delta h = H / (N_{levels} + 1)$ is the unit height, H is the maximum height, and N_{levels} is the total number of quantization levels, $p_{(m)}$ and $p_{(m,n)}$ stand for height profile and are positive integers within the limit [0, N_{levels}], and *rect*( ) is the rectangle function. Here, the integer m in Equation (2.1) represents the index of groove in the 1D form. And the integers m and n in Equation (2.2) represent the index of pixels in the X and Y directions in the 2D form. In practice, the polychromat topography $p_{(m)}$ and $p_{(m,n)}$ are either given by a random generator function in MATLAB ('rand') or by the optimization algorithm that will be described later.

The diffractive optic element works by modulating the wavefront of the incoming light, which is abstracted as a signal processing system (see Figure 1.1). As mentioned earlier, the diffractive optic studied in this work only modulates the phase of the wavefront while leaving the amplitude intact since the optic is made of a transparent dielectric material. The material absorption within the spectrum of interest (visible band 400nm to 700nm in general) is negligible. To be more specific, the phase imparted by one pixel in the diffractive optic is essentially determined by its local height (or thickness). This phase at a certain wavelength λ is expressed by [1]:

$$\varphi(x;\lambda) = \frac{2\pi}{\lambda} \cdot \Delta h \cdot p_{(m)} \cdot \left[n(\lambda) - 1 \right] \tag{2.3}$$

$$\varphi(x,y;\lambda) = \frac{2\pi}{\lambda} \cdot \Delta h \cdot p_{(m,n)} \cdot \left[n(\lambda) - 1 \right] \tag{2.4}$$

Equations (2.3) and (2.4) are for 1D and 2D forms of polychromat, respectively. They are basically relative phase change between with and without the presence of a pixel in the diffractive optic. Here, $n(\lambda)$ is the real part of the refractive index of the polychromat material and 1 is the refractive index of vacuum. Note that the phase $\varphi(x;\lambda)$ and $\varphi(x,y;\lambda)$ is linearly proportional to individual pixel height: $h_{(m)}=\Delta h \times p_{(m)}$ and $h_{(m,n)}=\Delta h \times p_{(m,n)}$, as indicated in Figure 2.2. Therefore, thicker structure accumulates more phase change. Yet, the phase is always modulo of 2π.

Note that the pixel width, Δ, is dictated by the resolution available to our lithography machine. In this work, we are limited to Δ=3μm. Alternative tools with advanced optical projection systems may enable resolution as high as Δ=1μm. The maximum height of the pixels H can in theory be any arbitrary value. However, on one hand, it has to be larger

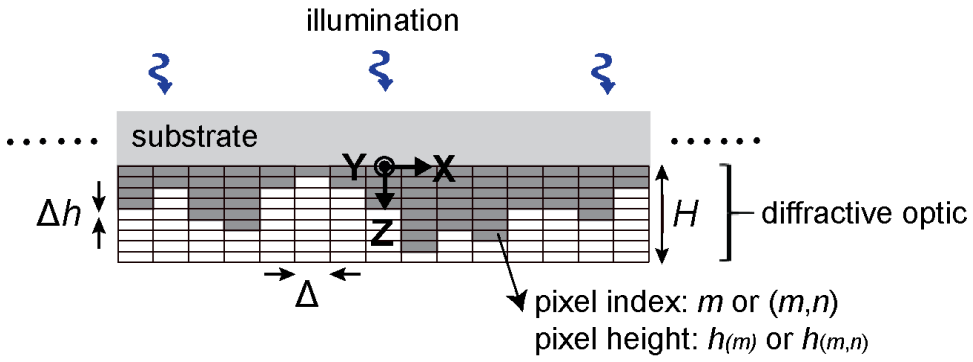

Figure 2.2. Schematic of the digital diffractive optic element (polychromat). Only a cross-section view of its 1D form is shown for simplicity. It is discretized into uniform pixels of width Δ.

than the one that gives 2π phase change; otherwise, the thinner the whole structures, the poorer optical efficiency it gets. On the other hand, thicker structures with larger aspect-ratios become difficult to pattern, though they potentially offer higher efficiency. In our current work, the aspect ratio is no more than 1:1, indicating maximum height $H \leq 3\mu m$. In addition, the unit height Δh is determined by how well our lithography process can define the depth. A minimum Δh of 13.9nm was used in our microlithography project (see Chapter 5); besides, we also used Δh=28.6nm and Δh=50nm in other works.

Based on Equation (1.7), the complex diffraction pattern of wavelength λ at distance d from the diffractive optic is calculated by the Fourier transform [1,2]:

$$U(x',\lambda,d) = \frac{e^{ikd}}{i\lambda d} \cdot \int g_{illum}(x,\lambda) \cdot T(x,\lambda) \cdot e^{i\frac{k}{2d}\cdot(x'-x)^2} dx. \qquad (2.5)$$

$$U(x',y',\lambda,d) = \frac{e^{ikd}}{i\lambda d} \cdot \iint g_{illum}(x,y,\lambda) \cdot T(x,y,\lambda) \cdot e^{i\frac{k}{2d}\cdot\left[(x'-x)^2+(y'-y)^2\right]} dxdy. \qquad (2.6)$$

Again, these two equations are for 1D and 2D forms, respectively. The wave-number is $k=2\pi/\lambda$; $g_{illum}(x,\lambda)$ and $g_{illum}(x,y,\lambda)$ are the incoming wavefronts of the illumination beam.

In our current design model, we assume that the source is a uniform plane wave at normal incidence $g_{illum}(x,\lambda)=1$ or $g_{illum}(x,y,\lambda)=1$. $T(x,\lambda)$ and $T(x,y,\lambda)$ are the transmission functions of the diffractive optic, defined by $T(x,\lambda)=\exp(i\varphi(x,\lambda))$ and $T(x,y,\lambda)=\exp(i\varphi(x,y,\lambda))$. In the signal process point of view, $g_{illum}(x,\lambda)$ and $g_{illum}(x,y,\lambda)$ are the inputs, $U(x',\lambda,d)$ and $U(x',y',\lambda,d)$ are the outputs, and the exponential terms in the integrals of Equations (2.5) and (2.6) represent the impulse response of the diffraction system. Since Fresnel transform is fundamentally a convolution between the transmission function and the impulse response function, the diffraction pattern U can be simply calculated by Fourier transforming the product of these two functions and then doing an inverse Fourier transform of that. The intensity distribution of the diffraction field is $I=|U|^2$. In modeling and optimizing the polychromat design, to avoid aliasing, a periodic boundary condition is usually implied in either one or two directions for its 1D and 2D forms, respectively. In Figures 2.1 and 2.2, the diffractive optic is discretized into a grid width of Δ, although numerical computations of diffraction patterns may take finer grids by oversampling the structures, leading to more accurate approximation to the integrals in Equation (2.5). Usually, a simulation grid size of 1μm is considered in calculation. Note that all the computational efforts are executed in the MATLAB programming environment.

2.1.2 Dispersion measurement

According to Equations (2.3) and (2.4), the phase is directly related to material dispersion, therefore it is crucial to know the refractive index data as accurately as possible. Here, the material dispersion curve was measured by a Woollam Variable Angle Spectroscopic Ellipsometer (VASE), which basically measures the reflectivity of a thin film coated on a substrate illuminated by polarized light at different wavelengths and a

set of angles of incidence. The real and imaginary parts of the refractive index can be extracted by fitting the measurement data. Our spectrum of interest is from 400nm to 800nm, and the incidence angle is from 70^o to 75^o.

There are two materials considered to pattern polychromat: Shipley 1813 and SC1827. They are both commercially available positive photoresist, widely used in the laboratory environment for integrated circuits (IC) and micro-electro-mechanical system (MEMS) applications. They can both be deposited uniformly on either silicon or glass substrate by spin coating. Since the upper bound of the measurable film thickness (<1μm) is much lower than the normal thickness of these two spin-coated materials, we need to spin the thinned ones for the purpose of dispersion measurement only. For both materials, we mixed the original photoresist with propylene glycol methyl ether acetate (PGMEA, a developer for SU-8) with ratio of 2:1. Then, using a spin rate of 3000rpm (on silicon wafer) and 1min soft bake at 110^oC on a hotplate, we were able to achieve thin films with 200nm ~ 300nm thickness. Figure 2.3(a) is a photograph of a typical sample for dispersion measurement.

Figures 2.3(b) and (c) are the measured and extracted dispersion curves of Shipley 1813 and SC1827 photoresists, respectively. The real part of the refractive index is around 1.6 to 1.7, and the imaginary part is negligible in the visible band, although a small amount of absorption can be observed in the blue spectrum (350nm to 500nm). That is also why these materials look yellowish under ambient lighting. The curves show that both materials exhibit stronger dispersion in the short wavelength (blue and green) than in the long wavelength (red and near-infrared), which strictly follows the commonly used Lorentz model of material dispersion.

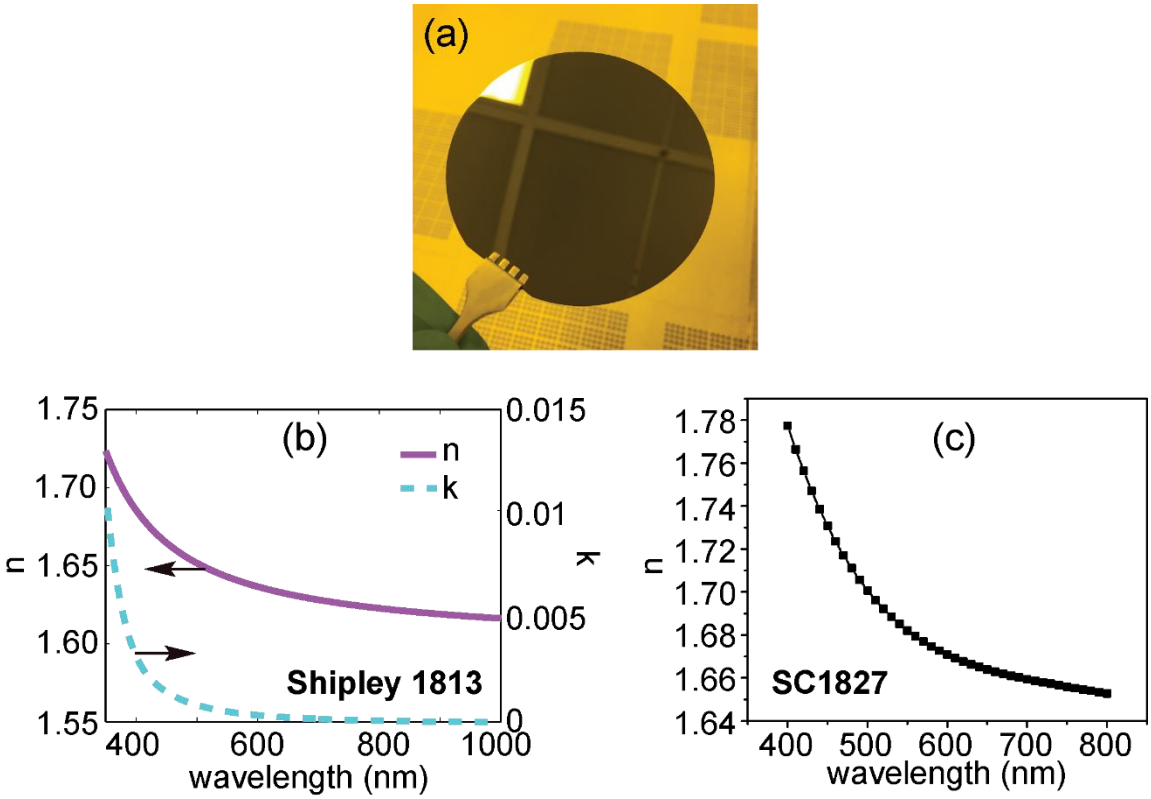

Figure 2.3. Refractive index measurement. (a) Photograph of a thin film sample spin coated on silicon substrate for dispersion measurement. Dispersion curves for Shipley 1813 (b) and SC1827 (c) measured and extracted by Woollam Ellipsometer.

2.2 Device Fabrication

2.2.1 Grayscale lithography

The pixelated multilevel microstructures of the diffractive optic can be patterned by grayscale lithography technique [4]. Lithography is a process ubiquitous in micro- and nano-fabrication facilities [5,6]. In traditional lithography, UV light illuminates the mask, which is de-magnified and projected onto the photoresist. The photoresist records the image of the mask. Depending on whether it is a positive or negative photoresist, the exposure region is removed or remained after development in designated developers. In this way, the patterns of the mask can be transferred to photoresist and then to other material layers or substrate. Usually binary masks are used, which have transparent and

opaque regions. Thus, in conventional lithography, the doses at exposed locations, determined by either positive or negative masks, are uniform in idea situations. In contrast, grayscale lithography exposes different locations of the photoresist by different doses in grayscale. Since most photoresists are nonlinear materials in terms of recording latency images, different exposure doses lead to different depths after development. For example, a lower dose applied in positive photoresist results in a shallower structure. The relationship between exposure dose and the final development depth is usually characterized in a photoresist datasheet as a contrast curve. Different doses cause different degrees of chemical reactions, and thus different percentages of reactants. This gives different dissolution rates (or solubility) in the developer. For a development time, structures of different depths (or heights) are ultimately formed (see Figure 2.4(a)). In this work, we utilized a commercial patterning tool – Heidelberg microPG101, which is functionalized with grayscale lithography (see Figure 2.4(b)).

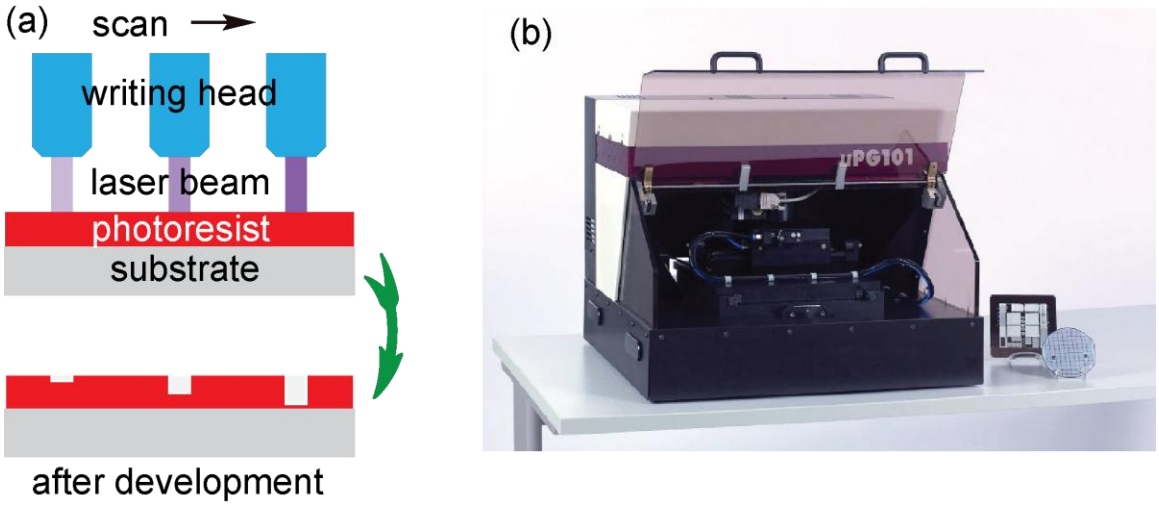

Figure 2.4. Grayscale lithography. (a) Schematic illustration of the grayscale lithography technique. The write head exposes the photoresist by different doses when scanning across the sample, resulting in structures of different depths after development. A positive photoresist is assumed here. (b) A photograph of the grayscale lithography tool – Heidelberg microPG101.

The machine works in a direct-laser-writing (DWL) mode. This means that the write head focuses a UV laser beam (405nm), scans across the sample surface point by point, and simultaneously exposes the sample. The mechanical positioning accuracy in addressing each exposure point is less than 100nm. The spatial spread of each exposure, or width of the PSF of the write head, is measured around 2.5μm, which, based on the official specs, provides spatial resolution as high as 3μm. This is why the minimum feature size in all current projects is Δ=3μm. The modulation of exposure dose is achieved by neutral density filters installed in the system.

As clearly shown in Equations (2.3) and (2.4), it is critical to know the exact relationship between exposure dose and the resultant structure depth so that the fabricated device has the correct height (or phase) distribution. The closer the fabricated one is to the designed one, the better efficiency it can potentially offer. Therefore, before patterning the polychromat, we need to calibrate this photoresist contrast curve. A straightforward test design is give in Figure 2.5(a), which includes grayscales from 0 to 99 arranged in sequence. Note that the microPG101 machine can only expose a maximum of 100 grayscale levels. The sample is prepared such that the film thickness is greater than the designed maximum height H, and a laser power has to be chosen judiciously so that it matches the maximum height H. Figures 2.5(b) – (e) summarize the curves of four calibration examples. The materials and laser powers used are given as well. Often, a number of calibration measurements are averaged to give a smooth and accurate curve. Although the calibration is consistent over time, due to the drift of the tool, the cleanroom environment and other contributing parameters over time, new calibrations are required almost every two to three months.

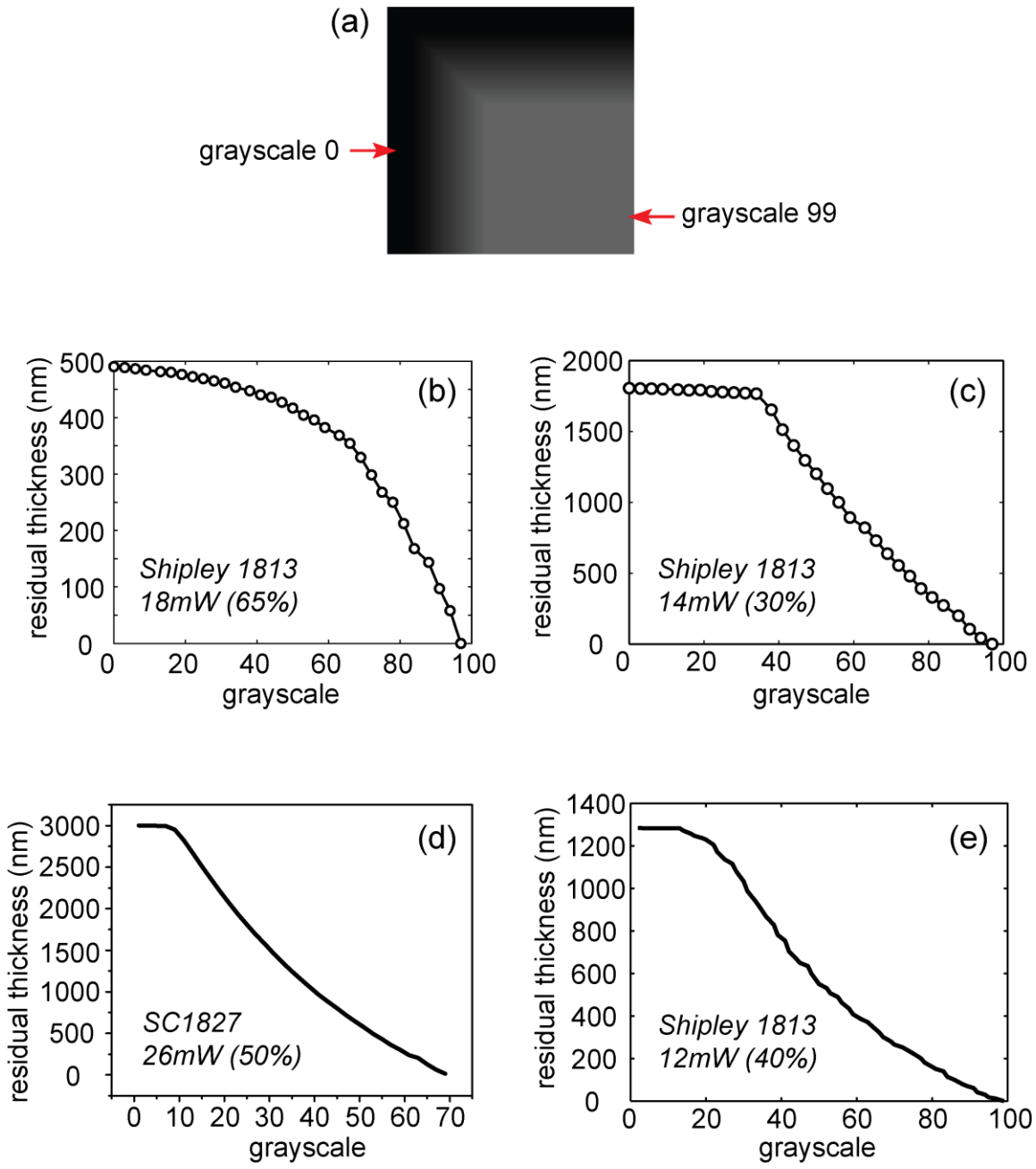

Figure 2.5. Calibration of the lithography tool. (a) A design example for grayscale lithography calibration. It varies from 0 to 99 in two directions. (b) – (e) Four calibration curves for different polychromat materials and laser powers. The designed maximum heights are (b) 430nm for microlithography project (see Chapter 5); (b) 1800nm for photovoltaics project (see Chapter 3); (c) 3000nm for super-achromatic lens project (see Chapter 4); (d) 1200nm for imaging projects (see Chapters 6 and 7).

2.2.2 Fabrication procedure

A standard procedure is developed for patterning the polychromat by grayscale lithography. The following is a typical example:

1) RCA clean a 2-inch diameter fused silica wafer.
    a. Put the glassware in DI water and heat the beaker up to 70^{o}C on a hotplate.
    b. Mix NH_4OH and H_2O_2 with ratio NH_4OH:H_2O_2:DI water = 1:1:5.
    c. Await chemical reactions in the beaker for 10min to 15min, meanwhile keeping the temperature between 70^{o}C to 80^{o}C.
    d. Dispose waste liquids in the beaker and rinse the glassware by running DI water, then dry them by N_2.
2) Spin coat HMDS on the fused silica wafer (200μm thickness), 45sec @ 6000rpm. Leave it in the fume hood for 10min for sufficient evaporation.
3) Spin coat Shipley 1813 photoresist, 45sec @ 4000rpm with ramp rate 1000rpm/s for the first 5sec.
4) Soft bake on a hotplate for 90sec @ 115^{o}C.
5) Dehydration in fume hood for at least 1hr.
6) Gray-scale exposure by the Heidelberg microPG101 with 3μm mode. Power: 12mW; duration factor: 40%; mode: unidirectional; scan-scale: 2.74MHz.
7) Development in AZ MIF 300 developer for 1min.
8) Rinse in DI water for 1min. Dry the sample by carefully blowing N_2.

Parameters, tools, and materials included in the above procedure can be modified according to different requirements. For instance, the substrate can be either silicon wafer (any orientation and type) or soda-lime glass substrate. For silicon and fused silica wafer,

a hotplate is good for soft bake, while an oven is needed for glass substrate (1mm thick) due to the low thermal conductance of glass. Usually, soft bake in an oven takes 40min to 60min. Three different types of developers can be used. They are 352, AZ 1:1 and AZ MIF 300. Based on experimental results, they are basically interchangeable because they provide a similar development rate. Additionally, the same development rate can be achieved by diluting 351 developer with DI water (1:5 ratio). Note the final polychromat and the calibration sample have to be prepared under exactly the same conditions.

Undesired scattering from surface roughness may deteriorate the device performance. Therefore, it is important to characterize and control the surface roughness within a reasonable limit. Figure 2.6 plots the surface measured by atomic-force-microscopy (AFM, Bruker Dimension Icon). It works in VeecoScanAsyst mode. The surfaces of both polychromat materials (Shipley 1813 and SC1827) are quite smooth, with roughness root-mean-square (RMS) less than 10nm. This roughness RMS is below 2.5% of the

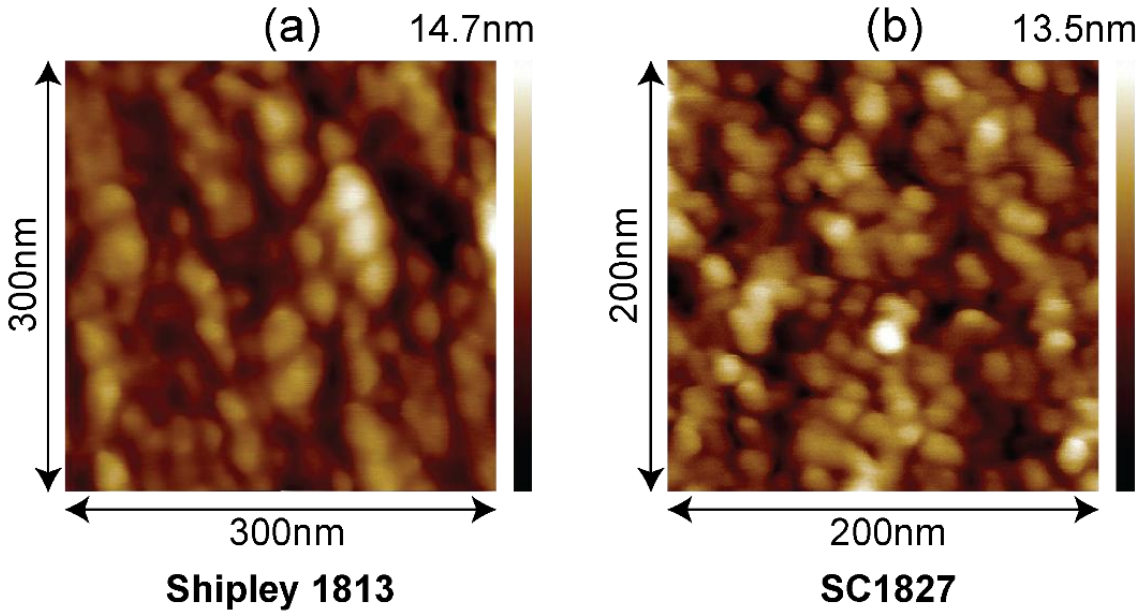

Figure 2.6. Surface roughness measurement by AFM. The thin film materials are (a) Shipley 1813 (300nm by 300nm area) and (b) SC1827 (200nm by 200nm area).

shortest wavelength considered (λ=400nm), thus bringing trivial impacts on the diffractive optic's efficiency. Keeping the fabrication condition and procedure unchanged, this measured surface roughness is constant over all the samples and also over time.

2.2.3 Polychromat

Some exemplary micrographs and AFM measurements of the fabricated polychromats are given in Figures 2.7 and 2.8. The micrographs are taken by both the Olympus MX51 and the Keyence VHX-5000 microscopes with various magnifications factors. Oblique illumination is utilized in the latter microscope so as to manifest the 3D structures via increasing image contrast. The AFM measurement is conducted using VeecoScanAsyst mode with -2.0 Volt vertical alignment so that it can manage deep structures of high aspect-ratios accurately without damaging the AFM tip. For a scan field of 512×512 pixels, this typically takes 8min to complete and the maximum measurable depth is around 2μm.

Figures 2.7 and 2.8 are for 1D and 2D polychromats, respectively. The micrographs in Figures 2.7(a) and (b) are taken by back illumination, while those in Figures 2.7(c) and (d) are taken by front illumination. The polychromat grooves exhibit different colors due to thin film interference with various thicknesses [7]. The AFM result confirms the height-varying topography of the designed diffractive optic. In its 1D form, it is pixelated along the X direction and the height of each pixel is assigned such that altogether they offer the desired optical performances. The topography is uniform along the Y direction. The discretization grid is 3μm wide. The edges between two pixels (or grooves) are slightly rounded due to the optical proximity effect present in any lithography system [8].

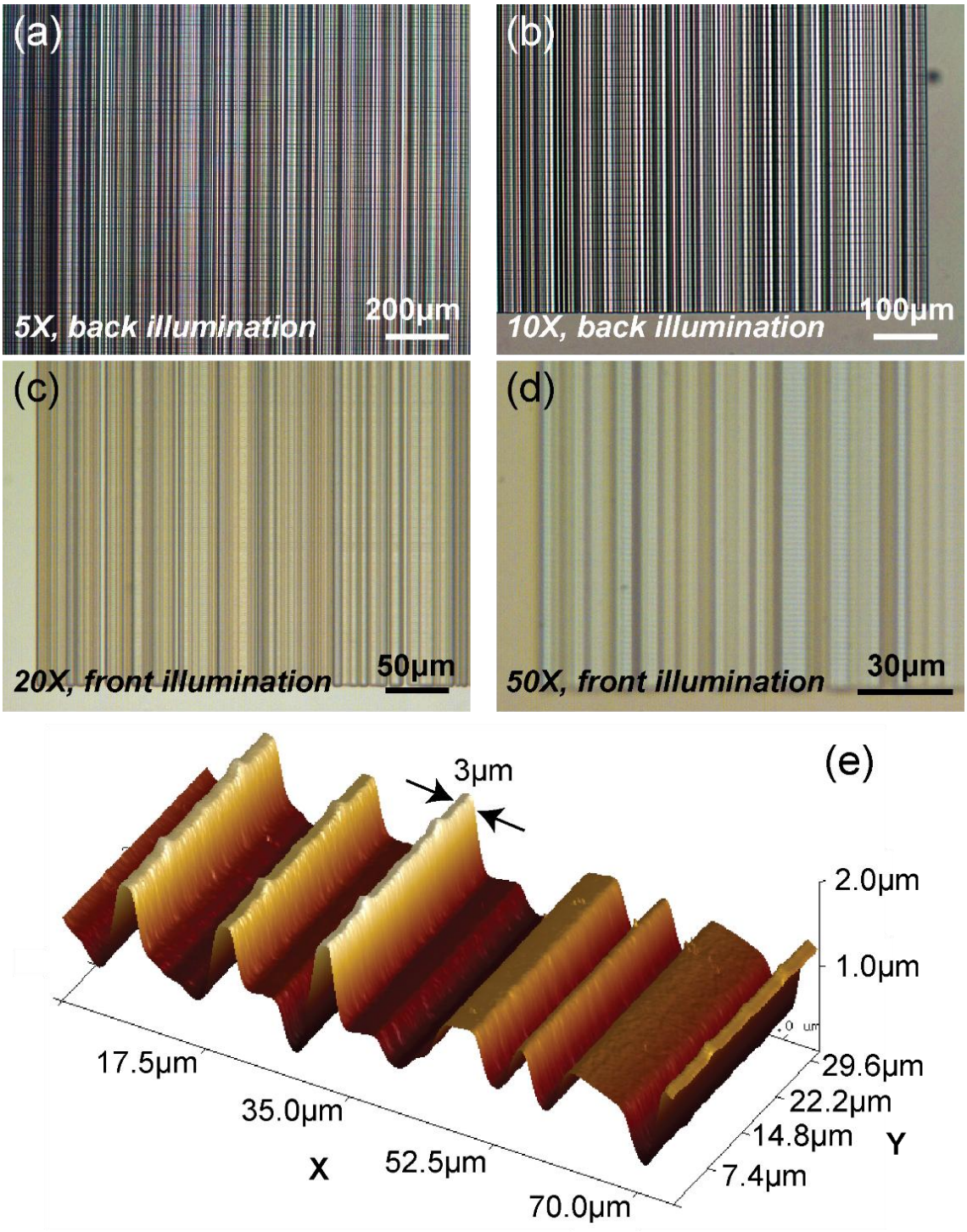

Figure 2.7. Optical micrographs of the fabricated 1D polychromats with (a) 5X, (b) 10X, (c) 20X and (d) 50X magnifications. 3D view of an AFM measurement of a segment (70μm by 30μm area) of the fabricated 1D polychromat. The maximum height is 1.2μm and the groove width is 3μm.

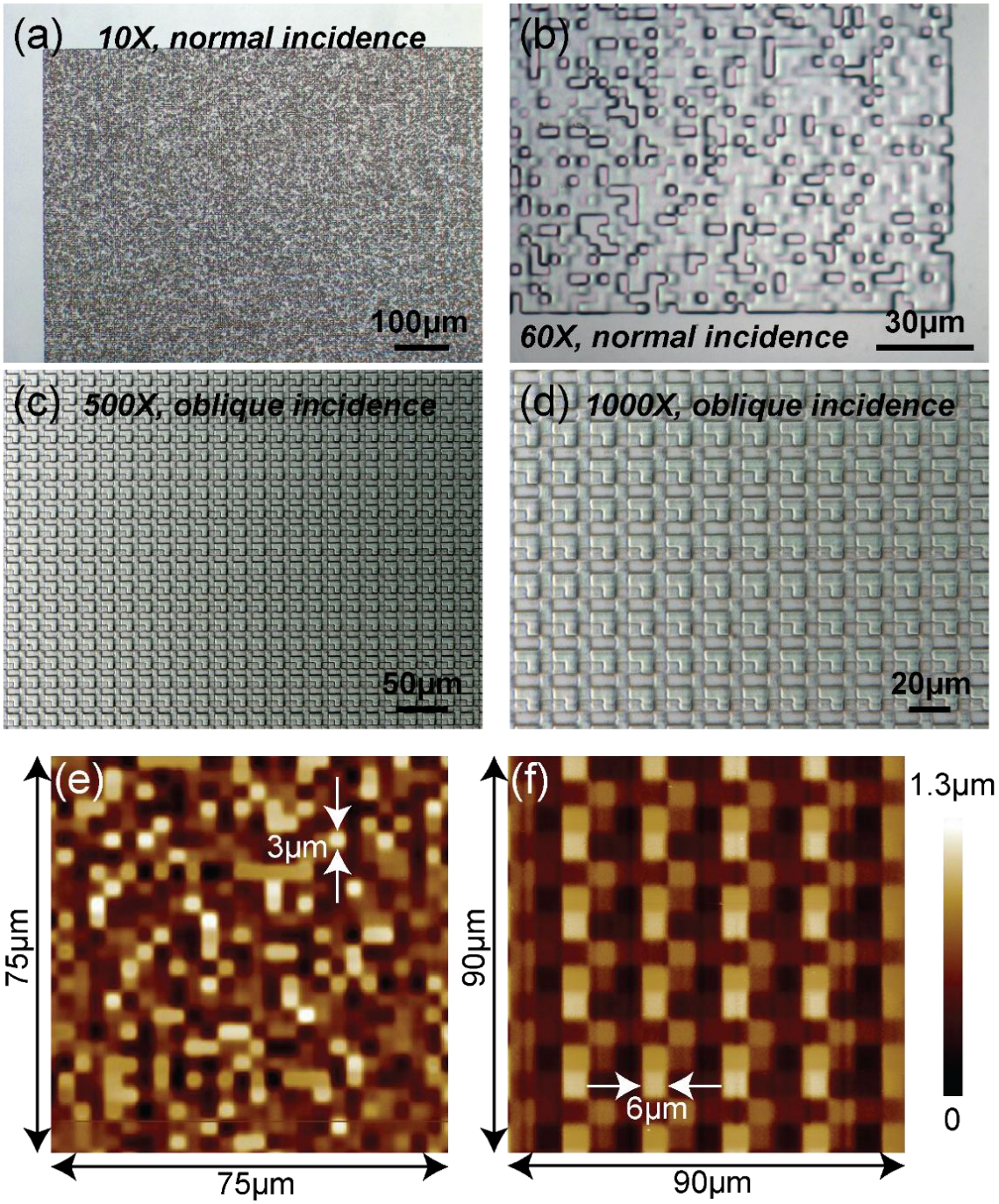

Figure 2.8. Optical micrographs of the fabricated 2D polychromats with (a) 10X, (b) 60X, (c) 500X and (d) 1000X magnifications. The first polychromat has a pixel size of 3μm (a) and (b); the second one has a pixel size of 6μm (c) and (d). AFM measurements of (e) 75μm by 75μm area and (f) 90μm by 90μm area of the fabricated 2D polychromats. The maximum height is about 1.2μm. The pixel sizes of 3μm (e) and 6μm (f) are marked.

This effect can be computationally corrected by well-developed algorithms [8]. Nevertheless, according to the experimental tests carried out later, this does not have much influence on our results.

The similar results on 2D polychromats are shown in Figure 2.8. The first sample has a random height profile with pixel size of Δ=3μm (Figures 2.8(a), (b) and (e)); the second one has a periodic height profile with pixel size of 6μm (Figures 2.8(c), (d) and (f)). The periodicity is 18μm×18μm. The micrographs of the first polychromat were taken using the Olympus MX51 under normal incidence and front illumination. Those of the second one were taken using the Keyence VHX-5000 under oblique incidence and front illumination to enhance image contrast. The shadows created by the 3D structures are clearly seen (Figures 2.8(c) and (d)). The 2D AFM measurements demonstrate uniform square pixels with correct dimensions. Multiple height levels can be observed and the height within one pixel seems very consistent. Later profilometer measurements confirm average height error well below 100nm, sufficient to exhibit acceptable performances.

2.2.4 Scanscale calibration

Note that the trivial horizontal lines present in Figure 2.7(a) – (d) are due to imperfect scanscale calibration. Scanscale is a parameter preset in the Heidelberg microPG101 machine, which determines the speed of acoustically actuated write head scan. These periodic lines may induce undesired scattering in the direction orthogonal to the diffraction structures. To eliminate these artifacts, we need to calibrate the scanscale parameters and pick the best one. Figure 2.9 plots the heights of these lines at various scanscale values. The micrographs of the exposed samples and the screen shots of the profilometer measurements are summarized as the insets. Here, we use a design of

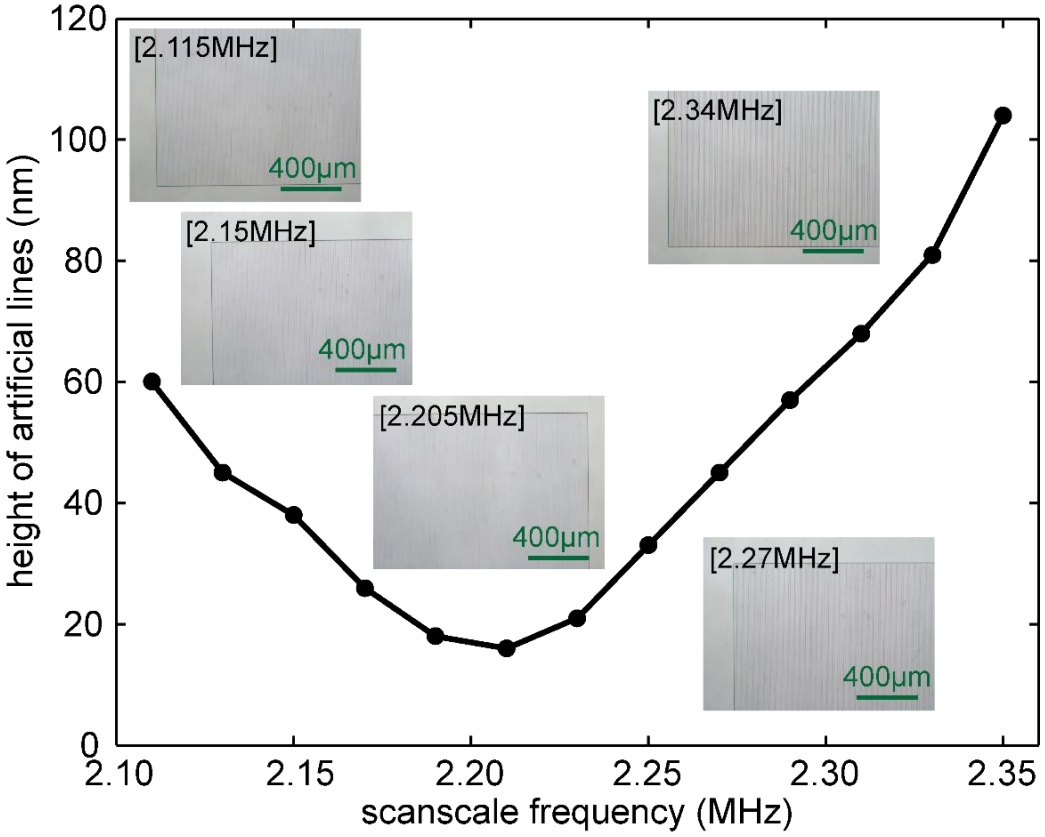

Figure 2.9. Scanscale parameter calibration curve. The height of artificial line drops to a minimum at 2.205MHz frequency. Insets: micrographs of the exposed samples at various scanscale frequencies.

uniform exposure as our test sample. Scanscale frequency of 2.205MHz seems to give the smallest height of artificial line. This is also proved by the corresponding micrograph, which has the smoothest surface.

2.3 Device Replication

Although it takes only one lithography step to pattern the diffractive optic, it is potentially time-consuming and costly to manufacture many of these products using this technique. Since the polychromat studied is essentially an ultrathin piece of flat optic, it may be easily replicated by nanoimprint lithography (NIL) for mass production [9]. Roll-to-roll imprint is capable of rapidly reproducing nano- and micro-structures in large scale

with excellent accuracy, and is considered a promising technology to revolutionize future nanofabrication. As a first step of proof of concept, we adopted a simple method, hot embossing, to show that it can be replicated onto rigid, highly transparent materials [10,11]. The patterns on photoresist are first transferred to a PDMS mold and then transferred to polystyrene. The first part of the replication process follows these steps:

1) Place a disposable plastic container on a scale. Silicone elastomer base (Sylgard 184) and curing agent are poured in a 10:1 wt (base : curing agent), then mixed vigorously by hand using a plastic fork for ~5 mins.
2) The mixture is poured onto the substrate and wrapped with aluminum foil.
3) Place the substrate with PDMS mixture on top in a vacuum desiccator for about 30 mins.
4) The substrate is then placed in an oven at 60^{o}C for 5 hours to cure PDMS.
5) A razor blade is used to peel the cured PDMS off the substrate.

In the second part of the replication process, a bonding tool (EVG 520 IS), is used:

1) A PDMS mold is placed on the polystyrene sample, sandwiched between two 4" silicon wafers (one on the top of PDMS mold and another at the bottom of polystyrene). This whole stack was placed on the chuck of the bonding tool.
2) Use the following recipe: equalizer temperature 2^{o}C; heating temperature 110^{o}C with ramp of 20^{o}C/min; timer set to 5min; wait pressure 5e-3mbar; start and stop piston pressures are 700N and 1700N; another timer set to 5min; then final wait temperature 45^{o}C.

The photographs and micrographs of the samples at stages of the replication process are summarized in Figures 2.10(a) – (c) and Figures 2.10(d) – (f), respectively. The

photoresist master is patterned on a glass substrate (Figures 2.10(a) and (d)) by grayscale lithography. The unexposed region looks yellowish since the photoresist has some absorption in the blue and UV wavelengths. The mold is in PDMS (Figures 2.10(b) and (e)), which is very flexible. The final replica is in polystyrene (Figures 2.10(c) and (f)), which is rigid and highly transparent.

Figures 2.11(a) and (b) are the AFM-measured profiles of the PDMS mold and the polystyrene replica. For simplicity we used a Δ=10μm pixel width. Based on the comparison of structure heights, the discrepancies between the photoresist and the polystyrene are 50nm – 100nm, within 10% of the maximum height *H*. This proves that we can easily replicate the polychromat with reasonable accuracy. Our later numerical analysis shows that this discrepancy is sufficient to provide acceptable optical performances.

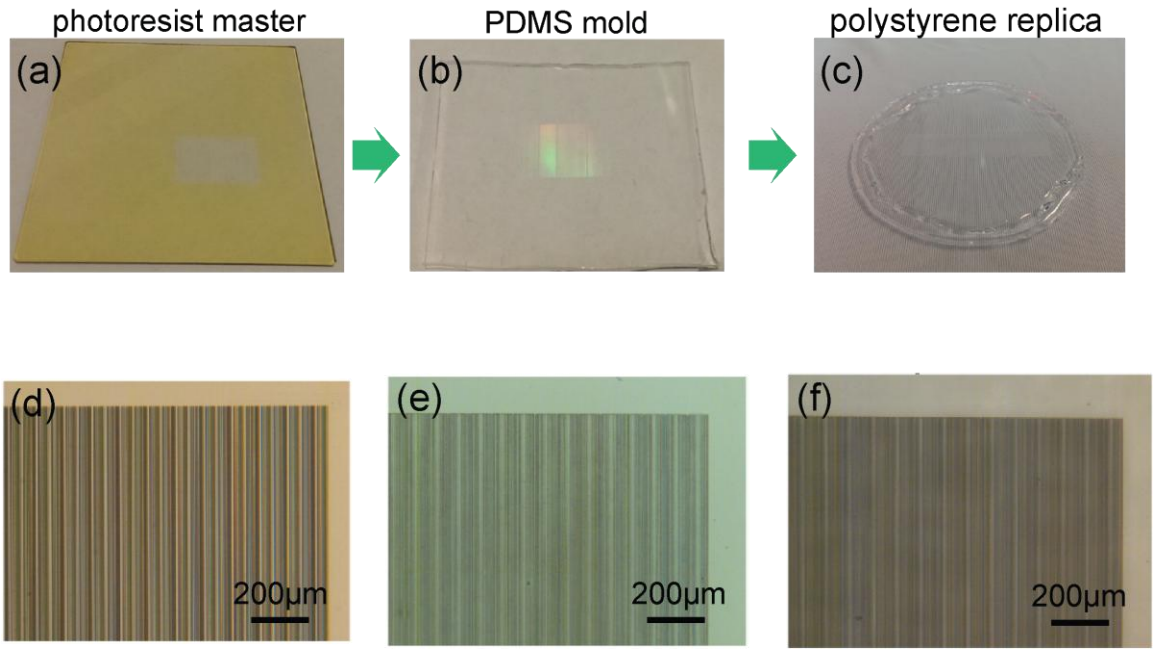

Figure 2.10. Photographs (a)-(c) and micrographs (d)-(f) of the samples at three replication stages. (a) and (d) photoresist by grayscale lithography; (b) and (e) PDMS mold; (c) and (f) polystyrene replica. (Credit: Nabil Mohammad, University of Utah)

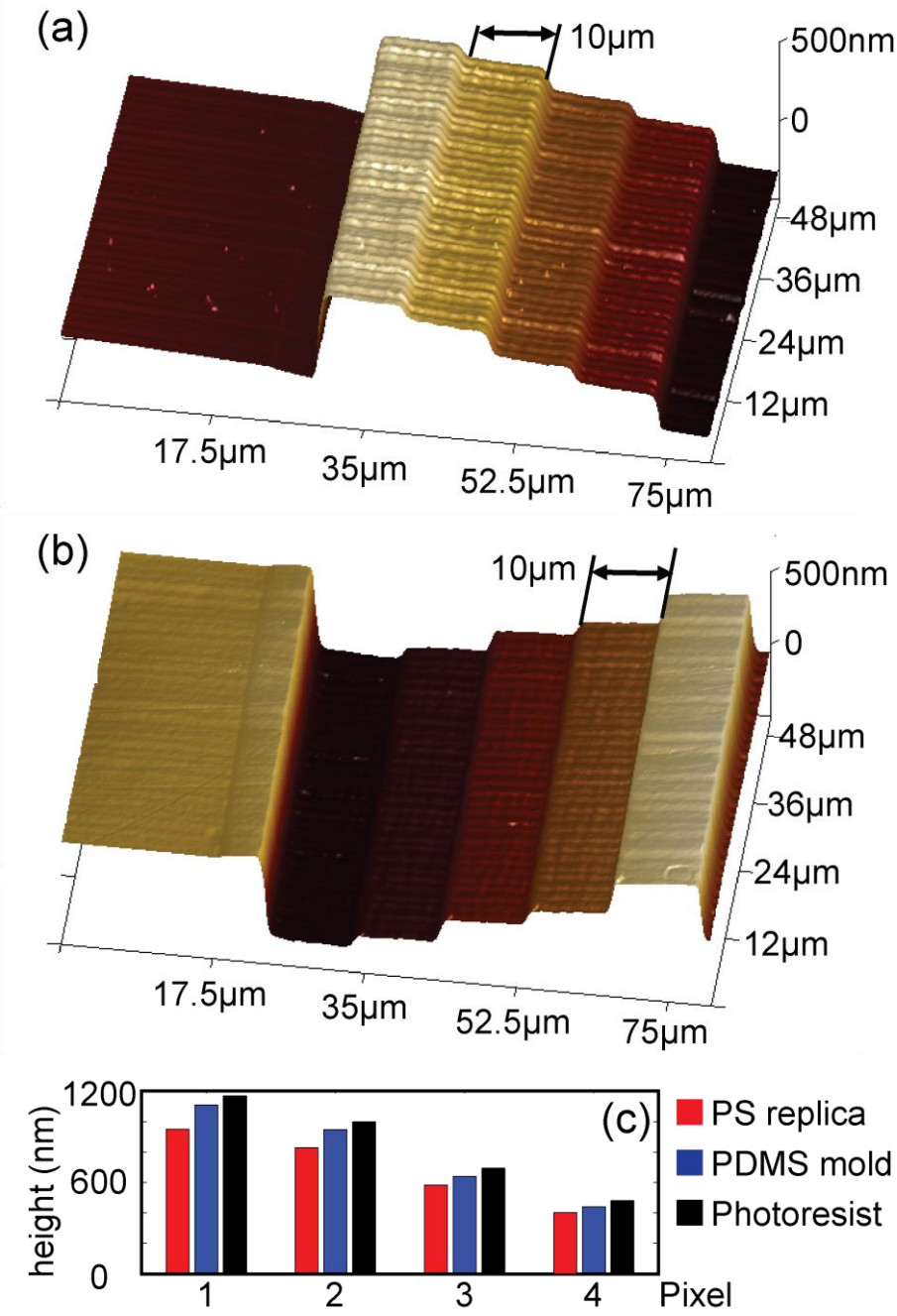

Figure 2.11. AFM measurements of the (a) PDMS mold and (b) polystyrene replica. The structures have 10μm groove width and maximum height of 1.2μm. (c) Comparison of heights in photoresist, PDMS mold, and polystyrene replica.

2.4 Direct Binary Search

2.4.1 Algorithm

To solve for the nonlinear optimization problem in this work, we implemented a modified version of the well-known direct-binary-search algorithm (DBS) [1,12]. This algorithm is applied in two problems: one is to search for optimal height (or phase) distribution of the diffractive optic for the nonimaging applications; the other is to solve the inverse problem in multispectral imaging. Now, we take the first task as an example.

Of course, like all other kinds of optimization algorithms, we need to find the figure-of-merit (FOM) to be maximized. The definitions for different applications are elaborated in each corresponding chapter. The optimization algorithm begins with the generation of an initial solution. Usually, a random height distribution (generated by the 'rand' function in MATLAB) is used. Since this is a local search method, the algorithm is sensitive to the choice of initial condition. If a poor initial solution is chosen, it might suffer from premature convergence or it will take longer to arrive to a satisfactory optimum state. Therefore, we ran a number of optimizations with different random initial solutions, and the best outcome was selected.

The DBS algorithm proceeds in an iterative manner. In one iteration, all pixels in the height distribution are perturbed in a predesigned manner (such as a random sequence). After picking up a pixel, a positive unit perturbation ($+\Delta h$) is first tried. If the updated FOM is increased, then this perturbation is kept, otherwise a negative unit perturbation ($-\Delta h$) is applied to this pixel. If the new FOM is increased, then this negative perturbation is kept, otherwise it goes on to the next pixel. The guessed height distribution is renewed accordingly. One iteration stops when all pixels are traversed. Termination conditions

guarantee convergence, such as a maximum number of total iterations or a minimum threshold of FOM improvement between two neighbor iterations. An algorithm flow chart for 1D polychromat is shown in Figure 2.12.

Figure 2.13(a) plots an example of DBS optimization algorithm. It optimizes the polychromat for photovoltaics project. The FOM versus times of iteration rises rapidly in the first 10 iterations from almost 0 to more than 25 and then converges to a plateau. The number of changed pixels decreases gradually from almost 3000 down to 0. This phenomenon indicates that the algorithm is insensitive to fabrication errors since reasonable amounts of variations have only trivial influence. In theory, this is owing to the fact that it is a perturbation-based iterative approach.

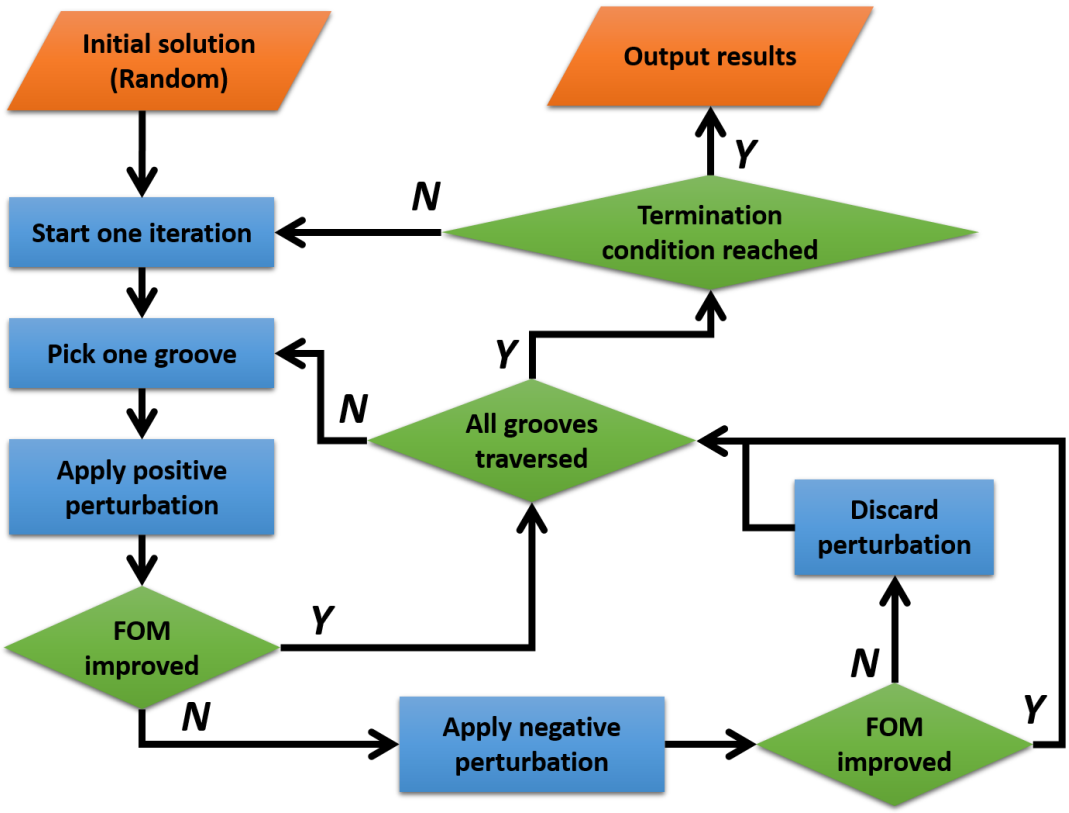

Figure 2.12. Flow chart of the DBS algorithm to optimize the height distribution of the diffractive optic. The 'groove' can be replaced by 'pixel'.

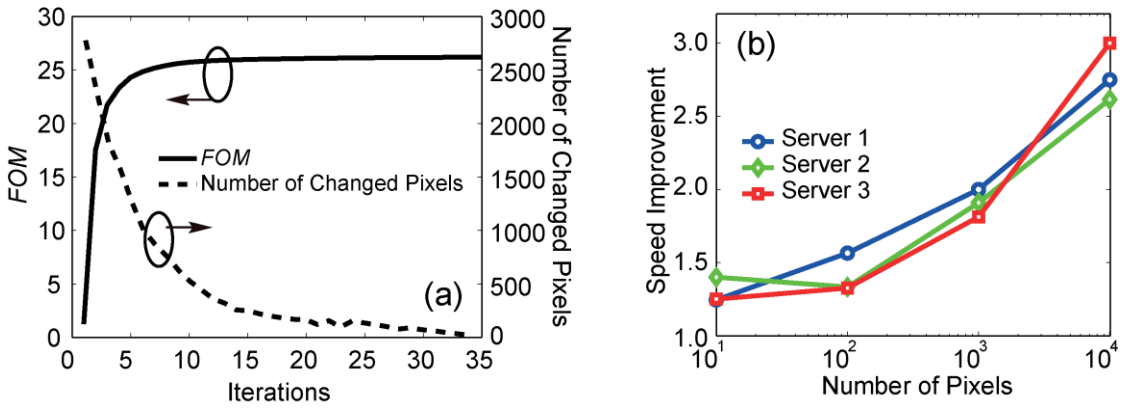

Figure 2.13. Results of the DBS algorithm. (a) The evolution of FOM and the number of changed pixels during DBS optimization. (b) Computation speed improvements using the perturbation method.

The same algorithm is adopted for spectrum and image reconstruction in the computational spectroscopy and computational multispectral imaging projects. The problems in these two projects are both reduced and generalized by the equation $\mathbf{x}=\mathbf{A}^{-1}\mathbf{b}$. Here, the pixels to be perturbed are the elements in matrix **x**, and the FOM to be minimized during optimization is defined as the residual norm $\|\mathbf{b}-\mathbf{A}\mathbf{x}\|_2$. Note that matrix **A** describes the imaging system, also known as the spatial-spectral point-spread-function (SS-PSF), and **b** is the multiplexed image captured by a camera.

2.4.2 Perturbation method

Calculating diffraction using Fresnel transformation can be time-consuming, especially when this process is repeated a number of times. In order to facilitate the computation of diffraction fields in the DBS algorithm, a perturbation method was implemented based on the linearity of the system in the Fresnel diffraction regime. The field in the image plane (both 1D and 2D) updated after perturbation can be expressed by

$$U_{new}\left(x',\lambda,d\right)=U\left(x',\lambda,d\right)+U_{pert}\left(x',\lambda,d\right). \tag{2.7}$$

$$U_{new}(x',y',\lambda,d) = U(x',y',\lambda,d) + U_{pert}(x',y',\lambda,d). \tag{2.8}$$

$U(x',\lambda,d)$ and $U(x',y',\lambda,d)$ are the original field distributions before perturbation. The term induced by single perturbation at the m or (m,n) pixel with height $p_{(m)}$ or $p_{(m,n)}$ are

$$U_{pert}(x',\lambda,d) = \left(e^{i\alpha(\lambda)\cdot(p_{(m)}\pm 1)} - e^{i\alpha(\lambda)\cdot p_{(m)}}\right)\cdot U_c(x',\lambda,d). \tag{2.9}$$

$$U_{pert}(x',y',\lambda,d) = \left(e^{i\alpha(\lambda)\cdot(p_{(m,n)}\pm 1)} - e^{i\alpha(\lambda)\cdot p_{(m,n)}}\right)\cdot U_c(x',y',\lambda,d). \tag{2.10}$$

$$U_c(x',\lambda,d) = \frac{e^{ikd}}{i\lambda d}\cdot\int g_{illum}(x,\lambda)\cdot rect\left(\frac{x-m\Delta x}{\Delta x}\right)\cdot e^{i\frac{k}{2d}\cdot(x'-x)^2}dx. \tag{2.11}$$

$$U_c(x',y',\lambda,d) = \frac{e^{ikd}}{i\lambda d}\cdot\iint g_{illum}(x,y,\lambda)\cdot rect\left(\frac{x-m\Delta x}{\Delta x}\right)\cdot rect\left(\frac{y-n\Delta y}{\Delta y}\right)\cdot e^{i\frac{k}{2d}\cdot\left[(x'-x)^2+(y'-y)^2\right]}dxdy. \tag{2.12}$$

Using the perturbation method, Figure 2.13(b) gives the improvement curve of computation speed with different numbers of pixels, tested on three high-performance computing servers on the university campus, compared to the Fresnel transformations in Equations (2.5) and (2.6). Clearly it demonstrates that speed enhancement becomes more profound when solving for problems with larger dimensions. In a particular design with 3000 pixels, an average speed enhancement of 2.5X is observed.

2.5 Regularization Algorithm

In the imaging applications of the polychromat, it is essential to extract unknown information, such as spectrum flux or hyperspectral data cubes, from the captured monochrome images. Although DBS-based optimization algorithm may be taken as a

candidate solver, it suffers from slow speed and a tendency to converge to a local extremum. Thus it is critical to implement an efficient noniterative approach that outputs solutions in real-time. We turn to regularization since, mathematically speaking, the issues that we face are inverse problems.

As mentioned earlier, the imaging system, or the forward problem in another word, can be expressed as $\mathbf{b}=\mathbf{Ax}$, where $\mathbf{x}$ is unknown information, $\mathbf{A}$ is the system matrix, and $\mathbf{b}$ is the measured data or image. In theory, we can always do the direct inversion $\mathbf{x}=\mathbf{A}^{-1}\mathbf{b}$. However, in practice, this is problematic since the matrix $\mathbf{A}$ is extremely ill-conditioned, with an enormously large condition number. In order to obtain reasonable solutions for these types of problems that do not satisfy the Hadamard requirements, regularization methods are developed [13], and they have been particularly applied in biomedical imaging, geophysics, and image deblurring [13].

To begin with, we need to analyze the system matrix $\mathbf{A}$ by singlular-value-decomposition (SVD), which decomposes the matrix $\mathbf{A}$ into a representation of a sequence of singular values and a set of left and right singular vectors:

$$\mathbf{A} = \mathbf{U}\boldsymbol{\Sigma}\mathbf{V}. \tag{2.13}$$

In Equation (2.13), $\boldsymbol{\Sigma}$ is a diagonal matrix with the singular values as its diagonal elements, arranged in a descending manner ($\sigma_1 \geq \sigma_2 \geq \sigma_3 \geq \ldots \geq \sigma_k$). The columns of $\mathbf{U}$ and $\mathbf{V}$ matrices (u_1, u_2, $u_3 \ldots u_k$, and v_1, v_2, $v_3 \ldots v_k$) contain the $k \times 1$ left and right singular vectors, respectively. SVD is equivalent to a Fourier expansion of the system matrix. The vectors u_i and v_i are the frequency components and σ_i are the coefficients of the components ($i=1,2,3 \ldots k$).

From the SVD point-of-view, any forward problem diminishes the high-frequency components in u_i and v_i. However, the inverse process attempts to magnify those high-frequency parts. The regularization technique stabilizes the problem by minimizing both the residual norm $\|\mathbf{Ax}\text{-}\mathbf{b}\|_2$ and the solution norm $\|\mathbf{x}\|_2$. Usually, a regularization parameter ω is selected to balance these two terms. Here, we focus on a widely used method called Tikhonov regularization. Mathematically, its goal is stated as

$$\min\left\{\left\|\mathbf{Ax}-\mathbf{b}\right\|_2^2+\omega^2\left\|\mathbf{x}\right\|_2^2\right\}. \tag{2.14}$$

It can be equally formulated as applying filter factors to solution vectors, from the computational perspective:

$$\mathbf{x}_\omega=\sum_{i=1}^{n}\phi_i^{[\omega]}\frac{u_i^T\mathbf{b}}{\sigma_i}v_i. \tag{2.15}$$

$$\phi_i^{[\omega]}=\frac{\sigma_i^2}{\sigma_i^2+\omega^2}. \tag{2.16}$$

Equation (2.16) is the expression of the filter factor. In Equation (2.15), we call $\boldsymbol{x}_\omega$ the Tikhonov regularization solution with parameter ω. The parameter ω is selected based on the widely known L-curve technique. Much too small ω leads to results overwhelmed by noises, while much too large ω leads to oversmoothed distorted results. Note that the system matrix **A** has to be a square matrix.

Next, we will use an example to explain how regularization approach works. A simple system is constructed with the system matrix **A** (2000×2000 elements)

representing the spatial-spectral point-spread-function of a diffractive optic with random topography. The unknown is vector **x** (2000×1 elements) and the measured data is **b** (2000×1 elements). Figure 2.14(a) plots the singular values σ_i in logarithm scale and Figure 2.15 summarizes some of the left singular vectors u_i. The singular vectors oscillate faster with increasing i. This is further validated by the Fourier transform of the singular vectors u_i. Based on the dashed line, the low frequency and high-frequency regimes can

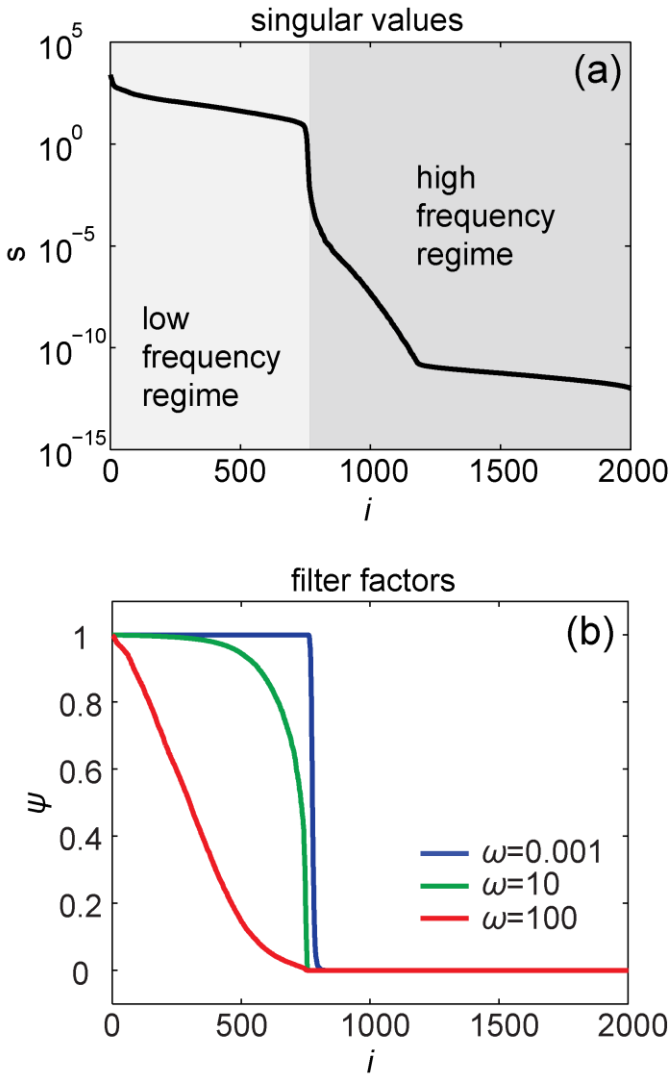

Figure 2.14. Singular values and filter factors in the regularization method. (a) Singular values σ_i of an exemplary system matrix **A** plotted in logarithm scale. (b) Filter factors ψ_i for different regularization parameter (ω) values.

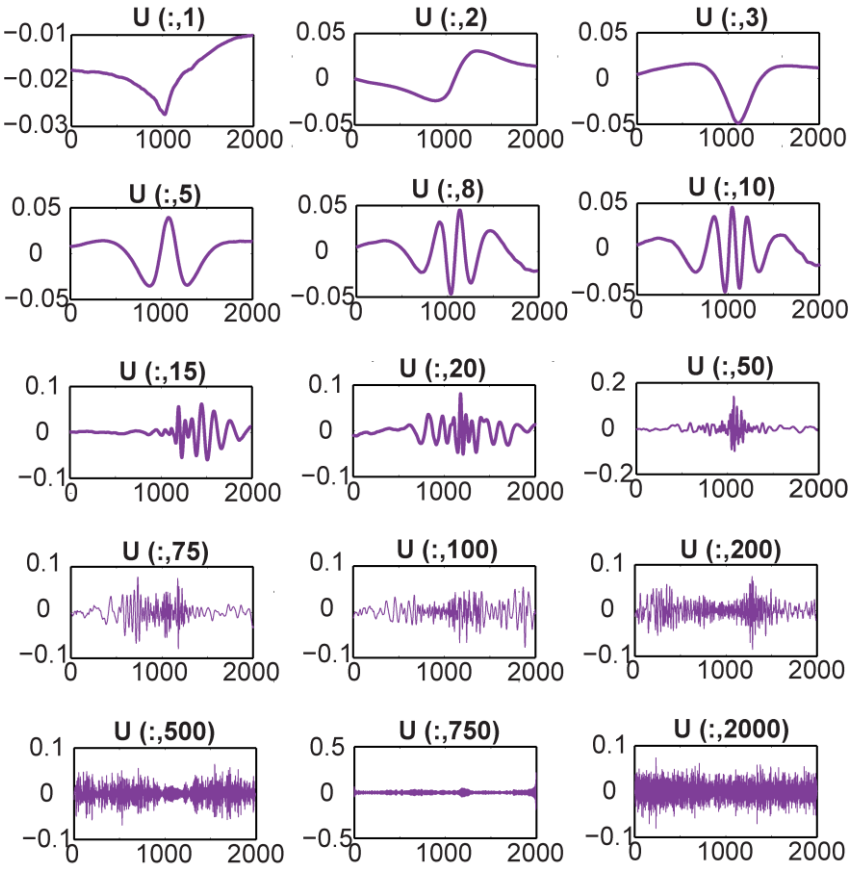

Figure 2.15. Examples of left singular vectors u_i in the **U** matrix after SVD.

be apparently separated (Figure 2.16(a)). As can be seen in Figure 2.14(a), the singular values drop slowly in the low-frequency regime (i<750) but then falls drastically in the high-frequency regime (i>750). In essence, regularization computes the solution **x** by combining the singular vectors of all the frequencies with the coefficient of each frequency determined by its filter factor as defined by Equation (2.16). Filter factors of different parameter ω values are given in Figure 2.14(b). Larger ω tends to smooth the solution with a slope-shape filter and vice versa. To explain this, the L-curve of solution norm $\|\mathbf{x}\|_2$ versus residual norm $\|\mathbf{Ax}-\mathbf{b}\|_2$ is plotted in Figure 2.16(b), and the insets compare the ground truth and the solutions obtained by different ω values. An optimal ω=1.857, roughly around the corner of the L-curve, offers the best solution.

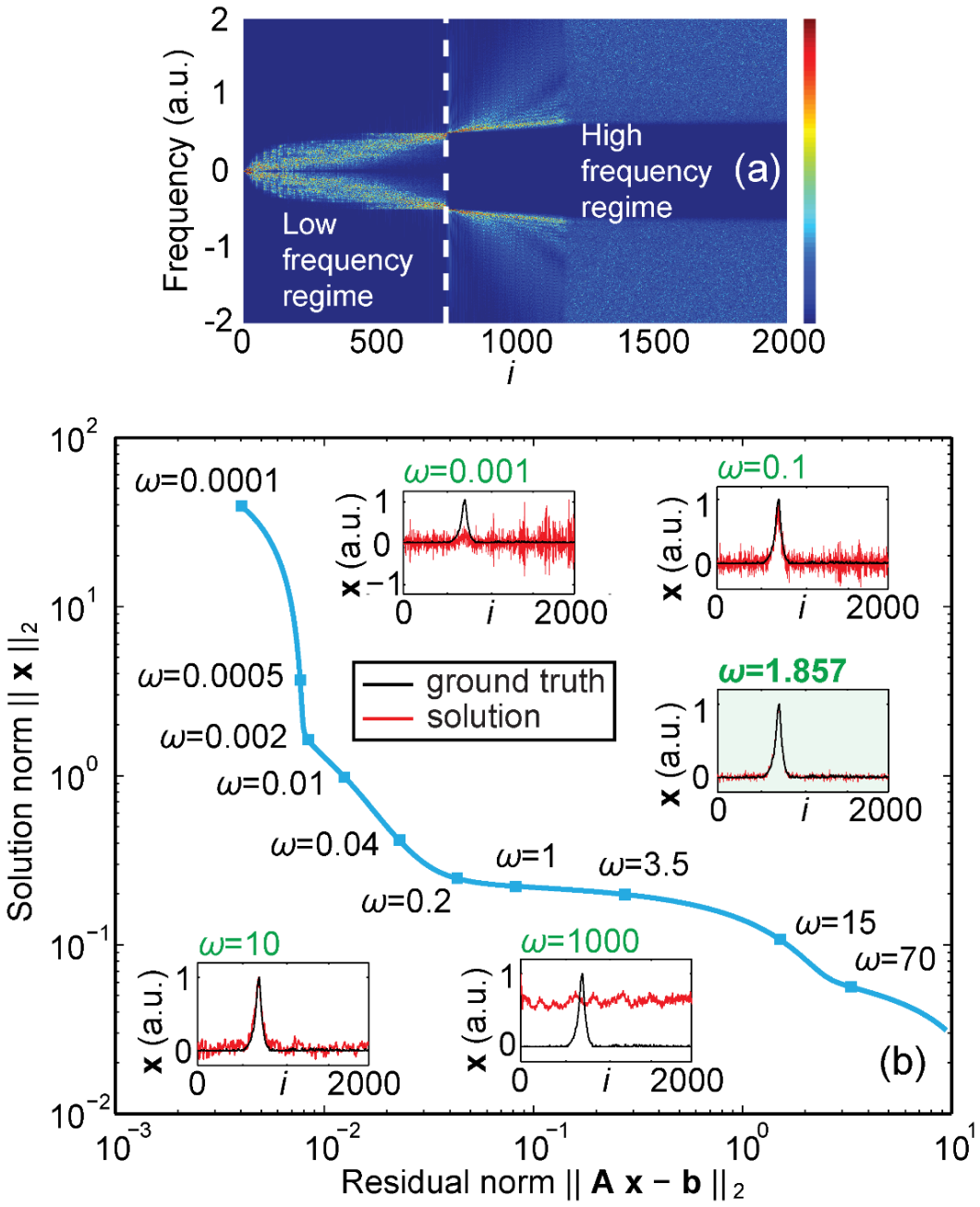

Figure 2.16. Results of the regularization method. (a) Each column i represents the Fourier transform of the singular vector u_i of an exemplary system matrix **A**. The low- and high-frequency regimes are labelled. (b) L-curve for selecting the regularization parameter ω in Tikhonov regularization method. Reconstruction results by using ω=0.001 (top left inset), ω=0.1 (top right inset), ω=1.857 (middle right inset), ω=10 (bottom left inset), and ω=1000 (bottom right inset). The best result is obtained by ω=1.857. The solution data are in the red line and the ground truth data are in the black line. They are normalized.

2.6 Optical Characterization Setup

2.6.1 Scanning-spectrometer setup

An optical characterization setup is built to measure the spatial-spectral point-spread-function (SS-PSF) of the polychromat designed and fabricated for nonimaging applications. The schematic and some photographs of the setup are shown in Figure 2.17. It works by measuring the spectrum at each spatial point in the image plane of the polychromat.

Firstly, a broadband (white) laser beam generated by a supercontinuum source (SuperK EXTREME, NKT Photonics) is expanded by an achromatic biconcave lens (ACN254-075-A, f=-75mm, Thorlabs). Two concave mirrors (CM127-010-P01, f=9.5mm and CM750-500-P01, f=500m, Thorlabs) are cascaded to collimate and further expand the beam diameter to about 3 inches. Excellent degree of collimation is the key to get accurate characterization data. Then two silver mirrors guide the beam to the measurement side of the setup, enclosed in the black box in Figure 2.17(a).

The collimated broadband laser beam illuminates the backside (or right side) of the diffractive optic. Usually, the polychromat is patterned on the left side of the substrate. A single-mode-fiber (SMF) tip (QP8-2-SMA, Ocean Optics) connected to a portable spectrometer (Ocean Optics Jaz) is mounted onto a motor-actuated multiaxis stage with 1-inch maximum range of movement and 0.1μm movement precision (Z825B, Thorlabs). In the photovoltaics project (Chapter 3), only one axis (X) is used; in the super-achromatic lens project (Chapter 4), two axes (X and Z) are used; and in the high-sensitivity color imaging project (Chapter 6), all three axes (X, Y and Z) are used. The SMF has a core diameter of ~8μm and is placed precisely at the image plane (gap is d).

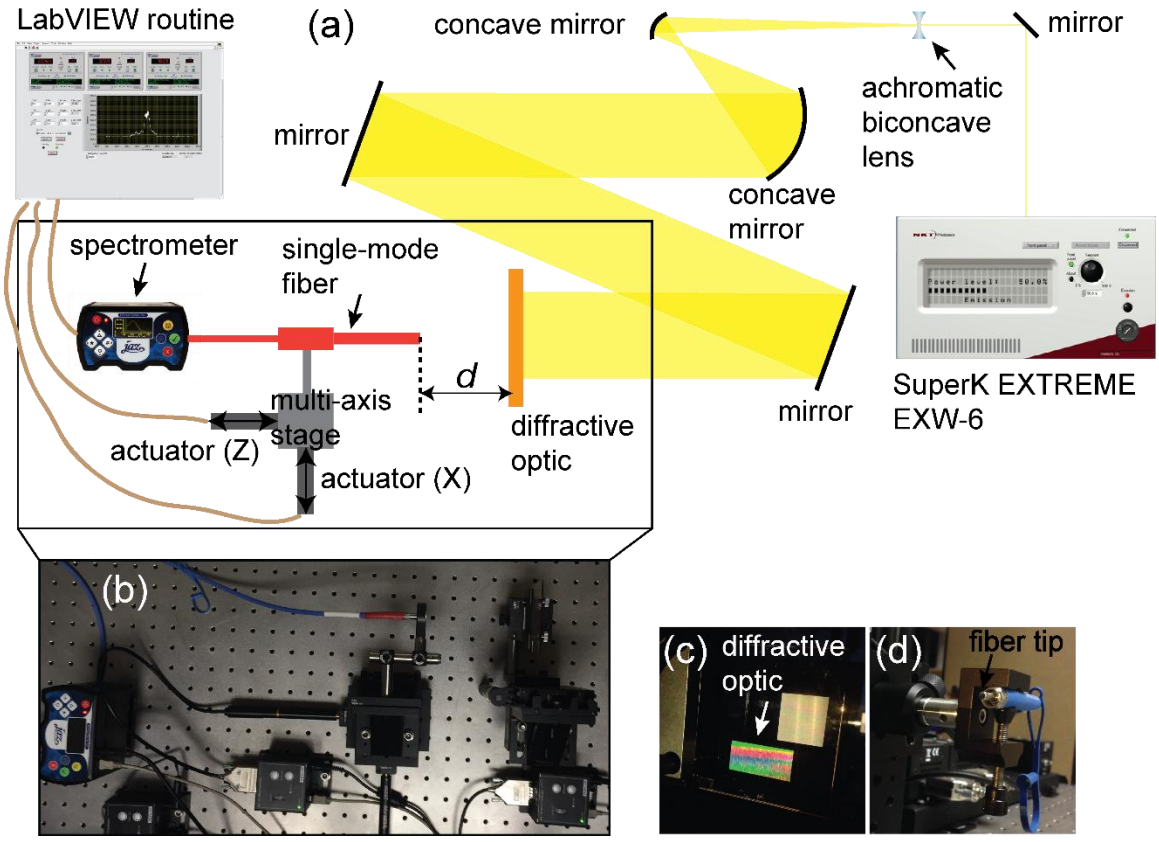

Figure 2.17. Scanning-spectrometer setup. (a) Schematic of the setup characterizing the spatial-spectral point-spread-function of the diffractive optic by scanning-spectrometer approach. (b) Photograph of the measurement side of the setup (black box in (a)). (c) Close-up photograph of the diffractive optic illuminated by broadband light. (d) Close-up photograph of the SMF tip mounted on the multiaxis stage.

Delicate control over this gap is another key towards successful measurements. Note that the polychromat needs to be aligned perpendicular to the optical path while the fiber has to be in line with the optical path. The spectrometer and the actuators are controlled via a custom-built LabVIEW routine.

The fiber tip is scanned across the entire image space of the polychromat. The finite diameter of the fiber tip and the stage accuracy undoubtedly limit the resolution of the measured spectral-spatial map. A numerical deconvolution in postprocessing may recover high-resolution sharp measurements. The SS-PSF of 1D and 2D polychromats are

$$PSF(x',\lambda) = \frac{I(x',\lambda) - I_{dark}(\lambda)}{I_{ref}(\lambda) - I_{dark}(\lambda)}. \quad (2.17)$$

$$PSF(x',y',\lambda) = \frac{I(x',y',\lambda) - I_{dark}(\lambda)}{I_{ref}(\lambda) - I_{dark}(\lambda)}. \quad (2.18)$$

In Equation (2.17) and (2.18), $I(x',\lambda)$ and $I(x',y',\lambda)$ are the intensities measured by spectrometer at position x' or (x',y') and wavelength λ. And $I_{ref}(\lambda)$ is the reference spectrum when the beam passes through a bare glass substrate coated with uniform unpatterned polychromat material (either Shipley 1813 or SC1827 photoresist). It is prepared under the same condition with the same film thickness. $I_{dark}(\lambda)$ is the dark measurement without light. This SS-PSF data are equivalent to the simulation results from Equations (2.5) and (2.6). Other specs of the polychromat, such as optical efficiencies, can be directly calculated from this SS-PSF data.

2.6.2 Scanning-pinhole setup

In the single-shot hyperspectral imaging project, we devised a scanning-pinhole setup to calibrate the spatial-spectral point-spread-function of the diffractive optic. Here this SS-PSF data are referred to as the system matrix (**A**), as discussed in Section 2.4. Our purpose is to record the multiwavelength PSFs of the imaging system when a single object point is located at all possible coordinates in the object plane.

The preconditioning optics are the same with the previous scanning-spectrometer setup (see Figure 2.17), except that a tunable bandpass filter (SuperK VARIA, NKT Photonics) is connected to the supercontinuum source to select different wavelengths. Its minimum bandwidth is 10nm. The layout and some photographs of the setup are shown

in Figure 2.18. More details on its working principles can be found in Chapter 7. The measurement side of the setup, enclosed in the black box in Figure 2.18(a), includes two parts: the object part and the imaging part. In this work, we introduce a circular pinhole (diameter φ=150μm, Thorlabs) as our object. It is mounted upon a two-axis (X and Y directions) motor stage (Z825B, Thorlabs) so that it can traverse all possible points in the designated object space. In our experiment, the field-of-view to be calibrated has an area of 3.6mm×3.6mm. However, diffraction through the pinhole does not have enough divergence to fill in the aperture of the following imaging lens. Therefore, an achromatic bi-convex lens (AC254-100-A, f=100mm, Thorlabs) is introduced before the pinhole and mounted on the same 2-axis stage using a cage mount (KT310, Thorlabs). The pinhole is carefully aligned at the lens focus. A small piece of diffuser is glued onto the backside of the pinhole to expand divergence as well. A close-up photograph of this part is given in Figure 2.18(d).

In the imaging part (Figure 2.18(c)), the imaging lens (MVL12WA, f=12mm, Thorlabs), the diffractive optic (polychromat), and the bare monochrome CMOS sensor (DMM22BUC03-ML, The Imaging Source) are fit in a cage mount for the purpose of easy alignment. As illustrated in Figure 2.18(a), the sensor is aligned to be exactly in the image plane of the imaging lens. Then the polychromat is placed at gap d from the sensor. Both the sensor and the polychromat are orthogonal to the optical path. Additionally, the imaging lens is adjusted to focus on the pinhole. Another LabVIEW routine is developed to configure and automate the tunable filter, the 2-axis stage, and the sensor.

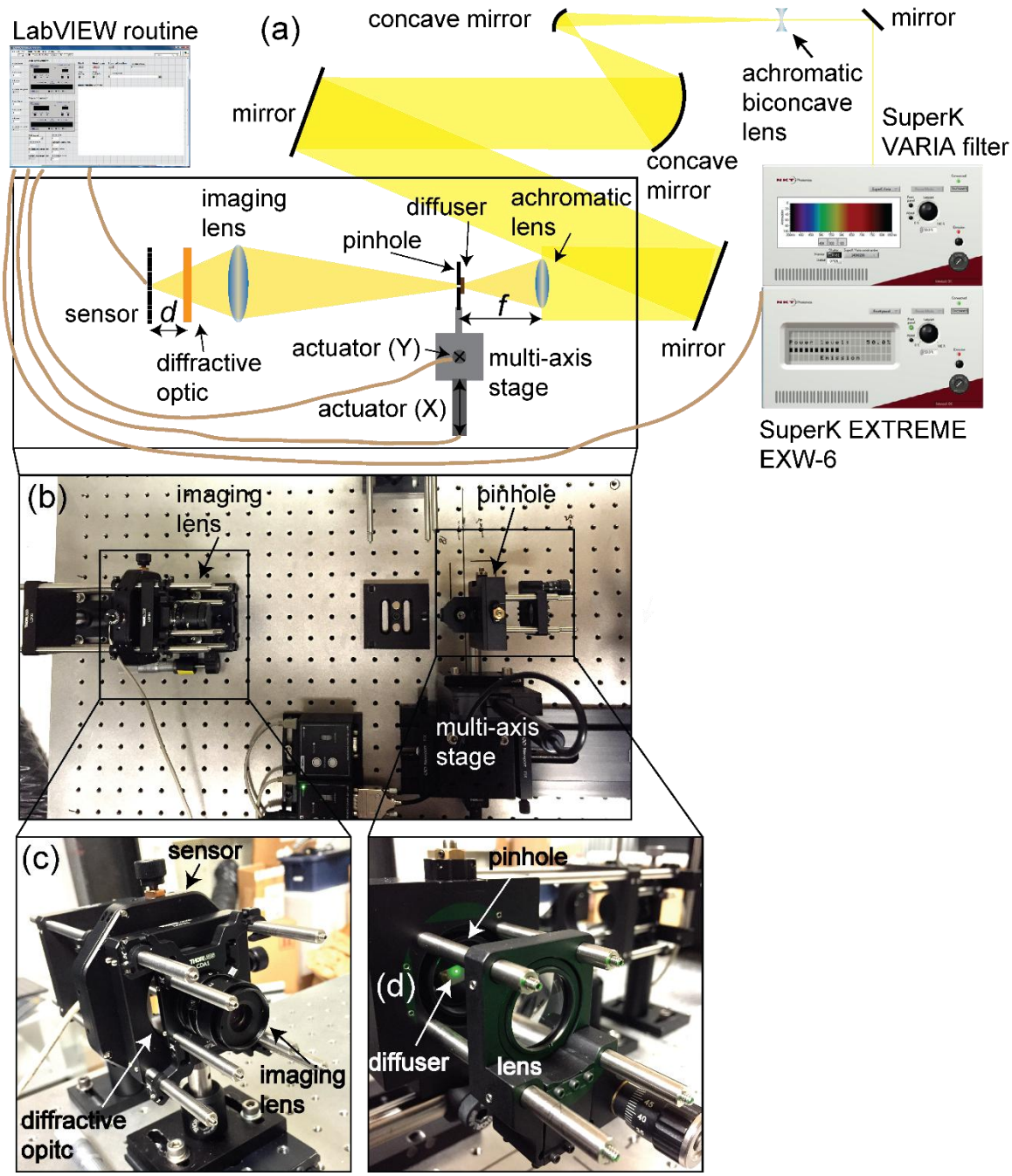

Figure 2.18. Scanning-pinhole setup. (a) Schematic of the setup characterizing the spatial-spectral point-spread-function of the diffractive optic by scanning-pinhole approach. (b) Photograph of the measurement side of the setup (black box in (a)). (c) Close-up photograph of the imaging part of the setup (left black box in (b)). (d) Close-up photograph of the object part of the setup (right black box in (b)).

2.7 References

[1] G. Kim, J. A. Domínguez-Caballero, and R. Menon, "Design and analysis of multi-wavelength diffractive optics," Opt. Express **20**, 2814-2823 (2012).

[2] J. W. Goodman, *Introduction to Fourier Optics* (Roberts and Company Publishers, 2005).

[3] B. Kress, and P. Meyrueis, *Digital Diffractive Optics: An Introduction to Planar Diffractive Optics and Related Technology* (John Wiley, 2000).

[4] K. Tostu, K. Fujishiro, S. Tanaka, and M Esashi, "Fabrication of three-dimensional microstructure using maskless gray-scale lithography," Sens. Actuators. A **130**, 387-392 (2006).

[5] T. Ito, and S. Okazaki, "Pushing the limits of lithography," Nature **406**, 1027-1031 (2000).

[6] S. Okazaki, "Resolution limits of optical lithography," J. Vac. Sci. Technol. B **9**, 2829-2833 (1991).

[7] M. Born, and E. Wolf, *Principles of Optics: Electromagnetic Theory of Propagation, Interference and Diffraction of Light* (Cambridge University Press, 1999).

[8] X. Wan, and R. Menon, "Proximity-effect correction for 3D single-photon optical lithography," Appl. Opt. **55**, A1-A7 (2016).

[9] L. J. Guo, "Recent progress in nanoimprint technology and its applications," J. Phys. D: Appl. Phys. **37**, R123-R141 (2004).

[10] T. W. Odom, J. C. Love, D. B. Wolfe, K. E. Paul, and G.M. Whitesides, "Improved pattern transfer in soft lithography using composite stamps," Langmuir, **18**, 5314-5320 (2002).

[11] V. N. Goral, Y.C. Hsieh, O. N. Petzold, R. A. Faris, and P. K. Yuen, "Hot embossing of plastic microfluidic devices using poly (dimethylsiloxane) molds," J. Micromech. Microeng. **21**, 017002 (2011).

[12] J. A. Dominguez-Caballero, S. Takahashi, and G. Barbastathis, "Design and sensitivity analysis of Fresnel domain computer generated holograms," Int. J. Nanomanufacturing **6**, 207 (2010).

[13] P. C. Hansen, *Discrete Inverse Problems: Insight and Algorithms* (SIAM Press, 2010).

CHAPTER 3

HIGH-EFFICIENCY MULTIBANDGAP PHOTOVOLTAICS

This chapter is adapted from the author's previous publication: Peng Wang, Jose A. Dominguez-Cabellero, Daniel J. Friedman and Rajesh Menon, "A new class of multi-bandgap high efficiency photovoltaics based upon broadband diffractive optics," Prog. Photovolt. Res. Appl. **23**, 1073-1079 (2015).

3.1 Abstract

A semiconductor absorber with a single bandgap is unable to convert broadband sunlight into electricity efficiently. Photons with energy lower than the bandgap are not absorbed, while those with energy far higher than the bandgap lose energy via thermalization. In this chapter, we demonstrate an approach to mitigate these losses via a thin, efficient, broadband diffractive microstructured optic that not only spectrally separates incident light but also concentrates it onto multiple laterally separated single-junction semiconductor absorbers. A fully integrated opto-electronic device model was applied in conjunction with a nonlinear optimization algorithm to design the optic. An experimental demonstration is presented for a dual-bandgap design using GaInP and GaAs solar cells, where a 20% increase compared to bare reference without the diffractive optic in total electric power is measured. Finally, we demonstrate that this framework of broadband diffractive optics allows us to independently design for the number of spectral bands and geometric concentration, thereby enabling a new class of multibandgap photovoltaic devices with ultrahigh energy-conversion efficiencies.

3.2 Introduction

Solar energy holds potential to become a significant source of energy in the near future [1]. The efficiency with which photons can be converted into charge carriers in a photovoltaic device is limited fundamentally by the Shockley-Queisser limit [2]. This upper bound arises from the fact that the solar spectrum stretches from ~350 nm to almost 2000 nm. Unfortunately, a single bandgap absorber is unable to convert all incident photons into charge carriers efficiently. Photons with energy below the bandgap are not absorbed at all, while photons with energy much higher than the bandgap tend to

lose the excess energy (beyond the bandgap) rapidly as heat within the semiconductor lattice, a process commonly referred to as thermalization. Recent work in the optimization of photonic properties has allowed a thin-film GaAs photovoltaic device to reach ~85% [3,4] of its Shockley-Queisser limit of 33.5% [5]. It is widely acknowledged that achieving efficiencies beyond this limit could have a tremendous technological impact. As has been noted earlier, the primary loss mechanisms that need to be overcome are nonabsorption and thermalization [6]. An effective approach is to separate the solar spectrum into smaller constituent bands and absorb these bands with band-matched absorbers. However, preconditioning of the incident sunlight to enable spectrum-splitting with conventional optical devices has proven to be impractical or inefficient. Spectrum-splitting using dichroic mirrors [7], beamsplitters [8], or prismatic elements [9] has been demonstrated. The main disadvantages of these approaches are their high cost, inability to scale to large areas, and bulky configuration, making them unsuitable for practical solar applications. For dichroic mirror-based designs, other factors such as Fresnel reflection losses from multiple interfaces also limit their scalability to a large number of spectral bands. Holographic spectrum splitting is highly inefficient over the broad solar spectrum. Furthermore, they suffer from degradation under long exposure to sunlight.

Nevertheless, the benefits of spectrum-splitting in photovoltaic devices have been demonstrated by vertically grown multijunction solar cells [10-12]. Although an impressive efficiency of 43.5% at a geometric concentration of 418X has been achieved [3], their widespread adoption is stifled by the high cost of epitaxial growth and the complexity of metamorphic growth [12]. Furthermore, in such devices the individual absorbers are connected in series and hence constrained to output the same current. This

is problematic since the photon density in the corresponding bands of sunlight may not be the same for the different absorbers. Such a rigid constraint will reduce net energy yield due to the temporal variations in the solar spectrum [13].

In this chapter, we present a new class of multibandgap high-efficiency photovoltaics based on a numerically optimized thin broadband diffractive optical element that we refer to as the "polychromat" [14]. The working principle of a polychromat-based photovoltaic device is demonstrated experimentally for the case of a dual-bandgap design using GaAs and GaInP absorbers. The numerical opto-electronic model is compared to measured data showing excellent agreement. Numerical simulations of ultrahigh energy conversion efficiency designs with multiple bandgaps at various concentrations are presented, demonstrating the flexibility of polychromat-based designs. Most notably, it is shown that an efficiency of over 50% may be achieved with an 8-bandgap design at a low concentration factor of 8X. The framework of the polychromat allows for independent control of the number of spectral bands and geometric concentration with high optical efficiencies, enabling a new class of multibandgap photovoltaic devices.

3.3 Methods

In its simplest dual-bandgap configuration, incident sunlight is diffracted by the polychromat such that the high-energy spectral band is localized on the left half of the image plane, while the low-energy spectral band is localized on the right half. By placing a high-bandgap cell on the left and a low-bandgap cell on the right, it is possible to extract more electrical energy compared to the case of normal illumination (without the polychromat). Furthermore, the polychromat also performs geometric concentration of 2X for each spectral band, since the input aperture area is twice that of each of the cells in

this specific configuration.

In this chapter, only 1D designs are considered, with varying heights in the X direction and uniform grooves in the Y direction. The smallest width of a groove or a polychromat pixel was constrained to 3μm to be compatible with the grayscale patterning process used for its fabrication. It is the smallest lateral feature size available by our lithography tool. The overall size of the optic was LX × LY = 10mm × 5mm, with each of the single-junction solar cells of size 5mm × 5mm. This makes totally 3334 grooves in one polychromat design. As indicated in Figure 3.1(a), the solar cells were placed side-by-side on the image plane (d=120mm away from the polychromat). The height of each pixel is allowed to vary between 0 and 1.8μm.

The single-junction solar cells were selected based upon the optimal bandgaps as well as the practical availability of the materials. These were a GaInP cell with a bandgap of 1.8eV and a GaAs cell with a bandgap of 1.4eV. Both cells were grown on GaAs substrate by atmospheric-pressure organometallic vapor phase epitaxy. They have stacks of Se-doped n-type emitters (0.1μm thick for both) and Zn-doped p-type bases (2.8μm thick for GaInP and 3.5μm thick for GaAs). Electroplating and photolithography defined the gold grid fingers, and heavily n-doped GaAs worked a contact layer between emitters and metal fingers. A ZnO/MgF_2 double-layer was deposited on top for antireflection. The measured external quantum efficiencies (EQEs) of these cells are shown in Figure 3.1(b), confirming that the GaInP cell has strong absorption in the visible spectrum, while the GaAs cell has absorption that extends into the near-infrared portion of the spectrum.

The polychromat was designed numerically based upon an integrated optoelectronic model [15] and by applying a novel expanded version of the direct-binary-search (DBS)

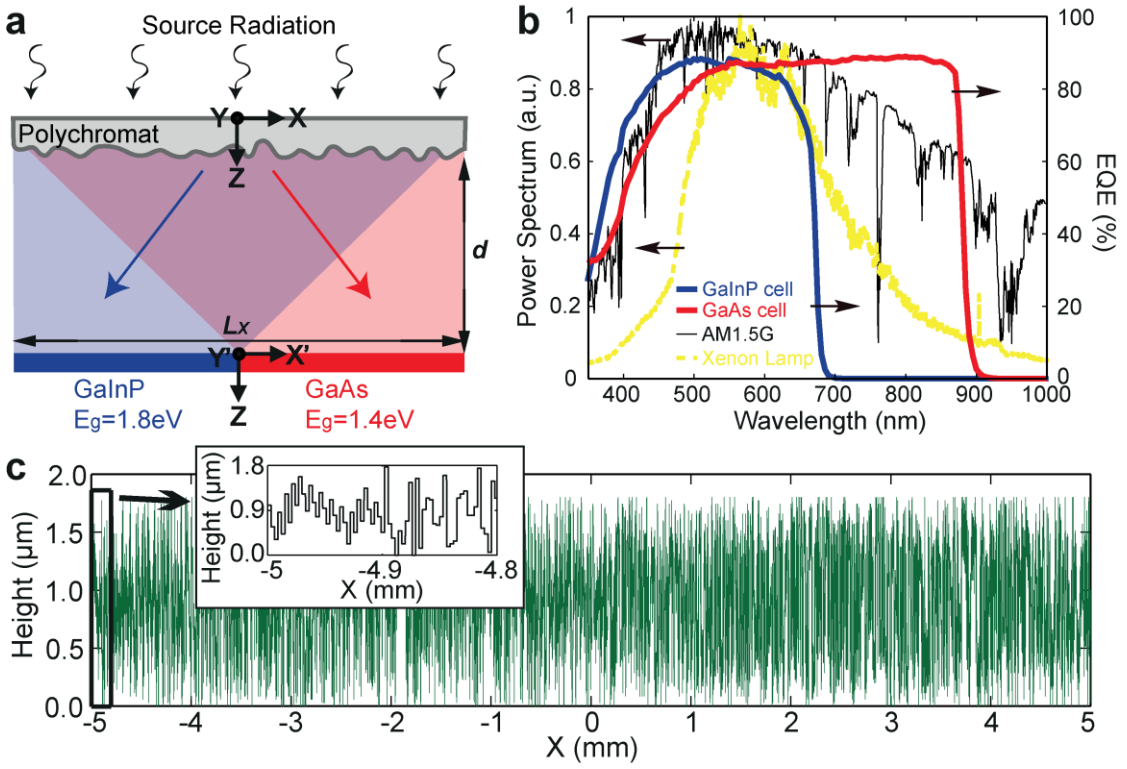

Figure 3.1. (a) Schematic showing the polychromat spectrally separating incident sunlight and concentrating the two bands onto a GaInP cell and a GaAs cell. (b) Measured external quantum efficiencies of the GaInP and GaAs cells, and normalized power spectra of the AM1.5G and the Xenon lamp used in our experiments (total power = 300W). (c) Height profile of the designed polychromat with 3μm pixel size and 1.8μm maximum height (Inset: magnified view of the first 200μm of the design).

algorithm [16-18]. The objective of the design was to maximize the total output electric power. The algorithm proceeds in such a progressive manner that each polychromat groove experiences perturbation during each iteration. Whether a negative or a positive perturbation is valid is determined by the updated optimization objective (or figure-of-merit, FOM). A unit perturbation of Δh=28.6nm is applied. A dual-bandgap polychromat design example is shown in Figure 3.1(c) as pixel-height distributions. Note the multilevel structure as shown in the inset figure.

The polychromat was fabricated using grayscale lithography on a thin film of commonly used Shipley 1813 photoresist. An optical micrograph of the fabricated optic

is shown in Figure 3.2(a). The inset in the figure shows an atomic-force micrograph of a small portion of the optic delineated by the white square. This image confirms the height distribution and the width of the pixels. Pixel width of 3μm is clearly seen and marked. We measured the standard deviation of the errors in pixel-heights due to fabrication errors as about 100nm. Further numerical analysis and experimental measurements show that this error is sufficient to provide acceptable performances.

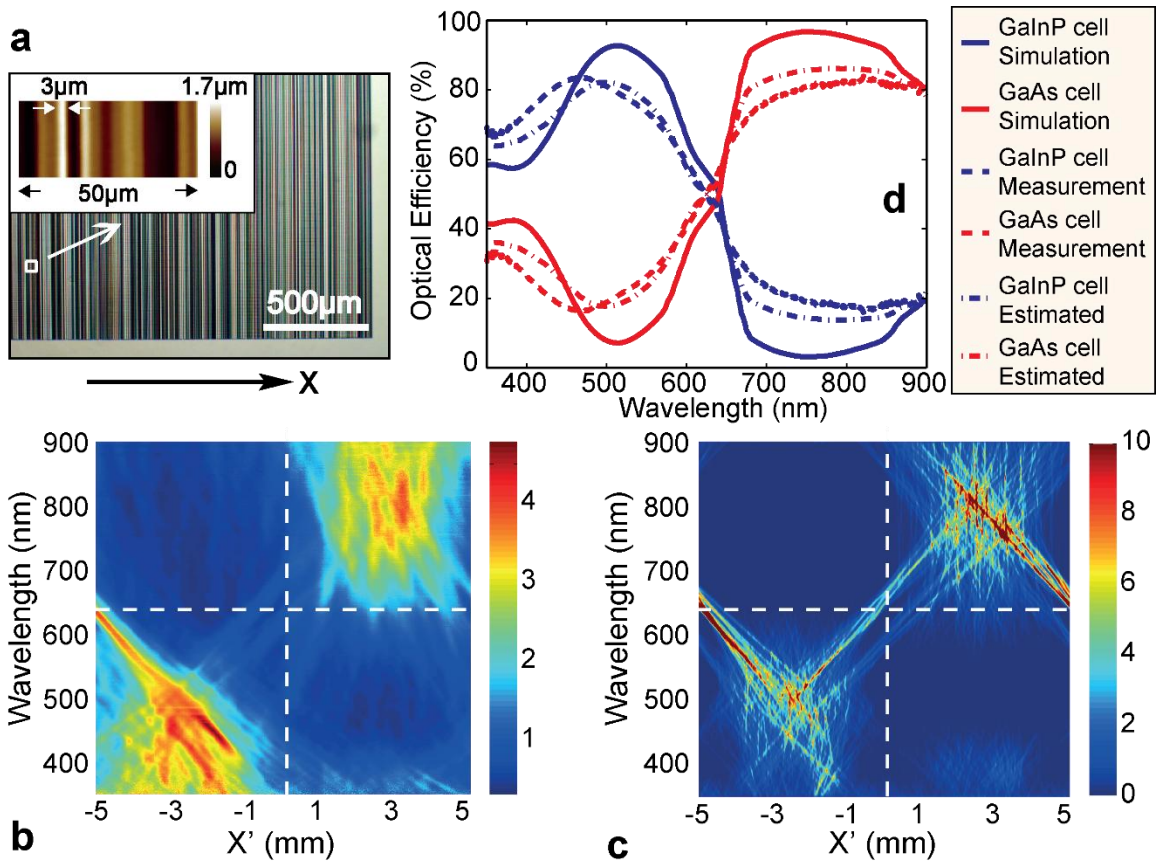

Figure 3.2. Polychromat design and optical characterization results. (a) Microscopic image of the designed and fabricated polychromat with back illumination (Inset: atomic-force micrograph of a small portion of the polychromat delineated by the white block). Spatial-spectral intensity distribution at the image plane measured (b) and simulated (c). (d) Spectral efficiency of the polychromat for the two bands. Blue lines are for the GaInP cell and red lines are for the GaAs cell. Solid lines are from simulations of the designed polychromat, dashed lines are from real measurements, and dotted-dashed lines represent estimations by considering the corrected dispersion data of Shipley 1813 photoresist and fabrication error with standard deviation of 100nm.

3.4 Experimental Results

The polychromat was optically characterized by measuring the spectral characteristics of its diffraction pattern at the image plane that is d=120mm away from the polychromat. The resulting spectral transmission efficiency is shown in Figure 3.2(d). The transmission efficiency is calculated as the ratio of the total power at the image plane integrated over the left or right absorber area, respectively, and divided by the total input power integrated over the entire polychromat area. The numerical simulation (solid lines) shows that the average optical efficiency is 85%. The measured efficiency is also shown (dashed lines) and has an average efficiency of 75%. They are both mean values of the optical efficiencies of two spectrum bands: high-energy band (averaged from 400nm to 630nm) and low-energy band (averaged from 630nm to 900nm). The reduction in efficiency for the measured polychromat was the result of a combination of errors introduced during fabrication in the pixel heights (~100nm) and errors in the dispersion data of the photoresist. A second numerical simulation was run including these height and dispersion errors (dotted-dashed lines), resulting in a much better match between our numerical model and the measured data. In addition, a spatial-spectral image map was created for the original simulation by the Fresnel transform [16] and the measured data (see Figure 2.17 and Equation (2.17)) and is shown in Figure 3.2(c) and Figure 3.2(b), respectively, which also demonstrate excellent agreement. The spectrally integrated intensity distribution is calculated to offer reasonable uniformity across the entire solar cell surfaces. However, in order to benefit the concentrated photovoltaics (CPV) to a greater extent, the DBS-based algorithm can also be readily implemented to improve spatial uniformity of intensity. The illumination was spatially collimated white light from a

Xenon lamp, whose power spectrum is plotted in Figure 3.1(b). As expected, the high-energy photons are localized to the left half of the image plane, while the low-energy photons are redirected to the right half.

The solar cells were characterized independently by measuring their current-voltage curves under conventional illumination (reference, without polychromat) and spectrum-split illumination (with polychromat), both using the same source. As shown in Figure 3.3(a), spectrum-splitting with the polychromat increases the short-circuit current-density of the GaInP cell by 58% (simulation) and by 26% (measurements). This can be understood by the increase in the high-energy photons that are redirected towards the GaInP cell by the polychromat. In the reference case, such photons that land on the right-hand side of the image plane completely miss the GaInP cell (which is placed on the left-hand side of the image plane). The open-circuit voltage of the GaInP cell shows an increase of 7% (simulation) and of 4% (measurements), likely due to the increased photon flux [19]. On the other hand, the GaAs cell (which is placed on the right-hand side of the image plane) loses the redirected high-energy photons compared to the reference. Although some of the low-energy photons are redirected towards the GaAs cell by the polychromat from the left-hand side of the incident beam, the overall effect is such that the short-circuit current-density of the GaAs cell increases by 5% (simulation) and by 13% (measurements), as shown in Figure 3.3(b). Its open-circuit voltage also increases slightly by 2.3% (simulation) and by 2.9% (measurements). The fill-factors of both the cells are maintained during spectrum-splitting. As a result, the power-density of both cells show increase as illustrated in Figures 3.3(c) and 3.3(d). The simulations predict the peak-power-density of the GaInP cell to increase by 69% and that of the GaAs cell to

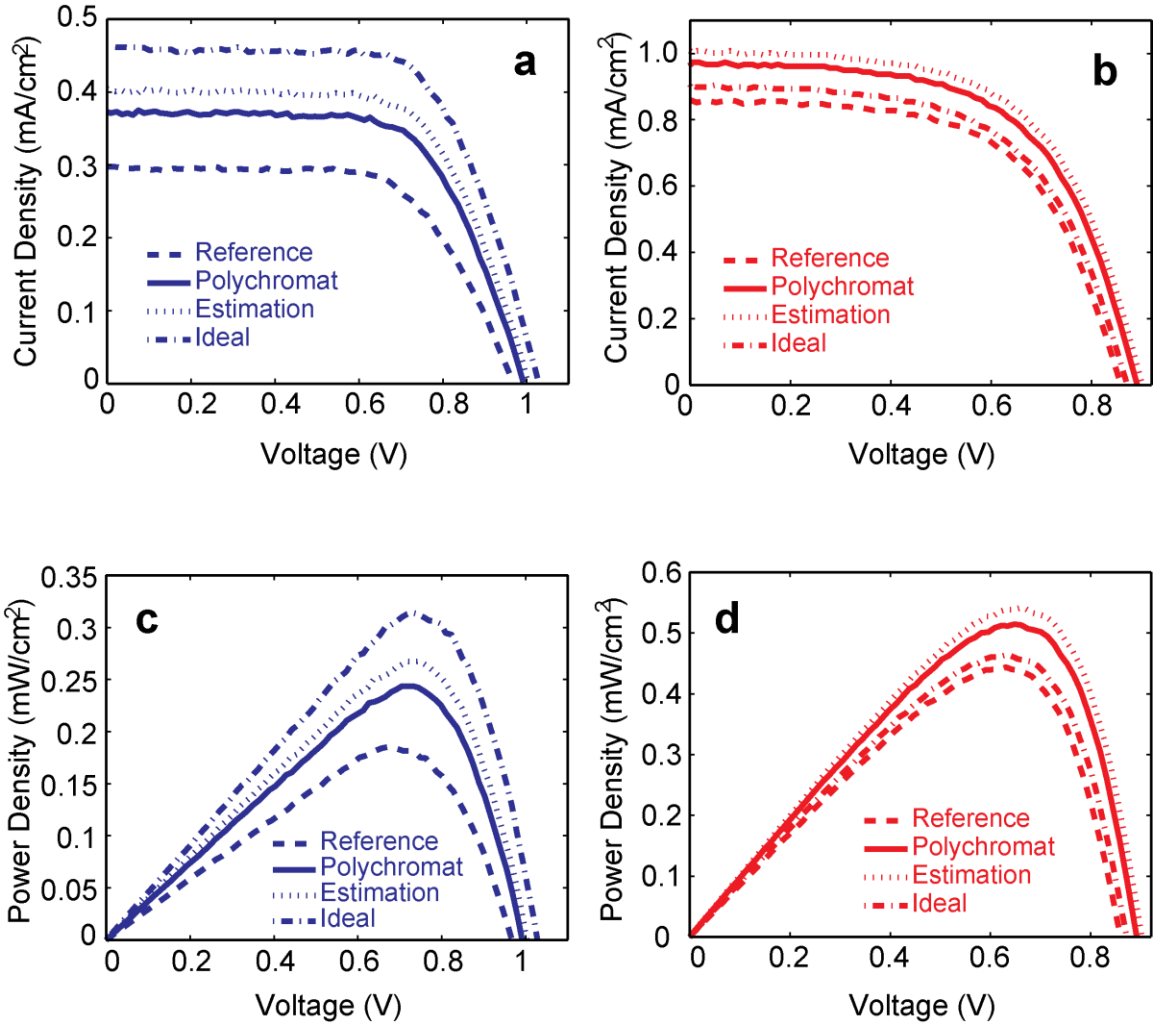

Figure 3.3. Electrical measurement results. (a) J-V curve of the GaInP cell. (b) J-V curve of the GaAs cell. (c) P-V curve of the GaInP cell. (d) P-V curve of the GaAs cell. Solid lines are derived from measurements with spectrum-splitting by polychromat. Dashed lines stand for reference measurements without polychromat. Dotted lines are simulation results estimated by considering the measured spectral efficiencies. The simulated ideal cases with the designed polychromat are represented by dotted-dashed lines. The method for calculating the solar cell electronic response curves are detailed in the Supplementary Materials of this chapter.

increase by 7.7% under spectrum-split illumination compared to the reference. The measured peak power density increase for the GaInP and the GaAs cells are 29% and 16%, respectively. The combined power density from both cells under spectrum-split conditions is predicted to increase by 26%, and the corresponding measured increase is 20%.

The discrepancies between simulation and measurement in device power output are primarily due to fabrication errors that degrade the polychromat transmission performance as discussed earlier. Specifically, as can be seen in Figure 3.2(b), the optical efficiency of the polychromat is reduced in the spectral range from 460 nm to 620 nm, which includes a significant portion of the input light spectrum (see Figure 3.1(b)). This means that some of the high-energy photons, which should have been redirected to the GaInP cell, are now incident on the GaAs cell. Thereby, the GaInP cell exhibits a smaller-than-expected increase and the GaAs cell shows a larger-than-expected increase in their respective short-circuit-current densities. By using the measured optical efficiency spectrum of the polychromat, we can estimate the electrical characteristics of the two cells, as illustrated by dotted lines in Figure 3.3. This estimation agrees well with the measured characteristics, thereby validating our optoelectronic model.

3.5 Numerical Analysis

The numerical optimization of the polychromat allows us to control the geometric concentration independently from the number of spectral bands. To illustrate this design flexibility, we redesigned the dual-band polychromat presented earlier, but with an increased concentration factor of 10X, as given in Figure 3.4(a). The optimized design of this polychromat is shown in Figure 3.4(b), while the corresponding spatial-spectral

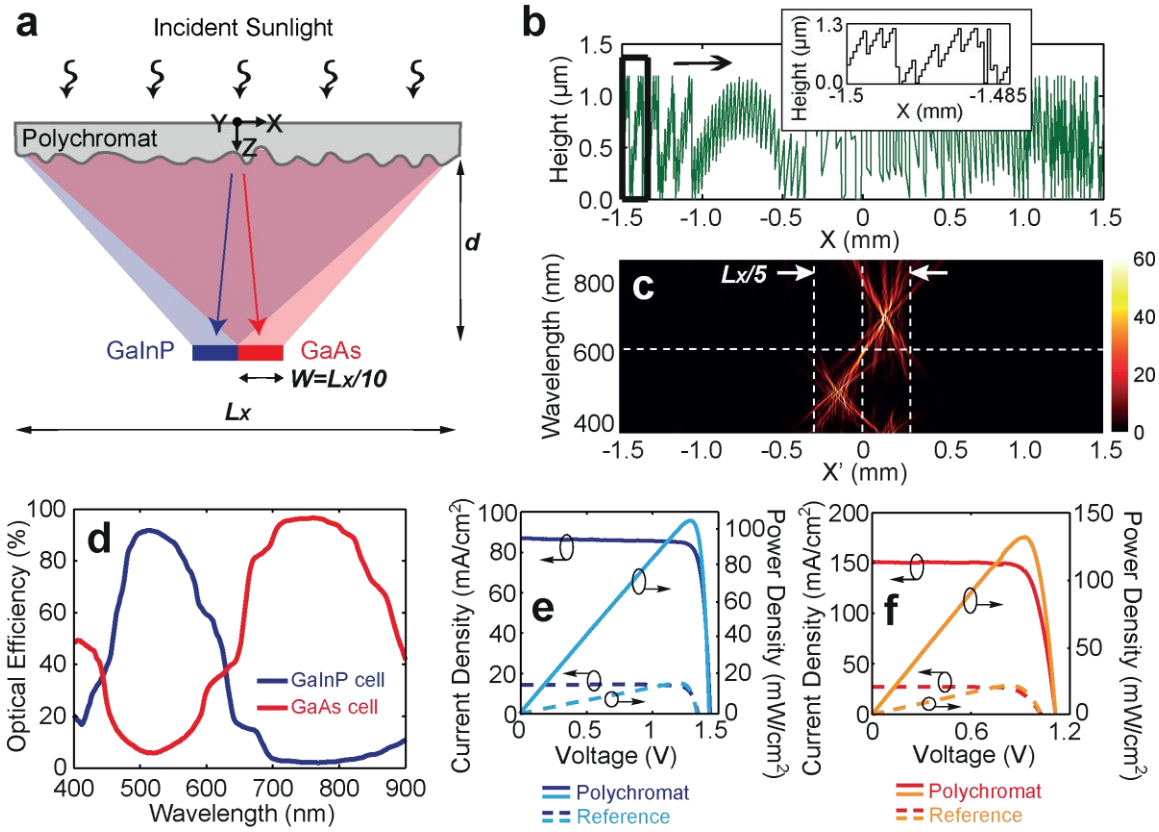

Figure 3.4. (a) Schematic showing a dual-band polychromat with a geometric concentration factor of 10X. (b) Optimized height profile of the polychromat in (a) (Inset: magnified view of the first 150μm). (c) Simulated spatial-spectral intensity distribution and (d) spectral efficiency distribution. Simulated electrical characteristics of (e) the GaInP cell and (f) the GaAs cell using this polychromat.

image map is shown in Figure 3.4(c), where two spectral bands and the geometric concentration are obvious. The optical efficiency spectrum in Figure 3.4(d) indicates that the two bands are separated with an average efficiency of ~80%. Simulated electrical performance described in Figure 3.4(e) for the GaInP cell and Figure 3.4(f) for the GaAs cell confirms that a net efficiency of ~27.7% could be achieved.

The ability to control concentration independently of the number of spectral bands is a powerful technique to enable ultrahigh efficiencies. We illustrate this in Figure 3.5(a), where four real absorbers were simulated under increasing geometric concentration

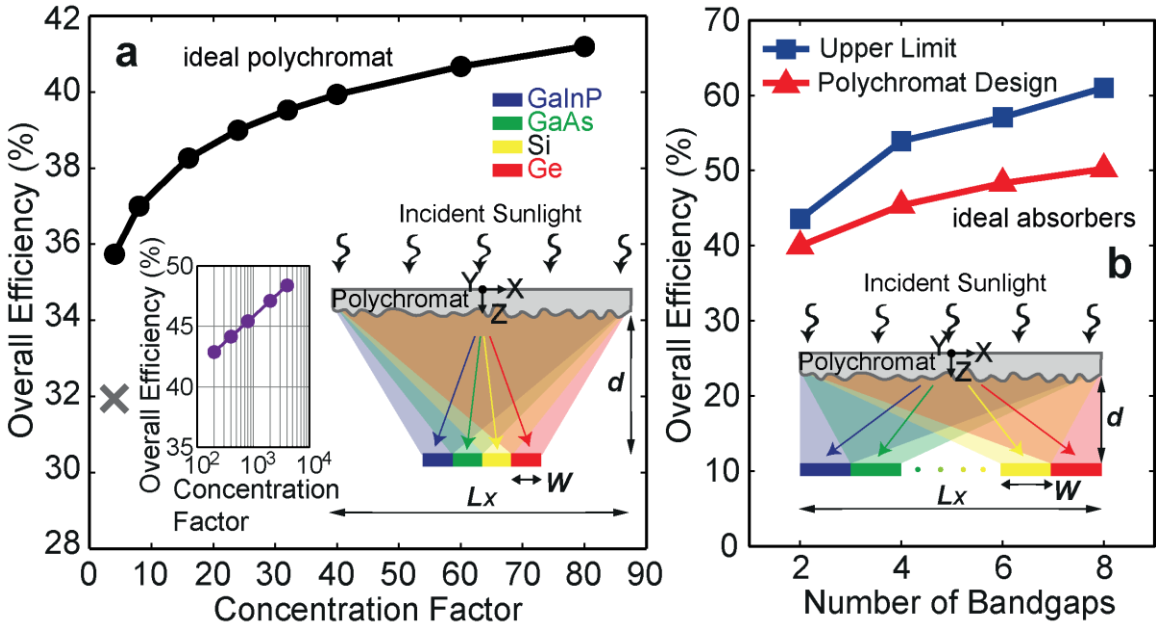

Figure 3.5. Independent control of the number of spectral bands and concentration using the polychromat. (a) Calculated net efficiency as a function of concentration factor for four real solar cells (GaInP, GaAs, Si and Ge) and assuming ideal polychromats with 100% optical efficiency (Left inset: the same plot in log scale with higher concentration factors, Right inset: illustration of the device incorporating the polychromat and four solar cells). A device with a designed polychromat at a concentration of 4X is shown by the gray cross. Concentration factor is augmented by increasing the polychromat aperture. (b) Calculated net efficiency as a function of the number of spectral bands assuming ideal absorbers of ideal bandgaps and 100% EQEs. Real polychromat designs were used for the red curve, while ideal polychromats with 100% optical efficiencies were assumed for the blue curve (Inset: schematic of the device with an arbitrary number of absorbers). In this case, the concentration factor equals the number of bands.

assuming an ideal polychromat (optical transmission efficiency of 100%). As expected, the increase in concentration not only increases the short-circuit current density but also the open-circuit voltage. An actual polychromat design with 4 bands at a concentration factor of 4X yields a net efficiency of ~32%. Higher optical efficiencies are achievable by judiciously choosing optimal geometric parameters, including propagation distance, pixel size, and number of pixels [16]. In practice, enhanced grayscale lithography technique with better precision and accurate calibration oppresses unwanted scattering and thus

gives rise to increased optical efficiencies. Refer to Chapter 2 for technical information on the calibration of grayscale lithography and scanscale parameter.

Finally, in Figure 3.5(b), we show four polychromats, each designed to spectrally separate and concentrate sunlight onto ideal photovoltaic absorbers of optimal combinations of bandgaps. The number of bands is increased from 2 to 8. In this case, the concentration factor is set to be equal to the number of bands. The upper bound of the photovoltaic efficiency assumes ideal polychromats are plotted on the blue curve, while the red curve assumes actual polychromat designs. It is noteworthy that a net efficiency >50% may be achieved with a polychromat that separates sunlight into 8 spectral bands and concentrates these bands by 8X. These simulations confirm that the polychromat allows one to flexibly design for an arbitrary number of spectral bands (and absorbers) and also for separately controlling the geometric concentrations. The polychromat-based photovoltaic architecture could also be easily adapted to various material systems with engineered bandgaps and quantum efficiencies, such as organic solar cells [20] and quantum dot solar cells [21]. Thus, it provides a new design framework enabling ultra-high-efficiency photovoltaic devices.

Since the polychromat is microfabricated, it is possible to integrate the polychromat into the cover glass of a photovoltaic device, which allows for ready scaling to large areas. An example design, whose form factor corresponds to a conventional photovoltaic panel, offers a 30% improvement in overall power conversion efficiency. Note that since the polychromat may be fabricated directly into glass, it can be extremely durable over prolonged exposure to sunlight. Moreover, the fabrication of the polychromat can be readily replicated over large areas using roll-to-roll processes [22,23].

3.6 Conclusions

Photovoltaic energy conversion is fundamentally an optoelectronic phenomenon. Therefore, it is critical to incorporate photonic principles into the design of such devices. In this chapter, we showcase a novel example of such an integrated device. A microstructured broadband optic that can spectrally separate sunlight into an arbitrary number of spectral bands and also concentrate these bands onto matched absorbers is utilized to enhance the net efficiency of the photovoltaic effect. By optimizing the number of spectral bands, the absorber materials, and the concentration factors in conjunction with conventional device properties, we can expect ultra-high-efficiency photovoltaics.

3.7 Supplementary Information

3.7.1 Figure-of-merit

We choose the total power conversion efficiency boost as our FOM defined as

$$FOM = \frac{\eta_{poly} - \eta_{ref}}{\eta_{ref}}. \tag{3.1}$$

$$\eta_{poly} = \frac{P_{poly} \cdot A_{cell}}{C \cdot A_{cell}}. \tag{3.2}$$

$$\eta_{ref} = \frac{P_{ref} \cdot A_{cell}}{N \cdot A_{cell}}. \tag{3.3}$$

Equations (3.2) and (3.3) represent the total power conversion efficiency for the case with and without polychromat. Here, we assume that all the subcells have the same areas, which holds for all the cases studied here. Therefore, P_{poly} is the sum of power density of all subcells when a polychromat design is present, and P_{ref} is the reference counterpart

with absence of polychromat. A_{cell} is the surface area of each single cell, C is the concentration factor, and N is the number of subcells of different bandgaps. Particularly in this case, the total power density outputs included in Equations (3.2) and (3.3) are expressed as

$$P_{poly} = J_{sc}^{GaInP} V_{oc}^{GaInP} FF^{GaInP} + J_{sc}^{GaAs} V_{oc}^{GaAs} FF^{GaAs}. \tag{3.4}$$

$$P_{ref} = J_{sc,ref}^{GaInP} V_{oc}^{GaInP} FF^{GaInP} + J_{sc,ref}^{GaAs} V_{oc}^{GaAs} FF^{GaAs}. \tag{3.5}$$

In Equations (3.4) and (3.5), J_{sc} stands for the short-circuit current density. For optimization, V_{oc} and FF are the measured open-circuit voltage and fill factor under Xenon lamp without the polychromat. For simplicity, we ignored the slight changes of V_{oc} and FF between different radiation conditions in the optimization procedure. However, a more rigorous model might be introduced to predict the power output with higher accuracy [15]. Moreover, we experimentally show that both J_{sc} and V_{oc} are increased as a result of the spectrum-splitting.

The short-circuit current density J_{sc} for each case is defined as

$$J_{sc}^{GaInP} = \int_{\lambda_{\min}}^{\lambda_{\max}} d\lambda \int_{-L_X/2}^{0} \frac{q\lambda}{hc} \cdot I_{poly}(x,\lambda) \cdot EQE^{GaInP}(\lambda) dx. \tag{3.6}$$

$$J_{sc}^{GaAs} = \int_{\lambda_{\min}}^{\lambda_{\max}} d\lambda \int_{0}^{L_X/2} \frac{q\lambda}{hc} \cdot I_{poly}(x,\lambda) \cdot EQE^{GaAs}(\lambda) dx. \tag{3.7}$$

$$J_{sc,ref}^{GaInP} = \int_{\lambda_{\min}}^{\lambda_{\max}} d\lambda \int_{-L_X/2}^{0} \frac{q\lambda}{hc} \cdot I_{ref}(x,\lambda) \cdot EQE^{GaInP}(\lambda) dx \tag{3.8}$$

$$J_{sc,ref}^{GaAs} = \int_{\lambda_{\min}}^{\lambda_{\max}} d\lambda \int_{0}^{L_X/2} \frac{q\lambda}{hc} \cdot I_{ref}(x,\lambda) \cdot EQE^{GaAs}(\lambda) dx \tag{3.9}$$

$I_{poly}(x,\lambda)$ is the light intensity distribution along X direction for wavelength λ in the case with the polychromat, and $I_{ref}(x,\lambda)$ is the reference when the incident light directly illuminates the array of solar cells. The spectrum is from λ_{min}=350nm to λ_{max}=900nm, and the integral can be approximated by the sum of multiple wavelength samples.

3.7.2 Experimental setup

Figure 3.6(a) is a photograph of the experiment setup for measuring the electrical responses of the solar cells. The cells were connected to a Keithley 2602A Source Meter by probes and measured independently. To estimate the power conversion efficiencies, we measured the total optical power passing through the polychromat using a Coherent PM10 broadband power meter, which gives a power intensity of 1.77 mW/cm^2.

3.7.3 Electrical characterization details

Relevant electrical parameters from the measurements are listed in the Table 3.1. P_{max} is the maximal power under voltage bias of V_{max} and current density of J_{max}. The fill factor is defined as $FF=(J_{max} \times V_{max}) / (J_{sc} \cdot V_{oc})$.

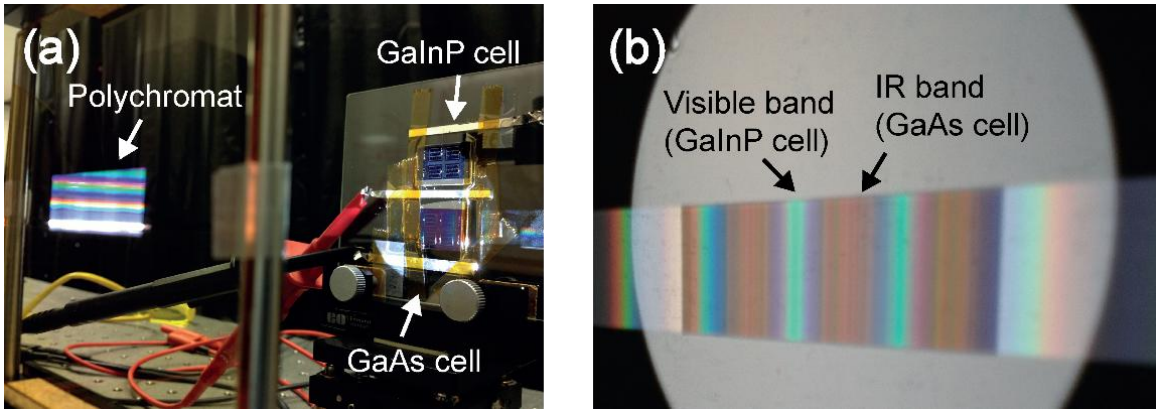

Figure 3.6. Photographs of electrical measurement. (a) Experiment setup for I-V curve measurements to evaluate power conversion efficiency. (b) Photograph at the imaging plane, demonstrating the effect of spectrum-splitting.

Table 3.1

Electrical measurement results of the solar cells

	J_{sc} (mA/cm^2)	V_{oc} (V)	J_{max} (mA/cm^2)	V_{max} (V)	*FF*	P_{max} (mW/cm^2)	**Power Boost**	**Efficiency**
GaInP								
Reference	0.296	0.96	0.282	0.67	0.67	0.190	NA	5.37%
Polychromat	0.373	1.00	0.343	0.71	0.66	0.245	29%	6.92%
Estimation	0.403	1.00	0.369	0.72	0.67	0.266	40%	7.51%
Ideal	0.467	1.03	0.438	0.73	0.67	0.322	69%	9.10%
GaAs								
Reference	0.860	0.86	0.698	0.63	0.60	0.440	NA	12.43%
Polychromat	0.973	0.88	0.796	0.65	0.60	0.509	16%	14.48%
Estimation	1.001	0.89	0.803	0.66	0.59	0.524	19%	14.80%
Ideal	0.905	0.88	0.746	0.63	0.60	0.474	7.7%	13.39%
Total								
Reference	NA	NA	NA	NA	NA	0.630	NA	17.80%
Polychromat	NA	NA	NA	NA	NA	0.754	20%	21.30%
Estimation	NA	NA	NA	NA	NA	0.790	25%	22.32%
Ideal	NA	NA	NA	NA	NA	0.796	26%	22.49%

3.8 References

[1] Optics and Photonics: Essential Technologies for Our Nation, (National Research Council, 2012): http://www.nap.edu/catalog.php?record_id=13491

[2] W. Shockley, and H. J. Quesisser, "Detailed balance limit of efficiency of p-n junction solar cells," J. Appl. Phys. **32**, 510-519 (1961).

[3] M. A. Green, K. Emery, Y. Hishikawa, W. Warta, and E. D. Dunlop, "Solar cell efficiency tables (version 39)," Prog. Photovolt: Res. Appl. **20**, 12-20 (2012).

[4] News on GaAs solar cell efficiency record: http://www.technologyreview.com/news/424435/alta-devices-breaks-solar-cell-record/

[5] O. D. Miller, E. Yablonovitch, and S. R. Kurtz, "Intense internal and external fluorescence as solar cells approach the Schockley-Queisser efficiency limit," arXiv:1106.1603 [physics.optics].

[6] A. Polman, and H. A. Atwater, "Photonic design principles for ultrahigh-efficiency photovoltaics," Nat. Mater. **11**, 134-137 (2012).

[7] S. Ruhle, A. Segal, A. Vilan, S. R. Kurtz, L. Grinis, A. Zaban, I. Lubomirsky, and

D. Cahen, “A two junction, four terminal photovoltaic device for enhanced light to electric power conversion using a low-cost dichroic mirror,” J. Renew. Sust. Energ. **1**, 013106 (2009).

[8] B. Mitchell, G. Peharz, G. Siefer, M. Peters, T. Gandy, J. C. Goldschmidt, J. Benick, S. W. Glunz, A. W. Bett, and F. Dimroth, “Four-junction spectral beam-splitting photovoltaic receiver with high optical efficiency,” Prog. Photovolt: Res. Appl. **19**, 61-72 (2011).

[9] M. Stefancich, A. Zayan, M. Chiesa, S. Rampino, D. Roncati, L. Kimerling, and J. Michel, “Single element spectral splitting solar concentrator for multiple cells CPV system,” Opt. Express **20**, 9004-9018 (2012).

[10] R. R. King, D. C. Law, K. M. Edmondson, C. M. Fetzer, G. S. Kinsey, H. Yoon, R. A. Sherif, and N. H. Karam, “40% efficiency metamorphic GaInP/GaInAs/Ge multijunction solar cells,” Appl. Phys. Lett. **90**, 183516 (2007).

[11] F. Dimroth, and S. Kurtz, “High-efficiency multijunction solar cells,” MRS Bulletin **32**, 230-236 (2007).

[12] J. F. Geisz, D. J. Friedman, J. S. Ward, A. Duda, W. J. Olavarria, T. E. Moriarty, J. T. Kiehl, M. J. Romero, A. G. Norman, and K. M. Jones, “40.8% efficient inverted triple-junction solar cell with two independently metamorphic junctions,” Appl. Phys. Lett. **93**, 123505 (2008).

[13] S. P. Philipps, G. Peharz, R. Hoheisel, T. Hornung, N. M. Al-Abbadi, F. Dimroth, and A. W. Bett, “Energy harvesting efficiency of III-V triple-junction concentrator cells under realistic spectral conditions,” Sol. Energ. Mat. Sol. C. **94**, 869-877 (2010).

[14] G. Kim, J. A. Dominguez-Caballero, H. Lee, D. J. Friedman, and R. Menon, “Increased photovoltaic power output via diffractive spectrum separation,” Phys. Rev. Lett. **110**, 123901 (2013).

[15] J. Nelson, *The Physics of Solar Cells* (Imperial College Press, London, 2004).

[16] G. Kim, J. A. Dominguez-Caballero, and R. Menon, “Design and analysis of multi-wavelength diffractive optics,” Opt. Express **20**, 2814-2823 (2012).

[17] P. Wang, and R. Menon, “Three-dimensional lithography via digital holography,” in *Frontiers in Optics 2012/Laser Science XXVIII, OSA Technical Digest* (online), paper FTu3A.4. http://www.opticsinfobase.org/abstract.cfm?URI=FiO-2012-FTu3A.4

[18] P. Wang, and R. Menon, “Optimization of periodic nanostructures for enhanced light-trapping in ultra-thin photovoltaics,” Opt. Express **21**, 6274-6285 (2013).

[19] S. P. Bremner, M. Y. Levy, and C. B. Honsberg, “Analysis of tandom solar cells

efficiencies under AM1.5G spectrum using a rapid flux calculation method," Prog. Photovolt: Res. Appl. **16**, 225-233 (2008).

[20] M. Kaltenbrunner, M. S. White, E. D. Glowacki, T. Sekitani, T. Someya, N. S. Sariciftci, and S. Bauer, "Ultrathin and lightweight organic solar cells with high flexibility," Nat. Commun. **3**, 770-777 (2012).

[21] V. Aroutiounian, S. Petrosyan, and A. Khachatryan, "Quantum dot solar cells," J. Appl. Phys. **89**, 2268-2271 (2001).

[22] L. J. Guo, "Recent progress in nanoimprint technology and its applications," J. Phys. D: Appl. Phys. **37**, R123-R141 (2004).

[23] C. Battaglia, J. Escarre, K. Soderstrom, L. Erni, L. Ding, G. Bugnon, A. Billet, M. Boccard, L. Barraud, S. D. Wolf, F. J. Haug, M. Despeisse, and C. Ballif, "Nanoimprint lithography for high-efficiency thin-film silicon solar cells," Nano Lett. **11**, 661-665 (2011).

CHAPTER 4

BROADBAND CHROMATIC-ABERRATION-CORRECTED LENS

This chapter is adapted from the author's previous publication: Peng Wang, Nabil Mohammad and Rajesh Menon, "Chromatic-aberration-corrected diffractive lenses for ultra-broadband focusing," Sci. Rep. **6**, 21545 (2016).

4.1 Abstract

We exploit the inherent dispersion in diffractive optics to demonstrate planar chromatic-aberration-corrected lenses. Specifically, we designed, fabricated, and characterized cylindrical diffractive lenses that efficiently focus the entire visible band (450nm to 700nm) onto a single line. These devices are essentially pixelated, multilevel microstructures. Experiments confirm an average optical efficiency of 25% for a three-wavelength apochromatic lens whose chromatic focus shift is only 1.3μm and 25μm in the lateral and axial directions. Superachromatic performance over the continuous visible band is also demonstrated, with averaged lateral and axial focus shifts of only 1.65μm and 73.6μm, respectively. These lenses are easy to fabricate using single-step grayscale lithography and can be inexpensively replicated. Furthermore, these devices are thin (< 3μm), error tolerant, have low aspect ratio (< 1:1), and offer polarization-insensitive focusing, all significant advantages compared to alternatives that rely on metasurfaces. Our design methodology offers high design flexibility in numerical aperture and focal length, and is readily extended to 2D.

4.2 Introduction

Recent work has suggested the use of metalenses for broadband achromatic focusing [1]. Here, we show that it is not necessary to invoke concepts of metasurfaces or metalenses to enable such focusing. Scalar diffractive optics, when designed appropriately, can readily enable ultrabroadband achromatic focusing. Such diffractive optics can be far simpler to manufacture and can allow for polarization-independent focusing. An ideal lens focuses one point in the object space to one point in the image space [2]. Almost all imaging systems suffer from chromatic aberrations, which means

that light of different wavelengths generates focal spots at different spatial locations [2]. This phenomenon deteriorates the performance of both imaging [3,4] and nonimaging [5] systems under broadband illumination. For instance, a color camera without chromatic-aberration correction will form spatially displaced and defocused images of the blue, green, and red channels.

Chromatic aberration is due to either the dispersion properties of the material or the structure of the optic. For refractive lenses, longer wavelengths focus at a farther distance, since in most dielectric materials, the refractive index decreases at longer wavelengths. Figure 4.1(a) illustrates the simple example of a bi-convex glass lens and the corresponding shift of its focus, calculated by the Lensmaker's equation [2]. The conventional diffractive lens (zone-plate), on the other hand, exhibits opposite chromatic aberration (Figure 4.1(b)) [6-8]. Diffraction angle is proportional to wavelength [2], and thus longer wavelengths are focused closer than shorter ones.

Chromatic aberration can be corrected approximately by using materials that exhibit complementary dispersion, as in an achromatic doublet and triplet [9-11]. However, this technique is cumbersome, since the number of materials equals the number of wavelengths where the chromatic aberrations are minimized [10,11]. The extra alignment makes these lenses expensive and bulky. Hybrid refractive-diffractive lenses perform slightly better, but their complexity is even higher [12-14]. Such designs that work for more than three wavelengths are seldom studied. An alternative approach is to use a phase-coded aperture [15], but this requires precise polishing of the glass surface. In all these cases, it is challenging to make such corrected lenses with microscale thickness. Ultrathin optic enables ultracompact imaging devices for wearable applications.

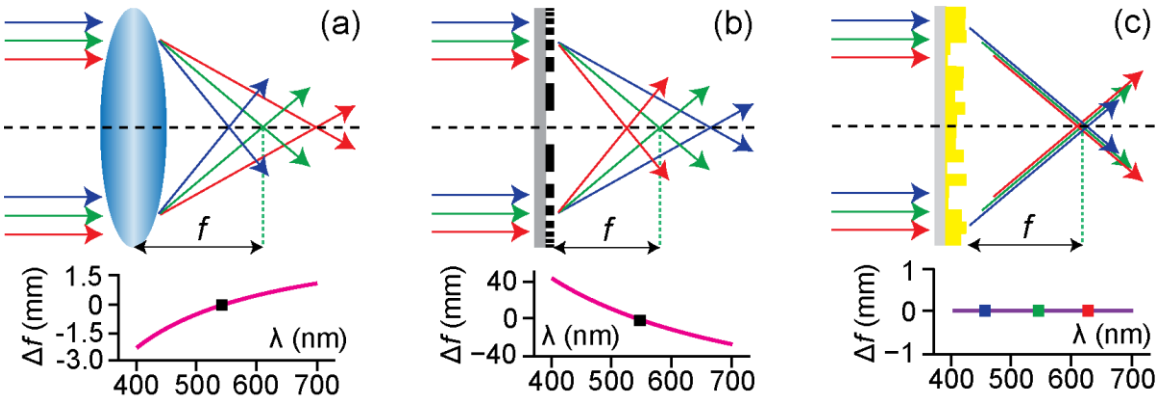

Figure 4.1. Focusing optics with nominal focal length f=120mm at λ=540nm (top row) and their calculated axial chromatic aberration Δf (bottom row). Normally incident uniform illumination is assumed. (a) Bi-convex refractive lens (BK7 glass). (b) Amplitude (binary) zone-plate. (c) Schematic explanation of the superachromatic diffractive lens. Ideally, focus shift over the entire spectrum remains zero.

Metasurfaces exploit surface plasmonic or nanophotonic phenomena to locally impart abrupt phase shift so as to purposely manipulate the diffraction pattern [16,17]. Previous studies showed its potential in anomalous reflection, anomalous refraction, and complex beam generation [16,18,19]. Here, we emphasize that metasurfaces are excellent when the vector properties of light must be manipulated, as in the case of a high-efficiency polarizer [20], but they are not required to manipulate the scalar properties of light. Diffractive optics is a better alternative. The fabrication requirements for metasurfaces are far more stringent in terms of both resolution and precision compared to diffractive optics. Furthermore, metasurfaces are by nature polarization sensitive [1,16-20]. Here, we reiterate that diffractive optics can readily enable broadband focusing, while still maintaining the planar architecture.

Here, we extend the concept of broadband diffractive optics [21-24] to super-achromatic focusing. Specifically, we designed, fabricated, and characterized 4 different planar cylindrical chromatic-aberration-corrected lenses. Each lens has a maximum

thickness of 3μm and a minimum feature size of 3μm. All the devices can be readily patterned using grayscale lithography and inexpensively replicated for mass production using imprint lithography [25,26]. The aberration-correction capabilities of our lenses are on par with or better than commercial doublets. Two types of lenses were constructed. One was designed for three discrete wavelengths, and the other for continuous broadband illumination.

4.3 Working Principles

The cross-sectional schematic of our chromatic-aberration-corrected diffractive lens (CACDL) is illustrated in Figure 4.2(a). The CACDL is composed of pixels that can be square (2D) or linear grooves (1D). In the devices described here, the grooves are of width Δ=3μm, and height, h_i, is assigned to the i^{th} groove. Each groove imparts a relative phase shift given by Equation (2.3). For simplicity, we utilize a positive-tone photoresist, SC1827, deposited on a soda-lime glass substrate as the device material. Again the grayscale lithography tool was employed to rapidly pattern the device in a single step, which is considered a big advantage.

In order to achieve superachromatic performance, we applied a modified direct-binary-search (DBS) algorithm to optimize the distribution of groove heights, h_i [27]. The target point-spread function (PSF) is defined as a diffraction-limited Gaussian with full-width-at-half-maximum (FWHM) determined by $w = \frac{\lambda}{2NA}$. The numerical aperture (NA) is given by $\sin\left(\tan^{-1}(\frac{2f}{L})\right)$, in which $L=N\Delta$ is the total length of the lens, N is the total number of grooves, and f is the design focal length. Compared to other optimization

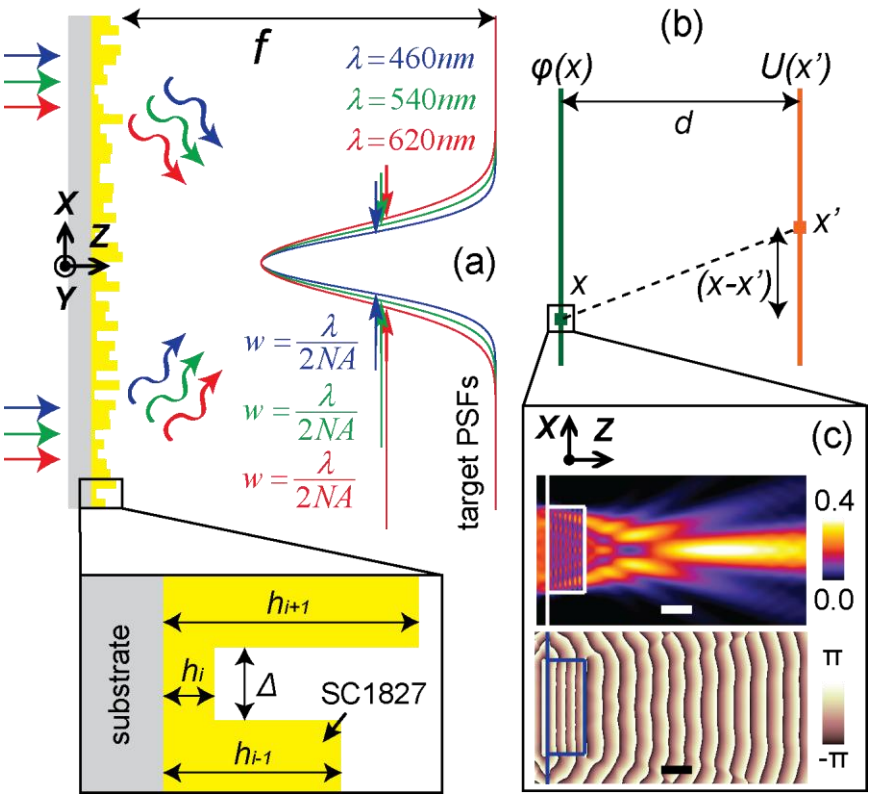

Figure 4.2. (a) Schematic of the chromatic-aberration-corrected diffractive lens (CACDL) with focal length, *f*. Our first set of CACDLs were designed to focus λ=460nm, 540nm and 620nm. The desired light-intensity distributions in the focal plane (or the point-spread functions or PSFs) are dictated by diffraction. This 1D CACDL is composed of linear grooves with a designed height, h_i. SC1827 is the photoresist used for fabricating the CACDL. (b) Illustration of transformation from a CACDL point, *x* to the focus, *x'*. (c) Intensity (top) and phase (bottom) distributions of light (λ=540nm) diffracted by a single groove (width = 3μm, height = 1.2μm, scale bars: 1μm) simulated using FDTD. Linear polarization along X was assumed.

algorithms for multiwavelength diffractive optics [28,29], our technique is applicable generally [20-24] and our approach is the first experimental demonstration of super-achromatic and continuous broadband focusing using diffractive optics.

The diffraction pattern in the focal plane is determined by the phase acquired by light transmitting the diffractive lens (Figure 4.2(c)) and that acquired via the optical path length in air (Figure 4.2(b)). For chromatic-aberration-corrected focusing at *x'*, three or more wavelengths must diffract from location *x* such that they interfere constructively at

the focus, *x'*. Our method for designing the diffractive lens realizes an optimal height distribution that can approximate such constructive interference. In our lens, there are *N* grooves, and each groove can occupy *P* discrete height levels. Therefore, the total degrees-of-freedom can be enormous, P^N. This allows extreme design flexibility, as illustrated later. We designed and fabricated four CACDLs (see Figure 4.3(a)). For each device, we assumed periodic boundaries during design and fabricated 7 periods, each of length *L*=8.4mm. The optical micrographs, profilometer measurements, and the scanning-electron micrographs of exemplary devices are shown in Figures 4.3(b), (c), and (d), respectively. The cross-sectional micrographs of a cleaved sample (Figure 4.3(d)) indicate that the grooves are rounded due to the resolution limitations of our lithography tool. Nevertheless, the average height within each groove was within 100nm of the

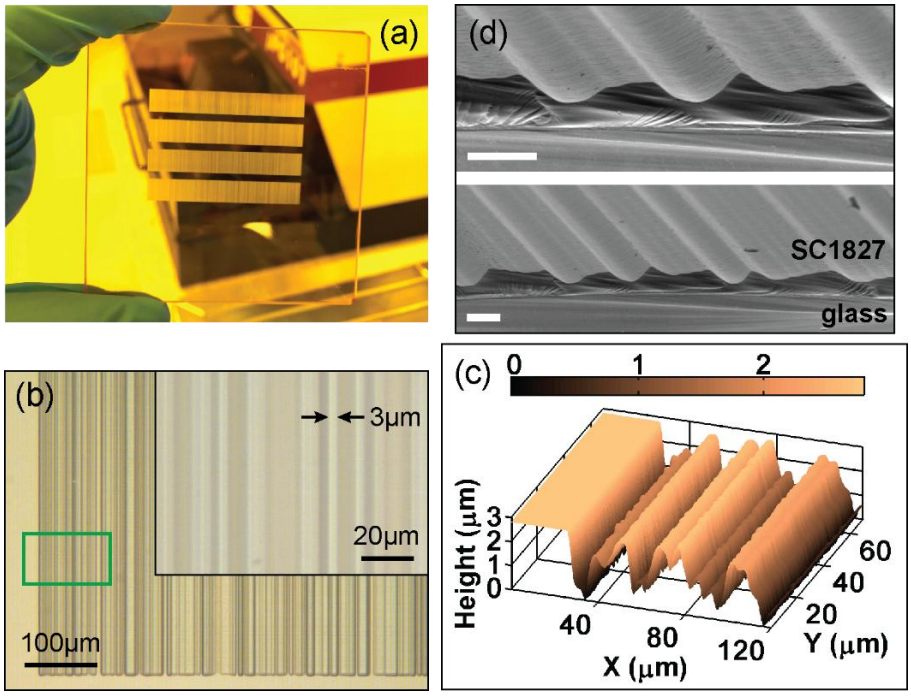

Figure 4.3. (a) Photograph of four CACDLs patterned on a glass substrate. (b) Optical micrograph of a corner of one CACDL. Inset: magnified view. (c) Profilometer image of the region in the green box in (b). The maximum height is ~3μm. (d) Scanning-electron-microscopy images of the cross-sections of two CACDLs (scale bars: 5μm).

design value. It is noteworthy that the maximum aspect ratio is 1:1, which is much smaller than that of the metalenses [1,30]. Furthermore, the lithographic resolution required for our CACDLs is only 3μm (5λ for λ=600nm), compared to ~100nm (0.065λ for λ=1550nm) for the metalenses [1]. To achieve broadband focusing in the visible region with the metalenses, one would require features of size 39nm and aspect ratios of over 3:1.

4.4 Experiments and Results

To experimentally demonstrate chromatic-aberration-corrected focusing, we illuminated each CACDL using a spatially collimated beam from a supercontinuum source (SuperK EXTREME EXW-6) that was first conditioned using a reconfigurable band-pass filter (SuperK VARIA). The filter allowed us to illuminate the CACDL with one discrete wavelength at a time (minimum bandwidth 10nm). Then, a single-mode fiber (SMF, core diameter ~8μm) connected to a spectrometer (Ocean Optics Jaz) was placed in the vicinity of the designed focus. The fiber was scanned using a motorized 2-axis stage with 3μm and 10μm steps along the X' and Z axes, respectively. The transmitted spectra were collected at each location. The final results were derived after subtracting the dark spectrum from the raw data and dividing by the reference spectrum (that transmitted through the unpatterned photoresist). See Figure 2.17 and Equation (2.17) for more details.

First, we consider the CACDLs designed for three discrete wavelengths (460nm, 540nm and 620nm). To demonstrate the flexibility of our approach, we designed 3 different lenses with the following parameters: number of grooves, N=2800, 2800, 280; focal length, f=120mm, 25mm and 10mm, which correspond to numerical aperture,

NA=0.035, 0.166 and 0.042, respectively. Figures 4.4(a)-(i) summarize the simulated and measured light-intensity distributions in the focal plane at the 3 design wavelengths. As expected, all 3 lenses exhibit clear apochromatic focusing. Scalar-diffraction simulations predict average optical efficiencies of 30.0%, 30.4% and 39.0% for the 3 designs. The corresponding measured average optical efficiencies are 24.9%, 23.0% and 21.5%, much higher than those of previously reported achromatic lenses [13]. Even higher efficiency (>50%) is possible with thicker microstructures. In theory, nonideal efficiency (<100%) is primarily due to lack of perfect interference (constructive at focus and destructive in the background). Generally speaking, this efficiency dictates the contrast or resolution in an optical system. Here, we define the optical efficiency as the ratio of power within the region defined by the first zero to the total incident power. We can also quantify the achromaticity of the CACDLs by measuring the lateral and axial focus shifts as a function of wavelength. These can be calculated by comparing the 2D PSF (X'Z plane) at each wavelength to that at the center wavelength, 540nm. The lateral and axial focus shifts for the first design were 0.32μm, 6.7μm (simulation), and 1.3μm, 25μm (experiment), respectively. These are better than what can be achieved using conventional refractive lens combinations [9].

Due to the finite diameter of the SMF core, the measured PSFs are wider than the actual distributions. This is especially obvious in the CACDL with the highest NA (Figures 4.4(d)-(f)). Fabrication errors as well as the limited acceptance angle of the SMF contribute to the reduction of optical efficiencies. The 2D PSFs (X'Z) of the first design at five wavelengths (460nm, 500nm, 540nm, 580nm and 620nm) are plotted in Figures 4.4(j)-(n) (simulation) and Figures 4.4(o)-(s) (measurement).

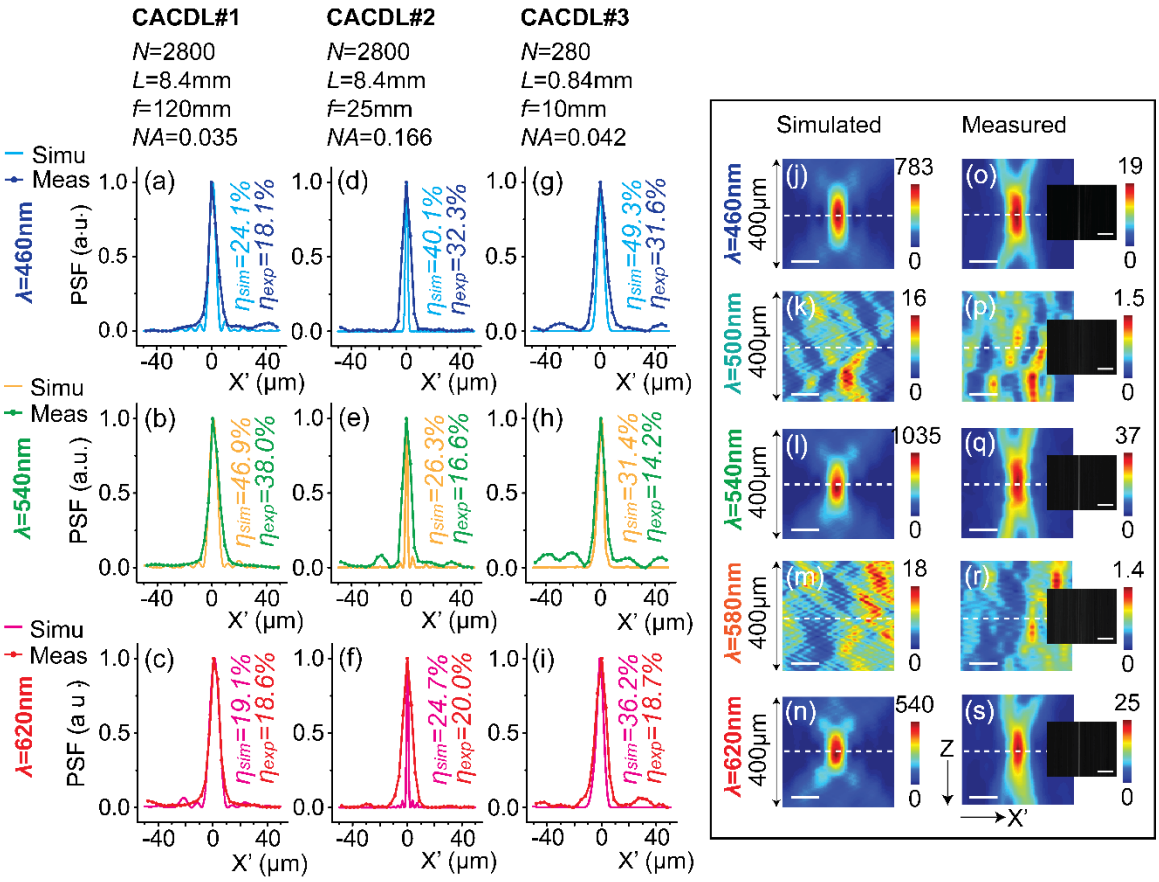

Figure 4.4. CACDLs for 3 discrete wavelengths (apochromats). The simulated and measured point-spread functions (PSFs) at λ=460nm ((a), (d) and (g)), λ=540nm ((b), (e) and (h)) and λ=620nm ((c), (f) and (i)). Each column represents one CACDL. Simulated ((j)-(n)) and measured ((o)-(s)) 2D PSFs of the first design for λ=460nm ((j) and (o)), 500nm ((k) and (p)), 540nm ((l) and (q)), 580nm ((m) and (r)) and 620nm ((n) and (s)) (scale bars: 20μm). Dashed white lines denote the focal plane. Insets: grayscale images of the focal plane captured by a monochrome CMOS camera when illuminated by the discrete wavelengths from the VARIA filter (scale bars: 1mm, exposure time =3ms).

The scalar-diffraction simulation has resolution of 0.2μm and 2.5μm in X' and Z directions. The measured plots are numerically interpolated into the same grid for visual comparison. At the vicinity of the nominal focal plane (white-dashed lines), focusing is clearly observed for only the design wavelengths (460nm, 540nm and 620nm). No focusing is found at the other wavelengths (Figures 4.4(k), (p), (m) and (r)). Another simple proof of apochromatic focusing is seen via the images captured at the focal plane

using a monochrome sensor (DMM22BUC03-ML, The Imaging Source) with illumination wavelength selected by the VARIA filter, shown as insets in Figures 4.4(o)-(s). Note that the SMF-spectrometer scheme was used to accurately measure PSFs (Figures 4.4(a)-(i) and (o)-(s)), since the spectrometer has higher spectral resolution (0.4nm) than the VARIA filter and larger dynamic range (16-bit) than the sensor (8-bit).

Next, we extended our CACDL to focus continuous broadband illumination across the visible spectrum (450nm – 690nm, super-achromatic). This is achieved by increasing the wavelength sampling to 5nm during design. It was designed with N=2500, focal length, f=280mm, and NA=0.013. The simulated and measured 1D PSFs in the design focal plane as a function of wavelength are plotted in Figures 4.5(a) and (b), respectively. Note that the plots are normalized to the peak at each wavelength to account for the spectrum of the source. The white dots (left) and crosses (right) indicate the lateral (Δx) and axial (Δf) focal-spot shifts in each figure. These shifts were obtained from the 2D (X'Z) PSFs. The simulated and measured 2D PSFs at 3 wavelengths are illustrated in Figures 4.5(d)-(f) and Figures 4.5(g)-(i), respectively. Again, the measurements were interpolated into the same resolution as the simulations. The lateral shift averaged over all wavelengths, $\overline{|\Delta x|}$, is 0.47μm (simulation) and 1.65μm (experiment). The axial shift averaged over all wavelengths, $\overline{|\Delta f|}$, is 23.5μm (simulation) and 73.6μm (experiment). Both shifts are significantly smaller than that of a diffractive lens optimized for single wavelength. The maximum axial-focus shift, Δf, is comparable to that of commercial achromatic doublets [9]. However, our CACDL is thin (planar), inexpensive, and composed of only a single material. The optical-efficiency spectrum is plotted in Figure 4.5(c). The discrepancies between the simulated and measured curves are primarily due

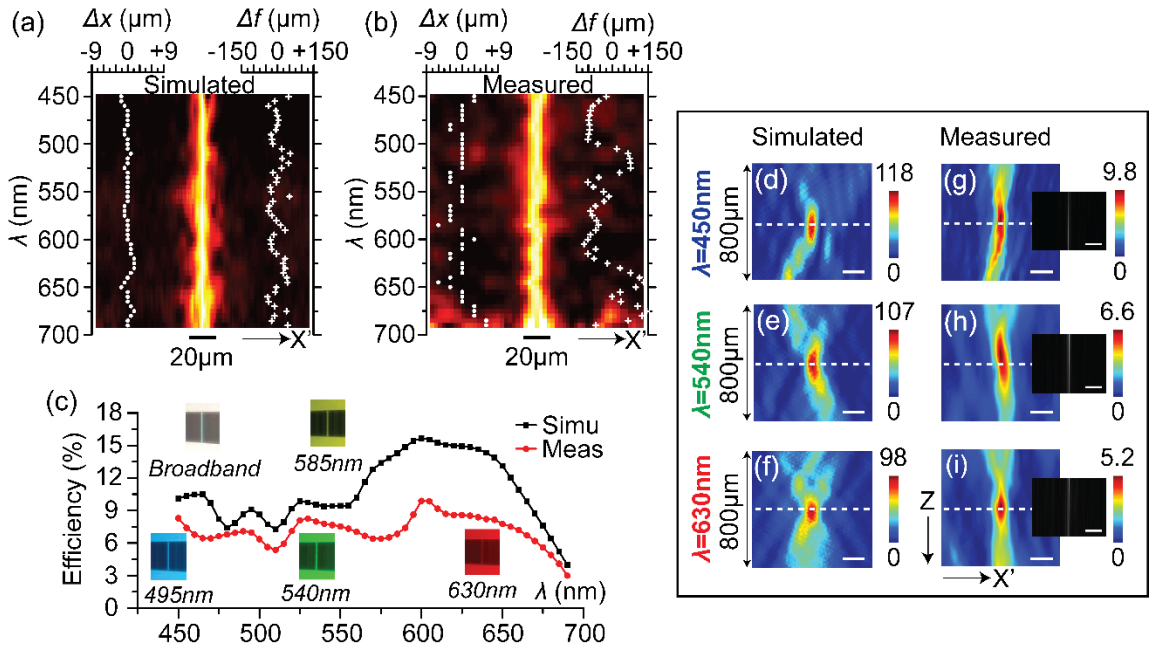

Figure 4.5. CACDL for broadband (450nm to 690nm) focusing (super-achromat). (a) Simulated and (b) measured 1D PSFs as a function of wavelength. Left insets: lateral-focus shift, Δx, versus wavelength (white dots). Right insets: axial-focus shift, Δf, versus wavelength (white crosses). (c) Simulated (black) and measured (red) optical efficiency as a function of wavelength. Insets: photographs of the focus on a white observation screen at various wavelengths. Simulated ((d)-(f)) and measured ((g)-(i)) 2D PSFs for λ=450nm ((d) and (g)), λ=540nm ((e) and (h)) and λ=630nm ((f) and (i)) (scale bars: 30μm). Dashed white lines delineate the focus. Insets: images of the focus captured by a monochrome sensor (scale bars: 1mm). Exposure time t=4ms.

to fabrication errors in the CACDL height profile. The efficiency drops at longer wavelengths. This can be prospectively compensated by appropriately weighting the efficiencies of different wavelengths during design [21] and by optimizing the patterning process. As before, monochrome images illuminated by the 3 wavelengths (selected by the VARIA) are shown as insets in Figures 4.5(g)-(i).

4.5 Discussions

The CACDLs are insensitive to the polarization state of the incident light. This is a strong advantage over metalenses, since most imaging systems require polarization-

independent focusing. To prove this, we illuminated the first CACDL design (from Figure 4.4(a)) with linearly polarized light and observed the focus while the polarization was rotated by 90 degrees. In our nomenclature, the transverse magnetic (TM) refers to electric field polarized along the degenerate direction Y of the CACDL, while the transverse electric (TE) refers to that polarized along the X direction (see inset of Figure 4.6(a)). The measured PSFs for the 3 design wavelengths (Figures 4.6(a)-(c)) are identical for the orthogonal polarizations. Furthermore, finite-difference-time-domain (FDTD) simulations of diffraction by a single groove (Figure 4.6(d)) confirm that both amplitude and phase of the diffracted light are identical for both polarizations. This is expected since the smallest period of the CACDL is 6μm, much larger than the wavelengths of interest.

In all micro-optics, fabrication errors have an important impact on the optical efficiencies. We numerically analyzed this impact by adding random errors with various standard deviations to the design-height distribution. The results plotted in Figure 4.7(a) indicate that the CACDLs are robust to height errors of up to ~100nm, which, in turn, corresponds to two height levels ($\Delta h = H/(P-1) = 50$nm). Therefore, our device is relatively tolerant of fabrication errors, which is consistent with previous devices designed using related techniques [20-24]. As expected, the efficiency decreases with increasing errors (left Y axis in Figure 4.7(a)) and the device with fewer grooves (CACDL#3) is more susceptible to fabrication errors [21,22]. This is because constructive interference gradually breaks down when the phase distribution deviates from the optimal design. Moreover, the wavelength-averaged axial-focus shift, $\overline{|\Delta f|}$, increases with errors (right Y axis in Figure 4.7(a)). For CACDL#1, $\overline{|\Delta f|}$ is maintained small when the error is less

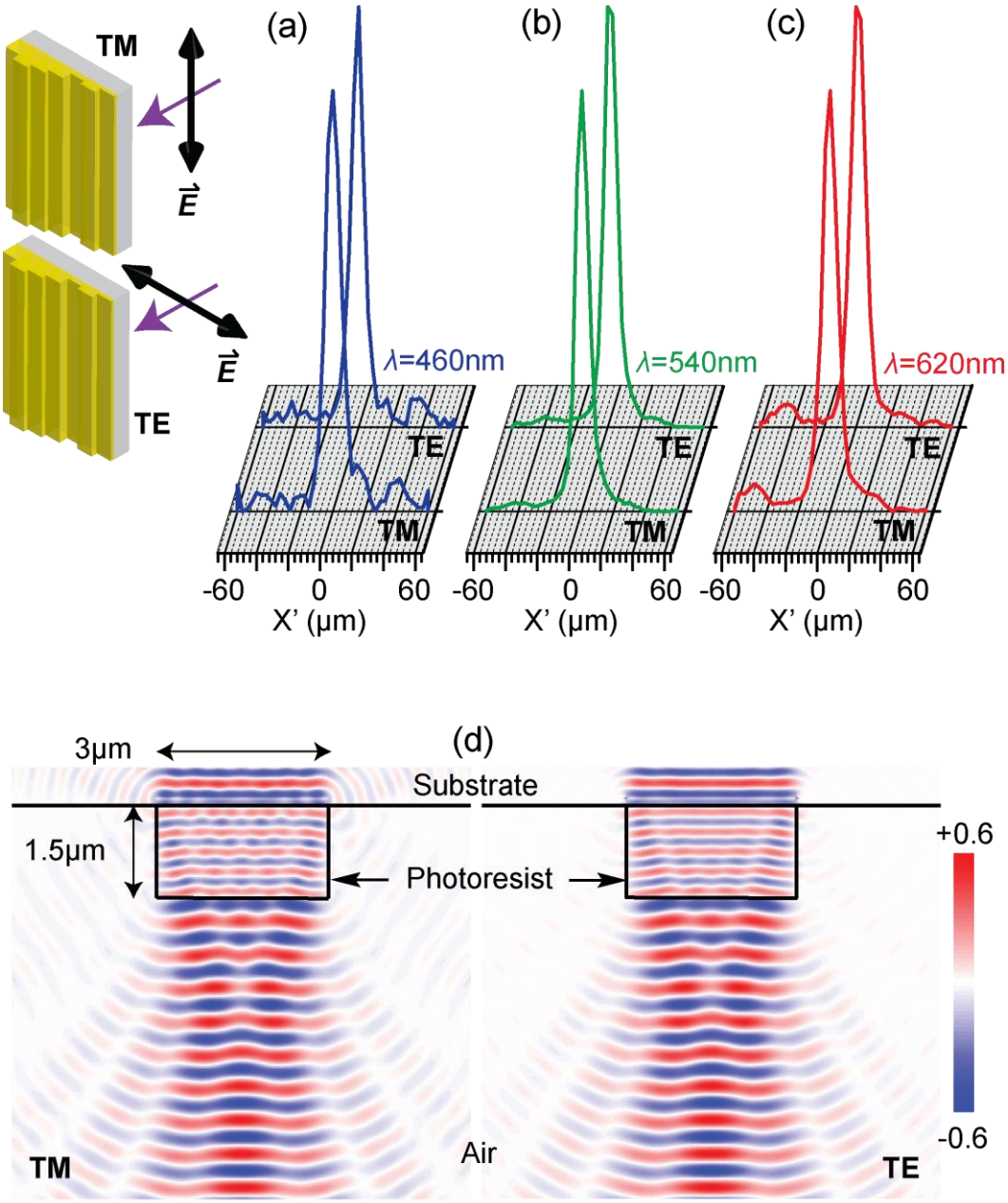

Figure 4.6. Impact of polarization. Measured PSFs of the CACDL#1 at the orthogonal polarizations for (a) λ=460nm, (b) λ=540nm and (c) λ=620nm. Inset: definitions of the incident polarization states. (d) Simulated electric-field distribution of light diffracted from one 3μm-wide and 1.5μm-high photoresist groove for TM (left) and TE (right) polarizations using FDTD.

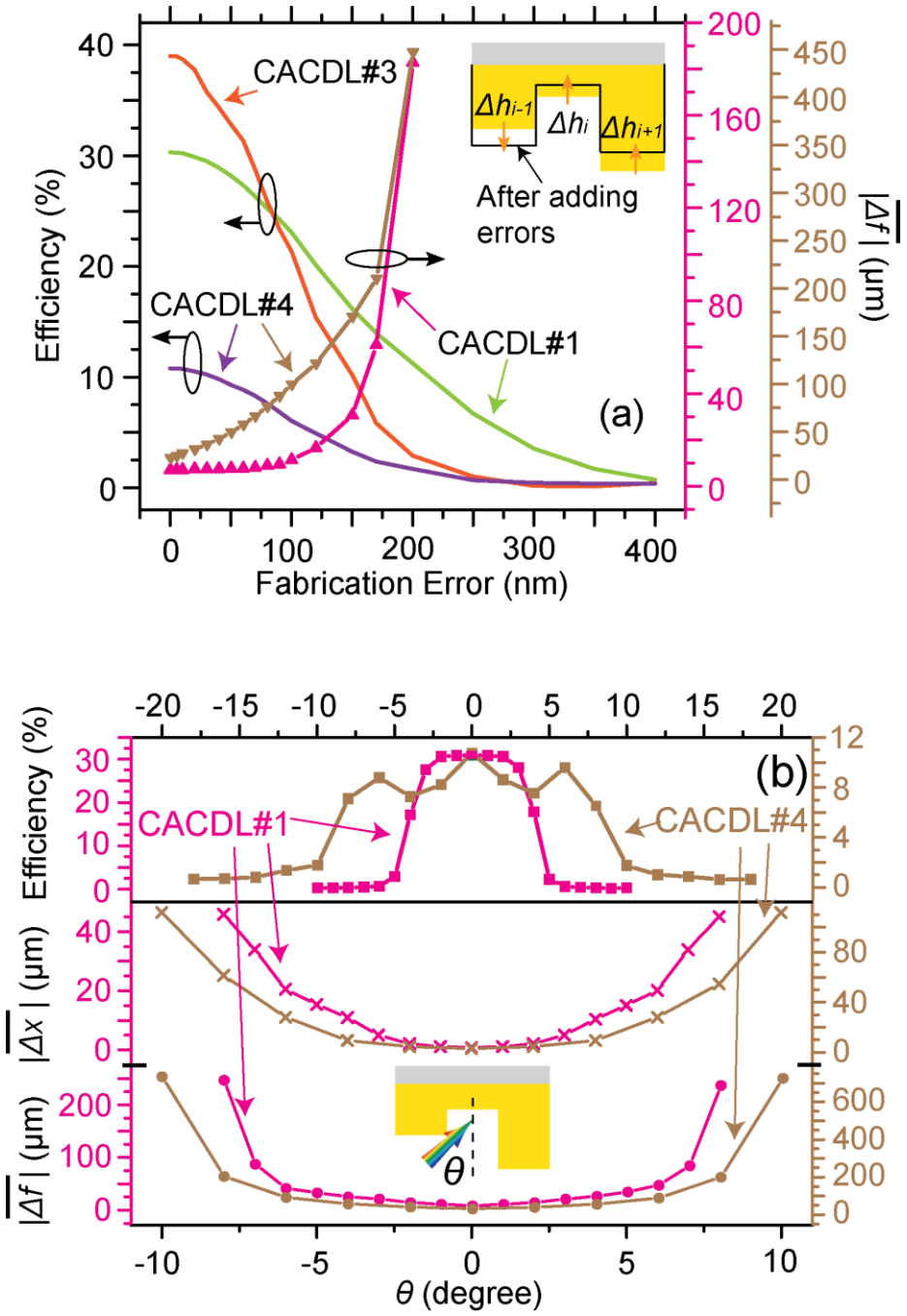

Figure 4.7. Impact of fabrication errors and oblique incidence. (a) Simulated wavelength-averaged optical efficiency (left Y-axis) and wavelength-averaged axial-focus shift (right Y-axis) as a function of fabrication errors. Inset: schematic showing how fabrication errors are applied. (b) Simulated wavelength-averaged optical efficiency (top) and wavelength-averaged lateral-focus shift (middle) and axial-focus shift (bottom) of two CACDLs as a function of the angle of incidence, θ. Middle and bottom panels share the same X coordinates. Inset: definition of θ.

than 100nm, while that of the CACDL#4 deteriorates rapidly. This is likely a consequence of the fact that broadband superachromatic focusing requires a more stringent phase matching compared to focusing only 3 wavelengths.

We also simulated the impact of oblique incidence (Figure 4.7(b)). The wavelength-averaged focus shifts both laterally and axially with change in incident angle, θ. Hence, the wavelength-averaged optical efficiency drops with off-normal incidence (top panel). Nevertheless, both studied CACDLs maintain their efficiencies over $\theta \sim \pm 4^{o}$. The wavelength-averaged lateral-focus shift, $\overline{|\Delta x|}$ (middle panel), and axial-focus shift, $\overline{|\Delta f|}$ (bottom panel), increase nonlinearly with θ. However, both designs preserve reasonable chromatic aberrations over $\theta \sim \pm 4^{o}$. Note that even though we assumed periodic boundaries during design, experiments suggest that this is not strictly necessary, as elaborated in the Supplementary Materials. Finally, although our devices were 1D, they can be readily extended to 2D [20,22,23] and also to any electromagnetic spectrum.

4.6 Supplementary Information

4.6.1 Figure-of-merit

The FOM considered in optimization is defined by

$$FOM = \frac{\sum_{i=1}^{N} \omega_i \cdot \mu_i}{N} - 10 \cdot \frac{\sum_{i=1}^{N} \omega_i \cdot \varepsilon_i}{N}. \tag{4.1}$$

The first term represents weighted efficiency averaged over totally N wavelengths. The second term is the weighted normalized absolute difference (between the simulated and the target functions) over N wavelengths. A factor 10 is introduced to balance these two

terms. The weighting coefficients ω_i balance contributions from different wavelengths. Proper selection of this group of parameters is critical to achieve the optimal solution.

The efficiency μ_i and the normalized absolute difference ε_i in Equation (4.1) are

$$\mu_i = \frac{\int_{x'_{\min}}^{x'_{\max}} I_i(x') \cdot T_i(x') dx'}{\int_{x'_{\min}}^{x'_{\max}} I_i(x') dx'} . \tag{4.2}$$

$$\varepsilon_i = \frac{\int_{x'_{\min}}^{x'_{\max}} \left| normalize(I_i(x')) - T_i(x') \right| dx'}{\int_{x'_{\min}}^{x'_{\max}} dx'} . \tag{4.3}$$

Here, $I_i(x')=|U(x',\lambda)|^2$ is simulated light intensity along X' direction at the image plane for the i^{th} wavelength. $T_i(x')$ is the target function for the i^{th} wavelength. x'_{min} and x'_{max} delimit the integration range from the leftmost to the rightmost of the CACDL design.

As the first-order approximation of a focusing PSF, the target function is defined as a Gaussian function centered at $(x'_{min} + x'_{max})/2$ with full-width-at-half-maximum (FWHM) W_i determined by the far-field diffraction limit:

$$T_i(x') = \exp\left\{ -\frac{\left[x' - \left(\frac{x'_{\min} + x'_{\max}}{2} \right) \right]^2}{\left(\frac{W_i}{2}\right)^2} \right\}. \tag{4.4}$$

$$W_i = \frac{\lambda_i}{2 \cdot NA}. \tag{4.5}$$

$$NA = \sin\left[\tan^{-1}\left(\frac{L_X/2}{f} \right) \right]. \tag{4.6}$$

In Equations (4.4) – (4.6), λ_i is the i^{th} wavelength. L_X is the total length of the CACDL design in X direction, and f is the designed focal length (gap between the CACDL and the image plane). Three $T_i(x')$ examples for λ_1=460nm, λ_2=540nm and λ_3=620nm are plotted in Figure 4.2(a).

4.6.2 Optimized CACDL designs

The height profiles of the optimized CACDL designs are plotted in Figure 4.8. CACDL#1 has 2800 3μm-wide grooves for focusing at 120mm. CACDL#2 has 2800 3μm-wide grooves for focusing at 25mm. CACDL#3 has 280 3μm-wide grooves for focusing at 10mm. CACDL#4 has 2500 3μm-wide grooves for focusing at 280mm. CACDL#1-#3 are designed for three discrete wavelengths, 460nm, 540nm, and 620nm, while CACDL#4 is designed for broadband spectrum from 450nm to 690nm.

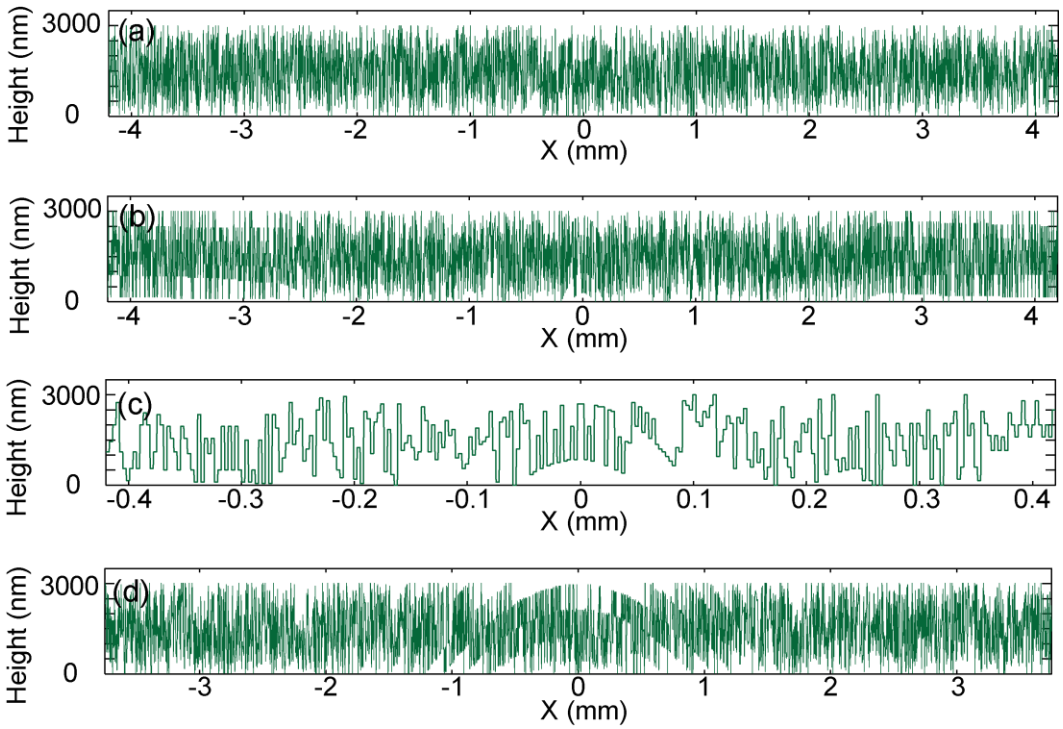

Figure 4.8. Optimized height profiles of the CACDL designs: (a) CACDL#1; (b) CACDL#2; (c) CACDL#3; (d) CACDL#4.

4.6.3 Effect of the number of CACDL periods

The multiwavelength PSFs of the CACDL#1 design are measured when the fabricated device is illuminated by different beam dimensions, adjusted by an iris. The effect of the number of CACDL periods is tested with 0.5, 1, 2, 3, 4, and 5 periods along the X direction. The optical efficiencies start to drop when the number of periods is fewer than 2 (Figure 4.9(a)). However, the efficiencies still remain reasonably high when the beam size only covers one CACDL period. In addition, the PSFs at three designed

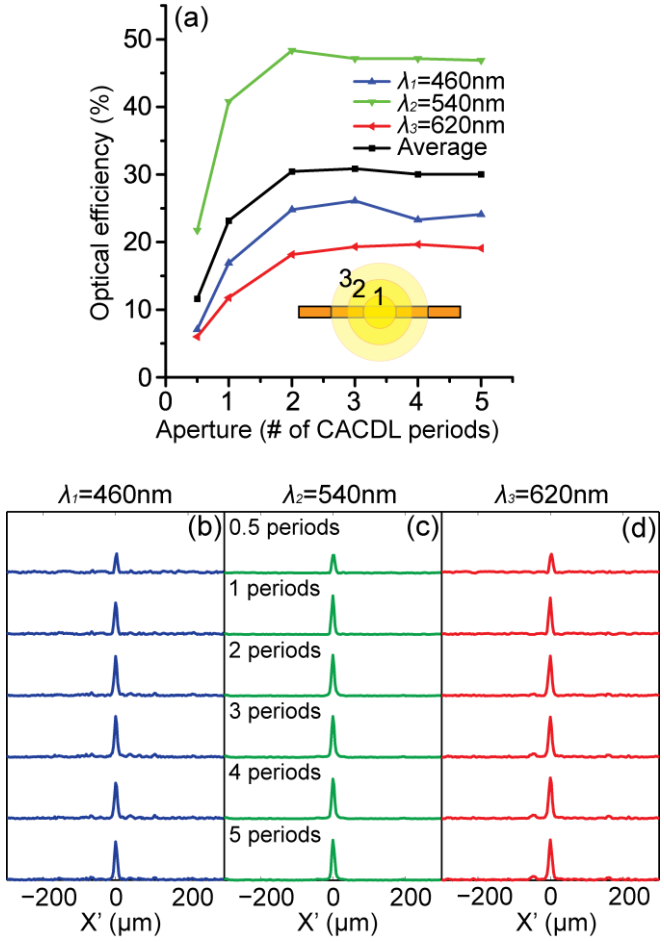

Figure 4.9. (a) Measured optical efficiencies when CACDL#1 is illuminated by a beam covering different numbers of CACDL periods. Inset: schematic of different beam sizes covering different number of CACDL periods. Measured PSFs at *f*=120mm when the CACDL is illuminated by different beam dimensions for wavelengths of (b) 460nm, (c) 540nm and (d) 620nm. Only the X'=-300μm to X'=300μm segment is displayed here.

wavelengths do not experience any obvious lateral shifts for the 0.5-5 range of the number of the CACDL periods (Figures 4.9(b)-(d)). This indicates that periodic padding is good but not necessary for our CACDL designs to work properly. This, on the other hand, gives us confidence to design a single diffractive lens without assuming periodicity.

4.6.4 Effect of refractive index measurement error

A Woollam Spectroscopic Ellipsometer is used to measure the refractive index of the CACDL material (SC1827) at different wavelengths. However, this measurement may experience some errors, leading to compromised CACDL performances since the phase shift imparted by the microstructure at wavelength λ is a function of refractive index $n(\lambda)$. Figure 4.10 numerically studies this effect, demonstrating that the devices are relatively tolerant of this measurement error. Within the ±0.1 error (equivalent to 1.6~1.8 range for a true value n=1.7), the average optical efficiencies remain acceptably high and the averaged absolute lateral focal spot shifts are still strongly suppressed.

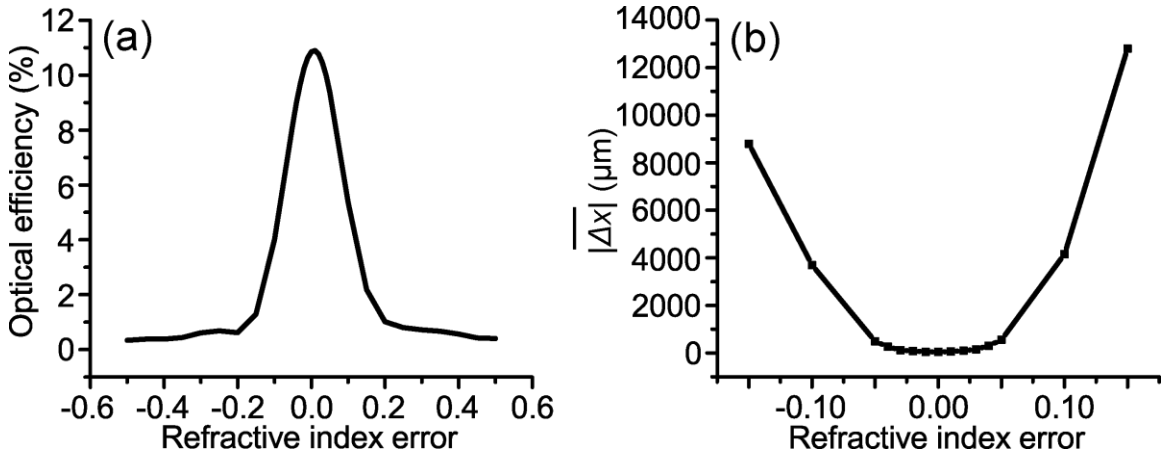

Figure 4.10. Numerical studies on the effect of the refractive index measurement errors (CACDL#4): (a) plot of the average optical efficiencies versus different refractive index errors (from -0.5 to +0.5); (b) plot of the averaged absolute lateral focal spot shifts versus different refractive index errors (from -0.5 to +0.5).

4.6.5 Ultrahigh-efficiency CACDL design

Figure 4.11 summarizes the simulation results of a CACDL with much higher optical efficiency by increasing the aspect ratio of the microstructure from 1:1 to 3.3:1 and increasing the number of grooves from 2800 to 4000. The device still has groove width of Δ=3μm, but the maximum height is increased to H=10μm and totally 201 quantization levels with unit height of 50nm. Note that such an aspect ratio is currently not practical, but it is used simply for proof-of-principle demonstration.

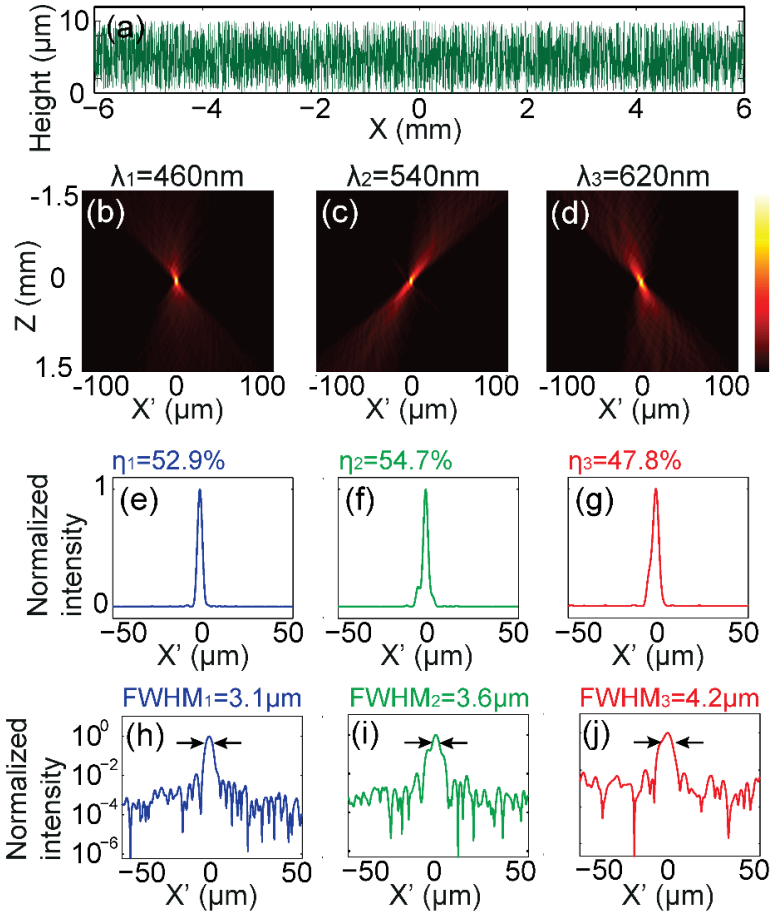

Figure 4.11. (a) Height profile of the ultrahigh-efficiency design. Inset: the magnified view of the first 0.3mm-long section. Simulated intensity distributions along propagation from X'=-100μm to X'=+100μm for λ=460nm (b), 540nm (c), and 620nm (d). Linear-scale plots of the focal spots at the focal plane from X'=-50μm to X'=+50μm for λ=460nm (e), 540nm (f), and 620nm (g). Logarithm-scale plots of the focal spots at the focal plane for λ=460nm (h), 540nm (i), and 620nm (j).

For simplicity, the CACDL was optimized for three discrete wavelengths (λ=460nm, 540nm, and 620nm). The designated focal length is f=80mm (NA=0.075). One period of CACDL is 12mm long in the X direction. The light intensity distributions along propagation (Z direction) are shown in Figures 4.11(b) – (d). Note that z=0 is the nominal focal plane and only the central part from X'=-100μm to X'=+100μm is shown for clarity. The optical efficiencies are 52.9%, 54.7%, and 47.8% at each of three wavelengths, respectively. The average efficiency is 51.8%. The FWHMs of the focal spots are 3.1μm, 3.6μm, and 4.2μm, respectively.

4.7 References

[1] F. Aieta, M. A. Kats, P. Genevet, and F. Capasso, "Multiwavelength achromatic metasurfaces by dispersive phase compensation," Science **347**, 1342-1345 (2015).

[2] M. Born, and E. Wolf, *Principles of Optics: Electromagnetic Theory of Propagation, Interference and Diffraction of Light* (Cambridge University Press, 1999).

[3] F. W. Campbell, and R. W. Gubisch, "The effect of chromatic aberration on visual acuity," J. Physiol. **192**, 345-358 (1967).

[4] P. Ruffieux, T. Scharf, H. P. Herzig, R. Volkel, and K. J. Weible, "On the chromatic aberration of microlenses," Opt. Express **14**, 4687-4694 (2006).

[5] E. Lorenzo, "Chromatic aberration effect on solar energy systems using Fresnel lenses," Appl. Opt. **20**, 3729-3732 (1981).

[6] R. Menon, A. Patel, D. Gil, and H. I. Smith, "Maskless lithography," Materials Today **8**, 26-33 (2005).

[7] H-Y. Tsai, H. I. Smith, and R. Menon, "Reduction of focal-spot size using dichromats in absorbance modulation," Opt. Lett. **33**, 2916-2918 (2008).

[8] X. Wan, B. Shen, and R. Menon, "Diffractive lens design for optimized focusing," J. Opt. Soc. Am. A **31**, B27-B33 (2014).

[9] Thorlabs, Unmounted Achromatic Doublets, AR Coated: 400-700nm. (2015) Available at: http://www.thorlabs.us/newgrouppage9.cfm?objectgroup_id=120 .

[10] A. Miks, and J. Novak, "Superachromatic air-spaced triplet," Appl. Opt. **53**, 6930-6937 (2014).

[11] Y-C. Fang, C-M. Tsai, J. MacDonald, and Y-C. Pai, "Eliminating chromatic aberration in Gauss-type lens design using a novel genetic algorithm," Appl. Opt. **48**, 2401-2410 (2007).

[12] N. Davidson, A. A. Friesem, and E. Hasman, "Analytic design of hybrid diffractive-refractive achromats," Appl. Opt. **32**, 4770-4774 (1993).

[13] A. Flores, M. R. Wang, and J. J. Yang, "Achromatic hybrid refractive-diffractive lens with extended depth of focus," Appl. Opt. **43**, 5618-5630 (2004).

[14] P. Valley, N. Savidis, J. Schwiegerling, M. R. Dodge, G. Peyman, and N. Peyghambarian, "Adjustable hybrid diffractive/refractive achromatic lens," Opt. Express **19**, 7468-7479 (2011).

[15] H. B. Wach, E. R. Dowski, and W. T. Cathey, "Control of chromatic focal shift through wave-front coding," Appl. Opt. **37**, 5359-5367 (1998).

[16] N. Yu, P. Genevet, M. A. Kats, F. Aieta, J-P. Tetienne, F. Capasso, and Z. Gaburro, "Light propagation with phase discontinuities: generalized laws of reflection and refraction," Science **334**, 333-337 (2011).

[17] A. V. Kildishev, A. Boltasseva, and V. M. Shalaev, "Planar photonics with metasurfaces," Science **339**, 1232009 (2013).

[18] F. Aieta, P. Genevet, N. Yu, M. A. Kats, Z. Gaburro, and F. Capasso, "Out-of-plane reflection and refraction of light by anisotropic optical antenna metasurfaces with phase discontinuities," Nano Lett. **12**, 1702-1706 (2012).

[19] X. Ni, A. V. Kildishev, and V. M. Shalaev, "Metasurface holograms for visible light," Nat. Commun. **4**:2807 1-6 (2013).

[20] B. Shen, P. Wang, R. Polson, and R. Menon, "An ultra-high efficiency metamaterial polarizer," Optica **1**, 356-360 (2014).

[21] P. Wang, J. A. Dominguez-Caballero, D. J. Friedman, and R. Menon, "A new class of multi-bandgap high-efficiency photovoltaics enabled by broadband diffractive optics," Prog. Photovolt: Res. Appl. **23**, 1073-1079 (2015).

[22] G. Kim, J. A. Dominguez-Caballero, and R. Menon, "Design and analysis of multi-wavelength diffractive optics," Opt. Express **20**, 2814-2823 (2012).

[23] P. Wang, and R. Menon, "Optical microlithography on oblique and multiplane surfaces using diffractive phase masks," J. Micro/Nanolith. MEMS MOEMS **14**, 023507

(2015).

[24] P. Wang, and R. Menon, "Computational spectrometer based on a broadband diffractive optic," Opt. Express **22**, 14575-14587 (2014).

[25] M. D. Galus, E. Moon, H. I. Smith, and R. Menon, "Replication of diffractive-optical arrays via photocurable nanoimprint lithography," J. Vac. Sci. Technol. B **24**, 2960-2963 (2006).

[26] L. J. Guo, "Recent progress in nanoimprint technology and its applications," J. Phys. D: Appl. Phys. **37**, R123-R141 (2004).

[27] P. Wang, and R. Menon, "Optimization of periodic nanostructures for enhanced light-trapping in ultra-thin photovoltaics," Opt. Express **21**, 6274-6285 (2013).

[28] W. H. Welch, J. E. Morris, and M. R. Feldman, "Iterative discrete on-axis encoding of radially symmetric computer-generated holograms," J. Opt. Soc. Am. A **10**, 1729-1738 (1993).

[29] T. R. M. Sales, and D. H. Raguin, "Multiwavelength operation with thin diffractive elements," Appl. Opt. **38**, 3012-3018 (1999).

[30] S. W. Kim, K. J. Yee, M. Abashin, L. Pang, and Y. Fainman, "Composite dielectric metasurfaces for phase control of vector field," Opt. Lett. **40**, 2453-2456 (2015).

CHAPTER 5

MICROLITHOGRAPHY ON OBLIQUE AND MULTIPLANE SURFACES

This chapter is adapted from the author's previous publication: Peng Wang and Rajesh Menon, "Optical microlithography on oblique and multiplane surfaces using diffractive phase masks," J. Micro/Nanolith. MEMS MOEMS **14**, 023507 (2015).

5.1 Abstract

Micropatterning on oblique and multiplane surfaces remains a challenge in microelectronics, microelectromechanics, and photonics industries. In this chapter, we describe the use of numerically optimized diffractive phase masks to project microscale patterns onto photoresist-coated oblique and multiplane surfaces. Intriguingly, we were able to pattern a surface at 90 degrees to the phase mask, which suggests the potential of our technique to pattern onto surfaces of extreme curvature. Further studies show that mask fabrication error of below 40nm suffices to conserve pattern fidelity. A resolution of 3μm and a depth of focus of 55μm are essentially dictated by the design parameters, the mask generation tool and the exposure system. The presented method can be readily extended for simple and inexpensive 3D micropatterning.

5.2 Introduction

Microstructures on oblique and nonplanar surfaces enable unique functionalities in photonics [1,2], electronics [3], and microelectromechanics [4,5], and provide a broad array of interesting applications in high-gain antennas [6], radio-frequency identification (RFID) devices [7], metamaterials [8], and transformation optics [9]. For instance, combining diffractive microstructures atop a curved refractive surface can minimize aberrations in lenses in a more compact way than the conventional methods by adaptive optics [10]. In addition, micropatterning on the sidewalls of implantable neural probes could potentially lead to an effective approach for recording 3D neural signals [11,12]. Meanwhile, shape modification in the vertical direction of microfluidic channels and 3D integration of multiple microfluidic channels may significantly enhance their performances [5,13].

Optical projection lithography (OPL) on planar silicon substrates is the workhorse of the semiconductor industry due to its high throughput, resolution, and accuracy [14]. In OPL, a photomask pattern is imaged with demagnification onto a planar photoresist layer that coats the silicon substrate. In general, it is difficult to utilize OPL to pattern nonplanar or oblique surfaces due to the limitations of the imaging optics. These limitations can be avoided by lens-less lithography that utilizes computer-generated holograms to project patterns directly onto the photoresist surface [15]. Thus far, these approaches only project the pattern onto a single plane surface. In this chapter, we extend this technique by designing diffractive optics that can manipulate the intensity of light in 3-dimensional space and thereby allow for patterning onto nonplanar and oblique surfaces. An alternative approach for lithography on nonplanar and oblique surfaces is to utilize a flexible template that contains a master pattern and apply this template conformally over the substrate. The pattern may be transferred via an imprint process [16-18] or simply by exposure to ultra-violet (UV) light through the template [19]. These approaches require contact with the substrate surface, which increases the potential for damage, increases defects, and reduces yield. Furthermore, these approaches perform well only for surfaces of small curvature since conformal contact is necessary. In contrast, our approach can be applied to surfaces of extreme curvature, as illustrated by the patterning of a substrate that is placed orthogonal to the diffractive mask.

5.3 Lithography Principles

Our approach was schematically explained in Figure 2.2. A spatially collimated, temporally coherent uniform UV beam illuminates the mask. The sample to be exposed is placed at a specified distance behind the mask, where the light intensity distribution in 3

dimensions is controlled. The mask is designed using an enhanced direct-binary-search (DBS) algorithm [20-28] where the optimization objective is to maximize intensity within prescribed patterns in multiple planes or within a 3D volume. In addition, the intensity uniformity within the target image has to be taken into account. Note that in optical lithography, the (positive-tone) photoresist serves as a nonlinear recording medium, where regions receiving energy higher than a threshold are selectively dissolved away in a developer. Hence, the mask only needs to ensure that the desired regions receive energy (which corresponds to light intensity multiplied by the exposure time) above a certain threshold (defined by the sensitivity of the photoresist at the exposure wavelength). The resulting mask is composed of an array of discrete pixels, either in one dimension (along X direction) or two dimensions (on XY plane), where each pixel in the array applies a phase shift to incident light. This resembles a traditional computer-generated-hologram (CGH), which is usually exploited to generate a complex beam or image [29]. The phase shift of each pixel is controlled during optimization. The array of optimal phase shifts is implemented as an array of pixels with varying heights, which are uniformly quantized by a unit height Δh. In its 1D form, Δx denotes its uniform pixel size. The diffractive mask was fabricated into a polymer layer (Shipley 1813) using grayscale lithography [21,22,26,30]. The pixels are again of size 3μm, constrained by the resolution of the tool. The maximum thickness of the polymer layer H (and hence, of each pixel in the array) was chosen so as to achieve the maximum phase shift of 2π: $H = \lambda / (n - 1)$, in which 1 is the refractive index of vacuum, in absence of the polychromat pixel. For a polymer refractive index of 1.76 and illumination wavelength of 325nm, this corresponded to 430nm.

Two mask designs in 1D (Figures 5.1(a) and (b)) and 2D (Figures 5.1(c) and (d)) were optimized. The light intensity patterns at multiple planes (or in 3D volume) U'(x',y',d) can be derived based on the transmission function of the mask T(x,y), which describes phase modulation (see Section 2.1). In the 1D case, the desired patterns are three groups of periodic lines. Linewidths of 30μm, 90μm, and 60μm and spacings of 60μm, 180μm, and 120μm are designated at $z=d_1=d_0$=80mm, $z=d_2=d_0+\Delta d$=81mm, and $z=d_2=d_0+2\Delta d$=82mm, respectively (see Figure 5.1(b)). The mask is LX=3mm long (1000 pixels). Each pixel is quantized into 32 levels so that Δh=13.9nm. The 2D target patterns are 'U', 'T', 'A' and 'H' letters separated by a gap of Δd=0.3mm with an initial distance of d_0=5mm (see Figure 5.1(d)). 18μm-wide lines are used to draw the patterns. Since they are periodic, each unit cell has dimension of LX×LY=180μm×180μm (60×60 pixels). The 2D phase mask has square pixel with $\Delta x=\Delta y$=3μm and unit height of Δh=6.8nm (64 levels). Ridges in Figure 5.1(b) and red parts in Figure 5.1(d) stand for places to be exposed in positive-tone photoresist.

5.4 Exposure Results

In Figure 5.2, the 1D diffractive phase mask was designed to project three groups of lines of varying widths and spacings onto three planes positioned at z=80mm, 81mm, and 82mm, respectively. Since this set of patterns has no variations in the Y direction, they could be exposed onto a plane tilted at 45^{o}, instead of three exposures at three planes. In this way, it is also possible to record all the intensity patterns along the Z direction. The optimized phase mask topography is plotted in Figure 5.2(b). Figure 5.2(c) shows an optical micrograph of the fabricated mask along with an atomic-force micrograph of the region delimited by the black rectangle. The simulated light intensity in the X'Z plane

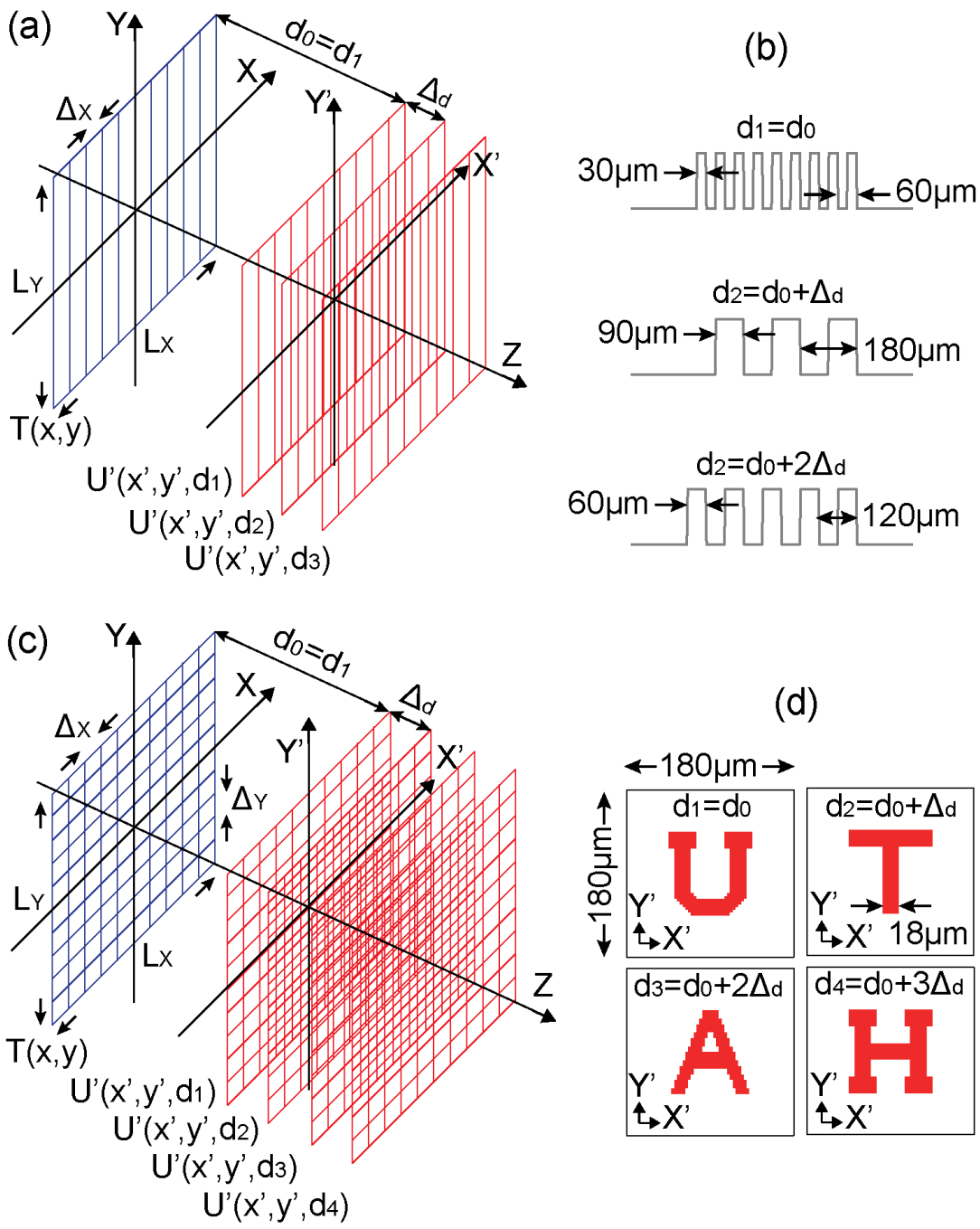

Figure 5.1. Schematic of microlithography on multiple planes by a 1D mask (a) and a 2D mask (c). Intensity distributions U' are generated at distances separated by Δ*d*. (b) Target exposure images at three planes. (d) Target exposure images with 180μm×180μm period at four planes. Linewidth is 18μm.

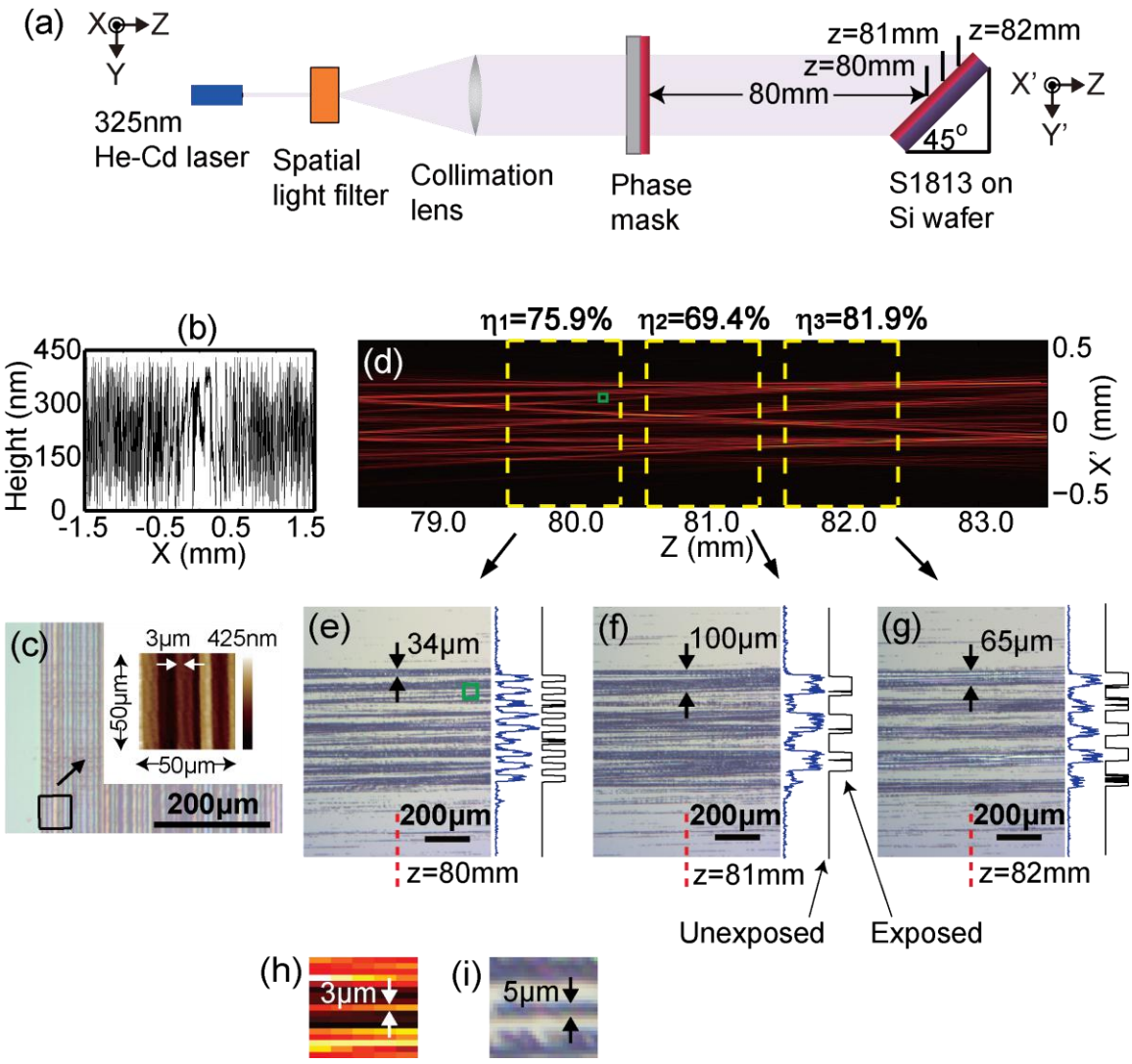

Figure 5.2. Lithography on a 45° tilted surface. (a) Schematic of the exposure setup. (b) Height profile of the optimized 1D phase mask. (c) Optical microscope image of one edge of the fabricated phase mask (inset: AFM measurement of a 50μm×50μm region, and Δ*x*=3μm pixel size is labeled). (d) Simulated intensity distribution in the X'Z plane, where Z is the direction of light propagation. Optical efficiencies at three planes are given. (e)-(g) Optical micrographs of the exposed and developed results at three regions enclosed by yellow blocks in (d). Measured linewidths at (e) *z*=80mm, (f) z=81mm and (g) z=82mm are 34μm, 100μm, and 65μm, respectively. Blue lines are simulated intensity distributions at three planes and black lines represent the estimated exposure outcomes by applying a proper threshold to the simulated patterns. (h) and (i) Magnified views of small areas delimited by the green boxes in (d) and (e), respectively. The labeled 3μm line in (h) is experimentally measured 5μm.

from z=78.5mm to z=83.5mm is shown in Figure 5.2(d). At the design planes corresponding to z=80mm, 81mm, and 82mm, the patterns corresponding to 9 lines (period=60μm), 3 lines (period=180μm), and 5 lines (period=120μm), respectively, are clearly visible. The optical efficiency, η, in one plane is defined as the ratio of the energy within the desired pattern to the total energy incident on the mask. The calculated optical efficiencies are denoted in the figure. The samples for lithography were silicon wafers coated with a 1.3μm-thick photoresist (Shipley 1813) and mounted on a holder that was placed at 45^o to the optical axis. The illumination power density at the mask plane was 0.635mW/cm^2, and the exposure time was 90s. The sample was developed in 352 developer for 60s. Optical micrographs of the patterns corresponding to the regions close to the planes at z=80mm, 81mm, and 82mm (rectangular blocks of yellow-broken lines in Figure 5.2(d)) are shown in Figures 5.2(e), (f), and (g), respectively. Excellent agreement with the simulation results is seen. The linewidths at three z positions (80mm, 81mm and 82mm) are 34μm, 100μm, and 65μm, respectively, which indicates deviation of +4μm, +10μm, and +5μm. These errors, together with the undesired exposures outside the designated line regions, are partially ascribed to overexposure. The simulated light intensity at three positions are plotted as blue lines beside the micrographs in Figures 5.2(e)-(g). By applying a proper threshold, it is possible to achieve clean lines with accurate widths and suppressed noises (black lines). Later numerical analysis will show how fabrication errors affect the exposure results. Additionally, a simulated 3μm line (Figure 5.2(h) representing the green box in Figure 5.2(d)) was measured roughly 5μm wide by exposure (Figure 5.2(i) representing the green box in Figure 5.2(e)). The slight difference is due to overexposure of the photoresist and the resolution of microscopy.

In the next experiment, another mask was designed to project 4 letters ‘U’, ‘T’, ‘A’ and ‘H’, onto X’Y’ planes corresponding to *z*=5mm, 5.3mm, 5.6mm, and 5.9mm, respectively, as illustrated in Figure 5.3(a). Figure 5.3(b) gives the topography of the designed mask. An optical micrograph of the fabricated mask along with an atomic-force micrograph of a small region is shown in Figure 5.3(c). Simulated light intensity distributions in the X’Y’ planes at the four planes are plotted in Figures 5.3(d)-(g). The corresponding optical efficiencies are also denoted in the figures. The measured optical intensity at the mask plane was 0.734mW/cm^2, and the sample was exposed for 52s. Optical micrographs of the corresponding exposed and developed patterns are shown in Figures 5.3(h)-(k). The experimental results agree very well with the simulation predictions. 21μm, 20μm, and 19μm widths are obtained for the 18μm lines by measurements. Arrays of the patterned letters are given by microscope images in Figures 5.3(l)-(o). The noise present in the exposure results in Figures 5.3(d)-(g) is likely due to both overexposure and mask fabrication errors. Figures 5.3(p) and (q) show the exposure patterns predicted by implementing high (critical exposure) and low (overexposure) thresholds to the simulated light intensity distributions in Figures 5.3(d)-(g). Compared to Figure 5.3(p), Figure 5.3(q) clearly includes more noise and approaches the experimental results in Figures 5.3(h)-(k) with better accuracy.

In a third experiment, the sample substrate was placed orthogonal to the diffractive mask as illustrated in Figure 5.4(a). For simplicity, the same phase mask as in Figure 5.3 was used. The simulated light intensity distribution in the X’Z plane is shown in Figure 5.4(c) and the optical micrograph of the exposed and developed pattern is shown in Figures 5.4(d) and (e). The pattern corresponds to the lower part of the four characters,

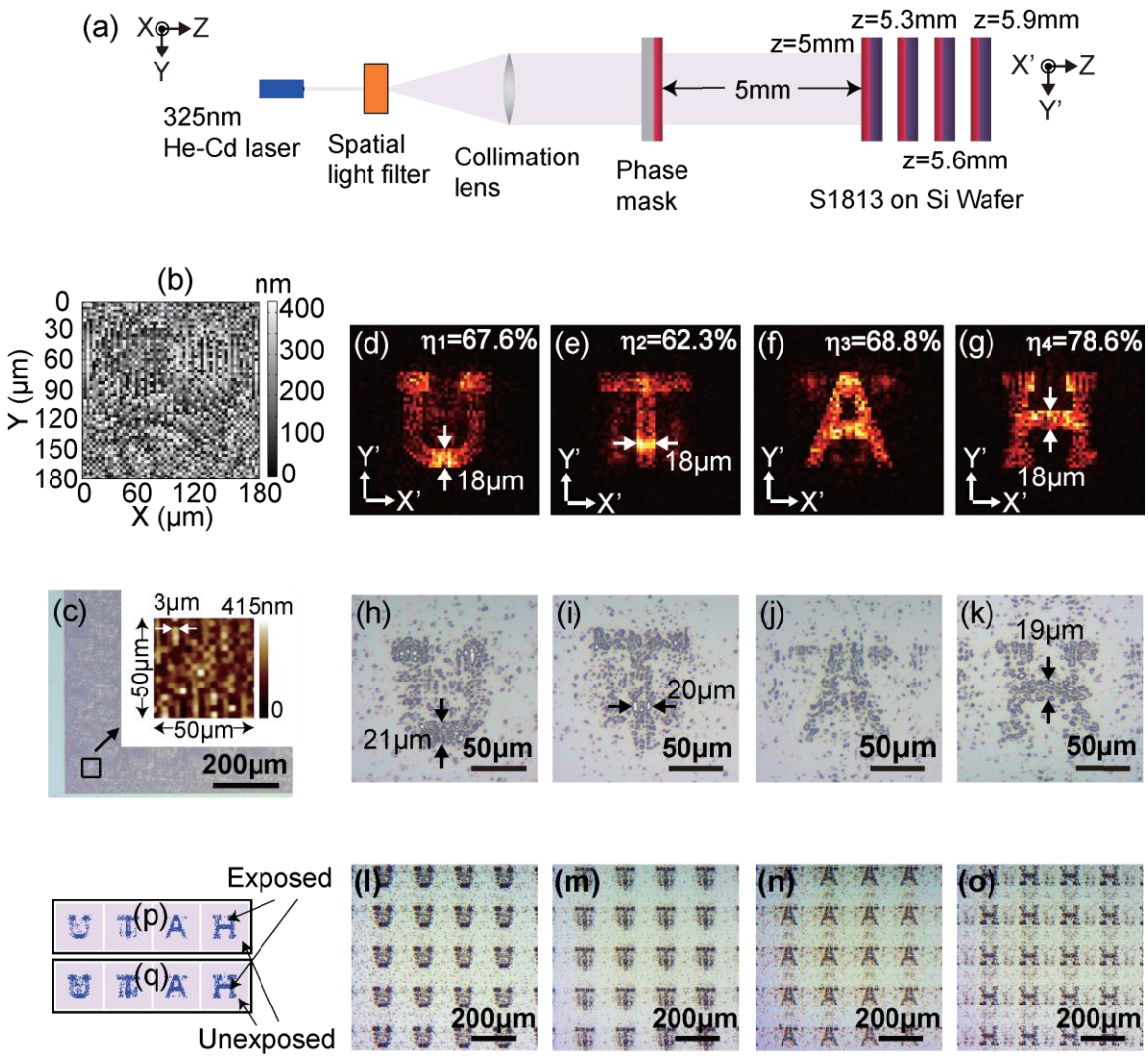

Figure 5.3. Lithography on multiple planes parallel to the mask. (a) Schematic of the exposure setup. (b) Height profile of the optimized 2D phase mask. (c) Optical microscope image of one corner of the fabricated periodic phase mask (inset: AFM measurement of a 50μm×50μm region, and 3μm pixel size is labeled). (d)-(g) Simulated intensity distributions of one period on the X'Y' plane. Optical efficiencies are given. (h)-(k) Optical micrographs of the exposed and developed results of one period. Designed 18μm lines have measured linewidths of 21μm, 20μm, and 19μm, respectively. (l)-(o) Optical micrographs of the exposed and developed results of the periodic arrays. (d), (h) and (l) are letter 'U' at *z*=5.0mm. (e), (i), and (m) are letter 'T' at *z*=5.3mm. (f), (j) and (n) are letter 'A' at *z*=5.6mm. (g), (k), and (o) are letter 'H' at *z*=5.9mm. Estimated exposure results by applying high (p) and low (q) thresholds.

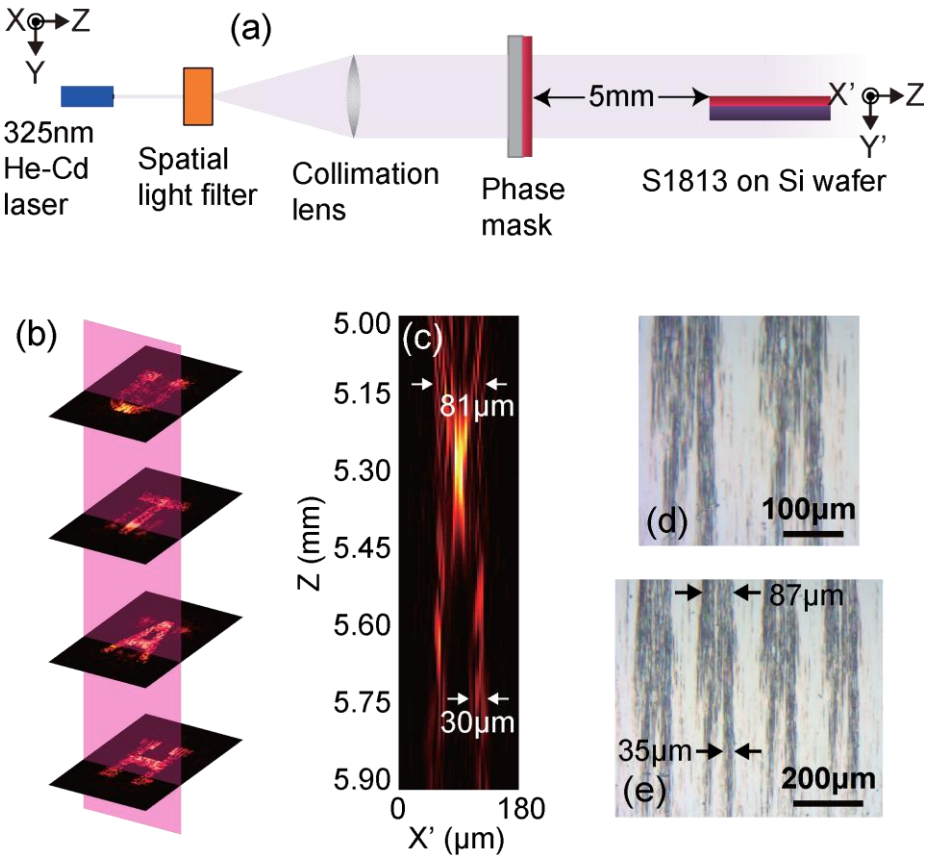

Figure 5.4. Lithography on a surface orthogonal to the mask. (a) Schematic of the exposure setup. (b) Schematic illustrating that the exposure plane (pink) is the X'Z cross-section of the intensity pattern of the phase mask that generates 'U' 'T' 'A' 'H' letters. (c) Simulated intensity distribution on the X'Z plane (pink surface in (b)). Optical micrographs of the exposed and developed results of two (d) and four (e) periods. Simulated 81μm and 30μm lines in (c) have measured linewidths of 87μm and 35μm in (e), respectively.

i.e., the fat line at bottom of 'U' (z=5mm), the center line of 'T' (z=5.3mm), the legs at the bottoms of 'A' and 'H' (z=5.6mm and z=5.9mm). A cross-section schematic is depicted in Figure 5.4(b). Note that several periods (spacing of 180μm) of the design in Figure 5.4(b) were fabricated on the mask. This resulted in repeated patterns, as indicated in Figures 5.4(d) and (e). The agreement between the two patterns indicates that the diffractive mask is capable of patterning onto surfaces of extreme obliqueness. In this case, the surface is perpendicular to the diffractive mask. The measured laser intensity at the diffractive mask

was 0.748mW/cm^2 and the exposure time was 30min. The exposure time is significantly increased compared to Figure 5.3 due to the large angle between the light propagation direction and the surface of the photoresist. Nevertheless, patterns with micron-scale fidelity can be achieved. Simulated features of 81μm and 30μm (Figure 5.4(c)) are 87μm and 35μm wide (Figure 5.4(e)) because of overexposure and mask fabrication error.

5.5 Analysis

5.5.1 Fabrication error

Since the designed mask generates a three-dimensional light field by introducing spatial phase modulation, it is necessary to pattern microstructures as approximate to the optimized height distribution as possible. Therefore, it is important to understand how fabrication error of the diffractive phase mask affects its performance. Figure 5.5 plots the calculated optical efficiencies where Gaussian noise with zero mean (μ) and various standard deviations (δ) are added to the original design. The efficiencies are reduced with increased standard deviations. Both Figures 5.5(a) and (b) indicate that errors with standard deviation greater than 100nm (~23% of the maximum height 430nm) lead to meaningless results where noise overwhelms the signal. With δ=40nm (~9% of 430nm), the 1D and the 2D masks have average optical efficiencies decreased from 70% and 60% to 54% and 45%. Insets of Figure 5.5(b) include the intensity distribution simulations of the 2D phase mask with applied errors (δ=5nm, 40nm and 100nm). 5nm error has trivial effect on the signal-to-noise ratio (SNR), but with 40nm error the patterns start to lose their accuracy. This also explains the undesired exposures observed in Figures 5.2(e)-(g) and Figures 5.3(h)-(k), which occurred outside the designated regions (defined in Figures 5.1(b) and (d)). Based upon measurements, the height error in our grayscale

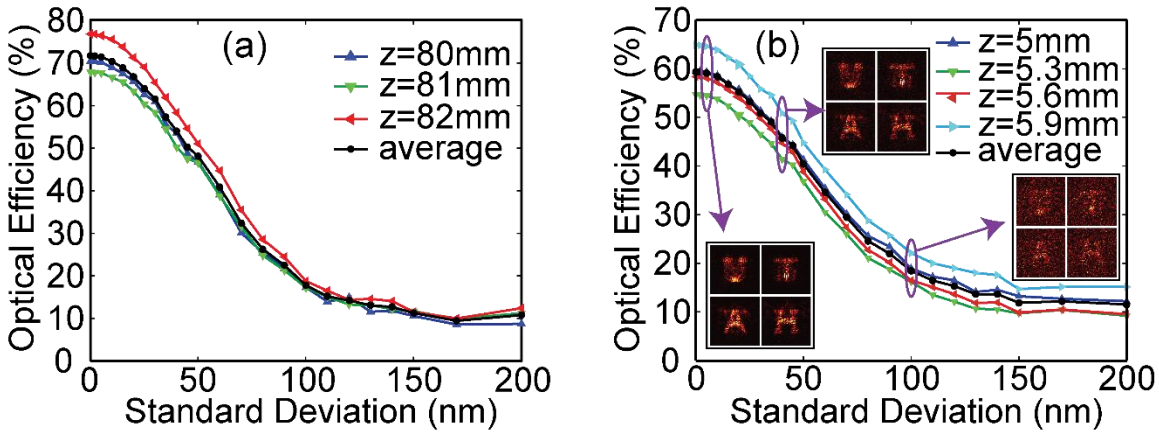

Figure 5.5. Optical efficiencies after adding Gaussian noises with zero mean and standard deviations from 0 to 200nm to the height distributions of the 1D (a) and 2D (b) phase masks. They are calculated at the designated exposure planes and take the average (black lines). Insets of (b): Simulated light intensity distributions at four planes separated by 0.3mm with low noise of δ=5nm (left), medium noise of δ=40nm (middle), and high noise of δ=100nm (right).

lithography is about 30nm. Hence, it is critical to suppress fabrication errors, especially δ<40nm, by accurate calibration, process parameter optimization, and better condition control.

5.5.2 Resolution

The spatial resolution by the proposed lithography technique is primarily defined by the fabrication resolution of the phase mask. We exploited the Heidelberg microPG101 machine with 3μm-write-head for grayscale patterning (Δx=Δy=3μm). Theoretically, the attainable resolution by OPL is defined by $C.D. = k_1 \frac{\lambda}{NA}$, in which λ is the illumination wavelength, NA is the numerical aperture of the projection lens and k_1 is a system-related scale coefficient [31-33]. For a pixelated phase mask $NA \approx \frac{\lambda}{2\Delta x}$. Usually, k_1 takes a value of 0.5, which results in a resolution $C.D. \approx \Delta x$. In Figures 5.2(h) and (i), a simulated

3μm line was measured 5μm wide due to overexposure and limited resolution of optical microscope. Similarly, the other measured linewidths are within +15% of the nominal values. Therefore, by optimizing exposure condition and minimizing mask fabrication error, it is possible to approach the predicted resolution. Additionally, smaller features can be achieved once an advanced mask generation tool is utilized (down to <1μm resolution).

5.5.3 Defocus

Depth of focus (DOF) is another issue considered in OPL systems. Generally, a projection lens has a DOF determined by $DOF = k_2 \frac{\lambda}{NA^2} = 4k_2 \frac{\Delta x^2}{\lambda}$, in which k_2 is another system-related factor [32-34]. Assuming k_2=0.5, DOF=55μm for a λ=325nm laser with Δx=3μm. Contrary to conventional 2D lithography, shorter DOF is desired in micropatterning on oblique and multiplane surfaces since more pattern changes are expected within a certain distance. This can be realized by reducing the pixel size of the phase mask and using a long-wavelength light source. The optical efficiencies at various defocus planes are plotted in Figure 5.6. The efficiencies drop to 60% at ±500μm and ±100μm defocus for both 1D (Figure 5.6(a)) and 2D (Figure 5.6(b)) masks. At -100μm plane (top inset of Figure 5.6(a)), letters ‘U’ and ‘T’ have well-preserved patterns while the other two experience obvious distortions. On the other hand, ‘A’ and ‘H’ look decent while the first two have worsened shapes at +100μm plane (bottom inset of Figure 5.6(b)). Thus, in exposure experiments, it is crucial to control the gap between the mask and the sample as close to the designed value as possible. In the current setup, the gap is adjusted on a track manually. A micrometer stage may be used in the future.

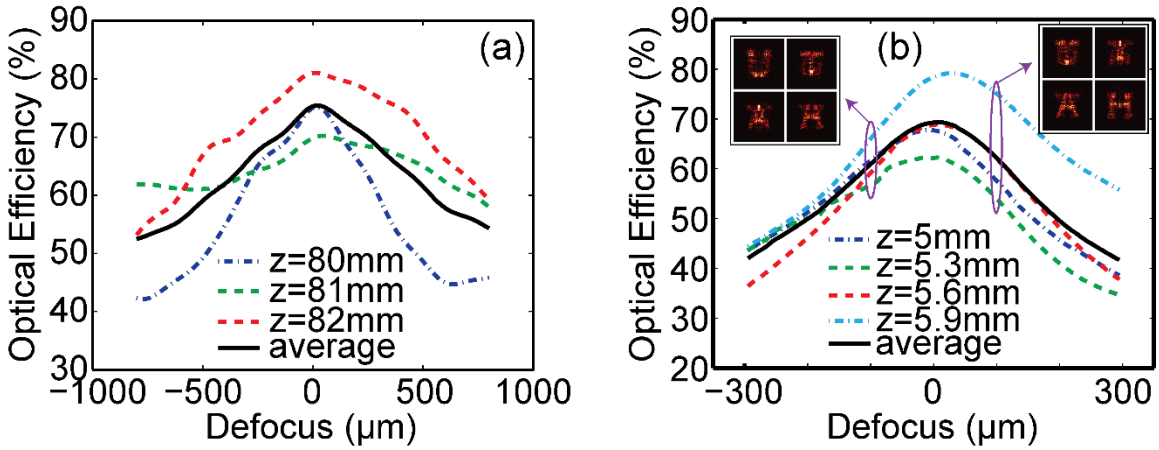

Figure 5.6. Optical efficiencies at various defocus locations of the 1D (a) and 2D (b) phase masks. They are calculated at different exposure planes and take the average (black lines). Insets of (b): Simulated light intensity distributions at four planes separated by 0.3mm at -100μm defocus (left) and +100μm defocus (right).

5.6 Conclusions

Managing light intensities in 3D space using broadband diffractive optics allows for a new and efficient technique to pattern microstructures on oblique and multiplane surfaces. Clearly, this technique can be extended to conventional 3D lithography. Compared to scanning two-photon lithographic techniques, the reported method is based on a single optical exposure and effectively avoids high-power pulsed lasers and slow scanning schemes [34,35]. Our technique can be readily adapted for high-throughput manufacturing. The diffractive phase mask allows for a large number of degrees of freedom, which permits generation of complex geometries in 3D space. The technique currently suffers from cross-talk between the patterns, as is evident in Figures 5.3(d)-(g). This effect can be reduced by the use of smaller fabrication pixels, which will provide many more pixels, and hence, more degrees of freedom for the optimization algorithm. Shrinking pixel size also helps in improving patterning resolution. Furthermore, our previous work in broadband diffractive optics [20] indicates that with a larger number of

pixels, the sensitivity of the projected pattern to pixel errors is also minimized. One challenge in the reported method is that resolution in the Z-axis is limited by the DOF of the diffractive-optical mask. Distances between exposure planes that are several multiples of this DOF are necessary to effectively separate different patterns. The DOF can be decreased by using smaller pixels and longer wavelengths. In addition, the computer-generated micro-optic device can be faithfully replicated and thus mass produced via roll-to-roll nanoimprint [18]. The next step is to explore its vast capabilities in 3D micropatterning.

5.7 Supplementary Information

5.7.1 Figure-of-merit

The figure-of-merit is defined as:

$$M = \sum_i W_i \cdot M_i = \sum_i W_i \cdot \left(A_i \cdot \eta_i - B_i \cdot \varepsilon_i \right). \tag{5.1}$$

Here, i is the order of plane. The propagation distance is $d_i=d_0+(i\text{-}1)\Delta d$, where d_0 is the initial distance and Δd is the gap between adjacent planes. η_i and ε_i represent optical efficiency and root-mean-square (RMS, uniformity) at each propagation plane, which are explicitly described as

$$\eta_i = \frac{\sum_{x'} \sum_{y'} \left| U_i \right|^2 \cdot I_i^T}{P_{in}}. \tag{5.2}$$

$$\varepsilon_i = \sqrt{\frac{\sum_{x'} \sum_{y'} \left\{ \left| U_i \right|^2 \cdot I_i^T - E_i \cdot I_i^T \right\}^2}{N_i^T}}. \tag{5.3}$$

Here, U_i and I_i^T are the light intensity distribution and the binary target image at plane i, respectively. The summation is over the entire image plane (X'Y'). P_{in} is the total incident power. In Equation (5.3), $E_i = \frac{\sum_{x'}\sum_{y'}|U_i|^2 \cdot I_i^T}{N_i^T}$ is the mean value of the light intensity of all the pixels inside the target region at plane i, and $N_i^T = \sum_{x'}\sum_{y'} I_i^T$ is the total number of pixels in the target image with a value of 1 at plane i. In Equation (5.1), A_i, B_i, and W_i represent the weighting factors for optical efficiency, RMS, and the overall metric M_i at plane i, respectively. During optimization, these values are judiciously adjusted until the diffraction patterns with both high efficiency and good uniformity are achieved.

5.8 References

[1] J. D. Joannopoulos, P. R. Villeneuve, and S. H. Fan, "Photonic crystals: putting a new twist on light," Nature **386**, 143-149 (1997).

[2] M. Campbell, D. N. Sharp, M. T. Harrison, and R. G. Denning, "Fabrication of photonic crystals for the visible spectrum by holographic lithography," Nature **401**, 53-56 (2000).

[3] R. S. Patti, "Three-dimensional integrated circuits and the future of system-on-chip design," Proc. IEEE **94**, 1214-1224 (2006).

[4] N. Miki, X. Zhang, R. Khanna, A. A. Ayon, D. Ward, and S. M. Spearing, "Multi-stack silicon-direct wafer bonding for 3D MEMS manufacturing," Sens. Actuators. A **103**, 194-201 (2003).

[5] E. Verpoorte, and N. F. De Rooij, "Microfluidics meets MEMS," Proc. IEEE **91**, 930-953 (2003).

[6] S. Egashira, and E. Nishiyama, "Stacked microstrip antenna with wide bandwidth and high gain," IEEE Trans. Antennas Propagat. **44**, 1533-1534 (1996).

[7] R. Want, "An introduction to RFID technology," IEEE Pervasive Comput. **5**, 25-33 (2006).

[8] D. Schurig, J. J. Mock, B. J. Justice, S. A. Cummer, J. B. Pendry, A. F. Starr, and

D. R. Smith, “Metamaterial electromagnetic cloak at microwave frequencies,” Science **314**, 977-980 (2006).

[9] H. Chen, C. Chan, and P. Sheng, “Transformation optics and metamaterials,” Nature Mater. **9**, 387-396 (2010).

[10] M. J. Booth, M. A. A. Neil, R. Juskaitis, and T. Wilson, “Adaptive aberration correction in a confocal microscope,” Proc. Natl. Acad. Sci. USA **99**, 5788-5792 (2002).

[11] C. Kim, R. Bhandari, M. Klein, S. Negi, L. Reith, P. Tathireddy, M. Toepper, H. Oppermann, and F. Solzbacher, “Integrated wireless interface based on the Utah electrode array,” Biomed. Microdevices **11**, 453-466 (2009).

[12] J. John, Y. Li, J. Zhang, J. Loeb, and Y. Xu, “Microfabrication of 3D neural probes with combined electrical and chemical interfaces,” J. Micromech. Microeng. **21**, 105011 (2011).

[13] A. W. Martinez, S. T. Phillips, and G. M. Whitesides, “Three-dimensional microfluidic devices fabricated in layered paper and tape,” Proc. Natl. Acad. Sci. USA **105**, 19606-19611 (2008).

[14] T. Ito, and S. Okazaki, “Pushing the limits of lithography,” Nature **406**, 1027-1031 (2000).

[15] J. A. Dominguez-Caballero, S. Takahashi, and G. Barbastathis, “Design and sensitivity analysis of Fresnel domain computer generated holograms,” Int. J. Nanomanufacturing **6**, 207 (2010).

[16] M. Galus, E. Moon, H. I. Smith, and R. Menon, “Replication of diffractive-optical arrays via photocurable nanoimprint lithography,” J. Vac. Sci. Technol. B **24**, 2960-2963 (2006).

[17] K. S. Chen, I. K. Lin, and F. H. Ko, “Fabrication of 3D polymer microstructures using electron beam lithography and nanoimprinting technologies,” J. Micromech. Microeng. **15**, 1894-1903 (2005).

[18] L. J. Guo, “Nanoimprint lithography: methods and material requirements,” Adv. Mater. **19**, 495-513 (2007).

[19] J. G. Goodberlet, and B. L. Dunn, “Deep-ultraviolet contact photolithography,” Microelectron. Eng. **53**, 95-99 (2000).

[20] G. Kim, J. A. Dominguez-Caballero, and R. Menon, “Design and analysis of multi-wavelength diffractive optics,” Opt. Express **20**, 2814-2823 (2012).

[21] P. Wang, J. A. Dominguez-Caballero, D. J. Friedman, and R. Menon, “A new

class of multi-bandgap high efficiency photovoltaics enabled by broadband diffractive optics," Prog. Photovolt. Res. Appl. **23**, 1073-1079 (2015).

[22] P. Wang, C. G. Ebeling, J. Gerton, and R. Menon, "Hyper-spectral imaging in scanning-confocal-fluorescence microscopy using a novel broadband diffractive optic," Opt. Commun. **324**, 73-80 (2014).

[23] G. Kim, and R. Menon, "An ultra-small 3D computational microscope," Appl. Phys. Lett. **105**, 061114 (2014).

[24] P. Wang, and R. Menon, "Optimization of periodic nanostructures for enhanced light-trapping in ultra-thin photovoltaics," Opt. Express **21**, 6274-6285 (2013).

[25] P. Wang, and R. Menon, "Optimization of generalized dielectric nanostructures for enhanced light trapping in thin-film photovoltaics via boosting the local density of optical states," Opt. Express **22**, A99-A110 (2013).

[26] P. Wang, and R. Menon, "Computational spectroscopy based on a broadband diffractive optic," Opt. Express **22**, 14575-14587 (2014).

[27] M. A. Seldowitz, J. P. Allebach, and D. W. Sweeney, "Synthesis of digital holograms by direct binary search," Appl. Opt. **26**, 2788–2798 (1987).

[28] T. R. M. Sales, and D. H. Raguin, "Multiwavelength operation with thin diffractive elements," Appl. Opt. **38**, 3012–3018 (1999).

[29] B. Kress, and P. Meyrueis, *Digital diffractive optics: an introduction to planar diffractive optics and related technology* (John Wiley, 2000).

[30] K. Tostu, K. Fujishiro, S. Tanaka, and M Esashi, "Fabrication of three-dimensional microstructure using maskless gray-scale lithography," Sens. Actuators. A **130**, 387-392 (2006).

[31] S. Okazaki, "Resolution limits of optical lithography," J. Vac. Sci. Technol. B **9**, 2829-2833 (1991).

[32] H. Wang, G. Yuan, W. Tan, L. Shi, and T. Chong, "Spot size and depth of focus in optical data storage system," Opt. Eng. **46**, 065201 (2007).

[33] B. J. Lin, "The k_3 coefficient in nonparaxial λ/NA scaling equations for resolution, depth of focus, and immersion lithography," J. Microlith. Microfab. Microsyst. **1**, 7-12 (2002).

[34] S. Maruo, O. Nakamura, and S. Kawata, "Three-dimensional microfabrication with two-photon-absorbed photopolymerization," Opt. Lett. **22**, 132-134 (1997).

[35] W. Zhou, S. M. Kuebler, K. L. Braun, T. Yu, J. K. Cammack, C. K, Ober, J. W. Perry, and S. R. Marder, “An efficient two-photon-generated photoacid applied to positive-tone 3D microfabrication,” Science **296**, 1106-1109 (2002).

CHAPTER 6

ULTRA-HIGH-SENSITIVITY COLOR IMAGING

This chapter is adapted from the author's previous publication: Peng Wang and Rajesh Menon, "Ultra-high-sensitivity color imaging via a transparent diffractive-filter array and computational optics," Optica **2**, 933-939 (2015).

6.1 Abstract

Conventional color imaging requires absorptive color-filter arrays, which exhibit low light transmission. Here, we replace the absorptive color-filter array with a transparent diffractive-filter array (DFA) and apply computational-optics techniques to enable color imaging with a sensitivity that is enhanced by a factor as high as 3.12. The DFA diffracts incident light onto a conventional monochrome sensor array to create intensity distributions that are wavelength dependent. By first calibrating these wavelength-dependent intensity distributions, and then applying computational techniques, we demonstrate single-shot hyperspectral imaging and absorption-free color imaging.

6.2 Introduction

Color imaging provides information in the spectral domain with very important applications in our daily life, scientific research, industrial processes, etc. Color can represent critical information such as body temperature, material composition, and aesthetics. Conventional cameras employ an absorptive color-filter array (also referred to as the Bayer filter) to determine the color of spatial pixels [1]. It is usually composed of an array of square color subpixels placed over a sensor array such that one color sub-pixel is aligned to one sensor pixel. Each color subpixel transmits one primary color (red, green, or blue) while absorbing the rest. Therefore, its overall light transmission is low. Lower transmission leads to compromised light sensitivity. Furthermore, such color-filter arrays require multiple aligned lithography steps for their manufacture, which can be cumbersome. Here, we demonstrate a transparent diffractive-filter array that can be easily and inexpensively fabricated to achieve color imaging with little absorption loss. The filter can also be readily replicated for mass production.

Recently, new filter designs have been proposed to overcome certain limitations of conventional Bayer filters [2,3]. Most of these designs aim to enhance color accuracy by tuning the transmitted spectral bands via nano or microstructures. Plasmonics-based color filters suffer from decreased light transmission due to parasitic absorption of the required metal layers [4-10]. In addition, these require very precise nanofabrication of subwavelength structures, which can be challenging and experience difficulties in extending to mass production. Alternative filters that utilize a variety of optical resonance effects have also been proposed. However, these exhibit very limited bandwidths [11-13]. Some of the devices also require multiple lithography steps [14]. A recent approach introduced complex nanophotonic deflectors above the sensor array, which demonstrated a two-fold improvement in light sensitivity [15]. However, the required nanostructures have large aspect ratios and are therefore difficult and expensive to manufacture.

The concept of a coded aperture was previously explored to construct a spectral imager [16]. Although it shows reasonable spectral resolution and image quality, this technique requires a coded (absorptive) aperture and a dispersion element (prism) to generate multispectral images. Extra relay lenses are also needed. An absorptive aperture clearly limits photon throughput and hence reduces sensitivity. Recently, commercial hyperspectral sensors have also been introduced [17]. In these, spectral selectivity is achieved via complex Fabry-Perot resonators integrated on top of the CMOS sensor. Not only does this technology require precise alignment between the filter array and the sensor array, but the filters themselves require expensive multilayer deposition techniques. Most importantly, the overall light transmission is greatly reduced due to the spectral selectivity of each filter in the array, and consequently sensitivity is degraded.

In this chapter, we overcome the limitations of all previous approaches by utilizing a fully transparent diffractive-filter array (DFA) that not only enhances light sensitivity by as much as 3.12 times, but is also significantly simpler to mass manufacture. Specifically, we replace the conventional Bayer filter by a multilevel DFA atop the conventional sensor array as shown in Figure 6.1(a). Light incident on the DFA diffracts and creates an intensity pattern on the underlying sensor array. We design the DFA such that the diffracted intensity pattern of each wavelength is unique. Then, we calibrate the response of the DFA to each wavelength, which we refer to as the spatial-spectral point-spread function. Finally, we apply computational techniques to recover the color information of any unknown incident illumination. The key advantages of our approach are (1) the DFA can be completely transparent, which allows all the light to be utilized for imaging and thus improves sensitivity; (2) the DFA can be easily fabricated using single-step grayscale lithography and mass manufactured using imprinting techniques [18,19]; (3) large tolerance to fabrication inaccuracy, since calibration comes after the filter is patterned and fixed; (4) minimal alignment is necessary between the DFA and the sensor array; (5) only one optical element (the DFA) is introduced to replace the Bayer filter; (6) the technique can be applied to any conventional sensor array (CMOS or CCD); and (7) the technique is easily extended to multi- and hyper-spectral imaging.

6.3 Principle of Operation

The basic schematic of our approach is shown in Figure 6.1(a). The DFA is composed of a periodic unit cell. In our implementation, this unit cell is composed of an array of 6×6 squares, each of size Δ=3μm. For our initial demonstration, the depth of each such square is randomly assigned. The DFA is placed at a distance *d* from the sensor array.

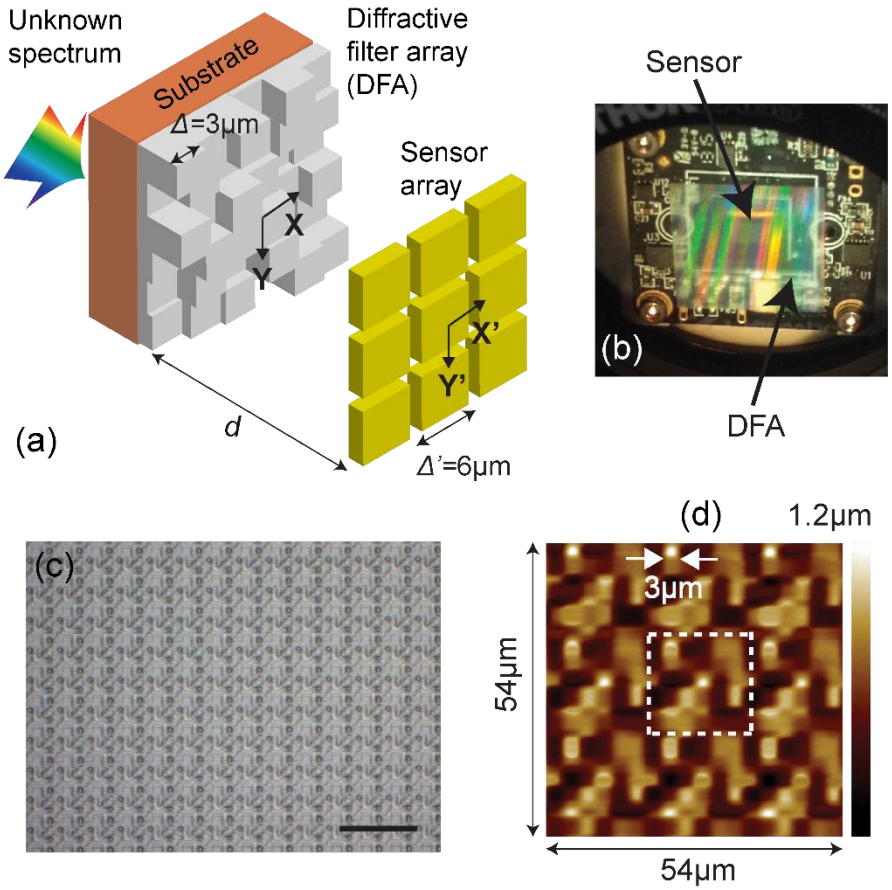

Figure 6.1. (a) Schematic of one spatial pixel of the color sensor composed of a unit cell of the DFA (6×6 squares) and 3×3 sensor pixels. One DFA unit cell offers color for one image pixel. (b) Photograph of the DFA-sensor assembly. (c) Optical micrograph of a portion of the fabricated DFA (scale bar: 50μm). (d) Atomic-force micrograph of a small region of the DFA. The dotted white rectangle delineates one DFA unit cell.

In our current implementation, one spatial pixel of the image is composed of an array of 3×3 sensor pixels, which in turn corresponds to one DFA unit cell. We utilized a commercial monochrome sensor with a pixel size Δ'=6μm (Model #: DMM22BUC03-ML, The Imaging Source). A photograph of the final assembly is shown in Figure 6.1(b). Grayscale lithography was used to pattern these multilevel diffractive optics in a single step [20,21]. It was made in positive photoresist (Shipley 1813) spin-coated on fused silica substrate. The depth of each square in the DFA was controlled between 0 and

1.2μm. An optical micrograph and an atomic force micrograph of different portions of the fabricated DFA are shown in Figures 6.1(c) and 1(d). Periodicity of 18μm×18μm and multilevel height distribution within one unit cell are clearly shown.

We first characterized the device by measuring the diffracted light intensity distribution on the sensor array as a function of wavelength. We call these data the spatial-spectral point-spread function (SS-PSF) of the DFA. This is analogous to our previous work in computational spectroscopy [21]. We built the same scanning spectrometer by placing the single-mode fiber input to a conventional spectrometer (Ocean Optics Jaz) on an automated 2-axis stage (Thorlabs). The DFA-sensor assembly was illuminated by collimated white light from a supercontinuum source (SuperK Compact, NKT Photonics). The scan axes of the stage were carefully aligned to the axes of the DFA-sensor assembly. The distance *d* between the DFA and the sensor was also carefully set using a manual micrometer stage with a precision of 10μm, which was shown to be sufficient from an analysis of the depth of focus of the DFA. Then, we captured a spectrum for each position of the stage, which resulted in a 3D SS-PSF (1 wavelength dimension and 2 spatial dimensions) matrix. This data were captured for 3 different values of *d*. Exemplary images (X'Y') at 5 wavelengths and the 3 values of *d* are shown in Figure 6.2(a). Note that as the wavelength changes, the diffracted image also changes. The spectral resolution of our technique relies on the decorrelation of the diffracted images at closely spaced wavelengths. We can quantify this effect via a correlation function that is calculated as a function of the wavelength spacing, δλ [21-23].

$$\mathbf{C}(x', y', \delta\lambda) = \frac{< \mathbf{PSF}(x', y', \lambda) \cdot \mathbf{PSF}(x', y', \lambda + \delta\lambda) >}{< \mathbf{PSF}(x', y', \lambda) > \cdot < \mathbf{PSF}(x', y', \lambda + \delta\lambda) >} - 1,. \qquad (6.1)$$

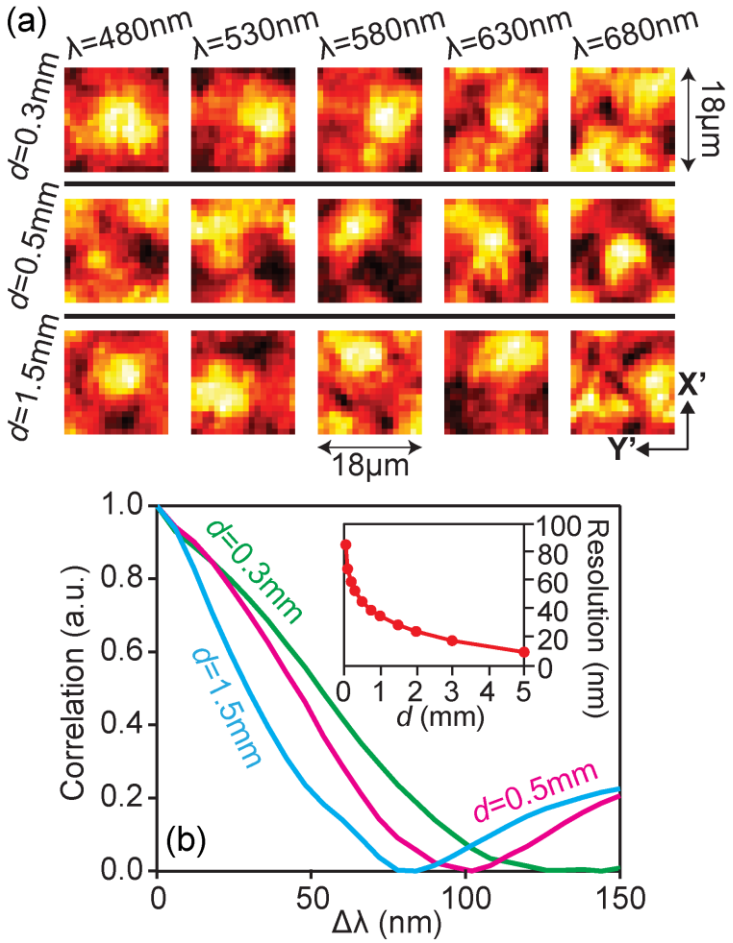

Figure 6.2. (a) Measured light intensity distributions of 5 wavelength samples at 3 different values of *d*. (b) Measured correlation of the diffracted light intensity as a function of spectral resolution for *d*=0.3mm (green line), 0.5mm (magenta line), and 1.5mm (cyan line). Inset: Measured spectral resolution as a function of *d*.

Here, **PSF**(*x'*,*y'*,*λ*) is the measured SS-PSF of the DFA. The correlation function, C(δλ), plotted in Figure 6.2(b), is averaged over the entire space (*x'*,*y'*). It is well known that this correlation function is also dependent on *d*. The spectral resolution is then defined as the wavelength spacing at which the image correlation, C(δλ), is 0.5. Thereby we can plot the spectral resolution as a function of *d* as shown in the inset of Figure 6.2(b). As expected, the spectral resolution increases with increasing *d*. However, as discussed later, the cross-talk between spatial pixels also increases with increasing *d*.

Therefore, an optimal choice of d is necessary. The spectral resolutions of the 2D DFA studied here are lower compared to previous 1D computational spectrometer designs [21] due to (1) smaller gap d and (2) fewer digitalized squares in each unit cell of the DFA. But it is sufficient for accurate color reconstruction, which will be shown later.

The diffracted intensity distribution of one image pixel (3×3 sensor pixels, $\mathbf{S}(x',y')$) can be modeled as $\mathbf{S} = \mathbf{PSF} \cdot \boldsymbol{\Psi}$, where $\boldsymbol{\Psi}(\lambda)$ is the compound photon flux spectrum, which is an element-wise multiplication of the unknown photon flux spectrum $\boldsymbol{\Phi}(\lambda)$ and the sensor's quantum efficiency $\mathbf{QE}(\lambda)$ [21,24]. Solving for $\boldsymbol{\Psi}(\lambda)$ from $\mathbf{S}(x',y')$ is an inverse problem. This problem can be solved by minimizing the residual norm $\|\mathbf{PSF}\cdot\boldsymbol{\Psi} - \mathbf{S}\|^2$. Here, we present 2 methods to solve this inverse problem. One is via a modified version of the iterative direct-binary-search (DBS) algorithm [21,25-30]. The second approach is based on singular-value-decomposition (SVD) of the system matrix, **PSF**, and regularization of the inverse problem [24]. This is a faster algorithm and is also less sensitive to noise. In this case, the optimal solution is mathematically represented as the weighted linear combination of the singular vectors of matrix **PSF** in the spectral domain. See Section 2.5 for more details on these algorithms.

6.4 Experiments

To demonstrate preliminary color reconstruction, we placed various color filters (Nikon) one at a time in the path of the collimated white light illuminating the DFA-sensor assembly. The results are summarized in Figure 6.3 for five colors: blue, green, red, yellow, and purple. The calculated spectral resolutions were 53nm, 45nm, and 29nm for d=0.3mm, 0.5mm, and 1.5mm, respectively (see inset in Figure 6.2(b)). Both the DBS method and regularization were used for spectrum reconstruction. The reconstructed

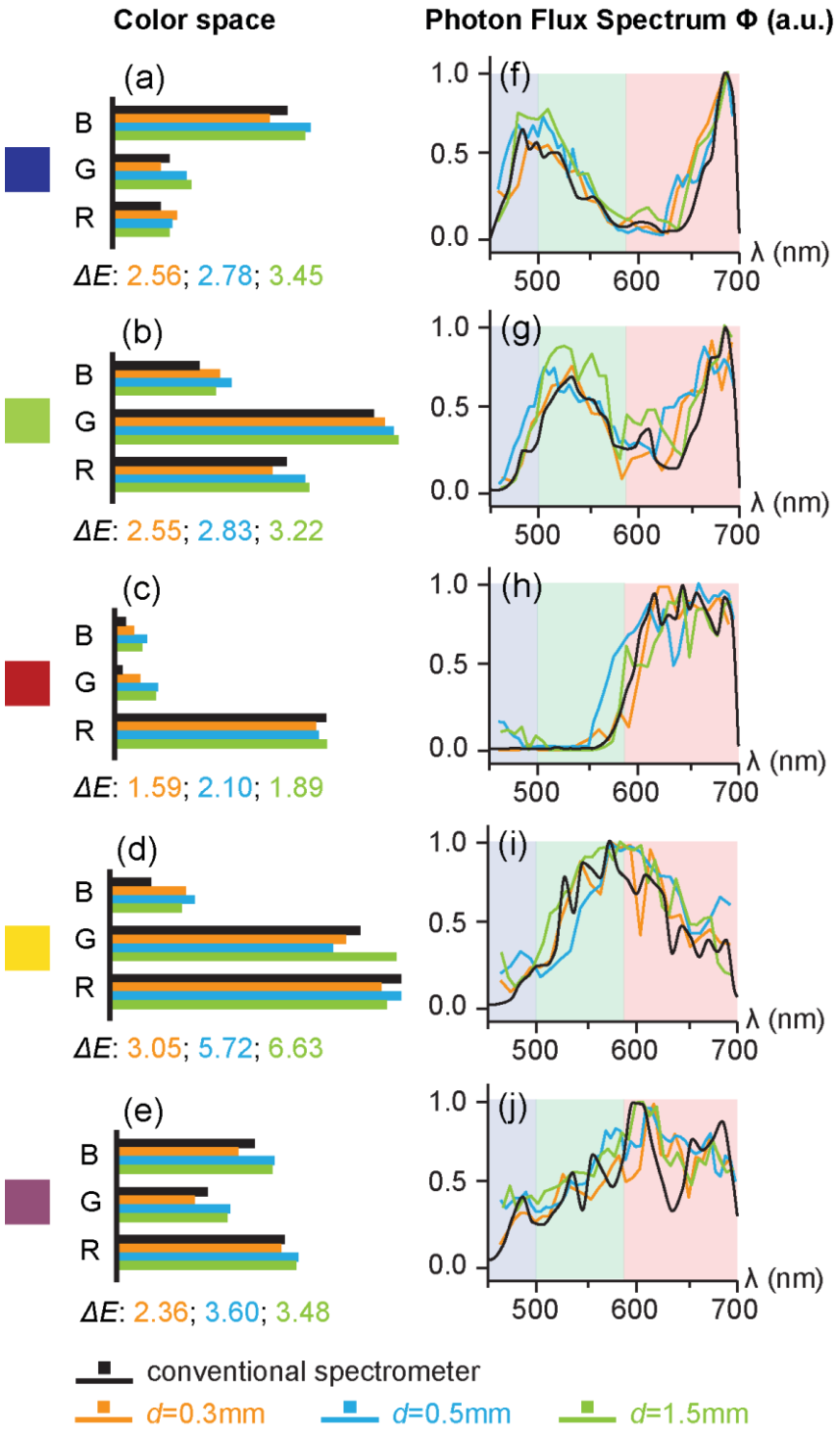

Figure 6.3. Reconstructed color ((a)-(e)) and photon-flux spectrum ((f)-(j)) of blue (a,f), green (b,g), red (c,h), yellow (d,i), and purple (e,j) colors. The experiments were conducted for three gaps, *d*=0.3mm (orange), 0.5mm (cyan), and 1.5mm (light green). The reference spectrum and color values are plotted in black. The spectra **Φ** are normalized. The delta E (ΔE) values based on CIE94 are also given.

spectra were compared to the spectra measured using a conventional spectrometer (shown in black). Noise present in the reconstructed spectra does not affect the color values significantly. RGB color values were calculated from the reconstructed spectra by integrating over the corresponding bands: 450nm to 500nm for blue (B), 500nm to 580nm for green (G), and 580nm to 700nm for red (R). They are then quantized into 8-bit (256 levels). The minimum wavelength was limited to 450nm by the supercontinuum source. The reconstructed color values agree very well with the actual color values (estimated from the measured spectra) and exhibit average errors of 5.62%, 7.50%, and 7.11% in terms of the 256 levels for d=0.3mm, 0.5mm, and 1.5mm, respectively. These are all well within the 10% color-error threshold and are acceptable for visual perception. A more rigorous standard for color accuracy test, delta E (or ΔE) values, based on CIE94 definition, are also summarized in Figure 6.3. The ΔE averaged over the five exemplary colors for d=0.3mm gap is 2.42, which is close to the previously proposed Just Noticeable Difference (JND) value of ~2.30 [31].

In order to demonstrate color imaging, we used the image of a rainbow printed on a transparency by a high-resolution printer. First, a conventional color sensor (Model #: DFM22BUC03-ML, The Imaging Source) was used to capture a reference image as shown in Figure 6.4(a). For fair comparison, the monochrome and the color sensor chips were identical, the only difference being the presence of the Bayer filter on the color sensor. The illumination system as well as the exposure times (14ms) were kept the same for both the conventional color sensor and our DFA-sensor. In our preliminary experiments, no lens was incorporated in the system (no magnification), and the sample was placed as close as possible to either the front surface of the conventional color sensor

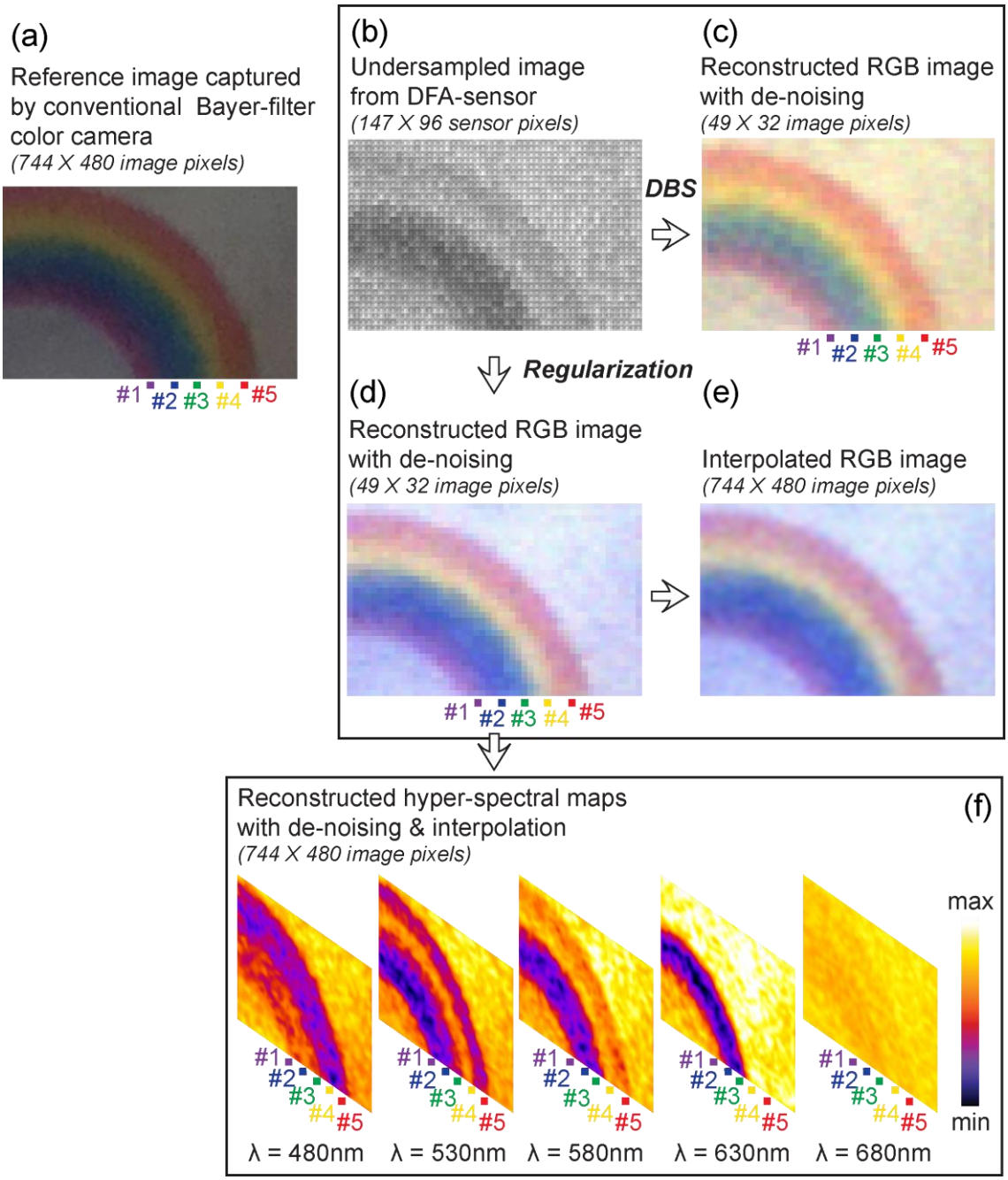

Figure 6.4. Experimental results of color imaging of a printed rainbow object. The exposure time is 14ms. (a) Reference image captured by a sensor with a Bayer filter. (b) Gray-scale image captured by our DFA-sensor assembly. It is undersampled to avoid cross-talk. Color image reconstructed from (b) using the DBS algorithm (c) and using the regularization algorithm (d). Both (b) and (c) are de-noised using the same filter. (e) Image interpolated to 744×480 image pixels from (d). (f) Reconstructed hyperspectral image at λ=480nm, 530nm, 580nm, 630nm, and 680nm. They are de-noised by filtering and then interpolated. The sensor chip used for reference in (a) is the same chip used for the image in (b). All other experimental conditions were also identical.

or to the DFA substrate. In practice, there was a small gap of ~50μm. For this experiment, we chose d=0.3mm.

The raw monochrome image corresponding to $\mathbf{S}(x',y')$ is shown in Figure 6.4(b). The corresponding color image reconstructed using DBS algorithm and regularization are shown in Figures 6.4(c) and (d), respectively. The latter image shows somewhat less numerical noise than expected [24]. By applying a simple filter in the Fourier domain, these images are de-noised. Both the reconstructed images are significantly brighter than the reference image. One of the constraints of DFA-based color reconstruction is the cross-talk that occurs between neighboring spatial pixels due to the diffraction of light. A simple approach to reduce the impact of cross-talk is to undersample the raw monochrome data and use the undersampled images for reconstruction. In order to undersample the image, we need to first estimate the spatial extent of the cross-talk using our diffraction model [29,32]. We calculated that cross-talk affects an area of 90μm×90μm (5×5 DFA unit cells), 150μm×150μm (8×8 DFA unit cells), and 450μm×450μm (25×25 DFA unit cells) at d=0.3mm, 0.5mm, and 1.5mm, respectively. Since here we used d=0.3mm, we undersampled the monochrome image at every 5th unit cell of the DFA, which is a sufficient spatial resolution for the rainbow image used here. The undersampling was applied to the raw image used for both the DBS method as well as regularization. It was undersampled from 744×480 sensor pixels to 147×96 sensor pixels (Figure 6.4(b)). Since each DFA unit cell corresponds to 3×3 sensor pixels (see Figure 6.1(a)), this leads to reconstruction of 49×32 image pixels. After de-noising, we further applied a simple interpolation algorithm to extend the reconstructed image using regularization (Figure 6.4(d)) to the same size as that of the reference image (744×480

sensor pixels). The resulting image is shown in Figure 6.4(e). This reconstructed color image is of the same quality as the reference image, but is considerably brighter as no absorptive color-filter array is used.

Interestingly, our imaging architecture can also be used as a single-shot hyperspectral imager. To illustrate this, the intensity distribution maps at 5 wavelengths are plotted in Figure 6.4(f). These are normalized as indicated by the colorbar. For clear illustration, we identify five color ribbons of the rainbow, labelled in Figures 6.4(a), (c), (d), and (f). The far end of the spectrum is close to infrared, therefore the λ=680nm map looks uniform and is thus excluded from our analysis. The blue ribbon (#2) and the green ribbon (#3) have signals only from λ=480nm channel and λ=530nm channel, respectively. The purple ribbon (#1) is composed of both blue (λ=480nm) and red (λ=630nm). The yellow region (#4) receives contributions from λ=530nm, 580nm, and 630nm channels. And the red part (#5) is consist of mostly λ=630nm signals and some λ=580nm signals. Here, the bandwidth to spectral resolution ratio is 250nm/53nm=4.72.

6.5 Discussion

The conventional Bayer filter is absorptive and therefore has low light transmission. In the RGB three-color scheme, each subpixel filter only lets one color pass through, while absorbing the other two colors. As a result, the final photon throughput cannot surpass 1/3. On the other hand, our DFA is transparent and all the photons could be utilized for imaging. Therefore, a 3-fold improvement in photon utilization rate as well as sensitivity is theoretically expected. To experimentally quantify the light-sensitivity enhancement of the DFA-based color sensor over the Bayer-filter-based color sensor, we averaged the signal intensity over the measured image as a function of exposure time for

both devices. As mentioned earlier, the sensor chip and the experimental conditions were identical for both devices. For the 8-bit sensors used in our experiments, the intensity values range from 0 to 255. At an exposure time of 20ms, the DFA-sensor assembly was saturated with average image intensity of 255. The measured values are plotted in Figure 6.5(a). The peak enhancement in light sensitivity of 3.12 was measured at an exposure time of ~7ms. An enhancement factor averaged over exposure times of 1ms to 20ms is 2.67. This is higher than what was previously reported with a more complex device [15].

As discussed previously, the spatial resolution of our DFA-sensor assembly is constrained primarily by the impact of cross-talk, which in turn is determined by the distance, *d*, between the DFA and the sensor. For higher spectral resolution, one prefers larger *d*. However, increasing *d* increases the area of cross-talk, which reduces the spatial resolution. We experimentally measured the modulation transfer function (MTF) to quantify this effect by imaging an object composed of periodic opaque (black) lines at various periods printed on a transparency. The object was again placed in close proximity to the DFA substrate as before. The MTF is calculated as a function of the spatial frequency, ν (the number of lines per unit length in cycles/mm) [32], via the relative contrast, $MTF(\nu) = C(\nu)/C_0(\nu)$, where $C(\nu)$ and $C_0(\nu)$ are the visibility (contrast) of the image and object, respectively. The visibility or contrast is defined as

$$C(\nu) = \frac{I_{\max}(\nu) - I_{\min}(\nu)}{I_{\max}(\nu) + I_{\min}(\nu)}, \tag{6.2}$$

where $I_{max}(\nu)$ and $I_{min}(\nu)$ are the maximum and the minimum image-intensity values. We measured the MTF for d=0.3mm, 0.5mm, and 1.5mm, and the results are plotted in

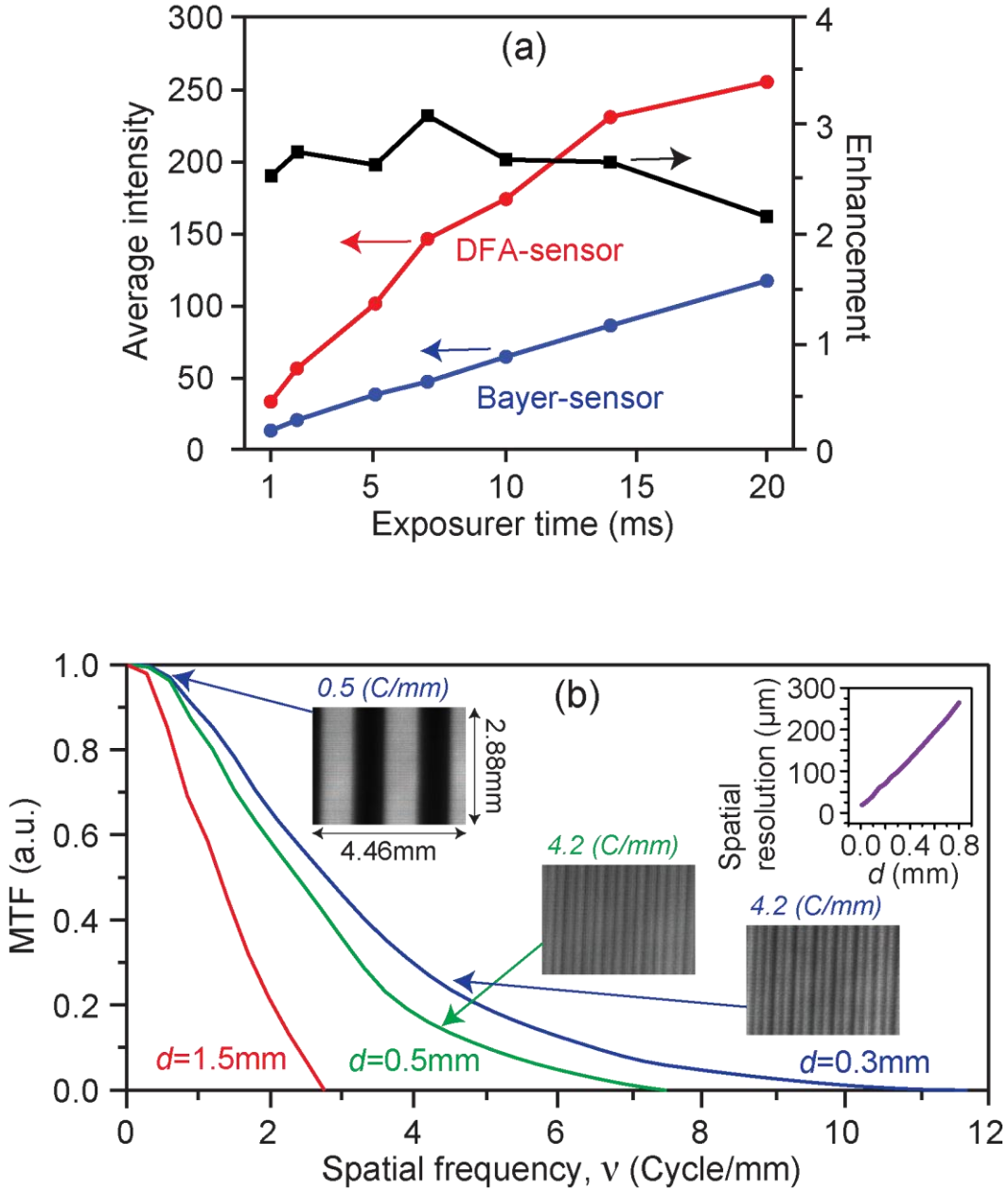

Figure 6.5. (a) The measured average image intensity from the Bayer-filter-based color sensor (blue line) and our DFA-sensor assembly (red line). The enhancement in sensitivity is plotted using a black line. (b) Measured MTF versus spatial frequency, *v* at *d*=0.3mm (blue line), 0.5mm (green line) and 1.5mm (red line). Left, center, and right bottom insets: captured gray-scale images of two spatial frequencies at two gaps. Right top inset: spatial resolution versus gap *d* estimated by numerical simulations of the far-field diffraction patterns.

Figure 6.5(b). The maximum spatial frequency, v (~11.8 cycles/mm), that was experimentally measured was limited by the resolution of the printer used to print the object pattern onto the transparency. The spatial resolution of our DFA-sensor assembly is then given by the cut-off spatial frequencies, which correspond to a resolution of 95μm, 143μm, and 380μm for d=0.3mm, 0.5mm, and 1.5mm, respectively.

These measured values agree well with the numerical predictions based on the cross-talk effect. Simulations of the far-field diffraction patterns also suggest an almost linear relationship between the spatial resolution and the gap d (see the inset of Figure 6.5(b)). This is because the diffraction angle is fixed for a fixed structure and wavelength. Here, the spatial resolution is determined by the minimum distance between two DFA unit cells when they are illuminated independently and the interactions of their diffracted fields become trivial. Note that higher spatial resolution may be achieved either by designing a better DFA or by applying computational techniques to compensate for cross-talk. See the Supplementary Information of this chapter for more details.

All our experiments were conducted by assuming on-axis illumination, and the DFA-sensor works best for on-axis illumination, as expected. Nevertheless, it is possible to calibrate the impact of off-axis illumination and reconstruct color images. Noise can be a limiting factor in all imaging systems. The color deviations observed in the reconstructed images (Figures 6.4(c) and (d)) are primarily ascribed to alignment errors, electronic noise, computational errors, and fabrication errors. Fortunately, they are not strong enough to obscure the image quality. Numerical studies on color accuracy as a function of noise level predict that a signal-to-noise ratio better than 20dB results in a color error of <10%.

6.6 Smaller Sensor Pixel

All the experiments and discussions so far are based on the 6μm sensor pixel. However, there is an emerging trend in both research and industry to reduce the size of the sensor pixels. Sensors with 1.67μm or even smaller pixels are commercially available and widely used. Such pixels suffer even more from poor light sensitivity. Here we show, using careful numerical studies, that our technology can drastically improve the sensitivity of such sensors as well.

First, we designed a new DFA, which has Δ=1μm and 5×5 squares in each unit cell. Each unit cell corresponds to one spatial pixel of the image and covers 3×3 sensor pixels with pixel size of Δ'=1.67um. This DFA also has a quasirandom topography, as depicted in Figure 6.6(a). The correlation function plotted in Figure 6.6(b) derived from the simulated SS-PSF at a gap of d=0.01mm indicates a spectral resolution of 44nm, which leads to a bandwidth-to-spectral-resolution ratio of 240nm/44nm=5.45. A test pattern is numerically synthesized and successfully reconstructed by regularization without any undersampling (Figures 6.6(c) and (d)). The spectrum of each point in the original object is numerically reconstructed by the pseudospectra of the R, G, and B channels. As anticipated, the DFA, together with the regularization algorithm, works well for the 1.67μm sensor pixel, except at the boundaries of abrupt color change, where cross-talk smears color accuracy. Scalar diffraction calculation estimates the lateral spread of the cross-talk (or spatial resolution) to be ~13μm. This is approximately 3 image pixels in our configuration, since one DFA unit cell is 5μm×5μm. Examples at five small areas (7×7 image pixels, or equivalently 35μm×35μm area) are summarized in Figure 6.6(e). At the boundaries of color change (areas #1, 2 and 3), severe color distortions are observed.

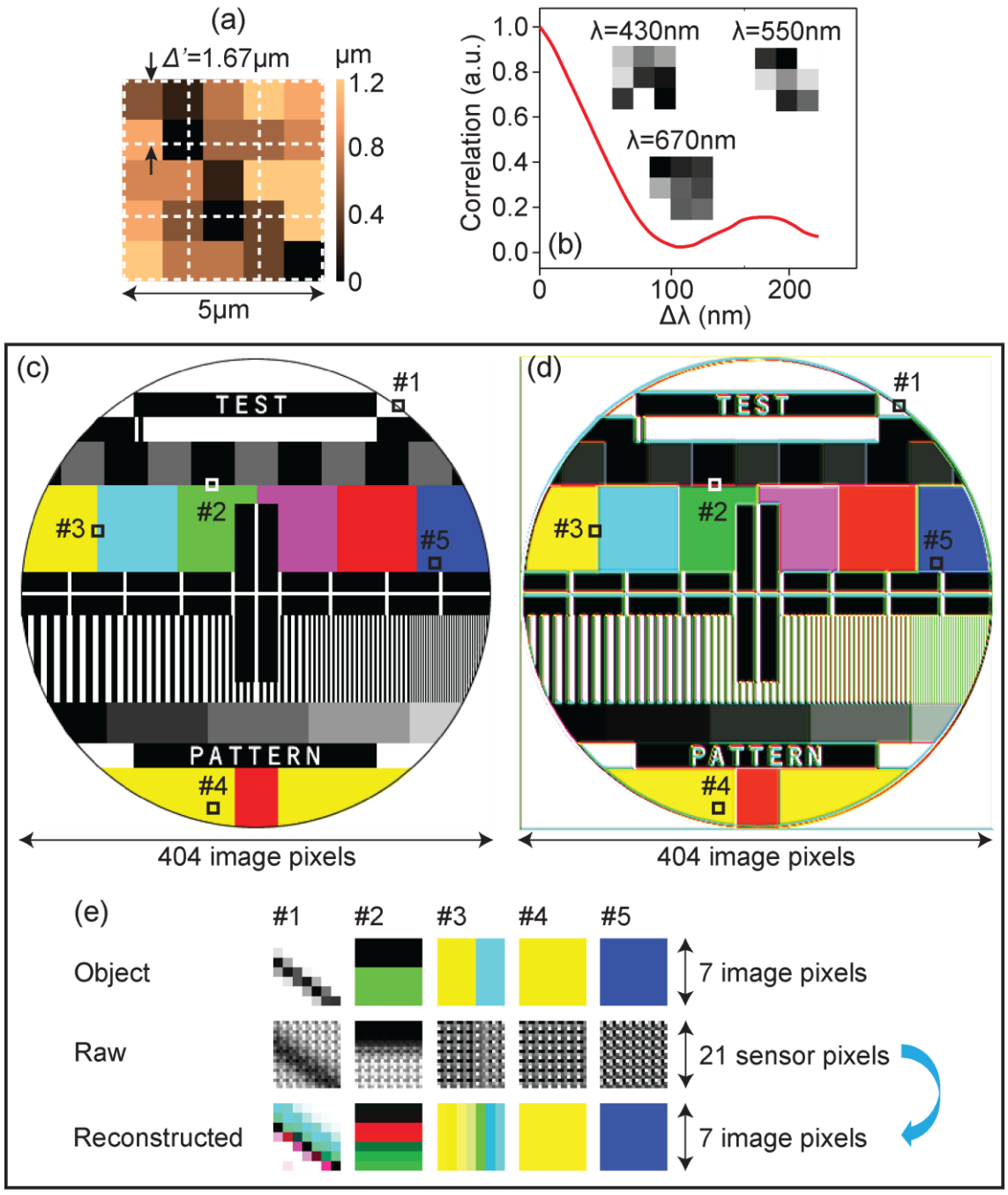

Figure 6.6. (a) Height profile of one unit cell of the DFA (5×5 1μm-squares) that covers 3×3 1.67μm-sensor pixels and represents one image pixel. Sensor pixels are delineated by dashed white lines. (b) Calculated spectral correlation function (insets: simulated SS-PSF received by one 3×3 sensor array at three representative wavelengths). Original test pattern (c) and the reconstructed image by regularization without undersampling (d). (e) The original objects, their numerically synthesized raw monochrome images and the reconstruction results at five small representative locations (7×7 image pixels) in the image.

The distortions are due to cross-talk effect. These ‘transition regions’ span around 3 image pixels, which is the same as that predicted by scalar diffraction computation. However, in the areas of uniform color (areas #4 and 5), our reconstructions demonstrate negligible distortion and noise. The absolute error between reconstruction and true images averaged over the entire image space is well below 5%. For this object of 404×404 image pixels, it takes roughly 30sec to complete reconstruction by regularization without implementing any parallel computation techniques on a Lenovo W540 laptop (Intel i7-4700MQ CPU @ 2.40GHz and 16.0GB RAM) for simplicity. Since each image pixel is independent without considerations of the cross-talk effect, the reconstruction algorithm can be highly parallelized and thus significantly accelerated using either multicore CPU or GPU chips and by storing calibration data in shared memory in advance. With the rapid evolution of microprocessor architecture and the development of semiconductor manufacturing, it will be prevalent and affordable to incorporate powerful computation units in imaging equipment.

Another critical benefit of using smaller sensor pixel is that the gap, *d*, can be significantly decreased, which is important for a compact sensor. In practice, this gap is limited by the thickness of the protective cover glass on the sensor chip. In principle, the DFA can be fabricated on the sensor chip directly [4,15].

In our approach, the spatial and spectral resolutions are traded off against one another via the gap *d*. Since both high spatial and spectral resolutions are desired in reality, we define a new parameter – resolution product (RP), which is the product of spatial and spectral resolutions. Figure 6.7(a) shows the simulated spatial and spectral resolutions as a function of *d* for the 1μm-square DFA (Figure 6.6(a)). Again, we assume uniform

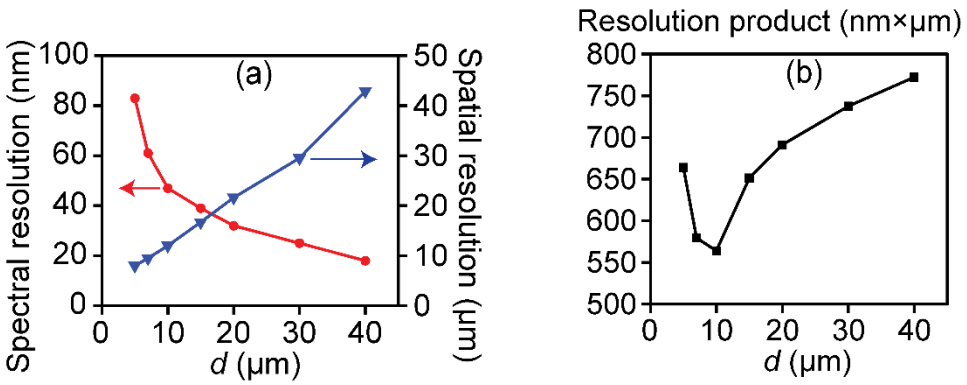

Figure 6.7. (a) Simulated spectral and spatial resolutions as a function of gap *d* for the 1μm-DFA in Figure 6.6(a). (b) Calculated resolution product at different gaps. The minimum occurs at *d*=0.01mm.

plane-wave illumination and a sample in proximity to the DFA substrate. Figure 6.7(b) plots the relationship between RP and *d*. Because the spectral resolution is a nonlinear function of *d* (increases rapidly at smaller *d* but decreases slowly at larger *d*), while the spatial resolution is approximately a linear function of *d*, there exists an optimum value, where the RP is minimized. In this case, the optimal point is at *d*~0.01mm. For this configuration, this gives the best choice of *d* at which both spatial and spectral resolutions are optimal.

6.7 Conclusion

We demonstrated a new color sensor that utilizes a transparent diffractive-filter array and computational methods. Our color sensor transmits significantly more light than conventional Bayer-sensors and we measured an increase in light sensitivity as high as 3.12. We applied two different computational techniques for color reconstruction. Diffractive-filters incur cross-talk, which limits the trade-off between spectral and spatial resolutions. We experimentally demonstrated a spatial resolution of 90μm and a spectral resolution of 53nm. Improvements in computational techniques by compensating for

cross-talk as well as oblique illumination can improve these trade-offs in the future. Simulations show its potential in sensors with pixel sizes of ~1.67μm. Our technique can also be used for single-shot hyperspectral imaging.

6.8 Supplementary Information

6.8.1 DFA-sensor assembly

The schematic of the DFA-sensor assembly is illustrated in Figure 6.8. Every critical dimension is labelled in detail. We are able to determine the gaps g=2.67mm, 2.87mm, and 3.87mm, between the front surfaces of optical mounts from the desired image distances d=0.3mm, 0.5mm, and 1.5mm, respectively. Note the custom-designed camera holder is machined out of a 2”-diameter Teflon rod. The assembly is fixed by M2 screws. The transparent cover film on top of the sensor is measured about 0.10mm thick.

6.8.2 Contact-imaging setup

In the color imaging experiment, we utilized the contact imaging mode (see Figure 6.9). The sample is color-printed on a piece of transparency. Then it is tightly glued upon a cleaned glass substrate. This is fixed on a cage mount and placed in proximity (~50μm) to the back side of the DFA substrate. The mount is controlled by a micrometer stage.

6.8.3 Color error tolerance

It is fundamental to understand how much color error is tolerable. Figure 6.10 shows a simple color error tolerance test. Different computer-generated random color errors in percentage of 256 levels (8-bit) are applied to three basic colors (blue, green, and red). Based on visual inspection, it seems that generally color errors below 10% are acceptable while errors beyond 10% give evident discrepancies.

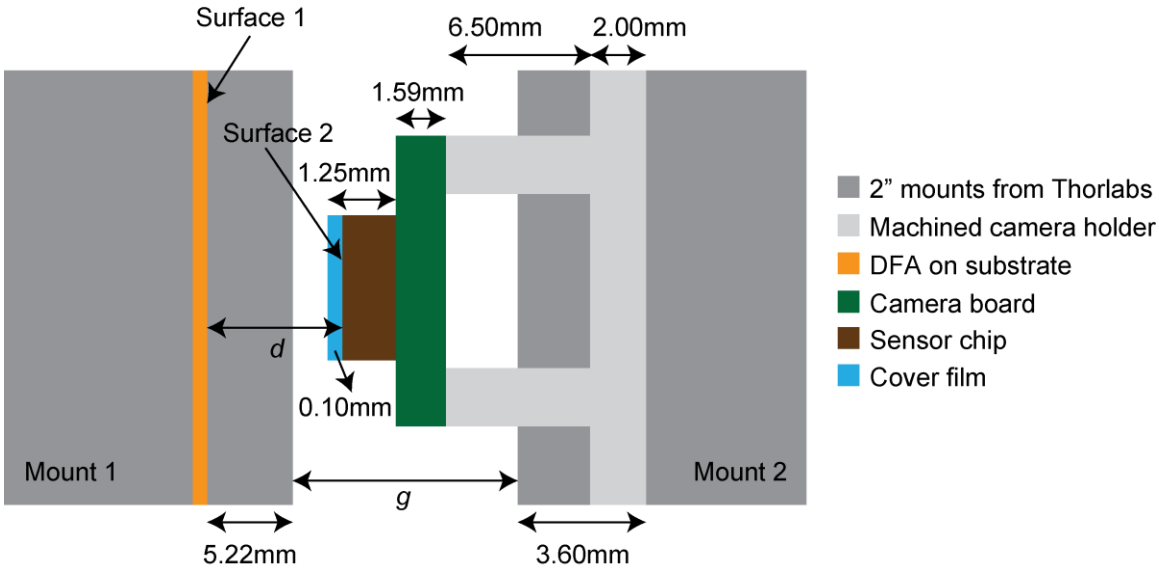

Figure 6.8. Configuration of the DFA-sensor assembly with labelled dimensions.

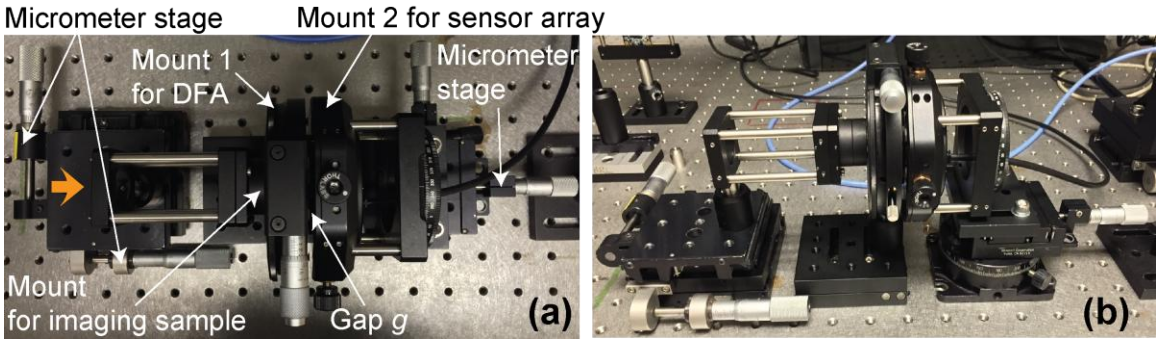

Figure 6.9. Photographs of the imaging setup. The expanded and collimated beam from a supercontinuum source illuminates from the left side. (a) Top view. (b) Side view.

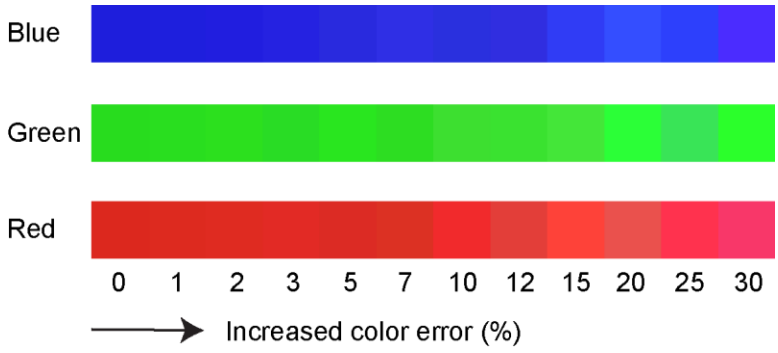

Figure 6.10. Color error tolerance test by adding random errors to three basic colors.

6.8.4 Cross-talk effect

Periodic boundary condition is assumed in the DFA device. Each repeating unit consists of 6×6 3μm pixels. Due to higher diffraction orders, light transmitted through one unit (or period) can affect its neighboring units. Basically, light spreads out. Therefore, an image from one unit represents actually the combined contributions from some of its neighboring units. Unless the color remains unchanged over a large number of units, the reconstructed color is compromised in accuracy. This is a cross-talk effect. It also dictates the ultimate spatial resolution. To evaluate this effect, we simulate diffraction patterns of one DFA unit at different propagation distances (Figure 6.11). Light with the longest wavelength possesses the greatest diffraction angle, therefore λ=700nm is considered. For d=0.3mm, the diffraction pattern is predominantly constrained within a region of about 90μm×90μm. For d=0.5mm and 1.5mm, the light energy is confined around the 150μm×150μm and 450μm×450μm regions.

To estimate spatial resolution, we conducted a test similar to Abbe's resolution criterion (Figure 6.12). Two diffraction patterns are placed next to each other at different displacements. To be consistent with our experiments, we assume the light source to be coherent. Take d=0.3mm, for example. When displacement is below 90μm, the two patterns interact with each other and it is difficult to distinguish them. The interference fringes at the boundary are very clear. When displacement goes beyond 90μm, there are negligible interactions. This critical displacement is taken as the spatial resolution.

6.8.5 Depth-of-focus

As previously mentioned, it is critical to make the gap d as close to the nominal value (used in SS-PSF calibration as well) as possible. Therefore, it is instructive to understand

the depth-of-focus of the DFA-sensor camera. We simulated color error (in % of the 256 levels) of the imaging system at various defocus locations, plotted in Figure 6.13. Applying a color error of 10% as the criterion, we can obtain depth-of-focus ±12μm, ±30μm, and ±60μm for three nominal gaps d=0.3mm, 0.5mm, and 1.5mm, respectively. These are well within the movement resolution of a commonly used micrometer stage (step size 10μm). Therefore, it is possible to control the gap between the DFA and the sensor with reasonable accuracy and thus achieve acceptable color reconstruction fidelity. The depth-of-focus is concluded to be linearly proportional to the gap d.

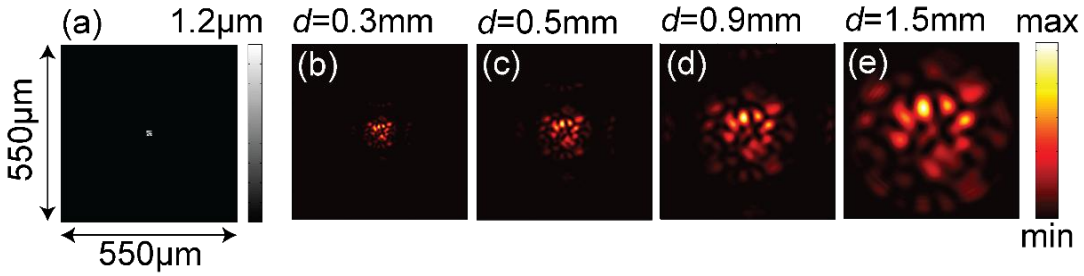

Figure 6.11. (a) Original design height distribution (18μm×18μm). (b)-(e) Simulated diffraction patterns of one single DFA unit at various distances d at λ=700nm.

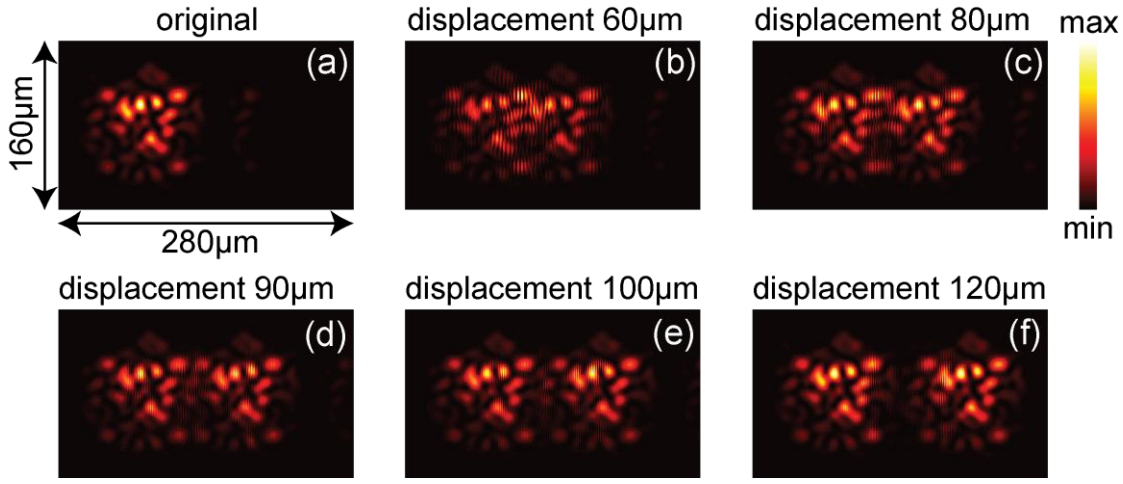

Figure 6.12. (a) Original diffraction pattern at d=0.3mm and λ=700nm. (b)-(f) Numerically synthesized diffraction patterns of two identical patterns separated by different displacements. 90μm is the critical displacement.

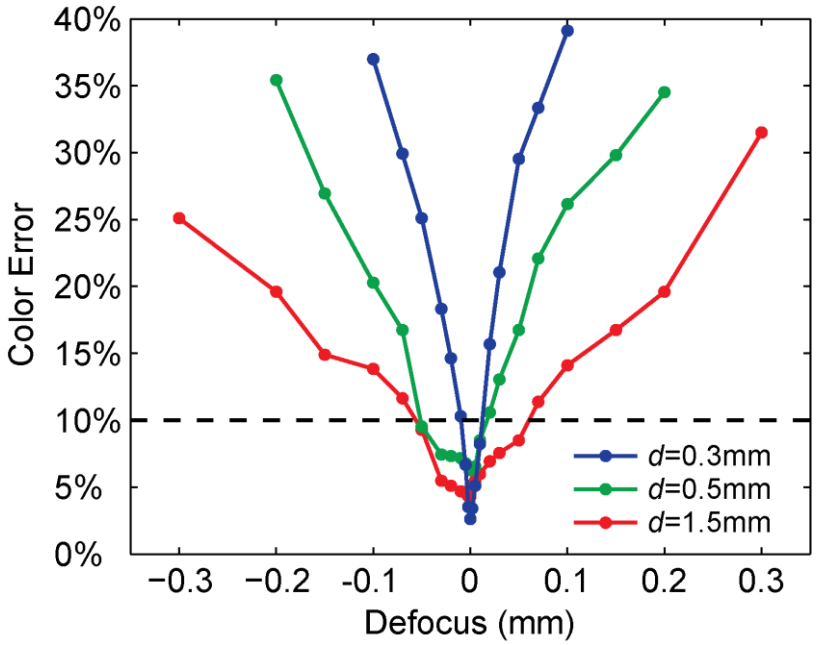

Figure 6.13. Plots of color errors in percentage versus defocus locations for three nominal gaps *d*=0.3mm (blue line), 0.5mm (green line), and 1.5mm (red line). The 10% color error tolerance threshold (black dashed line) is used.

6.8.6 Acceptance angle

Acceptance angle is important for diffraction devices since off-axis incidence imparts a phase shift to the wave-front that leads to a lateral shift of the diffraction pattern. Our calibration experiments assumed strictly normal incidence. An optical setup is devised to measure angular response. Here, lens 2, mounts 1 and 2 are fixed on a two-axis micrometer stage. Lens 1 first focuses the collimated beam, then off-axis illumination is created by moving lens 2, together with the DFA-sensor assembly, on the XY plane. Incident angles in two orthogonal coordinates are computed by $\theta x = \tan^{-1}(\Delta x/d)$ and $\theta y = \tan^{-1}(\Delta y/d)$, in which Δx and Δy are the movements relative to the central reference point (0,0).

An angular response function is defined by

$$R(\theta x,\theta y)=1-normalize(\sum_{x}\sum_{y}\left|I(\theta x,\theta y,x,y)-I(0,0,x,y)\right|). \qquad (6.3)$$

Here, $I(\theta x,\theta y,x,y)$ and $I(0,0,x,y)$ are the images at angle $(\theta x,\theta y)$ and normal incidence. Note that no sample is used. The second term in Equation (6.3) is the normalization over a set of angles $(\theta x,\theta y)$. The setup is in Figure 6.14. As shown in Figures 6.15(a)-(c), $R(\theta x,\theta y)$ drops with larger angles. This makes sense because as incoming light is more and more off normal, the image turns less and less similar to the one at normal incidence. By considering the angles at $R(\theta x,\theta y)$=0.5 as the acceptance angle θa, Figures 6.15(a)-(c) indicate that θa=0.19^{o}, 0.13^{o}, and 0.05^{o} for d=0.3mm, 0.5mm, and 1.5mm, respectively. They are all roughly equivalent to relative lateral shift of Δx~1μm. To guarantee the camera's performance, the angle of incidence has to be controlled within this limit.

6.8.7 Noise analysis

Alignment errors, electronic noises and computational errors all contribute to the discrepancies between the reconstructed color (or spectrum) and the true color (or spectrum) values. By numerically adding Gaussian noises with various standard deviations to the gray-scale raw images, Figure 6.16 summarizes the color errors (in percentage) versus the calculated signal-to-noise ratio (SNR) for different spectra. The spectra are randomly generated and the raw images are numerically synthesized with the knowledge of the calibrated SS-PSF. According to the 10% color error tolerance, they estimate a SNR threshold of 20dB ± 3dB.

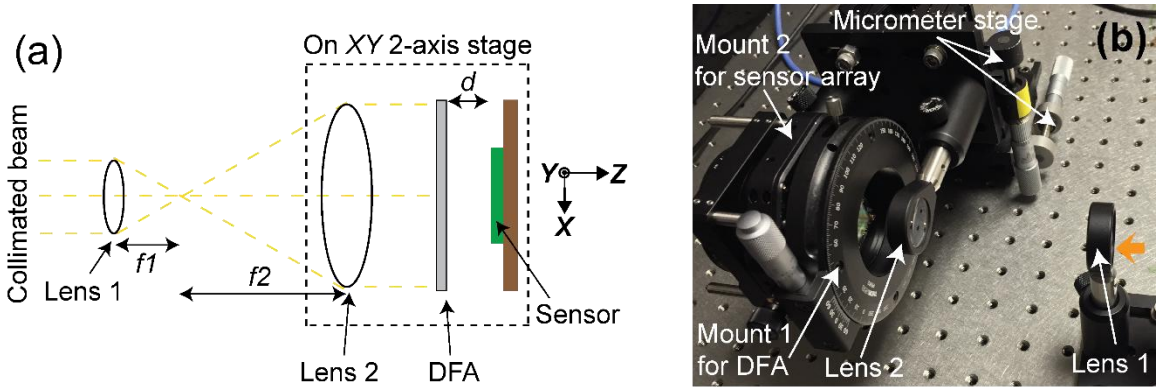

Figure 6.14. Schematic illustration (a) and photograph (b) of the angular response measurement setup.

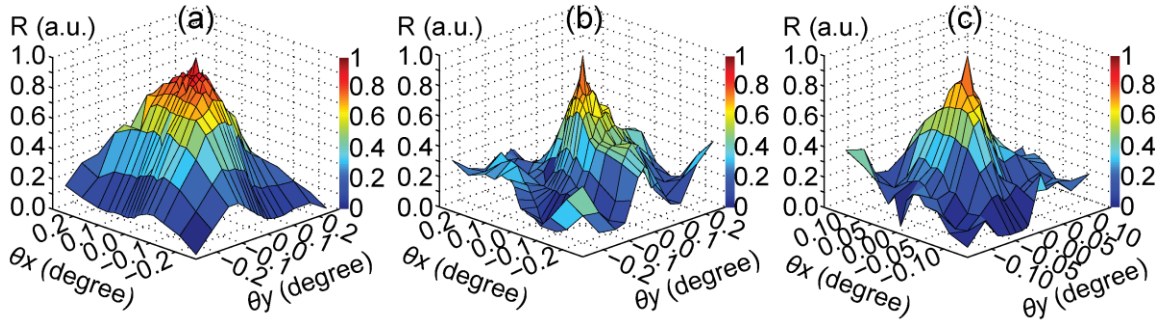

Figure 6.15. Measured angular response $R(\theta x,\theta y)$ at d=0.3mm (a), 0.5mm (b), and 1.5mm (c).

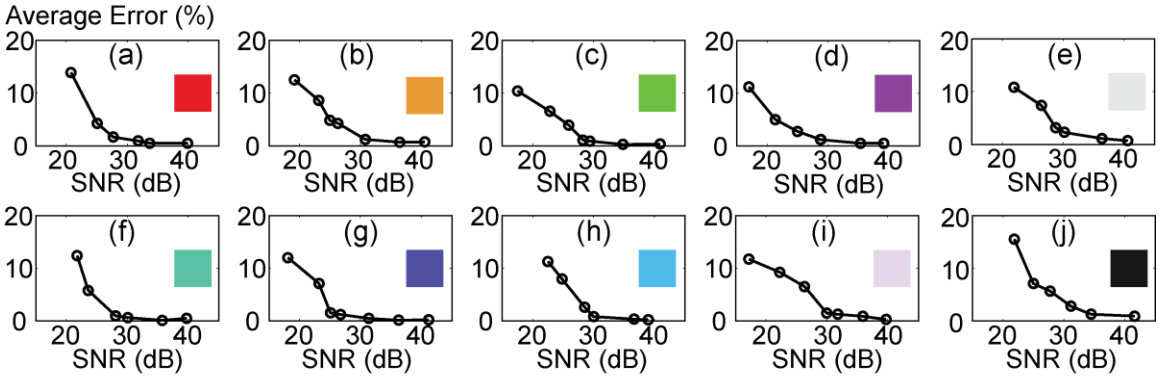

Figure 6.16. Color reconstruction error (in percentage) averaged over R, G, and B channels versus SNR levels for different random spectra (insets: the color of spectra).

6.9 References

[1] B. E. Bayer, "Color imaging array," US Patent 3,971,065 (1976).

[2] Y. Yu, L. Wen, S. Song, and Q. Chen, "Transmissive/Reflective structural color filters: theory and applications," J. Nanomater. 2014, (2014).

[3] N. Dean, "Colouring at the nanoscale," Nat. Photonics **10**, 15-16 (2015).

[4] P. B. Catrysee, and B. A. Wandell, "Integrated color pixels in 0.18-μm complementary metal oxide semiconductor technology," J. Opt. Soc. Am. A **20**, 2293-2306 (2003).

[5] K. Kumar, H. Duan, R. S. Hegde, S. C. W. Koh, J. N. Wei, and J. K. W. Yang, "Printing colour at the optical diffraction limit," Nat. Nanotechnology **7**, 557-561 (2012).

[6] Q. Chen, D. Das, D. Chitnis, K. Walls, T. D. Drysdale, S. Collins, and D. R. S. Cumming, "A CMOS image sensor integrated with plasmonic colour filters," Plasmonics **7**, 695–699 (2012).

[7] L. Lin, and A. Roberts, "Angle-robust resonances in cross shaped aperture arrays," Appl. Phys. Lett. **97**, 061109 (2010).

[8] E. Laux, C. Genet, T. Skauli, and T. W. Ebbesen, "Plasmonic photon sorters for spectral and polarimetric imaging," Nat. Photonics **2**, 161-164 (2008).

[9] S. Yokogawa, S. P. Burgos, and H. A. Atwater, "Plasmonic color filters for CMOS image sensor applications," Nano Lett. **12**, 4349-4354 (2012).

[10] S. P. Burgos, S. Yokogawa, and H. A. Atwater, "Color imaging via nearest neighbor hole coupling in plasmonic color filters integrated onto a complementary metal-oxide semiconductor image sensor," ACS Nano **7**, 10038-10047 (2013).

[11] K. Walls, Q. Chen, J. Grant, S. Collins, D. R. S. Cumming, and T. D. Drysdale, "Narrowband multispectral filter set for visible band," Opt. Express **20**, 21917–21923 (2012).

[12] A. F. Kaplan, T. Xu, and L. Jay Guo, "High efficiency resonance based spectrum filters with tunable transmission bandwidth fabricated using nanoimprint lithography," Appl. Phys. Lett. **99**, 143111 (2011).

[13] M. J. Uddin, and R. Magnusson, "Efficient guided-mode resonant tunable color filters," IEEE Photonics Technol. Lett. **24**, 1552–1554 (2012).

[14] L. Frey, P. Parrein, J. Raby, C. Pelle, D. Herault, M. Marty, and J. Michailos, "Color filters including infrared cut-off integrated on CMOS image sensor," Opt. Express

19, 13073–13080 (2011).

[15] S. Nishiwaki, T. Nakamura, M. Hiramoto, T. Fujii, and M. Suzuki, "Efficient colour splitters for high-pixel-density image sensors," Nat. Photonics **7**, 240–246 (2013).

[16] A. Wagadarikar, R. John, R. Willett, and D. Brady, "Single disperser design for coded aperture snapshot spectral imaging," Appl. Opt. **47**, B44-B51 (2008).

[17] M. Jayapala, A. Lambrechts, N. Tack, B. Geelen, B. Masschelein, and P. Soussan, "Monolithic integration of flexible spectral filters with CMOS image sensors at wafer level for low cost hyperspectral imaging," in *2013 International Image Sensor Workshop* (Snowbird, Utah, U.S.A.).

[18] L. J. Guo. "Recent progress in nanoimprint technology and its applications," J. Phys. D: Appl. Phys. **37**, R123-R141 (2004).

[19] M. D. Galus, E. Moon, H. I. Smith, and R. Menon, "Replication of diffractive-optical arrays via photocurable nanoimprint lithography," J. Vac. Sci. Technol. B **24**, 2960-2963 (2006).

[20] K. Reimer, H. J. Quenzer, M. Jurss, and B. Wagner, "Micro-optic fabrication using one-level gray-tone lithography," Proc. SPIE **3008**, 279-288 (1997).

[21] P. Wang, and R. Menon, "Computational spectrometer based on a broadband diffractive optic," Opt. Exp. **22**, 14575-14587 (2014).

[22] B. Redding, S. F. Liew, R. Sarma, and H. Cao, "Compact spectrometer based on a disordered photonic chip," Nat. Photonics **7**, 746-751 (2013).

[23] B. Redding, S. M. Popoff, and H. Cao, "All-fiber spectrometer based on speckle pattern reconstruction," Opt. Express **21**, 6584-6600 (2013).

[24] P. Wang, and R. Menon, "Computational spectroscopy via singular-value-decomposition and regularization," Opt. Exp. **22**, 21541-21550 (2014).

[25] P. Wang, and R. Menon, "Optimization of periodic nanostructures for enhanced light-trapping in ultra-thin photovoltaics," Opt. Express **21**, 6274-6285 (2013).

[26] B. Shen, P. Wang, R. Polson, and R. Menon, "An ultra-high efficiency metamaterial polarizer," Optica **1**, 356-360 (2014).

[27] B. Shen, P. Wang, R. Polson, and R. Menon, "An integrated-nanophotonics polarization beamsplitter with 2.4 × 2.4 μm2 footprint," Nat. Photonics **9**, 378-382 (2015).

[28] P. Wang, and R. Menon, "Optical microlithography on oblique and multiplane

surfaces using diffractive phase mask0s," J. Micro/Nanolith. MEMS MOEMS **14**, 023507 (2015).

[29] P. Wang, J. A. Dominguez-Caballero, D. J. Friedman, and R. Menon, "A new class of multi-bandgap high-efficiency photovoltaics enabled by broadband diffractive optics," Prog. Photovolt: Res. Appl. **23**, 1073-1079 (2015).

[30] P. Wang, C. G. Ebeling, J. Gerton, and R. Menon, "Hyper-spectral imaging in scanning-confocal-fluorescence microscopy using a novel broadband diffractive optic," Opt. Commun. **324**, 73-80 (2014).

[31] M. Mahy, L. Van Eycken, and A. Oosterlinck, "Evaluation of uniform color spaces developed after the adoption of CIELAB and CIELUV," Color Res. Appl. **19**, 105-121 (1994).

[32] J. W. Goodman, *Introduction to Fourier Optics.* (Roberts and Company Publishers, 2005).

CHAPTER 7

COMPUTATIONAL SINGLE-SHOT MULTISPECTRAL IMAGING

7.1 Abstract

Multispectral imagers reveal information imperceptible to humans and conventional cameras. Here, we demonstrate a compact single-shot multispectral video-imaging camera by placing a microstructured diffractive filter close to the image sensor. The diffractive filter converts spectral information to a spatial code on the sensor pixels. Following a calibration step, this code can be inverted via regularization-based linear algebra to compute the multispectral image. We experimentally demonstrated spectral resolution of 9.6nm within the visible band (430nm to 718nm). We further show that the spatial resolution is enhanced by over 30% compared to the case without the diffractive filter. Since no absorptive color filters are utilized, sensitivity is preserved as well. Finally, the diffractive filters can be manufactured using lithography and replication.

7.2 Introduction

Traditional imaging systems map one point in the object space to one point in the image space [1]. The point-spread function (PSF) is essentially determined by far-field diffraction and aberrations present in the system. Historically, advanced lens design and manufacturing techniques were developed to minimize all kinds of aberrations to achieve

the diffraction-limited PSF [1]. Over the past decades, several methods have been extensively explored to resolve subdiffraction features in super-resolution microscopy [2] by either shrinking the physical dimension of the PSF [3,4] or by using statistical estimation with preknowledge on the shape of the PSF [5,6]. However, these methods are not applicable to traditional imaging systems.

Electronic sensors can only detect light intensity. In order to distinguish colors, an absorbing color-filter array (generally called the Bayer filter) is placed on top of the sensor [7]. Typically, only three colors (blue, green and red) are measured. However, natural scenes contain multispectral information, which can be valuable for numerous applications. Conventional multispectral imagers (MSI) are expensive and cumbersome. A common MSI operates in a push-broom manner and utilizes a prism or grating to disperse light [8]. Its applications are limited to scenarios in which the MSI is scanned relative to the object such as on a satellite or on a conveyor belt. The optical design for such an MSI can be quite complex. A second category of MSI employs either liquid crystal tunable filters or acousto-optic tunable filters to modulate the input spectrum over time. The former filter suffers from reduced throughput and slow speed, while the latter is expensive and consumes a great deal of power [9,10]. All these techniques scan multiple 2D projections ((x,λ) or (x,y)) to acquire 3D multispectral data (x,y,λ), and hence, are slow. There is a need to acquire the 3D multispectral data in only one shot [11,12].

Single-shot multispectral imagers based on coded apertures have demonstrated reasonable image quality and spectral resolution [11,13]. However, the introduction of a patterned absorbing aperture, a dispersive element (prism), and relay optics increases the system size and complexity. Recently, multispectral sensors based on a tiled bandpass-

filter array have become commercially available. Fabry-Perot (FP) resonators are integrated on CMOS sensors to achieve spectral selectivity [14-16]. Unfortunately, these not only require expensive fabrication steps but also need precise alignment between the filter and the sensor and suffer from low sensitivity. These resonator-based filters may be replaced by plasmonics-based alternatives, but these incorporate subwavelength structures that are difficult to manufacture [17,18] and also suffer from low sensitivity due to parasitic absorption losses. Most importantly, tiled-filter-based imagers trade off spatial resolution with spectral resolution. Another popular method utilizes Fourier transform spectroscopy [19,20]. This technique is computationally intensive, since the interferogram is Fourier transformed to yield the spectrum. Furthermore, this method enforces a fundamental trade-off between spectral resolution and imaging speed, since higher resolution requires more interferogram images to be acquired.

In this chapter, we convert a conventional camera into a single-shot multispectral imager by inserting a thin diffractive filter in the near vicinity of the image sensor. By applying appropriate computational algorithms, we are able to achieve multispectral video imaging with improved spatial resolution. Our imager is schematically described in Figure 7.1. In a conventional imaging system under geometrical optics, the lens images single points (A & B) in the object plane (XY) onto single points (A' & B') in the image plane (X'Y'). In our system, we insert a thin diffractive filter in front of the image plane. Therefore, before converging to points A' and B', light is diffracted by the diffractive filter. The diffraction patterns received by the sensor, represented by the blue and red circles in Figure 7.1, are wavelength-dependent. The diffraction patterns also vary according to different spatial locations of their original points in the object plane (A &

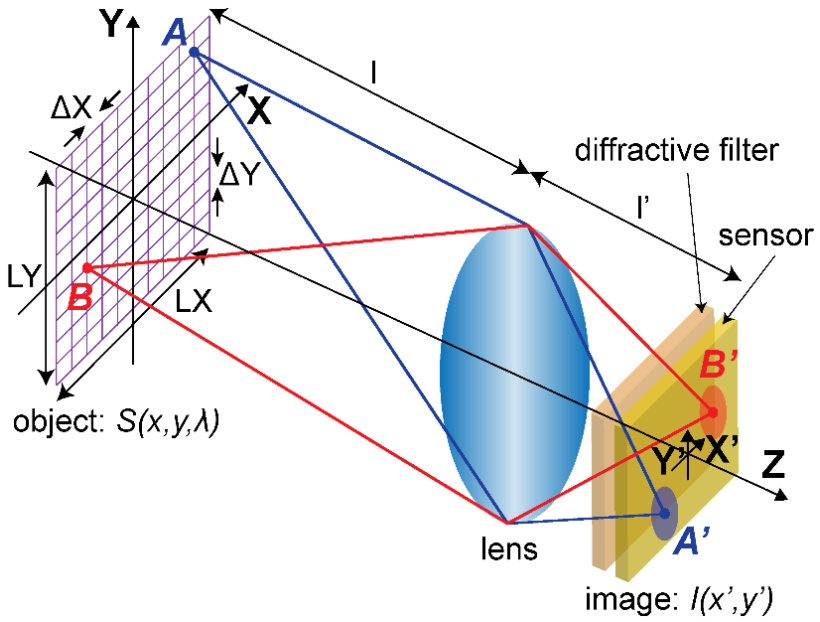

Figure 7.1. Schematic of the compact single-shot multispectral imager. A diffractive filter is placed in close proximity to the sensor. Due to diffraction through the filter, object points A and B are imaged to diffraction patterns (blue and red circles) surrounding points A' and B' on the sensor. The diffraction patterns depend on the wavelength and the spatial location of the object point.

B). The centers of the diffraction patterns, blue and red circles, still coincide with the points A' and B'. Therefore, one wavelength at one object point can uniquely corresponds to one diffraction pattern in the sensor plane.

7.3 Methods

According to the description above, the intensity distribution of the recorded image is basically a linear combination of the diffraction patterns of all the wavelengths at all the spatial points that contribute to the image. This can be expressed as a matrix multiplication: **I**=**AS**, where **S**(x,y,λ) is the unknown 3D multispectral data cube, **I**(x',y') is the intensity distribution of the 2D image on the sensor, and **A**$(x',y';x,y,\lambda)$ is the 5D matrix representing the response due to the diffractive filter. In our preliminary implementation, the object plane is discretized to 30×30 points, spaced by

$\Delta X=\Delta Y=120\mu m$ (purple grid in Figure 7.1). At each point, we compute 25 wavelengths between 430nm and 718nm in steps of 12nm. To experimentally calibrate the matrix, **A**, we mounted a pinhole on a 2D motorized stage to scan across the object grid and illuminated the pinhole by a supercontinuum source equipped with a tunable bandpass filter that selects the wavelengths (see Figure 2.18). Retrieving **S** from **A** and **I** is a typical inverse problem ($\mathbf{S}=\mathbf{A}^{-1}\mathbf{I}$) that can be readily solved via Tikhonov regularization [21]. Iterative algorithms are slow to converge and thus are not used here for video imaging [22,23]. Note that each frame is sufficient to obtain the multispectral data for that frame [11], and by piecing together multiple frames, multispectral video can be readily generated. The idea of extracting high-dimensional information from multiplexed data is adopted from previous work in computational spectroscopy [24-26].

The schematic of the diffractive filter is depicted in Figure 7.2(a). It is a 2D multilevel structure composed of a superlattice of period $P=18\mu m$ and constituent square pixel of size, $\Delta=3\mu m$ [27]. Each pixel is quantized into height levels and the maximum height is set to $1.2\mu m$ for ease of fabrication. Note that periodicity is not necessary in this application. For this preliminary demonstration, we simply chose the pixel heights from a pseudo-random set. The gap, *d*, between the diffractive filter (DF) and the sensor is approximately 0.5mm. We used a monochrome CMOS sensor (DMM22BUC03-ML, The Imaging Source) with sensor-pixel size $\Delta' = 6\mu m$. The DF is patterned in a transparent dielectric material (Shipley 1813 photoresist) coated on fused silica substrate via gray-scale lithography [28-30]. Figure 7.2(b) provides optical micrographs of the DF at two magnifications (VHX-5000, Keyence). The shadows in the images are created by oblique illumination to emphasize its 3D profile.

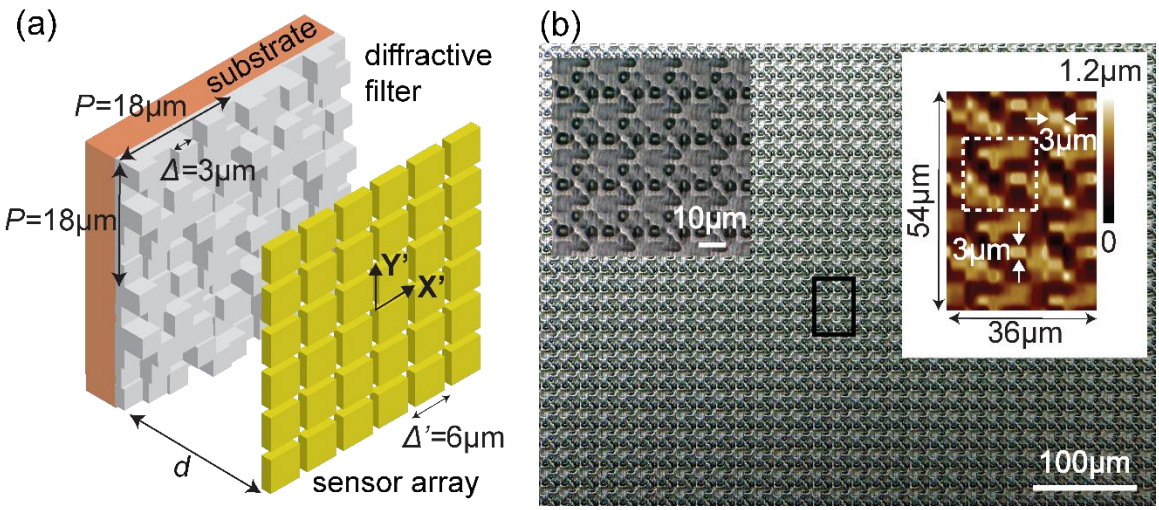

Figure 7.2. Diffractive filter. (a) Schematic of the assembly composed of the diffractive-filter (DF) and the sensor array. (b) Micrographs of the fabricated DF. Oblique illumination is applied to enhance contrast (left inset: images with larger magnifications; right inset: an atomic-force micrograph of the DF delimited by the black box in (b)).

An atomic force microscopy (AFM) image is shown as inset, where the white dashed square encloses one period and the 3μm features are clearly marked. A commercial lens (MVL12WA, Thorlabs) is placed in front of the DF.

Our first step is to measure the matrix **A**. This is achieved via a calibration setup (see Figure 2.18). A supercontinuum source (EXW6, NKT Photonics) is collimated and expanded, then illuminates the pinhole (diameter, φ=150μm). In order to ensure that the illumination overfills the aperture of the lens, the pinhole is mounted at the focus of an achromatic lens and a diffuser is glued to its back. The pinhole is stepped along the object grid (Figure 7.1) using a 2D stage (Z825B, Thorlabs). A tunable bandpass filter (VARIA, NKT Photonics) is used to select the wavelength for illumination. We utilized a bandwidth of 12nm for our experiments. Exemplary measured values of $\mathbf{A}(x',y';x,y,\lambda)$ are plotted in Figure 7.3(a). They are at five different object point locations (x,y) and four different wavelengths (λ). Note that this calibration only needs to be carried out once and

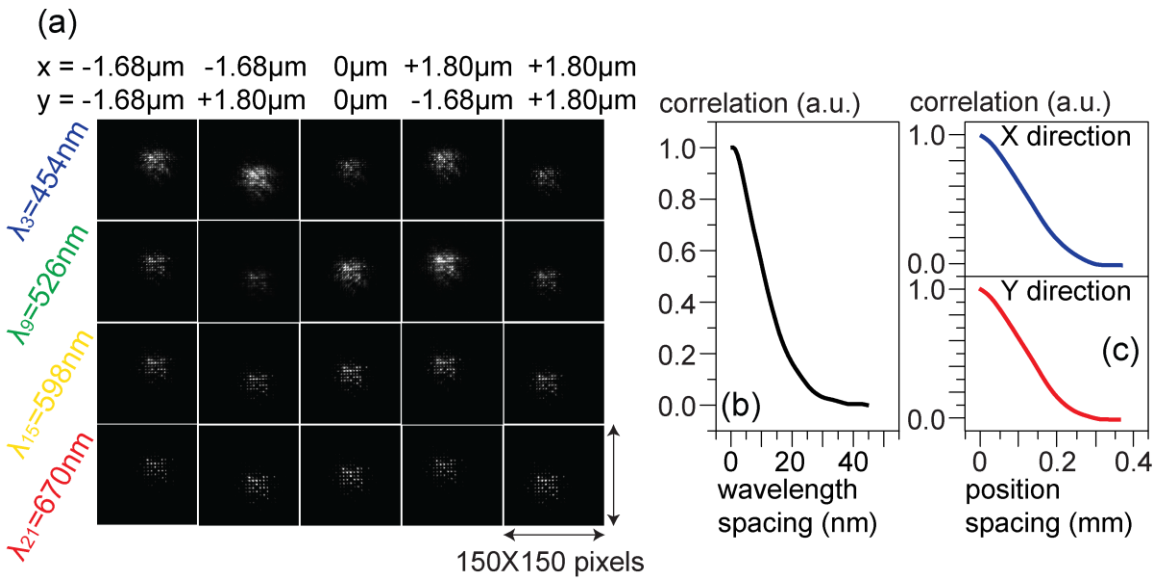

Figure 7.3. Calibration results. (a) Exemplary measured data for **A**(*x'*,*y'*; *x*,*y*,*λ*) at five spatial locations and four wavelengths. Each frame has 150×150 pixels. (b) Spectral correlation functions versus wavelength spacing. (c) Spatial correlation functions versus position spacing (top panel: X direction; bottom panel: Y direction). The wavelength scan step is 1nm and the spatial scan step is 10μm.

the data can be used for all frame reconstructions. As mentioned earlier, the data cube **S** has a dimension of 30×30×25=22500. In order to solve the inverse easily, **A** is defined as a square matrix and thus the raw image **I** needs to have a dimension of 150×150 pixels. They are cropped from the original camera images. From Figure 7.3(a), it is clear that the diffraction patterns changes with both wavelength and location. In other words, the point-spread function is both spatially and spectrally variant.

As in computational spectroscopy [24-26], we can compute the spatial and spectral resolutions via the cross-correlation between the diffraction patterns at the object coordinates, (*x*,*y*,*λ*). Figures 7.3(b) and (c) plot the spectral and spatial cross-correlation functions versus the sampling in the wavelength and spatial domains. The calculated spectral resolution, defined as the wavelength spacing when cross-correlation equals 0.5, is ~9.6nm. Note that this spectral resolution is slightly smaller than the spectral sampling

size, 12nm during calibration. The spatial resolution is defined in the same way. It is about 120μm, determined by the sampling (step) size of 120μm during calibration. Since the imaging lens provides a demagnification factor of 25×, the system should in theory have spatial resolution of 6μm×25=150μm for the 6μm sensor. The spectral and spatial resolutions are somewhat smaller than conventional values. This is due to the fact that our image reconstruction is analogous to fitting to a structured PSF, which can be theoretically shown to have a lower Cramer-Rao lower bound and thereby attain higher resolution. An example of such a technique that achieved higher spatial resolution in localization microscopy has been demonstrated before [31]. Here, we note that the similar principle operates in both the spectral and spatial domains. The employment of structured PSFs induced by diffraction also paves a new way for super-resolution microscopy.

7.4 Experimental Results

Various color images were displayed on the LCD screen of an iPhone 6 placed in the object plane. The raw monochrome data, $\mathbf{S}(x',y')$ are captured at exposure times to ensure that the sensor pixels are not saturated. A second optical path captured reference RGB images using the same lens and the same sensor chip but with the conventional Bayer filter array (DFM22BUC03-ML, The Imaging Source). Multispectral images were reconstructed as described earlier. Color (RGB) images were computed from the multispectral data for comparison to the reference images, using standard transmission functions for the Bayer-filter array. The results of six different objects are summarized in Figure 7.4. The multispectral data have 25 wavelengths, from 430nm to 718nm separated by 12nm and arranged into four rows (Figures 7.4(a) – (f)), roughly corresponding to blue, green, red, and near-infrared channels from top to bottom. The first example is a

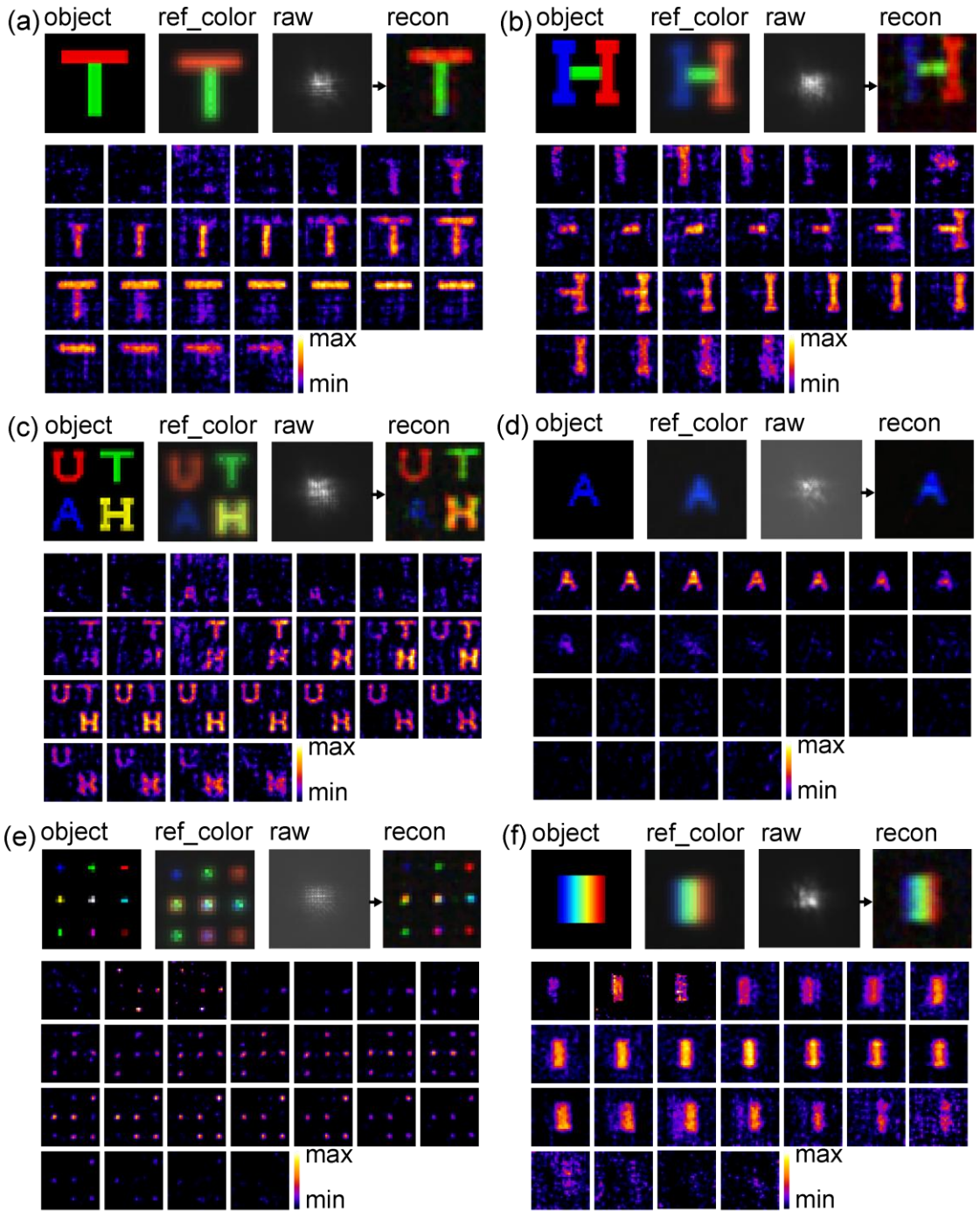

Figure 7.4. Experimental results of the multispectral frames and color images. The designed object patterns to be displayed, the reference RGB images, the raw monochrome images, and the reconstructed RGB images of the test patterns are shown as the top row. The normalized multispectral frames are plotted in the bottom four rows. The field-of-view is 3.6mm by 3.6mm. Six object patterns are tested: (a) 2-color letter 'T'; (b) 3-color letter 'H'; (c) 4-color letters 'UTAH'; (d) 1-color letter 'A'; (e) 7-color dot-array; (f) Rainbow.

2-color letter ‘T’. According to the multispectral images in Figure 7.4(a), the vertical green bar contains signals from λ=514nm to 598nm, while the top red bar contains signals from λ=586nm to 682nm. In the multispectral plots of Figure 7.4(b), the first, the second and the third rows contain blue, green, and red spectra of the left, the center and the right parts of the letter ‘H’, respectively. The plots of near-infrared in the fourth row are blurred and noisy due to low signal at those wavelengths. Figure 7.4(c) is an object of four letters, ‘U’ ‘T’ ‘A’ and ‘H’ of four different colors. The letter ‘A’ in the blue channel is not reconstructed properly, compared to the letters of other colors, primarily due to the brightness difference between the 4 color channels in the source (iPhone screen). Figure 7.4(d) illustrates excellent reconstruction of a single letter ‘A’ that consists of only one blue color. This indicates that applying high-dynamic-range algorithms and hardware will significantly improve the image quality. The nine-dot array in Figure 7.4(e) has more colors. The center white dot has signals contributed from all the wavelengths except the near-infrared row. The left middle yellow dot contains green and red spectra. The bottom purple dot has blue and red channels but leaves the green channel blank. Blue and green spectra contribute to the cyan dot at the right middle. The reconstructed spectra at the centers of the dots (normalized to its maximum) are plotted in Figure 7.5. The multispectral image of a rainbow is shown in Figure 7.4(f). The peak wavelength is red-shifted from left to right as expected. Our reconstructed images also suggest that we can attain better spatial resolution than the reference color camera. The shapes of the reconstructed color patterns are clearer and narrower than those of the reference. Extra noise in the reconstructed images is ascribed to mechanical alignment errors, sensor noise in both calibration and raw images, and inherent numerical errors of regularization

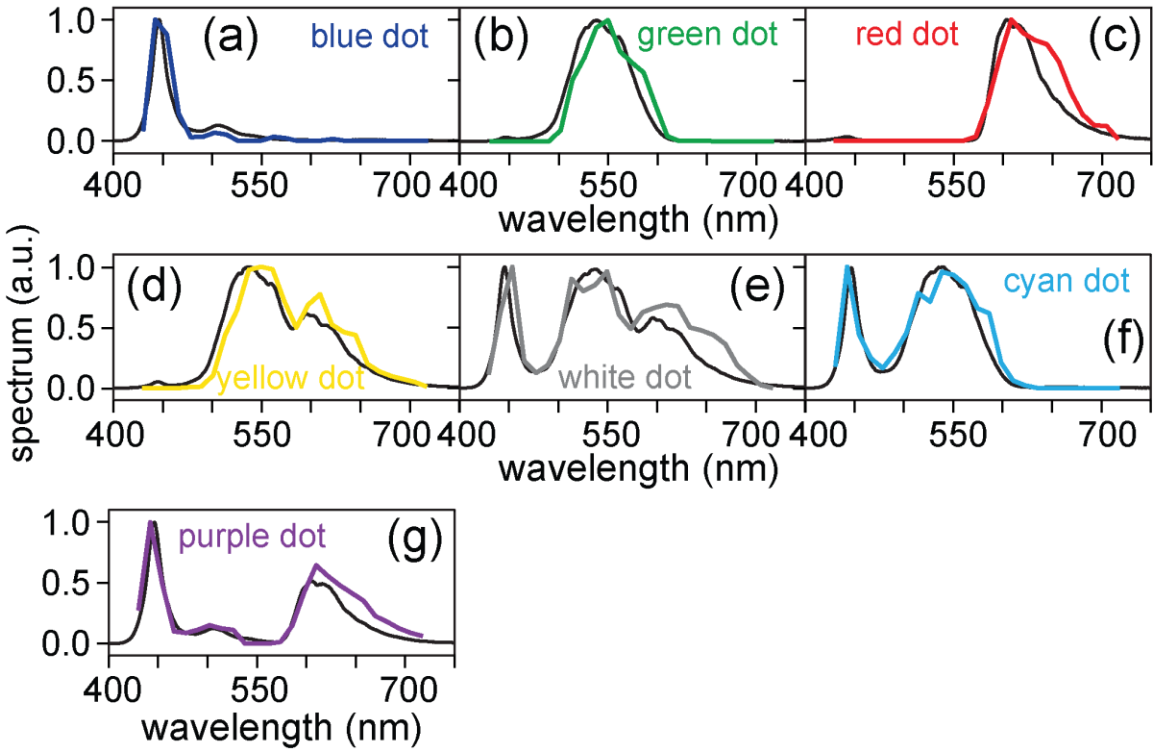

Figure 7.5. Normalized spectra of the dots of different colors in Figure 7.4(e).

algorithm. Currently, it takes ~1.3 sec to complete one frame reconstruction using regularization in MATLAB, running on a laptop workstation (Quad Intel i7 Core, 16GB RAM). Note that an optimal regularization parameter of ω=3.0 is used in all reconstructions. Further optimization of the reconstruction algorithm and hardware implementation will speed this up significantly.

We also made a short video combining different object patterns. Both the multispectral images and the color images can be reconstructed in almost real time using the proposed regularization-based algorithm. The reconstructed RGB color video matches with the original color video displayed on the iPhone screen quite well. Thereby, our DF-based imager prototype enables multispectral video-imaging, which is a strong advantage over previous technologies.

7.5 Analysis

7.5.1 Spatial resolution

To quantify the spatial resolution of our system, we measured its modulation transfer function (MTF). The object was composed of periodic lines of the same color. Since the iPhone 6 screen has a resolution of 326ppi (78μm pixel pitch), the minimum period of the test pattern was 2×78μm=156μm (or the maximum v=6.4cycles/mm in the spatial frequency domain). The measured MTFs along the X and Y axes, and three colors (blue, green, and red) are plotted in Figure 7.6(a). From the measured data, we observe that the spatial resolution (defined as the line-spacing where MTF = 0.1) is increased by 43% and 20% along the X and Y axes, respectively, averaged over the 3 colors, when compared to that obtained using the conventional Bayer filter in our reference camera. This is in stark contrast to conventional multispectral imagers, where spatial and spectral resolution are traded off against one another. Figure 7.6(b) shows the MTF test patterns and images at five different spatial frequencies and various colors. The reconstructed images have higher contrast when compared to the reference images. Although our default data type is the multispectral image, in Figure 7.6, only the reconstructed RGB color images are shown for simplicity.

As mentioned earlier, the increase in spatial resolution can be attributed to the use of a structured PSF. Our reconstruction of the multispectral image is analogous to the fitting of a point image to a PSF in localization microscopy [31]. In the same manner in which the localization precision is improved due to the structured PSF, here we attain increased spatial and spectral resolution when compared to the reference. This can be analyzed theoretically via the Cramer-Rao Lower Bound (CRLB).

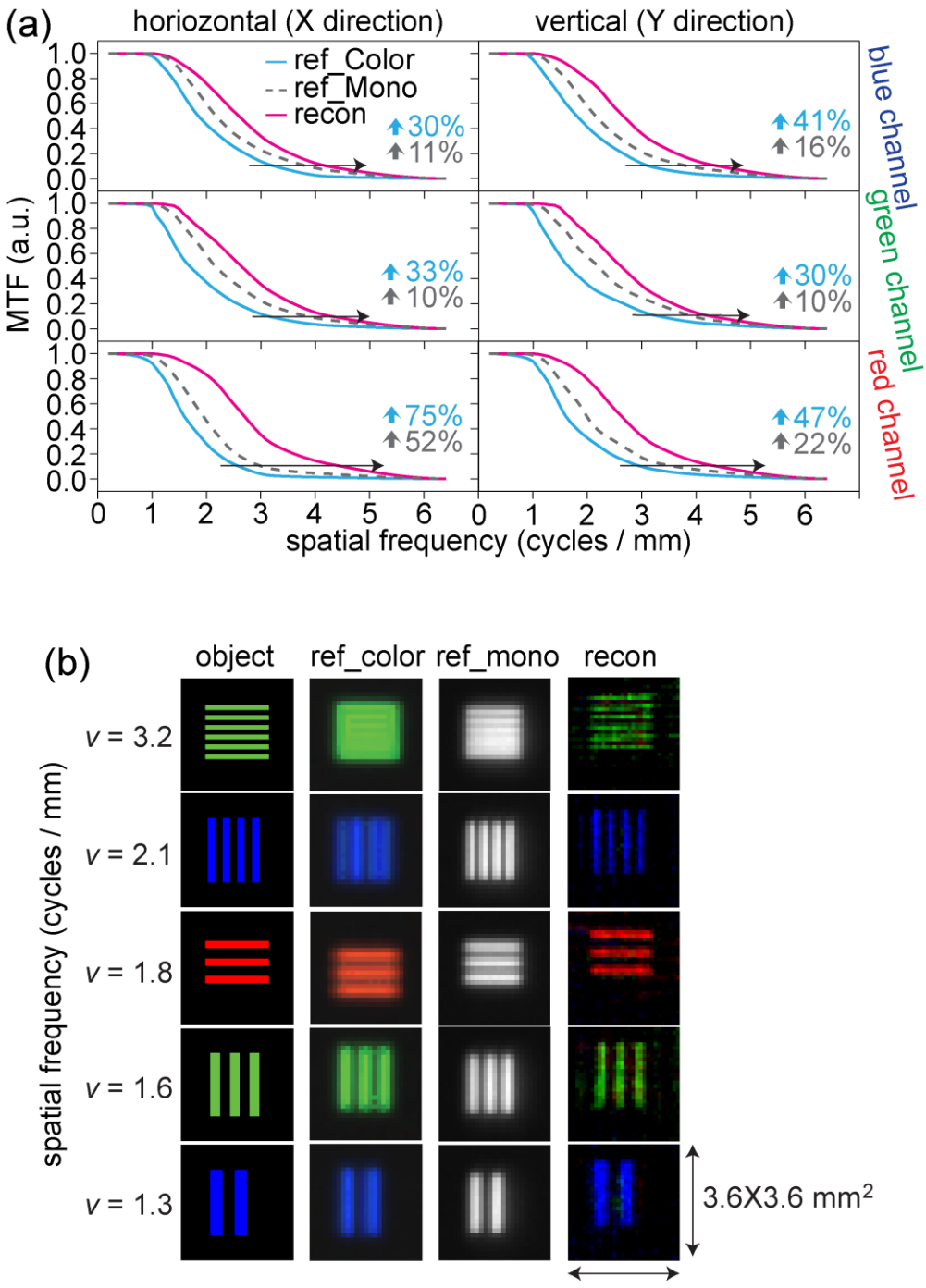

Figure 7.6. Results of spatial resolution tests. (a) Measured Modulation Transfer Functions (MTFs) in X and Y axes and three primary color channels. (b) Exemplary test object patterns at five spatial frequencies: their reference images by color and monochrome cameras and the reconstruction results.

7.5.2 Noise

Since our camera is based upon computational reconstruction, noise introduced by the operations during the reconstruction process has to be clarified. We studied the impact of noise by performing careful simulations, the results of which are summarized in Figure 7.7. Specifically, we manually added random noise (from a Gaussian distribution) of different standard deviations to a numerically synthesized sensor image, $\mathbf{I}(x',y')$, which is generated using the calibrated PSFs, $\mathbf{A}$, and the multispectral object, $\mathbf{S}(x,y,\lambda)$, via $\mathbf{I}=\mathbf{AS}$. The system is then inverted to compute the multispectral image using regularization as before. The multispectral image is then converted to the RGB color image. Finally, the error between the reconstructed color image and the object in three color channels, averaged over the entire image, is computed. Based on the curve of error versus signal-to-noise ratio (SNR), an SNR tolerance threshold of ~13dB (or equivalently 12 grayscale values for an 8-bit sensor) is estimated.

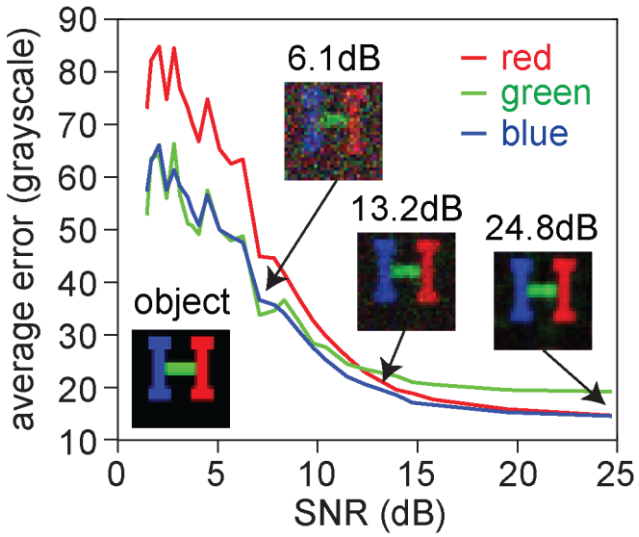

Figure 7.7. Averaged image reconstruction error versus signal-to-noise ratio (SNR) in three basic color channels. Gaussian noise is added to the numerically synthesized sensor image to change the SNR.

7.5.3 Depth-of-field and 3D imaging

Depth-of-field is another critical specification of any camera. To experimentally measure the depth-of-field, the multispectral PSFs were first captured at various planes of the object (the pinhole) corresponding to various values of defocus. Then, the root-mean-squares (RMS) of the differences between the PSF images at a given defocus and those at zero defocus were computed (see Figure 7.8(a)). As expected, the RMS increases with larger defocus and a depth-of-field (DOF) of ±15mm is predicted according to the 13dB threshold (or 12 grayscale, see Figure 7.7).

An important feature of our camera is the possibility of computational refocusing and extension to 3D multispectral imaging [32]. A simple experimental demonstration of this feature is illustrated in Figure 7.8(b). We first measured the multispectral PSFs at various planes that were displaced from the in-focus object plane, similar to the experiment performed for measuring the depth-of-field above. Then, a multispectral object was imaged at a plane that was shifted by 20mm from the in-focus object plane. As expected, the multispectral image computed using in-focus PSF data is distorted with significant color errors and noise. However, the correct multispectral image can be computationally obtained by simply using the PSF data from the defocus plane (+20mm). This points to the possibility of generating 3D multispectral images by calibrating the 3D space with the multispectral PSF data. However, the caveat is that this requires a lot more data as well as more computation.

7.5.4 Polarization-independence

For a general imaging system, it is important that the diffractive filter is polarization-insensitive. Many alternative color filters, such as those using plasmonics, suffer from

this major disadvantage of being polarization-sensitive [17,18]. To illustrate this, we experimentally captured the PSF at two orthogonal polarizations and verified that they are indeed identical. The magnified views of two diffraction patterns of the same multispectral object point (x=0, y=0, λ=550nm) illuminated by two orthogonal polarization states (TE and TM) are shown in Figure 7.9. Note that in all our calibration experiments above, we utilized randomly polarized light. However, an iPhone screen of almost linear polarization is used in imaging.

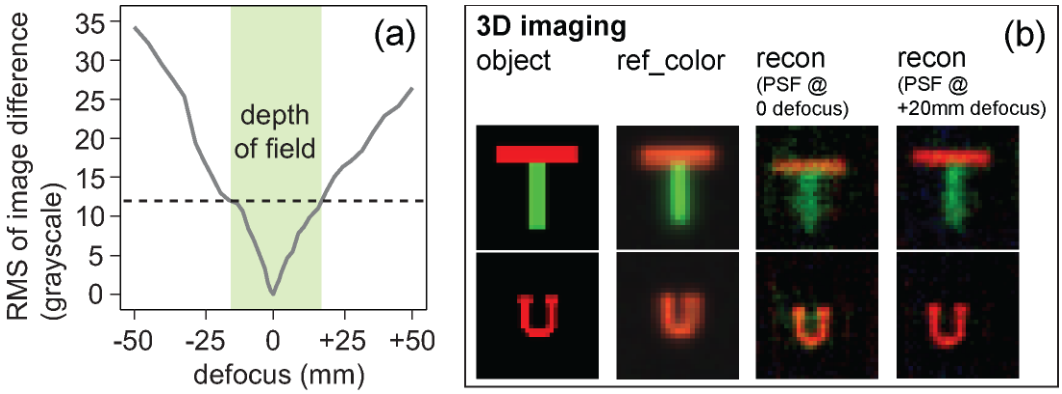

Figure 7.8. Depth-of-field analysis. (a) Root mean squares (RMSs) of differences between the PSF images with and without defocus. A depth-of-field is estimated (light green region). (b) Two experimental examples for 3D imaging: the 2-color letter 'T' and the 1-color letter 'U'.

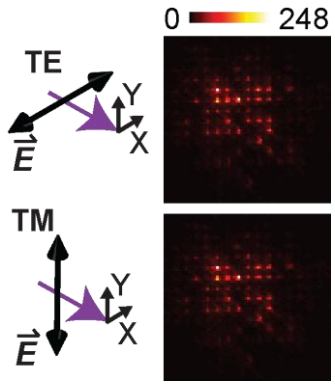

Figure 7.9. Magnified views of the experimentally calibrated PSFs illuminated by two polarization states. TE and TM polarizations are defined on the left side. They are of the same object point and the same wavelength. They are both 70×70 sensor pixels.

7.5.5 Dynamic range

Finally, we characterized the dynamic range of our camera. The reconstructed color images across a wide range of exposure times are summarized in Figure 7.10. The corresponding maximum pixel values in the raw monochrome images are listed as well. 17.86ms is the critical exposure time. The reconstructed images remain acceptable down to 5ms exposure time and becomes much too noisy beyond 2ms, where SNR is reduced drastically. Overexposure (>25ms) also deteriorates the reconstruction because more and more pixels are saturated and therefore the assumption of linearity breaks down. A high-dynamic-range (HDR) algorithm [32] may help to improve its performance remarkably.

7.6 Larger Field of view

In our preliminary demonstration here, the image size is restricted to 3.6mm×3.6mm, since the PSF is only calibrated over 30×30 object points with step size of 120μm. This is not a fundamental limitation of the technology, but was chosen for simplicity and to ensure fast reconstruction times. A simple approach to increase the image size can be demonstrated by using a sparse image composed of small blocks of color data as illustrated in Figure 7.11(a). The blocks are spaced such that we can treat them independently. This constraint can be removed in the future by accounting for the space overall in the reconstruction algorithms as was discussed previously [27]. Then each block (3.6mm×3.6mm) was calibrated and solved individually. The results are summarized in Figure 7.11(b). The reconstructed RGB color images of the other blocks are also shown. In any case, by further optimizing the calibration process and the reconstruction algorithms, it will be possible to perform fast multispectral full-frame video imaging in the future.

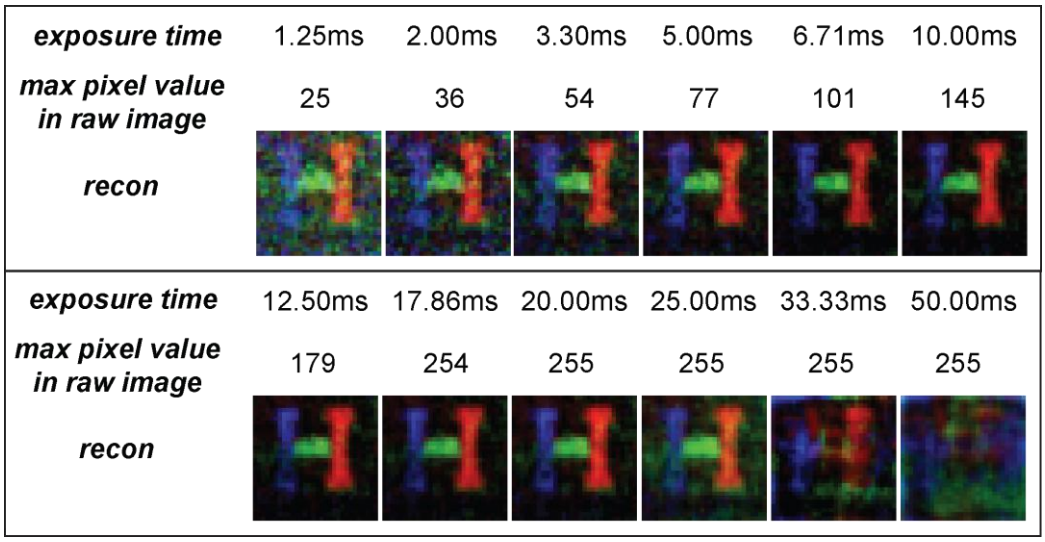

Figure 7.10. Reconstruction results of the 3-color letter 'H' object pattern at various exposure times. The maximum pixel values in their raw images are given.

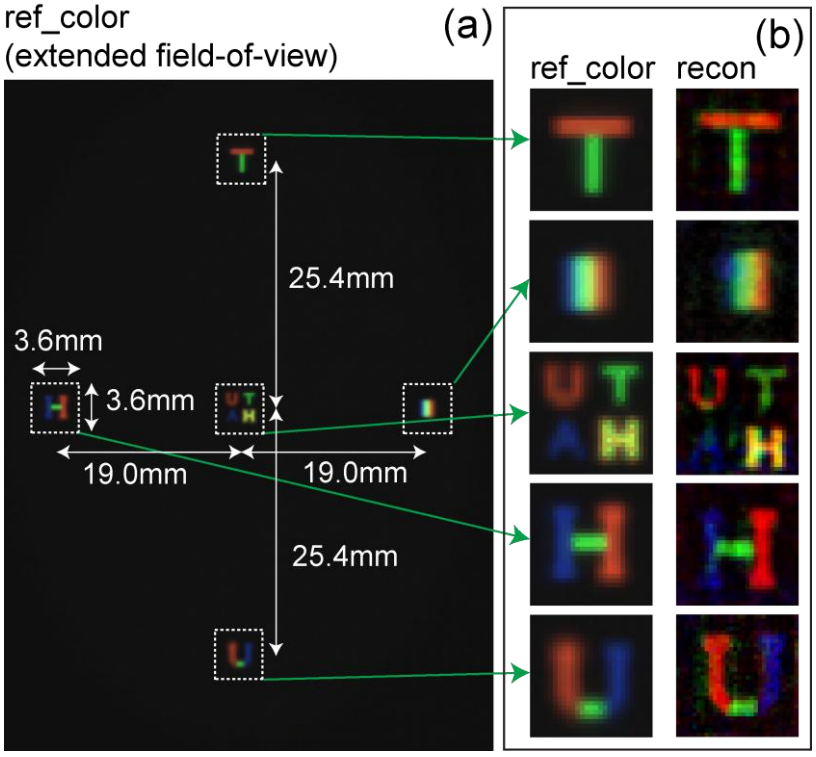

Figure 7.11. Experimental results on test patterns over a larger frame. Five small test patterns are included. (a) Reference color image of the whole pattern. The FOV of small patterns and the distance between them are labeled. (b) Reference color images of the individual small patterns and their reconstructed RGB color images.

7.7 Conclusion

In conclusion, we demonstrated computational single-shot multispectral imaging that preserves both spectral and spatial resolution by simply placing a diffractive filter atop the conventional sensor array and applying linear reconstruction algorithms. The system exhibits a spatially and spectrally variant PSF, where each multispectral object point (x,y,λ) is mapped to a set of sensor pixels (x',y'). This one-to-many mapping can be inverted via regularization, since it is a linear transfer function. The inversion process allows us to compute the multispectral image. We experimentally demonstrated spectral resolution of 9.6nm and spatial resolution of 4.2cycles/mm, which is higher than what can be achieved with the conventional camera. Since our diffractive filter does not absorb any light, the sensor utilizes all incoming photons. This is in contrast to the conventional color camera, where on average, 2/3rds of the light is unused due to absorption in the Bayer filter. By removing the Bayer filter, we further make the CMOS sensor fully compatible with the silicon fabrication process that is widespread in electronics. We also raise the intriguing possibility of computational 3D multispectral imaging with the extension to the computational acquisition of the multispectral light-field. Finally, we reiterate that our technology is equally applicable to any portion of the electromagnetic regime as long as the sensor demonstrates sufficient sensitivity.

7.8 References

[1] M. Born, and E. Wolf, *Principles of Optics: Electromagnetic Theory of Propagation, Interference and Diffraction of Light* (Cambridge University Press, 1999).

[2] S. W. Hell, "Microscopy and focal switch," Nat. Methods **6**, 24-32 (2009).

[3] S. W. Hell, and J. Wichmann, "Breaking the diffraction resolution limit by stimulated emission: stimulated-emission-depletion fluorescence microscopy," Opt. Lett.

19, 780-782 (1994).

[4] T. L Andrew, H-Y. Tsai, and R. Menon, "Confining light to deep subwavelength dimensions to enable optical nanopatterning," Science **324**, 917-921 (2009).

[5] M. J. Rust, M. Bates, and X. Zhuang, "Sub-diffraction-limit imaging by stochastic optical reconstruction microscopy (STORM)," Nat. Methods **3**, 793 - 796 (2006).

[6] E. Betzig, G. H. Patterson, R. Sougrat, O. W. Lindwasser, S. Olenych, J. S. Bonifacino, M. W. Davidson, J. Lippincott-Schwartz, and H. F. Hess, "Imaging intracellular fluorescent proteins at nanometer resolution," Science **313**, 1642-1645 (2006).

[7] B. E. Bayer, "Color imaging array," US Patent 3,971,065 (1976).

[8] P. Mouroulis, R. O. Green, and T. G. Chrien, "Design of pushbroom imaging spectrometers for optimum recovery of spectroscopic and spatial information," Appl. Opt. **39**, 2210-2220 (2000).

[9] N. Gat, "Imaging Spectroscopy Using Tunable Filters: A Review," Proc. SPIE **4056**, 50-64 (2000).

[10] F. Sigernes and etc., "Hyperspectral all-sky imaging of auroras," Opt. Express **20**, 27650-27660 (2012).

[11] N. Hagen, and M. W. Kudenov, "Review of snapshot spectral imaging technologies," Opt. Eng. **52**, 090901 (2013).

[12] T. Okamoto, and I. Yanaguchi, "Simultaneous acquisition of spectral image information," Opt. Lett. **16**, 1277-1279 (1991).

[13] A. Wagadarikar, R. John, R. Willett, and D. Brady, "Single disperser design for coded aperture snapshot spectral imaging," Appl. Opt. **47**, B44-B51 (2008).

[14] M. Jayapala, A. Lambrechts, N. Tack, B. Geelen, B. Masschelein, and P. Soussan, "Monolithic integration of flexible spectral filters with CMOS image sensors at wafer level for low cost hyperspectral imaging," in *2013 International Image Sensor Workshop* (Snowbird, Utah, U.S.A.).

[15] N. Gupta, P. R. Ashe, and S. Tan, "Miniature snapshot multispectral imager," Opt. Eng. **50**, 033203 (2011).

[16] K. Walls, Q. Chen, J. Grant, S. Collins, D. R. S. Cumming, and T. D. Drysdale, "Narrowband multispectral filter set for visible band," Opt. Express **20**, 21917–21923 (2012).

[17] E. Laux, C. Genet, T. Skauli, and T. W. Ebbesen, "Plasmonic photon sorters for spectral and polarimetric imaging," Nat. Photonics **2**, 161-164 (2008).

[18] S. Yokogawa, S. P. Burgos, and H. A. Atwater, "Plasmonic color filters for CMOS image sensor applications," Nano Lett. **12**, 4349-4354 (2012).

[19] R. Bhargava, and I. W. Levin, "Fourier transform infrared imaging: theory and practice," Anal. Chem. **73**, 5157–5167 (2001).

[20] E. N. Lewis, A. M. Gorbach, C. Marcott, and I. W. Levin, "High-fidelity Fourier transform infrared spectroscopic imaging of primate brain tissue," Appl. Spectrosc. **50**, 263-269 (1996).

[21] P. Wang, and R. Menon, "Computational spectroscopy via singular-value-decomposition and regularization," Opt. Express **22**, 21541-21550 (2014).

[22] P. Wang, and R. Menon, "Optimization of periodic nanostructures for enhanced light-trapping in ultra-thin photovoltaics," Opt. Express **21**, 6274-6285 (2013).

[23] B. Shen, P. Wang, R. Polson, and R. Menon, "An integrated-nanophotonics polarization beamsplitter with 2.4 × 2.4 μm2 footprint," Nat. Photonics **9**, 378-382 (2015).

[24] B. Redding, S. F. Liew, R. Sarma, and H. Cao, "Compact spectrometer based on a disordered photonic chip," Nat. Photonics **7**, 746-751 (2013).

[25] B. Redding, M. Alam, M. Seifert, and H. Cao, "High-resolution and broadband all-fiber spectrometers," Optica **1**, 175-180 (2014).

[26] P. Wang, and R. Menon, "Computational spectrometer based on a broadband diffractive optic," Opt. Express **22**, 14575-14587 (2014).

[27] P. Wang, and R. Menon, "Ultra-high-sensitivity color imaging via a transparent diffractive-filter array and computational optics," Optica **2**, 933-939 (2015).

[28] P. Wang, J. A. Dominguez-Caballero, D. J. Friedman, and R. Menon, "A new class of multi-bandgap high-efficiency photovoltaics enabled by broadband diffractive optics," Prog. Photovolt: Res. Appl. **23**, 1073-1079 (2015).

[29] P. Wang, and R. Menon, "Optical microlithography on oblique and multiplane surfaces using diffractive phase masks," J. Micro/Nanolith. MEMS MOEMS **14**, 023507 (2015).

[30] K. Reimer, H. J. Quenzer, M. Jurss, and B. Wagner, "Micro-optic fabrication using one-level gray-tone lithography," Proc. SPIE **3008**, 279-288 (1997).

[31] C. G. Ebeling, A. Meiri, J. Martineau, Z. Zalevsky, J. M. Gerton, and R. Menon, "Increased localization precision by interference fringe analysis," Nanoscale **7**, 10430-10437 (2015).

[32] G. Kim, and R. Menon, "An ultra-small three dimensional computational microscope," Appl. Phys. Lett. **105**, 061114 (2014).

[33] M. D. Galus, E. Moon, H. I. Smith, and R. Menon, "Replication of diffractive-optical arrays via photocurable nanoimprint lithography," J. Vac. Sci. Technol. B **24**, 2960-2963 (2006).

[34] L. J. Guo. "Recent progress in nanoimprint technology and its applications," J. Phys. D: Appl. Phys. **37**, R123-R141 (2004).

CHAPTER 8

OTHER WORKS ON NANOPHOTONICS PART 1:

LIGHT TRAPPING

This chapter is adapted from the author's previous publication: Peng Wang and Rajesh Menon, "Optimization of generalized dielectric nanostructures for enhanced light trapping in thin-film photovoltaics via boosting the local density of optical states," Opt. Express **22** A99-A110 (2014).

8.1 Abstract

Recent work has shown that using a high-index cladding atop a lower-index photovoltaic absorber enables absorption of light beyond the ergodic ($4n^2$) limit. In this chapter, we propose a generalized optimization method for deriving optimal geometries that allow for such enhancement. Specifically, we adapted the direct-binary-search algorithm to optimize a complex 2D multilayer structure with the explicit goal of increasing photocurrent. We show that such an optimization results in enhancing the local density of optical states in an ultrathin absorber, which forms a slot-waveguide geometry in the presence of a higher-index overcladding. Numerical simulations confirmed optical absorption approaching 100% and absorption-enhancement beyond the ergodic ($4n^2$) limit for specific spectral bands of interest. Our method provides a direct, intuitive and computationally scalable approach for designing light-trapping nanostructures.

8.2 Introduction

Photovoltaic devices with ultrathin absorbers allow for high charge-transport and carrier-collection efficiencies [1,2]. Furthermore, such devices could be manufactured with inexpensive scalable technologies [3]. Recent improvements in material quality have resulted in world-record device efficiencies of 20.4%, 18.7%, and 12% for CIGS, CdTe, and organic absorbers, respectively [4,5]. However, ultrathin layers are intrinsically poor absorbers of incident sunlight. Previously, random or simple geometries of micro- and nano-structures were utilized to scatter normally incident light at large angles into the absorber layer [6-9]. The resulting increased optical path lengths lead to higher absorption. It was pointed out that for thick absorbers, light absorption may be enhanced compared to an unpatterned absorber by a factor of up to $4n^2$, where n is the refractive

index of the absorber, called the ergodic limit [10-12].

Recent theoretical work suggested that light absorption might be enhanced beyond this limit in the case of absorbers with deep subwavelength thicknesses [13-16]. Specifically, this may be achieved in the case of an ultrathin absorber that is sandwiched between two cladding layers with a higher refractive index. This slot-waveguide configuration results in an increased local density of optical states (LDOS) into which incident light may couple [15,16]. In this chapter, we prescribe a specific methodology for designing nanophotonic structures to efficiently couple incident light into guided modes within such a slot-waveguide absorber. As a result, light absorption may be increased beyond the $4n^2$ limit and, thereby, the efficiency of ultrathin photovoltaic devices can be increased significantly.

8.3 Methodology

The schematic of the nanostructured photovoltaic device in 2 dimensions is illustrated in Figure 8.1(a). Variation exists in the designed dielectric nanostructure along the X axis, while it is uniform along the Z axis. We generalize the geometries based upon four nanostructured interfaces, namely those between air and the top cladding, top cladding and the absorber, absorber and the bottom cladding, and finally, bottom cladding and the back reflector. Two adjacent rectangular scatterers are placed at each interface. We have full freedom in controlling their heights, widths, and positions. As a result, we identify 22 variables that define the device geometry. Specifically, these structures scatter light-waves such that incident sunlight can be efficiently coupled into waveguide modes inside the low-index absorbing layer. The device is assumed to be periodic in X direction with period of Λ. The average thicknesses of the top cladding, absorber, and bottom cladding

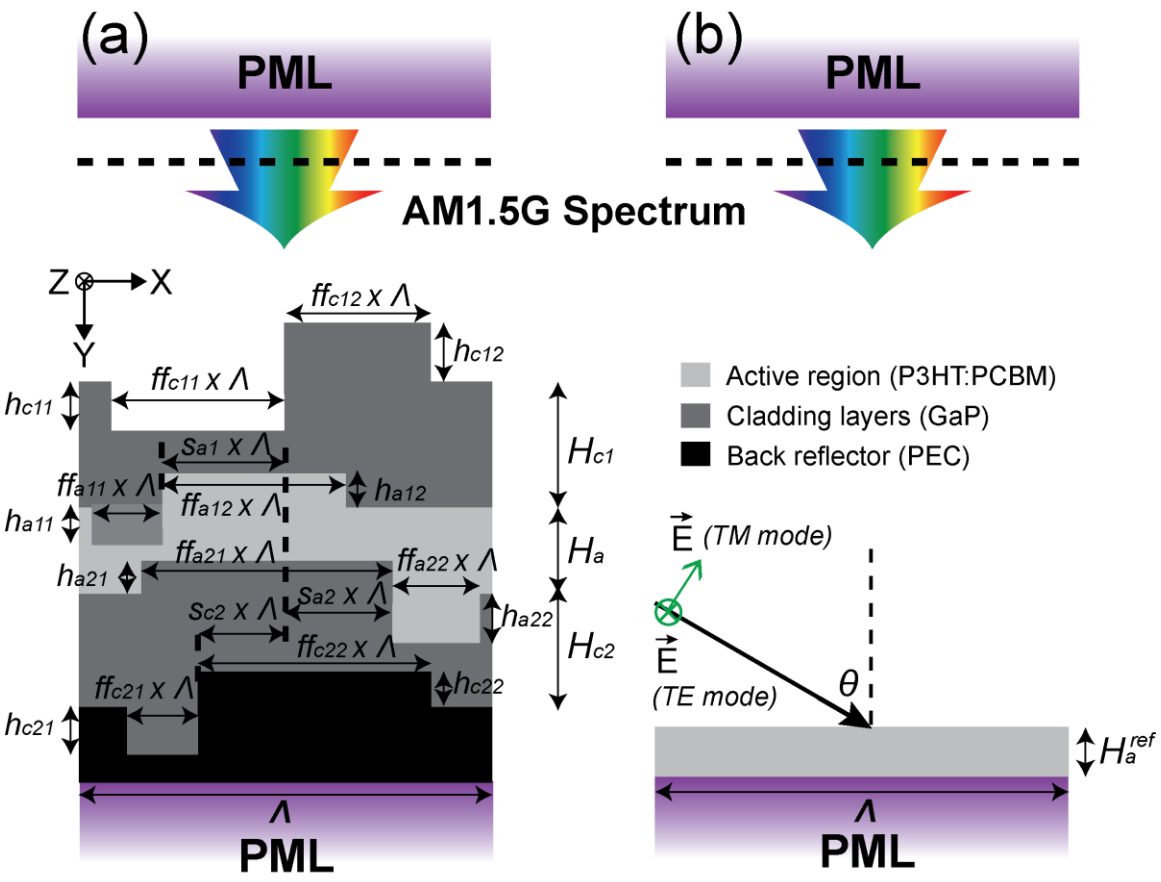

Figure 8.1. Schematic of the simulation model for optimization. (a) The photovoltaic device with light trapping nanostructures defined by 22 geometric parameters. (b) Reference device with the same volume of absorbing material as that of the structured design in (a). The angle of incidence is defined by θ. The TE and TM polarizations are defined as shown.

layers are H_{c1}, H_a, and H_{c2}, respectively. The average thickness of the absorber, H_a, is kept constant, while the remaining 22 geometric parameters are optimization variables.

We assume that the absorber is P3HT:PCBM [17,18] and that the cladding material is GaP, which has a higher refractive index [15,16]. Perfect metal is assumed for the back reflector for simplicity. The simulation was implemented via the finite-difference time-domain (FDTD) method [19]. The illumination is assumed to be spatially collimated, temporally continuous light propagating in the +Y direction from the top of the

computational domain. AM1.5G standard solar spectrum is assumed [20]. Bloch periodic boundary condition is imposed in the X direction since guided mode resonances (GMRs) are sustained by periodic structures. And perfectly matched layers (PMLs) are utilized at both the top and bottom terminals along the Y axis in the simulation unit cell. The angle of incidence, θ, and two orthogonal polarization states are defined in Figure 8.1(b).

The enhancement of short-circuit current density J_{sc} compared to a reference device with bare flat absorber (P3HT:PCBM) is considered as the figure of merit (FOM) during optimization. The effective thickness of the reference device, H_a^{ref}, is chosen such that the volume of the absorber is the same as that in the optimized device. The absorbance spectrum is expressed as [21]

$$A(\lambda) = \frac{\frac{1}{\Lambda}\cdot \iint\limits_{active} \frac{1}{2}\omega\varepsilon''(\lambda)\cdot\left|E(x,y,\lambda)\right|^2 dxdy}{P_{inc}(\lambda)}. \quad (8.1)$$

Here, λ is the wavelength, ω is the optical frequency, $\varepsilon''(\lambda)$ stands for the dispersion of the imaginary part of the permittivity of P3HT:PCBM, and $P_{inc}(\lambda)$ is the incident solar power. The integral is over the active region. The J_{sc} from the designed solar cell is [22]

$$J_{sc} = \int_{\lambda_{\min}}^{\lambda_{\max}} \frac{1}{\Lambda}\cdot\left(\frac{q\lambda}{hc}\cdot \iint\limits_{active} \frac{1}{2}\omega\varepsilon''(\lambda)\cdot\left|E(x,y,\lambda)\right|^2 dxdy\right)\cdot IQE(\lambda)\cdot d\lambda, \quad (8.2)$$

In Equation (8.2), $IQE(\lambda)$ represents internal quantum efficiency of P3HT:PCBM [17], q is the elementary charge, h is the Plank's constant, and c is the velocity of light. The integral over the entire spectrum of interest from λ_{min}=350nm to λ_{max}=850nm is numerically approximated by sum of a finite set of discrete wavelengths. The

enhancement spectrum is

$$E(\lambda)=\frac{A(\lambda)}{A_{ref}(\lambda)}=\frac{\iint\limits_{active}\left|E(x,y,\lambda)\right|^2 dxdy}{\iint\limits_{active}\left|E_{ref}(x,y,\lambda)\right|^2 dxdy}=\frac{U(\lambda)}{U_{ref}(\lambda)}. \tag{8.3}$$

The fraction defined in Equation (8.3) is also equivalent to the ratio of the total electromagnetic energy in the optimized versus the reference devices.

The local electromagnetic energy density is a product of the LDOS and the modal occupation number [15]. By assuming maximum modal occupation number, i.e., 100% coupling efficiency, the enhancement spectrum can be simplified as the ratio of LDOS in the optimized and reference devices. Applying an outer environment with a higher index of refraction is able to greatly enhance the LDOS. As a result, it is possible to achieve light trapping beyond the conventional ergodic limit, especially in the vicinity of the semiconductor band edge [15]. The optimization technique described in this study aims at realizing nanophotonic structures with maximized modal occupation numbers to take best advantage of the enhanced LDOS in the slot-waveguide. The DBS algorithm is again exploited for optimization, in which the 22 parameters are variable to be perturbed.

8.4 Results

The results of two optimized designs are summarized in this section. The reference absorber thicknesses (H_a^{ref}) for these designs are 42nm and 68nm for H_a=10nm and H_a=50nm, respectively. The optimized values of period, Λ, are 500nm, close to the wavelength of peak power density in AM1.5G solar spectrum [20]. The calculated J_{sc} at normal incidence are 10.1mA/cm^2 and 11.0mA/cm^2, respectively. These numbers

correspond to enhancement factors of 2.88 and 2.49 under the condition of normal incidence. Although these structures are challenging to pattern, recent breakthroughs in a variety of nanolithography techniques [26], especially roll-to-roll nanoimprint lithography, could pave a path towards low-cost mass production of such nanophotonic structures with reasonably high fidelity and repeatability [27,28].

Absorbance spectra of the optimized (in blue) and of the reference (in red) devices, at normal (solid lines) and oblique (θ=40^o, dashed lines) incidence, are shown in Figures 8.2(a) and (d). More than 60% of the incident photons between 450nm and 650nm are absorbed for carrier generation. Interestingly, this absorbance approaches 100% at ~600nm in Figure 8.2(a) and at ~550nm in Figure 8.2(d). Unfortunately, the parasitic absorption of light by GaP at shorter wavelengths constrains the achievable J_{sc}.

Figures 8.2(b) and (e) give the enhancement spectra, demonstrating significant enhancement at wavelengths close to the bandgap of the organic absorber (~750nm). This is achieved by the excitation of multiple guided-mode resonances inside the dielectric slot waveguide formed by the GaP-organic-GaP structure [13]. The optimized multilayer nanostructures at the interfaces allow incident light to couple energy efficiently into these GMRs. As expected for a lossy slot waveguide, the resonances with TE polarization are weaker than those with TM polarization [29]. The intensity distributions at the wavelengths of maximum enhancement are plotted in Figures 8.2(c) and (f).

In order to avoid tracking the sun, it is important that the light trapping mechanism operates even when the angles of incidence are oblique [30]. We analyze the designs under oblique illumination with θ as large as 60^o. As expected for GMRs, the resonances are red-shifted and the resonance peaks are reduced. The enhancement of J_{sc} is decreased.

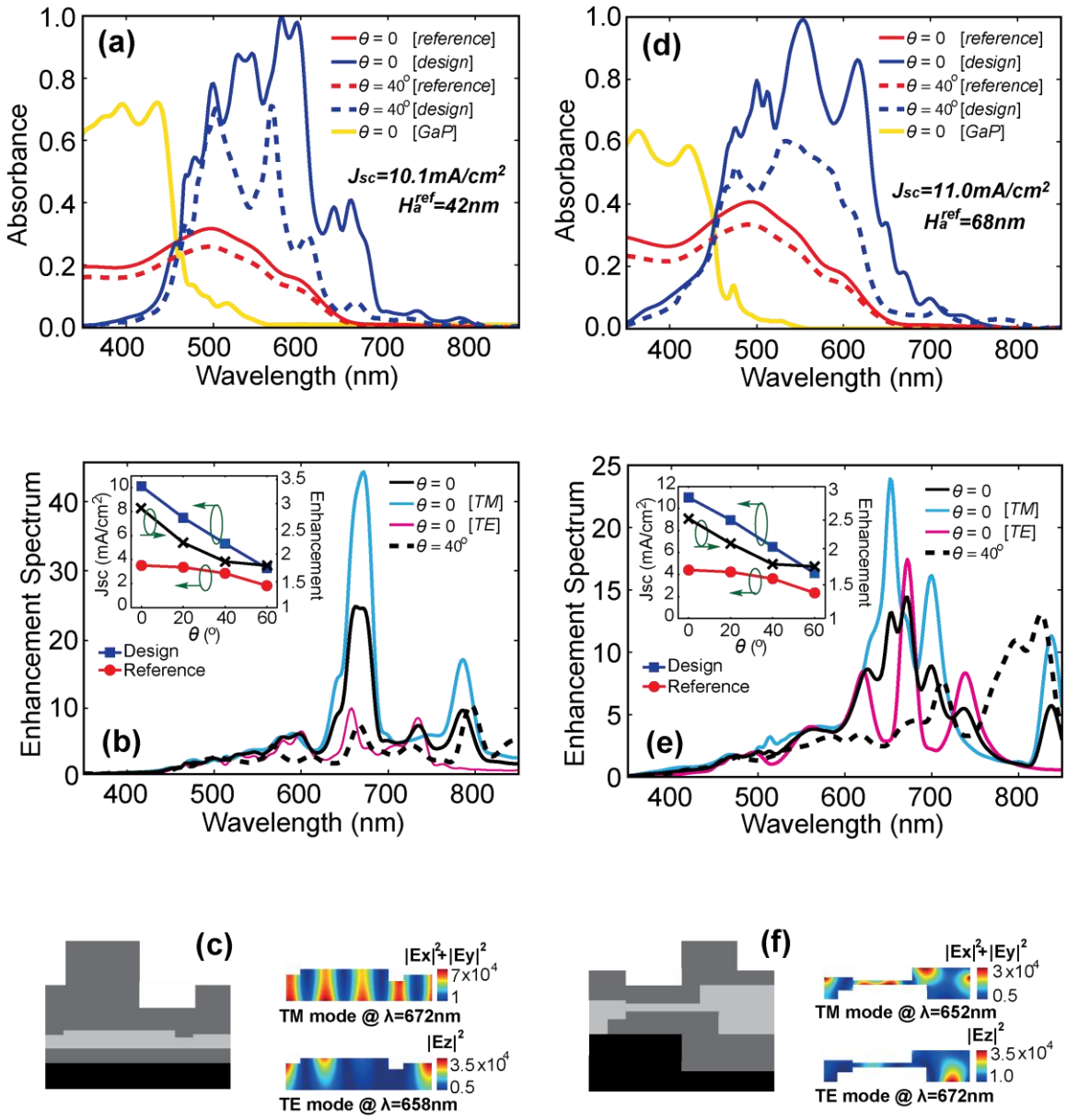

Figure 8.2. Two device geometries are again shown in (c) and (f), respectively. The corresponding absorbance spectra are plotted in (a) and (c), respectively. The corresponding current-density-enhancement spectra are plotted in (b) and (e), respectively. The insets in these figures showcase current-density and current-density enhancement as a function of incident angle, θ. The corresponding normalized intensity distributions at wavelengths of maximum current-density enhancement are shown in (c) and (f), respectively.

Nevertheless, the J_{sc} enhancement factors when averaged over all angles from 0 to 60^{o} are only slightly reduced to 2.22 and 2.12 for the two designs.

8.5 Beyond the Ergodic Limit

We compared the design in Figure 8.2(a) (design 1) to a previously optimized design that uses a lower-index cladding (indium-tin oxide or ITO) [31]. This latter design has an absorber thickness of 50nm and a slightly simpler geometry. Nevertheless, the comparison is instructive. For comparison, the absorbance spectra are shown in Figure 8.3(a) and (b). Despite a large fraction (~26.7%) of the incident solar spectrum being absorbed by the GaP layer, the benefit of utilizing GaP nanostructures instead of ITO is exemplified by the prominent absorption in P3HT:PCBM near its bandgap (600nm<λ<750nm). The traditional light-trapping limit suitable for a bulk absorber, also referred to as the ergodic limit, is expressed by [10-12]:

$$E^{Ergodic} = 4n_L^2, \tag{8.4}$$

in which n_L is the real part of the refractive index of the active layer of P3HT:PCBM [32]. An upper bound by using enhanced LDOS is defined by [16]:

$$E^{LDOS} = 4n_H^2, \tag{8.5}$$

where n_H is the real part of the refractive index of the cladding material GaP [33].

Enhancement spectra plotted in logarithmic scale clearly illustrate that a nanostructured high-index cladding provides significantly higher enhancement factors compared to those with a low-index cladding [13-16]. The solid blue line in Figure 8.3(c)

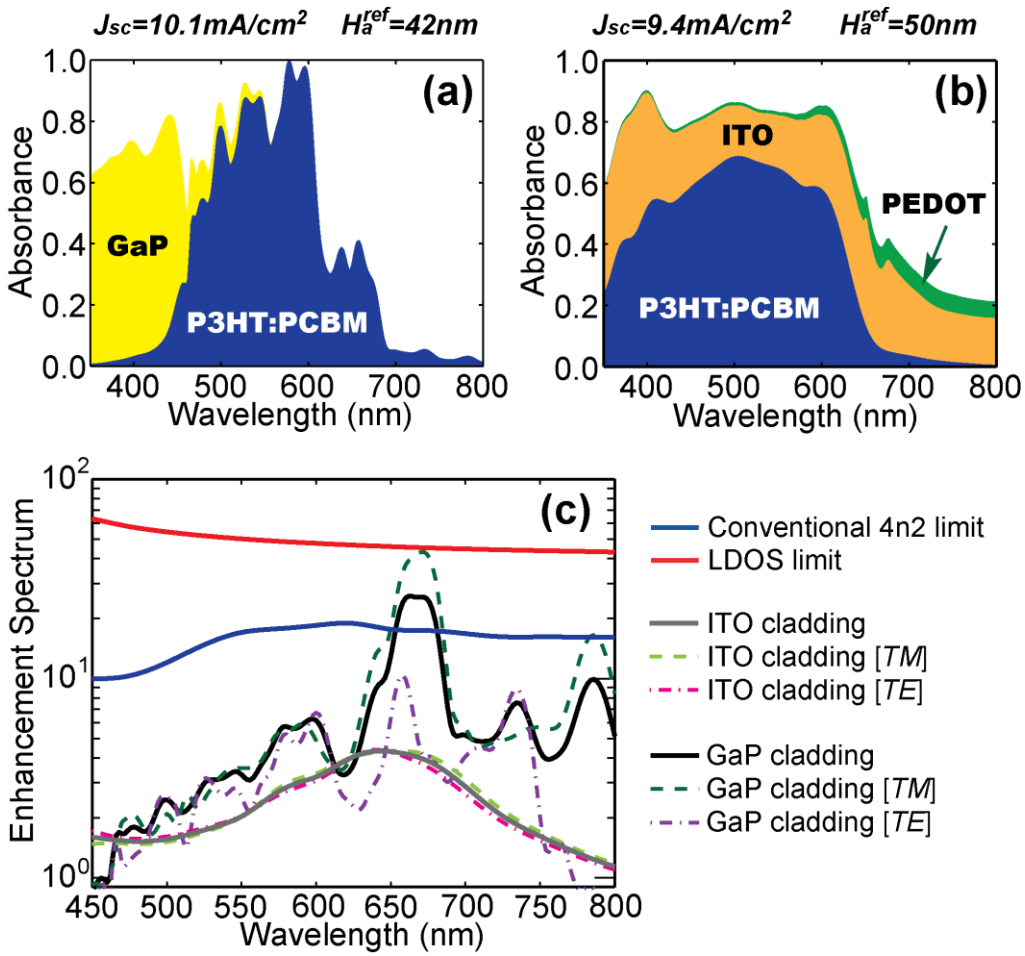

Figure 8.3. Impact of the refractive index of the cladding layer. The absorbance spectra for the optimized design with high-index-cladding (a) and (b) the low-index-cladding design (taken from Ref. [31]). (c) Current-density-enhancement spectra of the optimized designs and those corresponding to the ergodic limit and the LDOS limit.

indicates the ergodic ($4n^2$) limit [10]. The optimized device with a high-index cladding (black solid line) can provide enhancement beyond this limit for wavelengths close to the bandgap of the absorber. In fact, the TM resonant mode at 672nm (dark-green dashed line) allows for an enhancement factor that reaches the LDOS limit (red solid line). We can therefore conclude that the increased LDOS enabled by the high-index cladding is essential to couple incident light efficiently into GMRs and hence enable high light absorption in the ultrathin absorber layer.

8.6 References

[1] A. V. Shah, H. Schade, M. Vanecek, J. Meier, E. Vallat-Sauvain, N. Wyrsch, U. Kroll, C. Droz, and J. Bailat, "Thin-film silicon solar cell technology," Prog. Photovolt: Res. Appl. **12**, 113-142 (2004).

[2] H. A. Atwater, and A. Polman, "Plasmonics for improved photovoltaics devices," Nat. Mater. **9**, 205-213 (2010).

[3] C. Battaglia, J. Escarre, K. Soderstrom, L. Erni, L. Ding, G. Bugnon, A. Billet, M. Boccard, L. Barraud, S. D. Wolf, F. J. Haug, M. Despeisse, and C. Ballif, "Nanoimprint lithography for high-efficiency thin-film silicon solar cells," Nano Lett. **11**, 661-665 (2011).

[4] A. Goetzberger, C. Hebling, and H. Schock, "Photovoltaic materials, history, status and outlook," Mater. Sci. Eng. R **40**, 1-46 (2003).

[5] News reports on updated world records of thin-film photovoltaics efficiencies: http://www.pv-tech.org/ .

[6] V. E. Ferry, M. A. Verschuuren, H. B. T. Li, E. Verhagen, R. J. Walters, R. E. I. Schroppp, H. A. Atwater, and A. Polman, "Light trapping in ultrathin plasmonic solar cells," Opt. Express **18**, A237-A245 (2010).

[7] M. D. Kelzenberg, S. W. Boettcher, J. A. Petykiewicz, D. B. Turner-Evans, M. C. Putnam, E. L. Warren, J. M. Spurgeon, R. M. Briggs, N. S. Lewis, and H. A. Atwaters, "Enhanced absorption and carrier collection in Si wire arrays for photovoltaic applications," Nat. Mater. **9**, 239-244 (2010).

[8] K. Aydin, V. E. Ferry, R. M. Briggs, and H. A. Atwater, "Broadband polarization-independent resonant light absorption using ultrathin plasmonic super absorbers," Nat. Commun. **2**, 517-523 (2011).

[9] P. Wang, and R. Menon, "Simulation and optimization of 1-D periodic dielectric nanostructures for light-trapping," Opt. Express **20**, 1849-1855 (2012).

[10] E. Yablonovitch, "Statistical ray optics," J. Opt. Soc. Am. **72**, 899-907 (1982).

[11] E. A. Schiff, "Thermodynamic limit to photonic-plasmonic light-trapping in thin films on metals," J. Appl. Phys. **110**, 104501 (2011).

[12] H. R. Stuart, and D. G. Hall, "Thermodynamic limit to light trapping in thin planar structures," J. Opt. Soc. Am. A **14**, 3001-3008 (1997).

[13] Z. Yu, A. Raman, and S. Fan, "Fundamental limit of nanophotonic light trapping in solar cells," Proc. Natl. Acad. Sci. USA **107**, 17491-17496 (2010).

[14] M. A. Green, "Enhanced evanescent mode light trapping in organic solar cells and other low index optoelectronic devices," Prog. Photovolt: Res. Appl. **19**, 473-477 (2011).

[15] D. M. Callahan, J. N. Munday, and H. A. Atwater, "Solar cell light trapping beyond the ray optic limit," Nano Lett. **12**, 214-218 (2012).

[16] J. N. Munday, D. M. Callahan, and H. A. Atwater, "Light trapping beyond the 4n2 limit in thin waveguides," Appl. Phys. Lett. **100**, 121121 (2012).

[17] S. H. Park, A. Roy, S. Beaupre, S. Cho, N. Coates, J. S. Moon, D. Moses, M. Leclerc, K. Lee, and A. J. Heeger, "Bulk heterojunction solar cells with internal quantum efficiency approaching 100%," Nat. Photonics **3**, 297-303 (2009).

[18] M. Kaltenbrunner, M. S. White, E. D. Glowachki, T. Sekitani, T. Someya, N. S. Sariciftci, and S. Bauer, "Ultrathin and lightweight organic solar cells with high flexibility," Nat. Commun. **3**, 770-776 (2012).

[19] A, F. Oskooi, D. Roundry, M. Ibanescu, P. Bermel, J. D. Joannopoulos, and S. G. Johnson, "MEEP: a flexible free-software package for electromagnetic simulation by the FDTD method," Phys. Commun. **181**, 687-702 (2010).

[20] American Society for Testing and Materials (ASTM) Terrestrial Reference Spectra for Photovoltaic Performance Evaluation: http://rredc.nrel.gov/solar/spectra/am1.5/ .

[21] M. Kroll, S. Fahr, C. Helgert, C. Rockstuhl, F. Lederer, and T. Pertsch, "Employing dielectric diffractive structures in solar cells – a numerical study," Phys. Stat. Sol. **205**, 2777-2795 (2008).

[22] J. Nelson, *The Physics of Solar Cells* (Imperial College Press, 2004).

[23] G. Kim, J. A. Dominguez-Caballero, and R. Menon, "Design and analysis of multi-wavelength diffractive optics," Opt. Express **20**, 2814-2823 (2012).

[24] G. Kim, J. A. Dominguez-Gaballero, H. Lee, D. J. Friedman, and R. Menon, "Increased photovoltaic power output via diffractive spectrum separation," Phys. Rev. Lett. **110**, 123901 (2013).

[25] P. Wang, and R. Menon, "Three-dimensional lithography via digital holography," in *Frontiers in Optics 2012/Laser Science XXVIII*, OSA Technical Digest (online) (Optical Society of America, 2012), paper FTu3A.4. http://www.opticsinfobase.org/abstract.cfm?URI=FiO-2012-FTu3A.4

[26] T. L. Andrew, H. Tsai, and R. Menon, "Confining light to deep subwavelength dimensions to enable optical nanopatterning," Science **324**, 917-921 (2009).

[27] L. J. Guo, "Nanoimprint lithography: methods and material requirements," Adv. Mater. **19**, 495-513 (2007).

[28] S. Y. Chou, and W. Ding, "Ultrathin, high-efficiency, broad-band, omni-acceptance, organic solar cells enhanced by plasmonic cavity with subwavelength hole array," Opt. Express **21**, A60-A76, (2012).

[29] J. R. Nagel, S. Blair, and M .A. Scarpulla, "Exact field solution to guided wave propagation in lossy thin films," Opt. Express **19**, 20159-20171 (2011).

[30] P. Wang, and R. Menon, "Simulation and analysis of the angular response of 1D dielectric nanophotonic light-trapping structures in thin-film photovoltaics," Opt. Express **20**, A545-A553 (2012).

[31] P. Wang, and R. Menon, "Optimization of periodic nanostructures for enhanced light-trapping in ultra-thin photovoltaics," Opt. Express **21**, 6274-6285 (2013).

[32] W. H. Lee, S. Y. Chuang, H. L. Chen, W. F. Su, and C. H. Lin, "Exploiting optical properties of P3HT:PCBM films for organic solar cells with semitransparent anode," Thin Solid Films **518**, 7450-7454 (2010).

[33] Website of refractive index database: http://refractiveindex.info/

CHAPTER 9

OTHER WORKS ON NANOPHOTONICS PART 2:

INTEGRATED PHOTONICS

This chapter is adapted from the author's previous publication: Bing Shen, Peng Wang, Randy Polson and Rajesh Menon, "An integrated-nanophotonics polarization beamsplitter with 2.4 × 2.4 μm^2 footprint," Nature Photonics **9**, 378-382 (2015).

9.1 Abstract

We designed, fabricated, and characterized an integrated-nanophotonic polarization beamsplitter (PBS) with a footprint of 2.4μm × 2.4μm, which is the smallest PBS ever demonstrated. A nonlinear optimization algorithm was used to design the device for λ_0 = 1550nm. The PBS and the input/output waveguides can be fabricated in a single lithography step. We experimentally showed that the average transmission efficiency is greater than 70% (peak transmission efficiency ~80%) and extinction ratio is greater than 10 dB within a bandwidth of 32nm. Simulation results indicate that our device is tolerant to fabrication errors in device thickness of up to ±20 nm. We further designed, fabricated and characterized a mode-converting PBS, which not only separates the 2 polarization states, but also connects one multimode input waveguide to 2 single-mode output waveguides.

9.2 Background Introduction

Silicon-on-insulator (SOI) is the main materials-system used in integrated photonics due to the difference in refractive index between silicon and silicon dioxide. But this property results in strong birefringence, which leads to polarization-sensitive performance [1]. One solution to the problem is to compensate for polarization-mode dispersion, which requires a very challenging fabrication accuracy of 1nm [2]. A better solution is to employ devices that process different polarization states separately. However, this requires an efficient and compact polarization beam-splitter (PBS). The working principle of conventional PBS devices is based on either modal evolution [3,4] or interferometry. The latter typically includes multimode interference couplers (MMI) [5,6], directional couplers (DC) [7-14] and Mach-Zehnder interferometers (MZI) [15,16].

Among them, PBS based on DC is preferred, since they generally provide the smallest footprint. Directional couplers, in general, are composed of silicon waveguides [10,11], photonic crystals [12,14], slot waveguides [9] or the combination of silicon channel and slot waveguide [7]. For DC composed of silicon channels, H. Fukuda et al. have demonstrated a PBS of size 7μm × 16μm, exhibiting an extinction ratio of 15dB [11]. However, the fabrication precision required for the waveguides and the gap between the waveguides is very stringent due to its underlying phase-matching principle. In addition, the fundamentally small evanescent coupling prevents it from achieving large extinction ratios. Photonic-crystal-based DC is a plausible alternative for compact PBS devices [12,14]. But the light coupling between commonly used silicon waveguides and photonic-crystal waveguides is challenging. DC based on slot waveguides [9] or the combination of slot waveguides and silicon channels [7] could potentially enable a smaller device due to its tighter mode confinement within the slot. Combining slot waveguide and silicon channels, D. Dai et al. designed a PBS with a length of 6.9μm and an extinction ratio larger than 10dB [7]. Again, strict requirement on fabrication precision is inevitable due to its underlying phase-matching principle. Recently, X. Guan et al. proposed a DC-based PBS that is composed of a hybrid-plasmonic waveguide and a silicon nanowire [13]. This device is 1.9μm × 3.7μm. The incorporation of metal creates significant parasitic absorption losses and renders the process CMOS incompatible.

9.3 Methodology

In contrast to previous devices, we employ the concept of free-form metamaterials in our PBS device. Allowing the geometry of the metamaterials to be freely optimized enables devices that can be highly functional, yet also occupy a small footprint [17-19].

Nanopatterning enables one to engineer the refractive index in space at a deep sub-wavelength scale. Thereby, devices that achieve high-efficiency mode conversion in an extremely small area become feasible. Furthermore, these devices tend to rely on the coupling between a number of resonant nanophotonic modes, which promotes robustness to fabrication errors. Here, we designed, fabricated, and characterized an ultra-compact PBS with a footprint of only 2.4μm × 2.4μm for a design wavelength of 1.55μm and an extinction ratio larger than 12dB. We refer to this device as a nanophotonic PBS, and Figure 9.1(a) shows its geometry. It is patterned on a SOI substrate, where the thicknesses of the silicon and the oxide layers are 0.3μm and 3μm, respectively. Note that the device is also CMOS-compatible.

The device is composed of 20 × 20 pixels. One pixel is the shape of a square, whose side is 120nm. Unpolarized light, excited at the far end of the left input waveguide, illuminates the PBS. Then, TM and TE components of the input light are coupled into the top and bottom output waveguides with a calculated efficiency of 89% and 81%, respectively. From the simulations, we can clearly see that the incident light generates resonant modes within the nanophotonic device that are polarization dependent. These guided-resonant modes interact in such a manner as to satisfy the phase-matching conditions for the respective polarizations at the corresponding output waveguides. As a result, polarization splitting is achieved. In the device geometry in Figure 9.1(a), silicon is shown in black, while the absence of silicon (air) is shown as white. The device is designed such that thickness of the silicon layer in the nanophotonic region is the same as that in the waveguides, i.e., 300nm. This implies that our design can be fabricated in a single lithography step along with the waveguides.

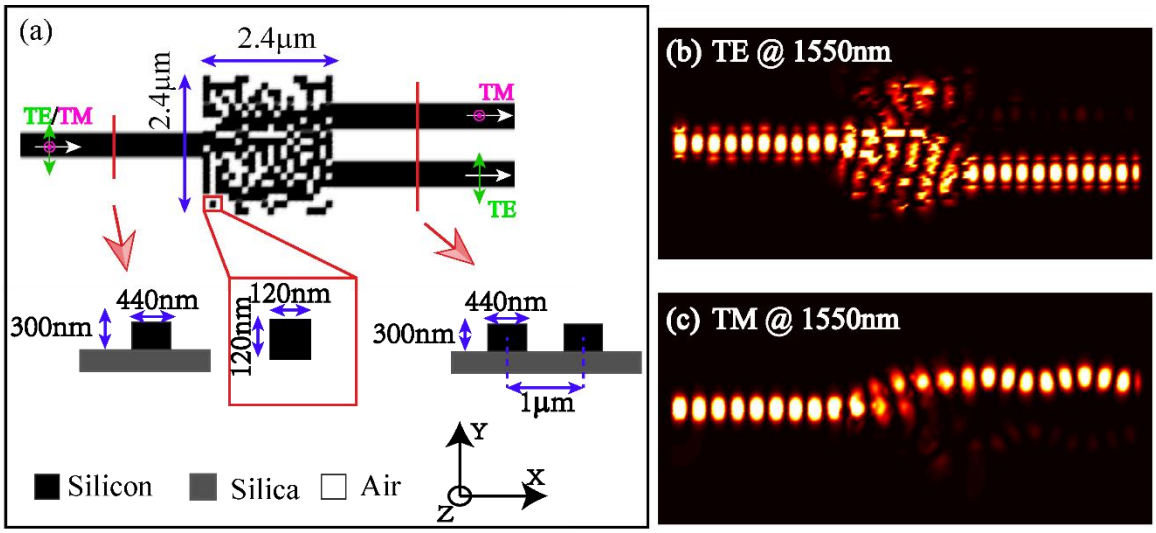

Figure 9.1. (a) Geometry of the nanophotonic polarization beamsplitter. Simulated steady-state intensity distributions for (b) TE and (c) TM polarized light at the design wavelength 1550nm. TE is polarized in the plane and vertical to the propagation direction as illustrated by the green arrows in (a), and TM is polarized out of plane as illustrated by red circles in (a).

The nanophotonic PBS was designed using a nonlinear search algorithm that we refer to as direct-binary search (DBS) [20-24]. The device is discretized into 120nm × 120nm silicon/air pillars, which we call "pixels". Each such pixel can occupy 2 states: silicon or air, which is flipped during optimization. The FOM is defined as the average transmission efficiency for TE and TM polarization states. Specifically, the fabrication process determines the size of the smallest feature, which is the pixel in our device. In general, it took about 140 hours to design one device. The electromagnetic fields within the device were simulated using finite-difference time-domain (FDTD) [25]. As mentioned earlier, our device was patterned in the top silicon layer (thickness = 300nm) of an SOI substrate. In principle, only one patterning step is required since the etch depths are the same. However, since we do not have access to high-resolution optical projection lithography, we opted for a 2-step process. First, optical patterning was used to

define all features down to a size of 3μm. Second, focused-ion-beam (FIB) lithography was used to define all the smaller features. Alignment marks were used. Reference devices that included the same tapers for normalization and an on-chip polarizer for polarization state alignment were also fabricated on the same substrate.

9.4 Results

A scanning-electron micrograph of the fabricated device is shown in Figure 9.2(a). Light was input and output via butt-coupling using lensed fibers to multimode waveguides, In order to increase the coupling efficiency, we incorporated tapers (4-μm length) between all single-mode waveguides and the multimode waveguides (3-μm width). The measurement system is sketched in Figure 9.2(b) [26]. Fibers used in the experiment are standard single-mode lensed fibers. The polarization controllers (PC1 and PC2) were first calibrated using the on-chip polarizer. The whole output path within the dotted frame in Figure 9.2(b) was first bypassed by connecting the output lensed fiber to the detector, and the on-chip polarizer was aligned. Adjusting PC1 and monitoring the output power set the input polarization state. Then the input lensed fiber was moved to illuminate a straight waveguide, and the output path within the dotted frame was inserted. The alignment between the output polarization plane and the polarizer was achieved by adjusting PC2. The polarization components of the output light could be selected by rotating the polarizer accordingly.

The experimental and simulated transmission efficiency and extinction ratio as a function of the input wavelength are shown in Figures 9.3(a) and (b), respectively. The experimental data are normalized to those of a straight waveguide with the same tapers. The measured values consistently follow the simulated curves. The decrease in measured

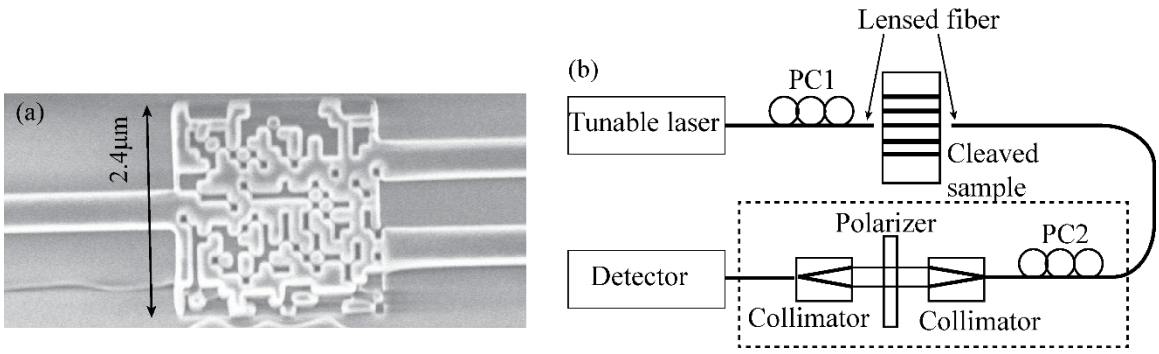

Figure 9.2. (a) Scanning-electron micrograph of fabricated device. (b) Measurement system setup.

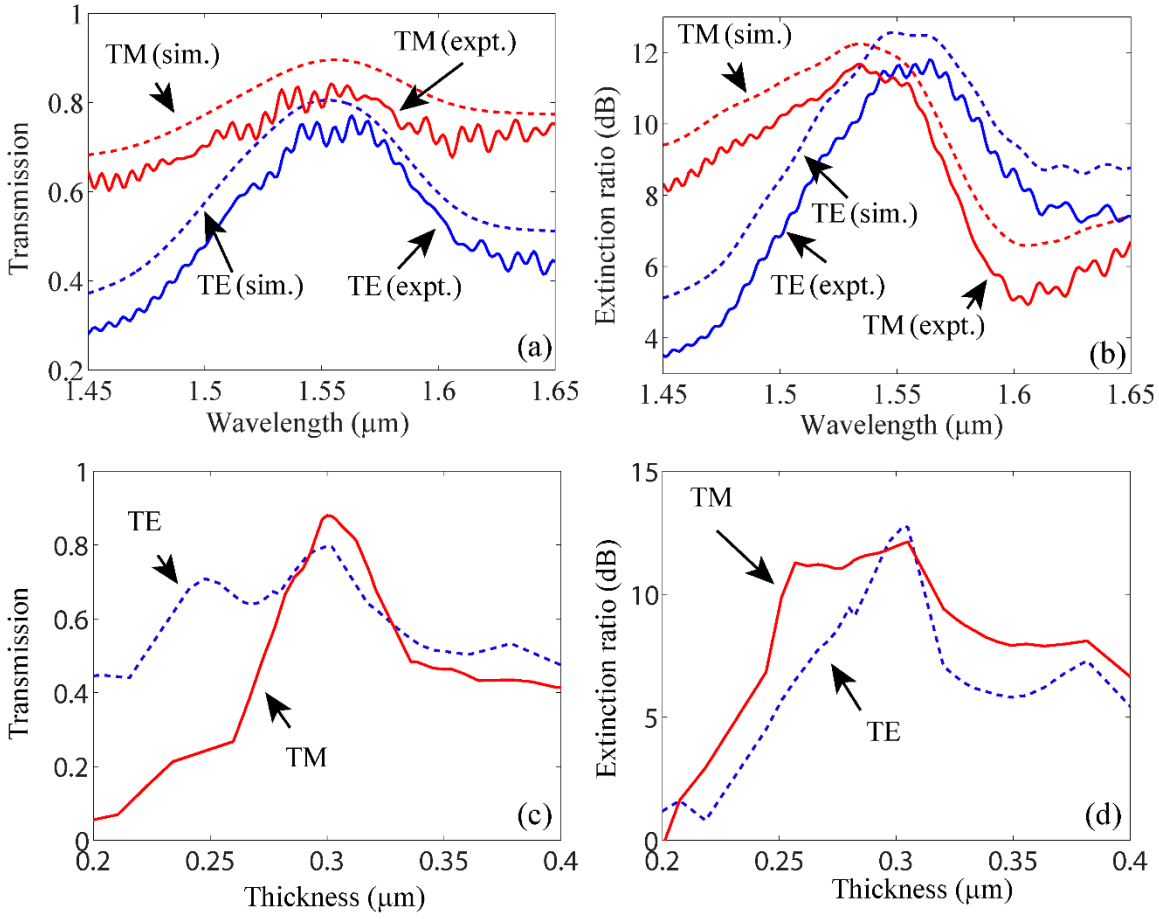

Figure 9.3. Measured and simulated (a) transmission efficiencies and (b) extinction ratio of the PBS for both polarizations. Measured and simulated data are shown using solid and dashed lines, respectively. Simulated (c) transmission efficiencies and (d) extinction ratio as a function of the device (silicon) thickness. For all figures, TE and TM polarizations are shown in blue and red, respectively.

efficiencies can be primarily attributed to small errors introduced during fabrication, which include device-thickness errors as well as line-edge roughness. The latter can cause out-of-plane scattering, which will reduce overall efficiencies. Improved fabrication processes can significantly reduce these effects. We believe that coherent interactions between light reflected from the lensed fiber and that from the waveguides cause the ripples in the measured spectra. We measured coupling efficiency of 71% and 80% for TE and TM at the design wavelength (1.55μm), respectively. The measured extinction ratios for TE and TM at the design wavelengths are 11.8 dB and 11.1 dB.

The operational bandwidth of our device, where the transmission efficiency is within 1dB of the peak value, is 83nm (1510nm to 1593nm). Such a large operating bandwidth is possible because the polarization-selection effect is the cumulative effect of a number of guided-mode resonances (rather than a single resonance).

In order to elucidate the tolerance of our device to small changes in device geometry, we simulated the impact of varying the top-silicon thickness on the device performance. The results for transmission efficiency and extinction ratio are illustrated in Figures 9.3(c) and (d), respectively. If the extinction ratio is allowed to fall to 3dB from the peak value, the devices can tolerate a variation in top-silicon thickness of up to ±20nm.

We also simulated the instantaneous field distributions within the PBS as a function of time. The nanophotonic device is composed of geometries that are much smaller than the wavelength. Therefore, the excited modes are evanescent. However, power is coupled between evanescent modes due to the close spacing. This results in multiple resonant modes that transfer power in a highly polarization-sensitive manner. Our design methodology encourages the power transfer of one polarization into one waveguide,

while the power in the orthogonal polarization is transferred to the second waveguide.

A closer look at the mode evolution with time shows that different mechanisms are responsible for guiding light in the 2 polarization states. For TE light (light polarized in-plane and vertical to the direction of light propagation), power is confined in the air gap between adjacent nanopillars and the slot-waveguide effect dominates due to boundary conditions. Thus, the silicon pillars actually act as the cladding layer while the air gaps act as the core layer to guide TE light. The opposite holds true for TM light (light polarized out of plane). That is, the air gaps act as the cladding layer and the silicon pillars act as the core layer to guide TM light.

9.5 More Functionalities

Complex nanophotonic structures allow one to design a single device that can implement multiple functions. To illustrate this concept, we designed, fabricated, and characterized a device that not only coverts light from a multimode waveguide to a single-mode waveguide but also splits the 2 polarizations. Mode conversion is typically achieved with a very long (100s of microns long) adiabatic taper [17]. For our device, however, polarization splitting and mode conversion are achieved simultaneously. The simulated transmission efficiencies at the design wavelength (1.55μm) for TE and TM are calculated as 80% and 83%, respectively. The corresponding simulated extinction ratios are 15.2dB and 14.4dB for TE and TM, respectively. The measured transmission-efficiency and extinction-ratio spectra are lower than the simulated spectra, but substantially agree. The measured peak transmission efficiencies for TE and TM are 58% and 71%, respectively. The measured extinction ratios for TE and TM are 13.88 dB and 13.77 dB, respectively. The measured efficiencies were lower than expected primarily

due to errors in alignment between the PBS and the waveguides. With a single-step lithography process, such alignment will be unnecessary and these errors should not manifest. Note that both polarization state separation and mode conversion are achieved within the 4μm × 3μm device area. Furthermore, we simulated the impact of device-geometry errors to evaluate the tolerance of our design. Specifically, we varied the device (silicon layer) thickness. The simulations indicate that if the extinction ratio is allowed to fall to 3dB of the peak, then the silicon-layer thickness can vary as much as ±17nm.

9.6 References

[1] C. Manolatou, S. G. Johnson, S. Fan, P. R. Villeneuve, H. A. Haus, and J. D. Joannopoulos, "High density integrated optics," J. Lightwave Technol. **17**, 1682–1692 (1999).

[2] H. Fukuda, K. Yamada, T. Tsuchizawa, T. Watanabe, H. Shinojima, and S. Itabashi, "Ultrasmall polarization splitter based on silicon wire waveguides," Opt. Express **14**, 12401-12408 (2006).

[3] W. Yuan, K. Kojima, B.Wang, T. Koike-Akino, K. Parsons, S. Nishikawa, and E. Yagyu, "Mode-evolution-based polarization rotator-splitter design via simple fabrication process," Opt. Express **20**, 10163–10169 (2012).

[4] M. R. Watts, H. A. Haus, and E. P. Ippen, "Integrated mode-evolution-based polarization splitter," Opt. Lett. **30**, 967-969 (2005).

[5] J. M. Hong, H. H. Ryu, S. R. Park, J. W. Jeong, S. G. Lee, E.-H. Lee, S.-G. Park, D. Woo, S. Kim, and B. H. O, "Design and fabrication of a significantly shortened multimode interference coupler for polarization splitter application," IEEE Photon. Technol. Lett. **15**, 72–74 (2003).

[6] Z. Tu, Y. W. Huang, H. X. Yi, X. J. Wang, Y. P. Li, L. Li, and W. W. Hu, "A compact SOI polarization beam splitter based on multimode interference coupler," Proc. SPIE **8307**, 830707 (2011).

[7] D. Dai, Z. Wang, and J. E. Bowers, "Ultrashort broadband polarization beam splitter based on an asymmetrical directional coupler," Opt. Lett. **36**, 2590-2592 (2011).

[8] J. Feng, and Z. Zhou, "Polarization beam splitter using a binary blazed grating coupler," Opt. Lett. **32**, 1662–1664 (2007).

[9] Y. Yue, L. Zhang, J.-Y. Yang, R. G. Beausoleil, and A. E. Willner, “Silicon-on-insulator polarization splitter using two horizontally slotted waveguides,” Opt. Lett. **35**, 1364–1366 (2010).

[10] I. Kiyat, A. Aydinli, and N. Dagli, “A compact silicon-on-insulator polarization splitter,” IEEE Photon. Technol. Lett. **17**, 100–102 (2005).

[11] H. Fukuda, K. Yamada, T. Tsuchizawa, T. Watanabe, H. Shinojima, and S. Itabashi, “Ultrasmall polarization splitter based on silicon wire waveguides,” Opt. Express **14**, 12401–12408 (2006).

[12] T. Liu, A. R. Zakharian, M. Fallahi, J. V. Moloney, and M. Mansuripur, “Design of a compact photonic-crystal-based polarizing beam splitter,” IEEE Photon. Technol. Lett. **17**, 1435–1437 (2005).

[13] X. Guan, H. Wu, Y. Shi, L. Wosinski, and D. Dai, "Ultracompact and broadband polarization beam splitter utilizing the evanescent coupling between a hybrid plasmonic waveguide and a silicon nanowire," Opt. Lett. **38**, 3005-3008 (2013).

[14] Maurice Sesay, Xin Jin, and Zhengbiao Ouyang, "Design of polarization beam splitter based on coupled rods in a square-lattice photonic crystal," J. Opt. Soc. Am. B **30**, 2043-2047 (2013).

[15] D. Dai, Z. Wang, J. Peters, and J. E. Bowers, “Compact polarization beam splitter using an asymmetrical mach–zehnder interferometer based on silicon-on-insulator waveguides,” IEEE Photon. Technol. Lett. **24**, 673–675(2012).

[16] L. B. Soldano, A. I. de Vreede, M. K. Smit, B. H. Verbeek, E. G. Metaal, and F. H. Green, “Mach-zehnder interferometer polarization splitter in ingaasp/inp,” IEEE Photon. Technol. Lett. **6**, 402–405 (1994).

[17] J. Lu, and J. Vučković, “Nanophotonic computational design,” Opt. Express **21**, 13351–13367 (2013).

[18] B. Shen, P. Wang, R. Polson, and R. Menon, "Integrated metamaterials for efficient and compact free-space-to-waveguide coupling," Opt. Express **22**, 27175-27182 (2014).

[19] A. Y. Piggott, J. Lu, T. M. Babinec, K. G. Lagoudakis, J. Petykiewicz, and J. Vučković, “Inverse design and implementation of a wavelength demultiplexing grating coupler,” Sci. Rep. **4**, 7210 (2014).

[20] G. Kim, J.-A. Dominguez-Caballero, H. Lee, D. J. Friedman, and R. Menon, “Increased photovoltaic power output via diffractive spectrum separation,” Phys. Rev. Lett. **110**, 123901 (2013).

[21] B. Shen, P. Wang, R. Polson, and R. Menon, "Ultra-high-efficiency metamaterial polarizer," Optica **1**, 356-360 (2014).

[22] P. Wang, and R. Menon, “Optimization of generalized dielectric nanostructures for enhanced light trapping in thin-film photovoltaics via boosting the local density of optical states,” Opt. Express **22**, A99–A110 (2014).

[23] B. Shen, P. Wang, and R. Menon, “Optimization and analysis of 3D nanostructures for power-density enhancement in ultra-thin photovoltaics under oblique illumination,” Opt. Express **22**, A311–A319 (2014).

[24] G. Kim, and R. Menon, “An ultra-small three dimensional computational microscope,” Appl. Phys. Lett. **105**, 061114 (2014).

[25] A. F. Oskooi, D. Roundy, M. Ibanescu, P. Bremel, J. D. Joannopoulos, and S. G. Johnson, “MEEP: A flexible free-software package for electromagnetic simulations by the FDTD method,” Comput. Phys. Commun. **181**, 687–702 (2010).

[26] L. Liu, Y. Ding, K. Yvind, and J. M. Hvam, "Efficient and compact TE–TM polarization converter built on silicon-on-insulator platform with a simple fabrication process," Opt. Lett. **36**, 1059-1061 (2011).

CHAPTER 10

SUMMARY AND FUTURE WORK

10.1 Summary

This dissertation extensively studied a new type of digital diffractive optic element, called polychromat. It is an ultrathin piece of flat optic for multiple imaging and nonimaging applications. It is essentially a pixelated microstructure with a quantized height profile. We developed an accurate numerical model based on scalar diffraction in Fresnel approximation and devised a direct-binary-search algorithm to optimize its optical performances. The optic is easily fabricated by single-step grayscale lithography and may be replicated by nanoimprint lithography. A standard recipe for device fabrication is developed. It can be readily replicated by the highly-developed nanoimprint lithography (NIL) technique in a cost-effective way for mass production.

In the first chapter, a background introduction was given, especially in diffractive optics and computational optics. The fundamental theory of scalar diffraction was elaborated as the basis of device physics. Chapter 2 included the numerical model of the polychromat device, the nonlinear DBS algorithm for design optimization, the standard fabrication protocol, the preliminary replication recipe, the computational algorithm for image reconstruction based upon regularization, and the brief descriptions of various optical characterization setups.

The following chapters described the imaging and nonimaging applications of the

polychromat device. Each chapter treated one application, including (1) solar spectrum splitter/concentrator to boost power-conversion-efficiency in planar multibandgap photovoltaics; (2) ultrathin flat diffractive lens that corrects chromatic aberrations continuously over the entire visible band; (3) diffractive phase mask to manipulate 3D light distribution for microlithography on oblique and multiplane surfaces; (4) computational color and multispectral imager that enhances photon throughput and thus light sensitivity by 3 times; (5) ultracompact computational snap-shot hyperspectral video-imaging with enhanced spatial resolution and potential of 3D imaging. Some other applications not included in this dissertation are (6) spectral splitter to enable multicolor and hyper-spectral laser-scanning confocal fluorescence microscopy [1]; (7) compact computational spectroscopy with large bandwidth-to-resolution ratio [2,3]; (8) computational hyper-spectral light-field imaging.

Before the conclusions and future works in Chapter 10, Chapters 8 and 9 briefly summarized other projects conducted alongside this dissertation work, mostly on the nanophotonics. The target was to optimize and analyze diverse subwavelength structures for two primary applications: (1) nanophotonic light trapping to enhance light absorption within the ultra-thin-film solar cells based on either conventional inorganic semiconductor (Silicon) or organic semiconductors [4-7]; (2) basic functional modules in integrated photonic circuits such as spectral-splitter, polarization-splitter, polarization rotator and free-space-waveguide coupler [8,9]. All these devices are simulated by the FDTD technique and optimized by the DBS algorithm. The nanostructures can be patterned by focused ion beam (FIB) milling.

10.2 Future Work

10.2.1 Ultra-high-efficiency photovoltaics

As discussed in Figures 3.4 and 3.5, our proposed diffractive optic element (or polychromat), as a spectrum splitter/concentrator, provides great flexibility in extending to large numbers of bandgaps (or sub-cells) and large concentration factors, as schematically depicted in Figure 10.1. Also, as pointed out in previous studies, more bandgaps and greater concentrations lead to higher power-conversion efficiency, even approaching the thermodynamic limit of photovoltaic efficiency [10,11]. In a recent publication, we experimentally characterized the photovoltaic system configured for three bandgaps (GaInP, GaAs and Si) and 3X concentration. It was demonstrated to boost power-conversion efficiency by 30%, compared to a bare reference device without the polychromat [12]. In our next steps, we will work on different combinations of the number of bandgaps and concentration factors, for example, 2-bandgaps with 3X concentration, and 3-bandgaps with 6X concentration. Better performances are anticipated in theory. Additionally, instead of using an artificial bright light source, such as a Xenon lamp or a supercontinuum source, we will incorporate the AM1.5G spectrum into our design model and device characterization experiment. A setup that is easy to operate and a standard procedure for outdoor measurement will be developed. Thereby, we can report on device evaluation specs in a more rigorous and more applicable manner.

10.2.2 Projection 3D patterning

Although microlithography on oblique and multiplane surfaces is already impressing in the realm of fabrication engineering, it is also intriguing to adapt our lithography technique based on diffractive phase mask to projection stereo-lithography.

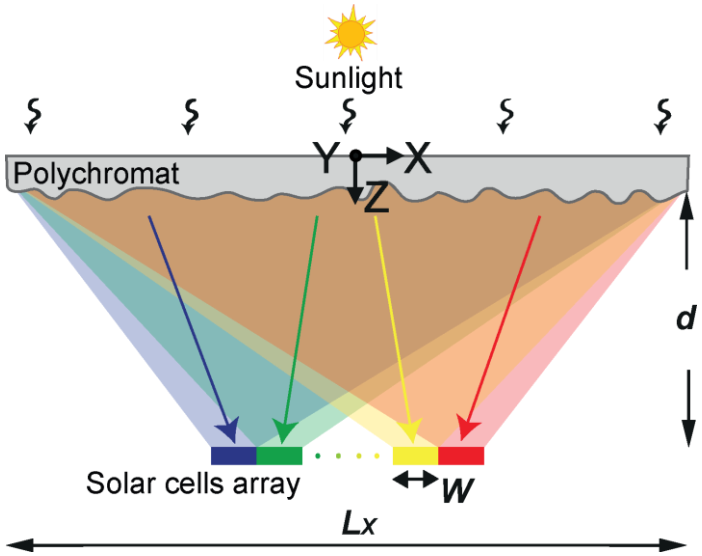

Figure 10.1. Schematic illustration of the ultra-high-efficiency photovoltaic system using the optimized diffractive optic element as spectrum splitter/concentrator. The array of solar cells of various bandgaps are placed at distance *d* from the polychromat.

3D structures, either microscale or nanoscale, find applications in various fields, including MEMS, biomedical devices, microfluidics, photonic crystals, etc. Conventional stereo-lithography utilizes two-photon polymerization and exposes the entire 3D space by scanning point-by-point. The benefits of our approach lie in: (1) it is a much faster process since only one exposure is enough to pattern complex 3D structures; (2) any arbitrary geometries can be available by proper optimization, given the spatial resolution in three dimensions determined by the feature size of the phase mask and the exposure wavelength. To be specific, we propose to exploit a mixture of HDDA monomer and PTBPO photo-initiator (wt. ratio 45.5:1), sensitive to 405nm laser, as the photoresist. This mixture was previously demonstrated to record complex 3D structures using multilayer exposure [13]. In the potential experiment, a collimated 405nm-laser beam shines upon the designed phase mask and generates 3D light distribution, which exposes the volume of photoresist mixture (see Figure 10.2).

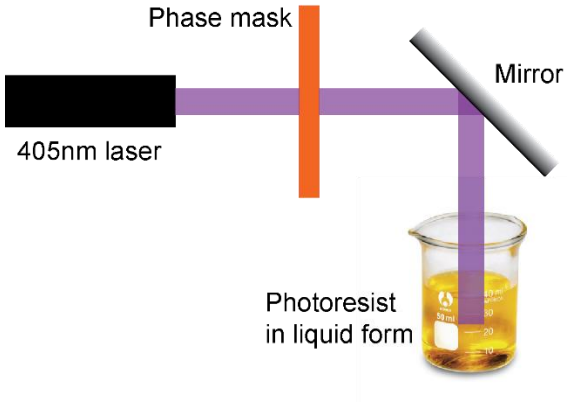

Figure 10.2. Schematic illustration of projection 3D patterning setup.

10.2.3 Multispectral imaging

In the computational single-shot multispectral imaging project, we will explore further modifications or alternative techniques that can be applied to offer real-time larger field-of-view imaging. There are two basic requirements. First, the new approach should be able to conduct image reconstruction over a large area using a small set of calibration data. In this way, full-frame multispectral imaging is made possible without a time-consuming calibration process. Secondly, the reconstruction algorithm needs to be fast since we are aiming at real-time imaging. To meet these criteria, one way is to engineer the diffractive filter purposely, instead of using one with computer-generated random topography. Our following step is to find a way to design the diffractive optic such that its spatial-spectral response can simplify and accelerate the calibration and image reconstruction process.

In addition, the spatial and spectral performances of the imaging system are also decided by the gap between the sensor and the polychromat. However, in our current experiment, this gap is primarily limited by the protection cover glass integrated on the sensor. A simple way to shrink this gap is by placing the polychromat directly on top of

the glass with optical adhesive. However, the margin areas on the sensor where we can apply adhesive is limited, hence we need to control the adhesive drop volume and diameter. We borrowed the idea from dip-pen lithography [14,15]. A simple test on a glass slide (Figure 10.3(a)) shows that when we pick some adhesive using a tip (such as a sharp tweezer) and make multiple drops in sequence, the drop diameter decreases gradually. The plot of drop diameter indicates that after 10 drops, we can achieve drop diameter as small as 400μm (Figure 10.3(b)). Figures 10.3(c) and (d) are the micrographs of the sensor before and after gluing the polychromat on the cover glass, respectively. Clearly, the adhesive has such small diameters that it does not block the sensor and the sensor is intact. Another direction of prospective works is to integrate the polychromat directly on the sensor surface, so as to on one hand enhance its imaging performance (especially light sensitivity) and on the other make the assembly more compact.

10.2.4 Light-field imaging

The computational single-shot multispectral imaging technique studied in Chapter 7 only deals with objects on the 2D plane, though 3D imaging can be made possible. In addition, the calibration measures the spatial domain. However, on the other side, the same diffractive filter may be implemented in imaging the 3D volume by calibrating the spatial frequency domain. In another word, it may open up a new application in light-field multispectral imaging [16]. More information could be extracted. Figure 10.4 gives a schematic of the calibration setup for light-field imaging. Here, lens 1 focuses the collimated broadband light, which is then collected and collimated again by lens 2 (similar with a 4F system). The first lens scans the 2D space so that the light coming out of the second lens is tilted at an angle θ, which is a function of the relative movement of

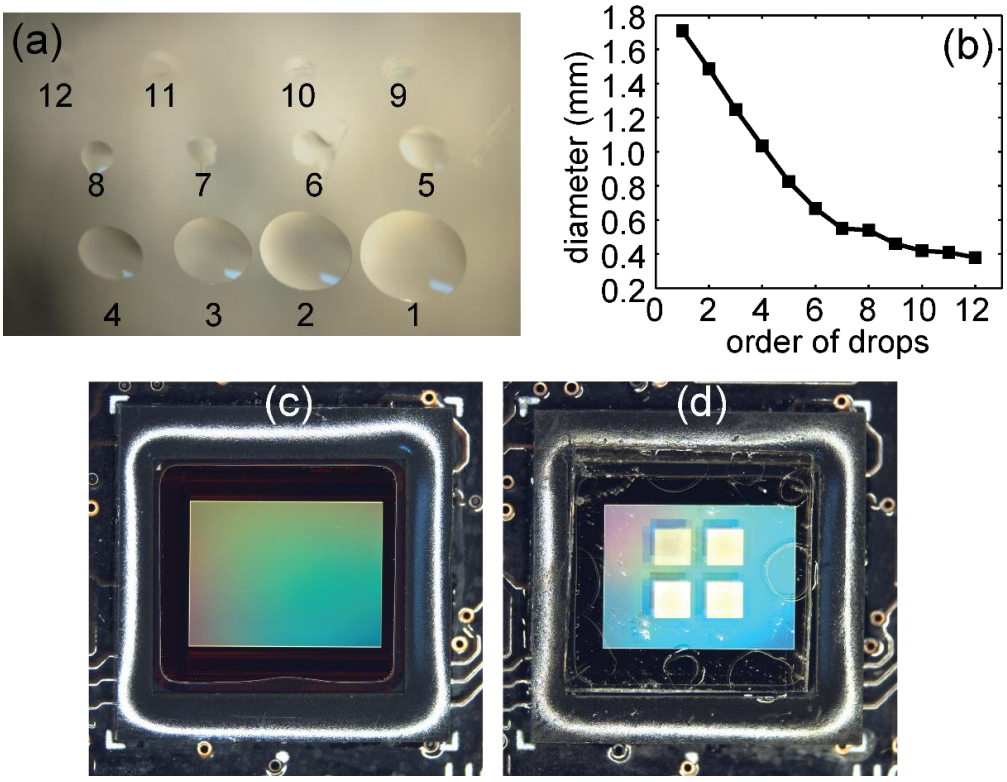

Figure 10.3. Optical adhesive drop test. (a) Micrograph of optical adhesive drops on glass slide. The order of drops are labelled. (b) Plot of drop diameter versus the order of drops. Micrographs of the CMOS sensor chip before (c) and after (d) applying the polychromat on its cover glass.

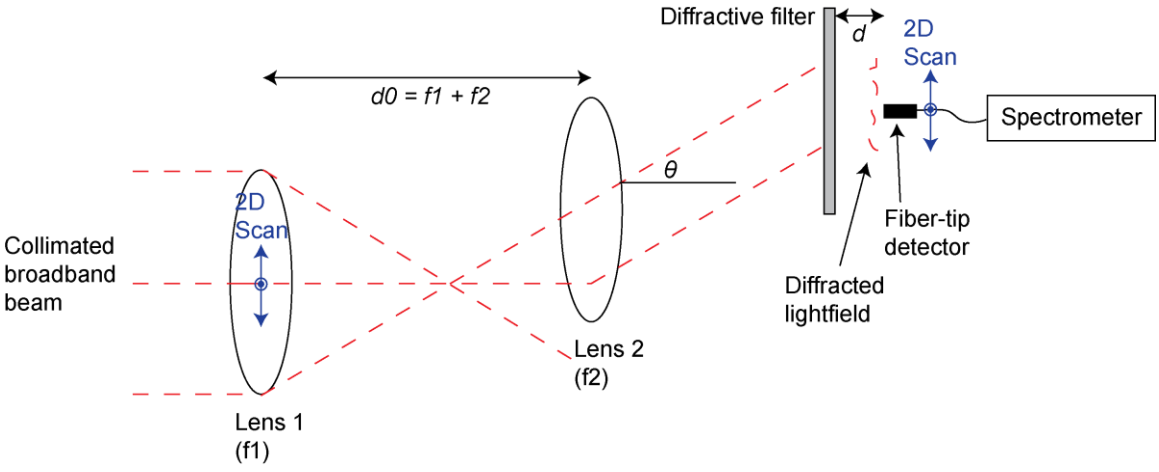

Figure 10.4. Schematic illustration of the calibration setup for light-field multispectral imaging.

lens 1. A scanning-spectrometer setup is utilized again to record the spatial-spectral responses of the diffractive filter illuminated by the collimated light of oblique incidence. In consequence, we are able to calibrate the spatial frequency domain. Light-field multispectral reconstruction can be realized by similar algorithms (iterative or noniterative, such as DBS or regularization). Note that only one snapshot is sufficient to recover the high-dimensional information.

10.3 References

[1] P. Wang, C. Ebeling, J. Gerton, and R. Menon, "Hyper-spectral imaging in scanning-confocal-fluorescence microscopy using a novel broadband diffractive optic," Opt. Commun. **324**. 73-80 (2014).

[2] P. Wang, and R. Menon, "Computational spectrometer based on a broadband diffractive optic," Opt. Express **22**, 14575-14587 (2014).

[3] P. Wang, and R. Menon, "Computational spectroscopy via singular-value decomposition and regularization," Opt. Express **22**, 21541-21550 (2014).

[4] P. Wang, and R. Menon, "Simulation and optimization of 1-D periodic dielectric nanostructures for light-trapping," Opt. Express **20**, 1849-1855 (2012).

[5] P. Wang, and R. Menon, "Simulation and analysis of angular response of 1D dielectric nanophotonic light trapping structures in thin-film photovoltaics," Opt. Express **20**, A545-A553 (2012).

[6] P. Wang, and R. Menon, "Optimization of periodic nanostructures for enhanced light-trapping in ultra-thin photovoltaics," Opt. Express **21**, 6174-6285 (2013).

[7] B. Shen, P. Wang, and R. Menon, "Optimization of 3D nanostructures for power-density enhancement in ultra-thin organic solar cells," Opt. Express **22**, A331-A319 (2014).

[8] B. Shen, P. Wang, R. Polson, and R. Menon, "Ultra-high-efficiency metamaterial polarizer," Optica **1**, 356-360 (2014).

[9] B. Shen, P. Wang, R. Polson, and R. Menon, "Integrated metamaterials for efficient and compact free-space-to-waveguide coupling," Opt. Express **22**, 27175-27182 (2014).

[10] A. Polman, and H. A. Atwater, “Photonic design principles for ultrahigh-efficiency photovoltaics,” Nat. Mater. **11**, 134-137 (2012).

[11] S. P. Bremner, M. Y. Levy, and C. B. Honsberg, “Analysis of tandom solar cells efficiencies under AM1.5G spectrum using a rapid flux calculation method,” Prog. Photovolt: Res. Appl. **16**, 225-233 (2008).

[12] N. Mohammad, P. Wang, D. J. Friedman, and R. Menon, “Enhancing photovoltaic output power by 3-band spectrum-splitting and concentration using a diffractive micro-optic,” Opt. Express **22**, A1519-A1525 (2014).

[13] J. Muskin, M. Ragusa, and T. Gelsthorpe, “Three-dimensional printing using a photoinitiated polymer,” J. Chem. Education **87**, 512-514 (2010).

[14] R. D. Piner, J. Zhu, F. Xu, S. Hong, and C. A. Mirkin, “Dip-pen nanolithography,” Science **283**, 661-663 (1999).

[15] S. D. Cronin, K. Sabolsky, E. M. Sabolsky, and K. A. Sierros, “Dip pen nanolithography and transfer of ZnO patterns on plastics for large-area flexible optoelectronic applications,” Thin Solid Films **552**, 50–55 (2014).

[16] R. Ng, M. Levoy, M. Bredif, G. Duval, M. Horowitz, and P. Hanrahan, “Light field photography with a hand-held plenoptic camera,” Stanford Tech Report CTSR (2005).